THESE DE DOCTORAT EN COTUTELLE

Présentée à

L'Université Tarbiat Modares et l'Université de Lille

Faculté des sciences à Université Tarbiat Modares

Ecole Doctorale Sciences pour L'Ingénieur Lille Nord-de France

Chimie inorganique et micro-nanosystèmes et capteurs

par Nasrin SHOKOUHFAR

Synthèse et caractérisation de nouvelles armatures métal-organique à base de zirconium à partir de ligands carboxylates et étude de leur application dans l'adsorption et la détection des pollutions de l'eau et la capture et la conversion du CO_2 et N_2

Soutenue le 11 decembre 2023 devant le jury composé de:

Rapporteur	Dr. Stéphane Cordier	Institut des Sciences Chimiques de Rennes, France
Rapporteur	Prof. Alireza Badiei	Université de Téhéran, Iran
Examinateur	Prof. Emmanuel Cadot	Institute Lavoisier of Versailles, France
Examinatrice	Dr. Marzieh Dadkhah Aseman	Université Tarbiat Modares, Iran
Invité	Prof. Rahmatollah Rahimi	Université des sciences et technologies, Iran
Invité	Prof. AlirReza Mahjoub	Université Tarbiat Modares, Iran
Directeur de thèse	Prof. Ali Morsali	Université Tarbiat Modares, Iran
Co-directeur de thèse	Dr. Rabah Boukherroub	IEMN, Université de Lille, France

JOINT DOCTORAL THESIS

Presented to

Tarbiat Modares University and University of Lille

Faculty of Basic Sciences at Tarbiat Modares University

Doctoral School of Sciences for Engineers Lille Nord-de France

Inorganic chemistry and Micro-nanosystems and sensors

by Nasrin SHOKOUHFAR

Synthesis and characterization of new zirconium-based metal-organic frameworks and investigation of their application in adsorption and detection of water pollutants, and CO_2 and N_2 capture and conversion

Defended on December 11, 2023 in presence of the jury composed of:

Reviewer	Dr. Stéphane Cordier	Institute of Chemical Sciences of Rennes, France
Reviewer	Prof. Alireza Badiei	University of Tehran, Iran
Examiner	Prof. Emmanuel Cadot	Lavoisier Institute of Versailles, France
Examiner	Dr. Marzieh Dadkhah Aseman	Tarbiat Modares University, Iran
Invited to jury	Prof. Rahmatollah Rahimi	Iran University of Science and Technology
Invited to jury	Prof. AlirReza Mahjoub	Tarbiat Modares University, Iran
Supervisor	Prof. Ali Morsali	Tarbiat Modares University, Iran
Co- Supervisor	Dr. Rabah Boukherroub	IEMN, University of Lille, France

Abstract

This thesis investigates the synthesis and characterization of Zr-based metal-organic frameworks (MOFs) and their applications in water treatment and solar fuel production. MOFs are porous materials composed of metal ions and organic linkers that exhibit tuneable structures and functionalities. These properties make them suitable for various applications, such as gas storage, catalysis, sensing, drug delivery, etc.

Water treatment is the process of removing contaminants from water to make it safe and clean for human use. One of the main contaminants in water are dyes, which are widely used in the textile, paper, and leather industries. Dye pollution can cause serious problems for aquatic life, human health, and aesthetic quality of water. To remove dyes from water, we synthesized a new Zr-MOF called TMU-66, which has a hollow sphere shape and an N-oxide functional group. TMU-66 can efficiently and selectively adsorb dye molecules through various interactions, such as electrostatic attraction, π-π stacking, and coordination bonding. TMU-66 exhibited an adsorption capacity of 472 mg/g for Congo red dye at pH 6.8 and 25 °C, one of the highest values achieved for MOF-based adsorbents so far.

Solar fuel production is the process of converting solar energy into chemical fuels that can be stored and used later. One of the most promising fuels is ammonia (NH_3), which can be produced from nitrogen (N_2) and water (H_2O) using sunlight as the energy source. This process is called N_2 photoreduction or photocatalytic nitrogen fixation. However, this process is challenging because N_2 is very stable and difficult to break apart. We modified another Zr-MOF called MOF-808 by adding a nitro group to its linker. The modified framework is able to absorb visible light and transfer electrons to N_2 molecules. We also combined MOF-808/NIP with another material called g-C_3N_4, which can enhance light absorption and electron transfer.

The resulting composite, MOF-808/NIP@g-C_3N_4, can produce up to 490 μmol ammonia per gram of composite per hour under visible light and ambient conditions.

In summary, the objectives of this thesis work were to investigate the potential of MOFs for two distinct applications, utilizing a conceptual design approach that incorporated bandgap engineering, structure modulation, and heterojunction composite materials. The findings revealed that MOFs can absorb water impurities and function as photocatalysts to achieve ammonia production through solar-powered N_2 photoreduction. This breakthrough has the potential to foster the creation of more effective and environmentally conscious technologies that tackle worldwide water pollution and ammonia production issues. These technologies are crucial in safeguarding our planet and guaranteeing a stable future.

Keywords: Zr-based metal-organic frameworks (MOFs), Water treatment, Congo red, TMU-66, N_2 photoreduction, MOF-808/NIP@g-C_3N_4

Résumé

Cette thèse porte sur la synthèse et la caractérisation de cadres métallo-organiques (MOF) à base de Zr et leurs applications dans le traitement de l'eau et la production de carburant solaire. Les MOF sont des matériaux poreux composés d'ions métalliques et d'éléments de liaison organiques qui présentent des structures et des fonctionnalités ajustables. Ces propriétés les rendent aptes pour diverses applications, telles que le stockage de gaz, la catalyse, la détection, l'administration de médicaments, etc.

Le traitement de l'eau consiste à éliminer les contaminants de l'eau afin de la rendre propre et sans danger pour l'homme. L'un des principaux contaminants de l'eau sont les colorants, largement utilisé dans les industries du textile, du papier et du cuir. La pollution par les colorants peut entraîner de graves problèmes pour la vie aquatique, la santé humaine et la qualité esthétique de l'eau. Pour éliminer les colorants de l'eau, nous avons synthétisé un nouveau Zr-MOF appelé TMU-66, qui a une forme de sphère creuse et un groupe fonctionnel N-oxyde. TMU-66 peut adsorber efficacement et sélectivement les molécules de colorant par le biais de diverses interactions, telles que les interactions électrostatiques, l'empilement π-π et la liaison de coordination. TMU-66 a présenté une capacité d'adsorption de 472 mg/g pour le colorant rouge Congo à un pH de 6,8 et à 25 °C, une des valeurs les plus élevées obtenues jusqu'à présent pour des adsorbants à base de MOF.

La production de combustibles solaires est le processus de conversion de l'énergie solaire en combustibles chimiques qui peuvent être stockés et utilisés ultérieurement. L'un des carburants les plus prometteurs est l'ammoniac (NH_3), qui peut être produit à partir d'azote (N_2) et d'eau (H_2O) en utilisant l'irradiation solaire comme source d'énergie. Ce processus est appelé photoréduction de N_2 ou fixation photocatalytique de l'azote. Cependant, ce processus est difficile car N_2 est très stable et difficile à décomposer. Nous avons modifié un autre Zr-MOF,

appelé MOF-808, en introduisant un groupe nitro dans le linker organique. Cette structure modifiée peut absorber la lumière visible et transférer des électrons aux molécules de N_2. Nous avons également combiné le MOF-808/NIP avec un autre matériau, le g-C_3N_4, pour améliorer l'absorption de la lumière et le transfert d'électrons. Le composite ainsi obtenue, MOF-808/NIP@g-C_3N_4, peut produire jusqu'à 490 µmol d'ammoniac par gramme de composite et par heure sous irradiation visible.

En résumé, les objectifs de ce travail de thèse étaient d'étudier le potentiel des MOF pour deux applications distinctes, en utilisant une approche conceptuelle qui intègre l'ingénierie de la bande interdite, la modulation de la structure et les matériaux composites à hétérojonction. Les résultats ont révélé que les MOF peuvent adsorber les impuretés de l'eau et fonctionner comme des photocatalyseurs pour produire de l'ammoniac grâce à la photoréduction de N_2 sous irradiation visible. Les résultats obtenus ouvrent des perspectives très intéressantes dans le domaine de traitement de l'eau polluée et de production d'ammoniac. Ces technologies sont cruciales pour sauvegarder notre planète et garantir un avenir stable.

Mots-clés : Cadre métallo-organique (MOF) à base de Zr, traitement de l'eau, rouge Congo, TMU-66, photoréduction de N_2, MOF-808/NIP@g-C_3N_4

ACKNOWLEDGMENTS

Wow, I can't believe it's finally over! After five years of hard work, sweat, and tears, I have completed my Ph.D. journey. It has been a fantastic adventure that took me from Iran to France and from chemistry to solar fuel technology.

It all started when I joined Professor Morsali's group at Tarbiat Modares University, where I fell in love with metal-organic frameworks (MOFs). These are fascinating materials that can trap molecules like a sponge or separate them like a sieve. I learned how to make and study them and had a lot of fun with my lab mates.

Then, I got the chance of a lifetime: an Eiffel Excellence Scholarship that allowed me to join the NanoBioInterfaces group at the Institute of Electronics, Microelectronics, and Nanotechnology (IEMN) at the University of Lille 1 Sciences and Technology of Lille. There, I met Dr. Boukherroub, who introduced me to the world of solar fuel production. I learned how to design and combine MOFs with graphite to make heterojunction composites that can adsorb visible light. I enjoyed working with people from different backgrounds and cultures.

First and foremost, I would like to thank God for giving me the strength, wisdom, and guidance to complete this journey. I would also like to thank my family, especially my parents and my brother, who have always been there for me and encouraged me to follow my dreams. I love you so much.

I am so grateful to my supervisors, Professor Ali Morsali and Dr. Rabah Boukherroub, for their support and inspiration. They taught me how to be a better researcher and a better person. I also want to thank my referees, Professor Emmanuel Cadot and Dr. Stéphane Cordier from France and Professor Alireza Badiei, Prof. Rahmatollah Rahimi**,** Prof. AlirReza Mahjoub, Dr. Marziyeh Dadkhah Asseman from Iran, for their valuable feedback and suggestions. I appreciate all the members of the NanoBioInterfaces group, the MOF group and the international offices of both Universities, for their friendship and collaboration. I also want to acknowledge Campus France and the French embassy in Iran for the Eiffel Excellence Scholarship program, the IEMN CNRS, and the Tarbiat Modares University for their funding and facilities.

Table of Contents

Chapter 1

Introduction

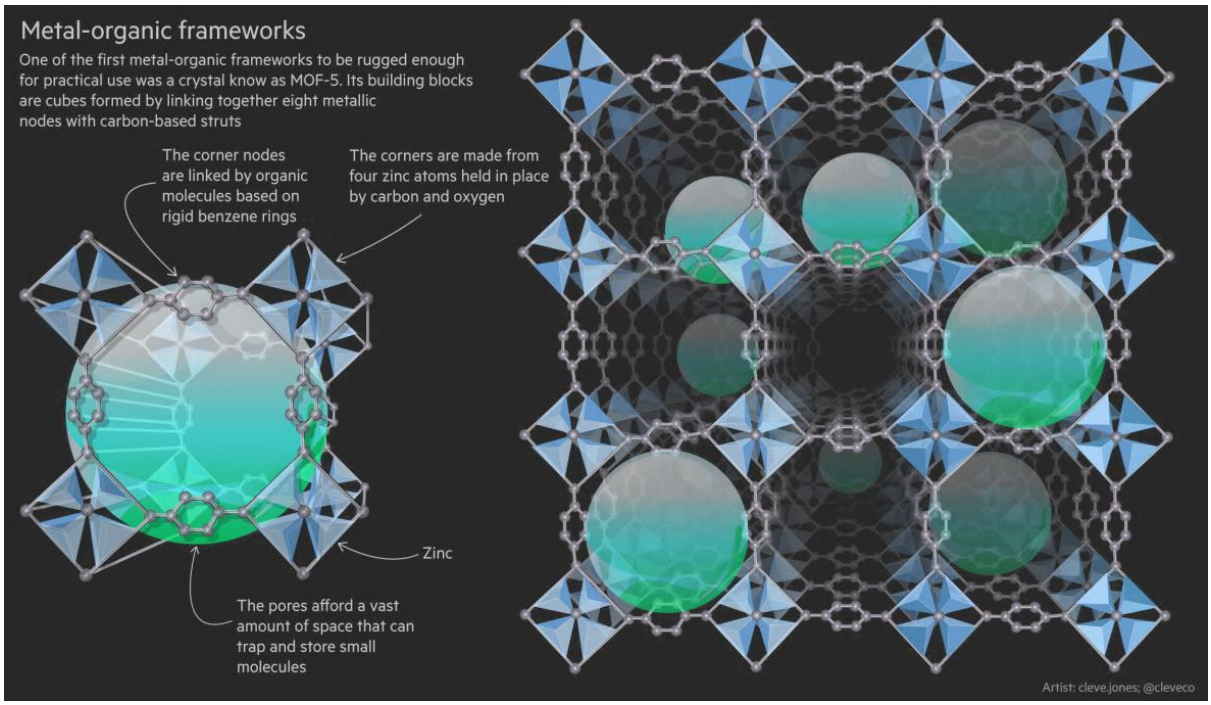

1. General Introduction

1.1 Supramolecular Chemistry

The discipline of chemistry has undergone a remarkable evolution since the early days of molecular chemistry, which consisted of interactions and combinations of atoms to create intricate molecules. Today, the field has expanded to encompass supramolecular chemistry, which delves into the fascinating study of non-covalent interactions between organized entities to produce intricate molecular assemblies.[1] These reversible interactions, which include hydrogen bonds, van der Waals forces, electrostatic and π-π interactions (Fig. 1.1), are essential in constructing complex materials and molecular machines.[2] Cooperative noncovalent interactions can form stable supramolecular complexes, despite their relative weakness compared to covalent interactions.

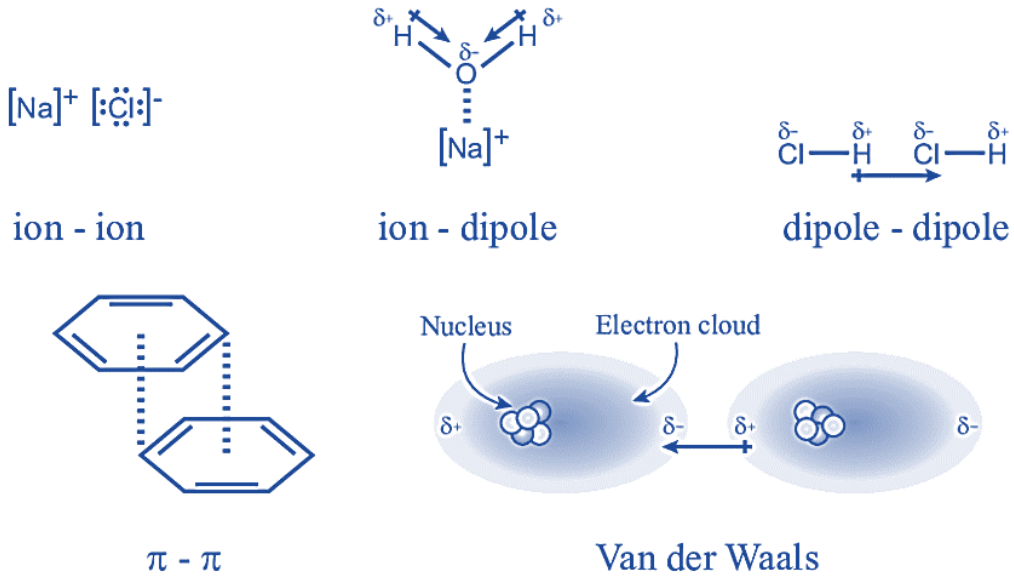

Figure 1.1. Examples of some supramolecular interactions.[3]

Supramolecular chemistry is a multidisciplinary field divided into two subgroups: host-guest chemistry and self-assembly. The difference between these two subgroups is related to the size and shape of the molecules involved. In biorecognition, host-guest interactions involve the convergence of binding sites within an organic molecule or ion, referred to as the host

component, with the diverging binding sites of a guest molecule or ion. These noncovalent complexes, as described by Donald Cram, are fundamental to various biological processes such as enzyme-inhibitor and antigen-antibody reactions, as well as coordination chemistry complexes where significant ligands act as hosts for metal cations.[4] Self-assembly refers to the natural and reversible process of smaller components combining supramolecular forces to form larger structures. It is crucial to comprehend and manipulate these principles, because the arrangement of their components frequently determines the properties of materials.[5]

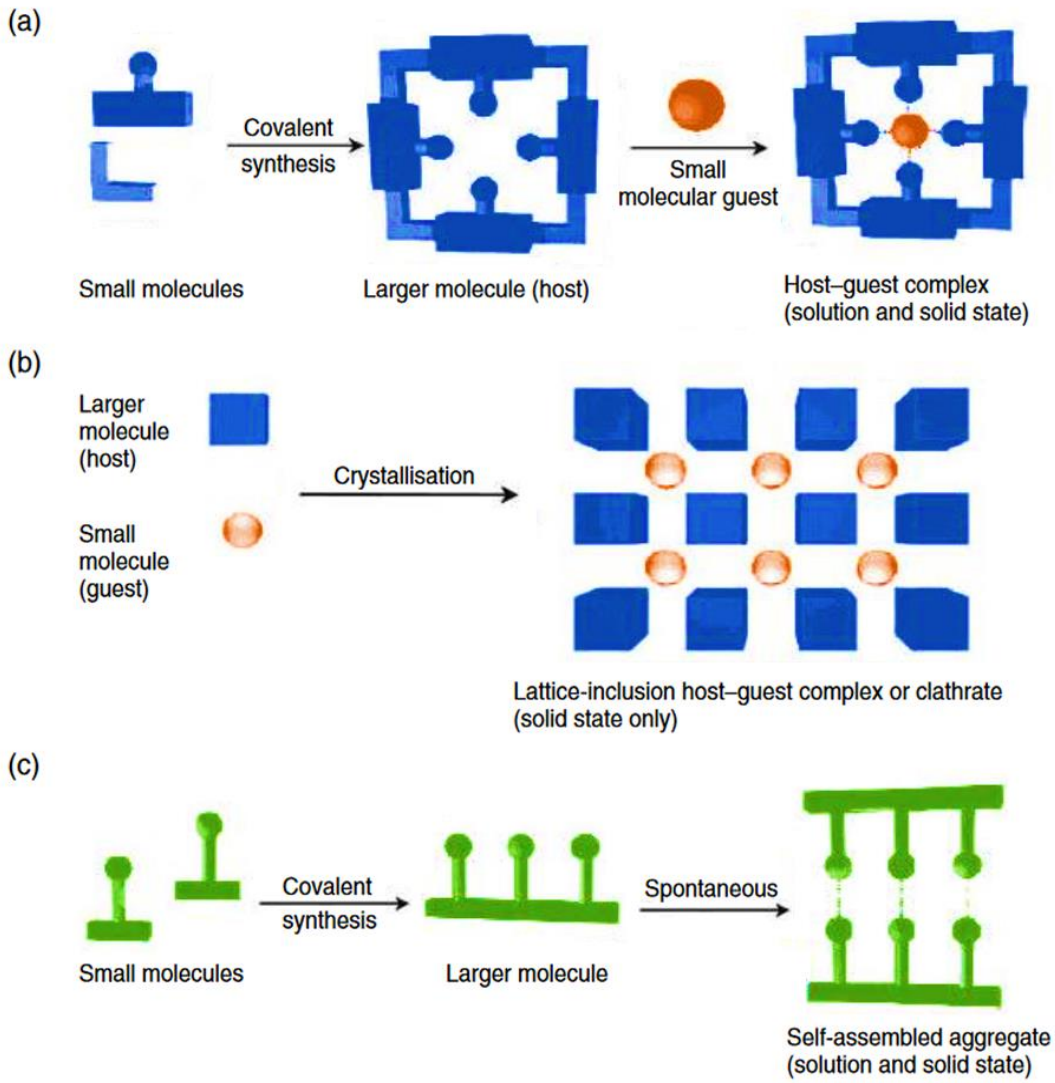

Figure 1.2 The development of a supramolecular system from molecular building blocks (binding sites represented by circles); (a) host–guest complexation; (b) lattice inclusion; (c) self-assembly between complementary molecules.[6]

1.1.1 Supramolecular Design

One of the key goals of supramolecular chemistry is to design and synthesize new materials with specific properties and functions. This includes materials with improved mechanical, optical, or electronic properties and specific catalytic or sensing capabilities. This is why, despite being a relatively young field, supramolecular chemistry has undeniably revolutionized various subfields, such as molecular recognition, molecular self-assembly, mechanically interlocked molecular architectures, template-directed synthesis, biomimetics, and molecular machinery.[6] Many noncovalent bonding interactions have been used by synthetic supramolecular chemists to create intricate and complicated structures. The first goal of supramolecular design is to provide predictability over the precise packing arrangement of structural elements in the solid state. Structure design and engineering principles and strategies are founded on two main concepts: a) supramolecular synthons, which are structural units having binding sites, and b) supramolecular interactions to hold synthons together. Supramolecular interactions are principally responsible for the packing of most crystals found thus far; therefore, information and insight obtained from studying such systems can be utilized in the rational design of innovative materials.[7,8] The qualities of a material are determined by the nature of its constituents and their interactions. Control over interactions and self-organization from suitable units enables the design of "smart" materials whose properties are dependent on molecular information. We concentrate on chemical approaches that are directed or templated to generate very complex functionalized three-dimensional coordination polymers.[9,10]

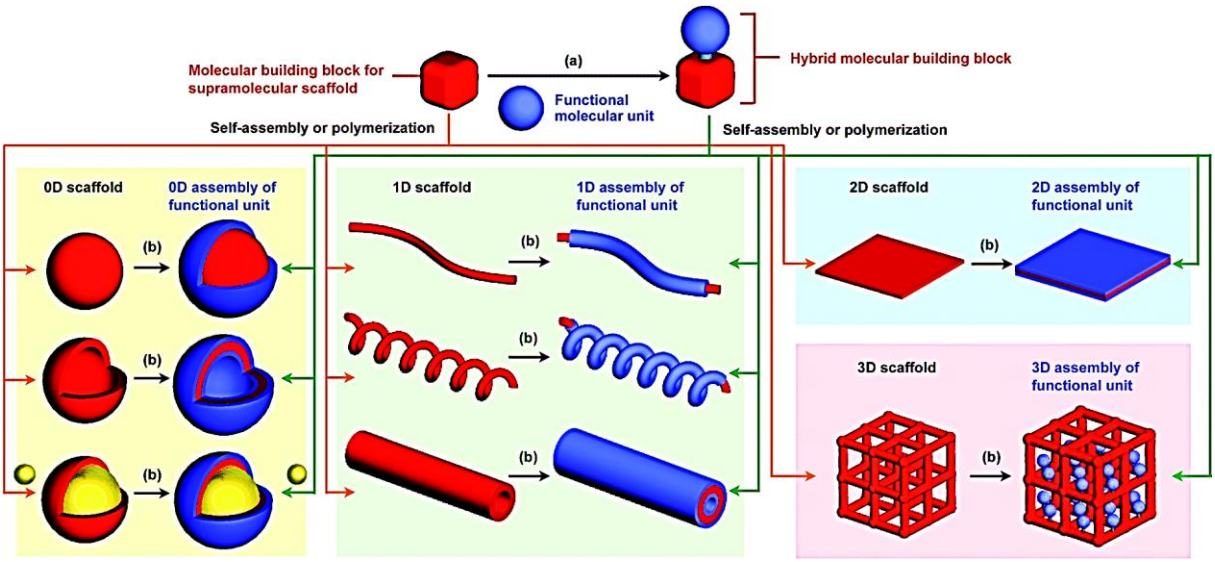

Figure 1.3. Schematic illustration of the types of supramolecular scaffolds for the controlled assembly of functional molecular units into well-defined 0D, 1D, 2D, and 3D structures. (a) Pre-functionalization and (b) post-functionalization. [11]

1.2 Coordination Chemistry

The study of coordination compounds or coordination complexes is known as coordination chemistry. These substances differ from standard covalent bonds in that they participate in coordinate (or dative) covalent bonds rather than sharing electrons from each of their two partner atoms. Coordination chemistry is crucial to properly studying chemistry since it is the chemistry of many of the metals and metalloids in the periodic table. On the other hand, understanding both organic and inorganic chemistry is even more essential, given the integration of organic moieties as ligands in coordination complexes. Although the nature of coordination compounds was gradually established and recognized throughout the 20th century, coordination chemistry was not developed until recently with the appearance of coordination polymers or metal-organic coordination networks.[12]

1.2.1 Coordination Polymers

Metal ions serve as “nodes” or connections, and ligands act as “linkers” in constructing coordination polymers, which can have an endless number of one-, two-, and three-dimensional network configurations. The geometry of the network depends on the shape, size, and density of the organic moieties as well as the coordination number of the metal nodes.[13,14] The careful selection of metal ions and ligands is the main factor in achieving a specific desired framework through rational synthesis. The choice of metal and linker together determines the structure of coordination polymers. Yet, many other metal-linker combinations might be used, making it challenging to choose materials for synthesis.[15,16] Figure 1.4 depicts the coordination polymer fabrication procedure. The capacity to tailor the desired architectural, chemical, and physical features of the resulting solid-state molecules is the coordination polymers’ key benefit. Coordination polymer bonds are mainly reversible, and faults in assembly can be remedied easily during crystal growth, in contrast to covalently bound organic polymers where mistakes are “locked-in” once created, leading to materials with highly periodic ordering. This method of ordering coordination polymers enables precise structure-property correlation through single-crystal X-ray crystallography. Supramolecular chemists are particularly interested in coordination polymers’ ability to emulate the structure and host-guest behavior of naturally occurring porous systems like zeolites.[17]

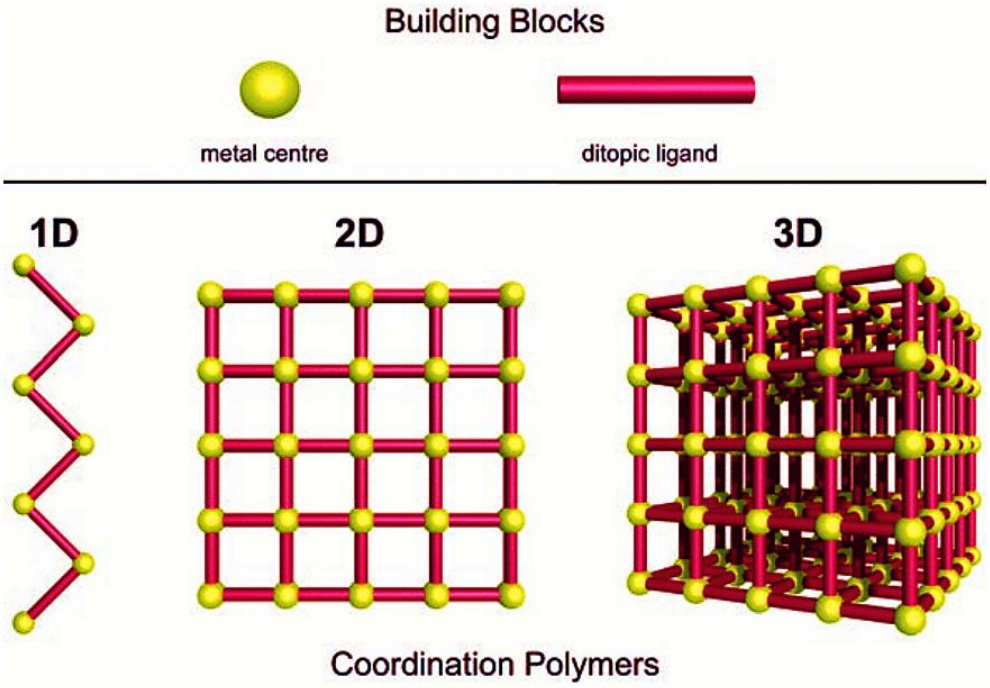

Figure 1.4. Scheme of coordination polymer formation.

In the field of porous materials, coordination polymers have recently assumed a significant role and contributed a new category to the existing taxonomy. Porous coordination compounds were divided into first, second, and third-generation groups in response to a recommendation made in 1998 (Figure 1.5).[18] The first-generation compounds contain microporous frameworks that can collapse irreversibly when the guest molecules are removed. These frameworks are only maintained by the guest molecules. When the guests are not present in the pores, the second-generation materials maintain their crystallinity, exhibit persistent porosity, and have solid and rigid frameworks. The third-generation compounds have adaptable and dynamic frameworks that change their channels or pores reversibly in response to external stimuli, including light, an electric field, and guest molecules. Many covalently bonded inorganic porous materials are categorized as second-generation compounds. On the other hand, porous coordination polymers could provide flexible and dynamic "third-generation compounds" in addition to robust "second-generation compounds."[18-20]

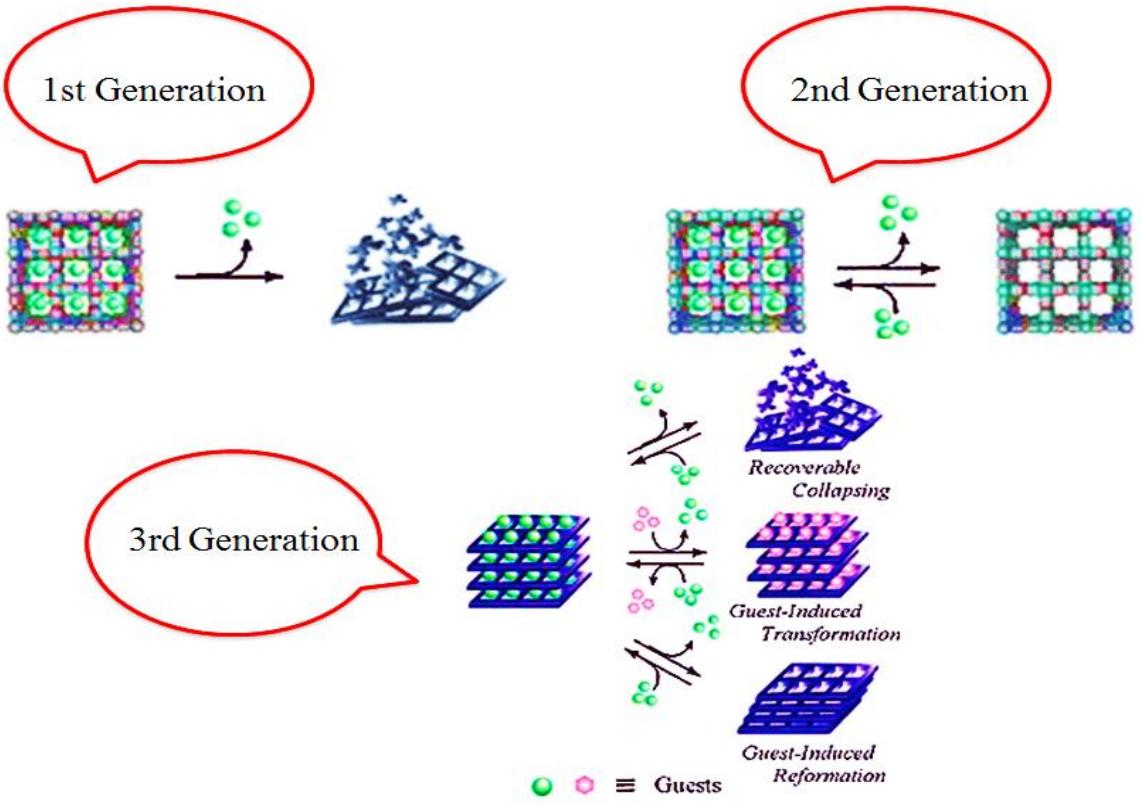

Figure 1.5. Classification of dynamic porous coordination polymers; ‘‘recoverable collapsing’’ (Type I), ‘‘guest-induced transformation’’ (Type II), and ‘‘guest-induced reformation’’ (Type III).[18]

1.3 Metal-Organic Frameworks (MOFs)

A study on coordination polymers was presented by Tomic in 1965.[19] The polymers were created using carboxylic acid linkers that had two or four coordination sites and were coordinated to metals with two, three, or four valence sites. The thermal stabilities of these polymers were analyzed and linked to the valency of the metal used, as well as the number of possible binding sites on the linker. This study played a key role in enhancing the understanding of the emergent properties of a particular subgroup of coordination polymers that would later be known as metal-organic frameworks (MOFs). Around two decades after that, Robson and Hoskins discussed that various scaffold-like materials with unlimited 3D frameworks ought to be readily accessible, versatile, and potentially valuable.[20] They hypothesized that it should be

possible to access materials with vast empty holes with low densities, while still preserving good thermal, chemical, and mechanical stability. The term "metal-organic framework" (MOF) was first used by Yaghi et al. a few years later when they reported using hydrothermal synthesis to create a 3D crystalline and open material.[21] The first framework to exhibit permanent porosity and prevent structural collapse after guest solvent molecules were removed from its pores was MOF-5, which Yaghi et al. published in 1999.[22] Shortly after, Ferey et al. successfully synthesized a highly stable MOF with large pores (30-34 Å) and high surface area using computational predictions and rational design.[23] The phrase "coordination polymer" can broadly refer to a variety of substances that may not be porous, but a metal-organic framework is a particular kind of three-dimensional crystalline coordination polymer with a framework that has relatively higher stability and permanent porosity. One gram of some MOFs has a surface area that is equivalent to an American football pitch (110 m by 49 m). If there are spaces in a solid's structure that are big enough to hold guest molecules, then it is said to be porous. According to IUPAC terminology, porous materials can be divided into three categories: microporous (pore size < 2 nm), mesoporous (2–50 nm), and macroporous (>50 nm), as illustrated in Figure 1.6.[23] Several early MOFs exhibited persistent microporosity containing pore sizes under 2 nm; in contrast, MOFs containing polydentate organic ligands exhibited mesoporous or even macroporous architectures.[24]

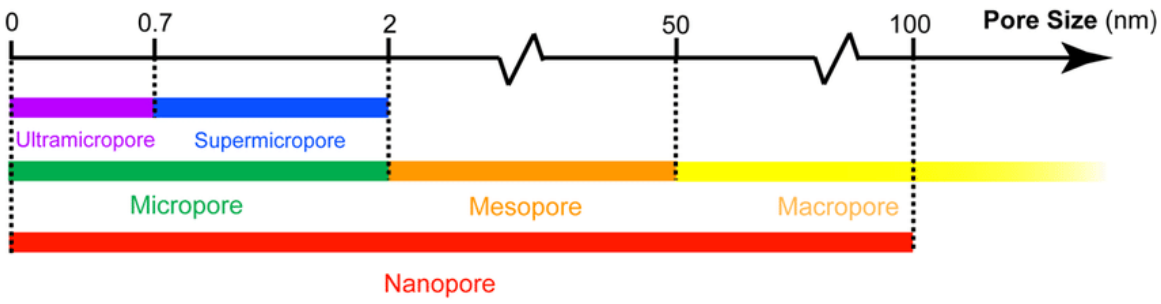

Figure 1.6. IUPAC classifications of pores based on pore width.[25]

MOFs typically consist of coordination-bound organic ligands and inorganic metal ions or metal clusters. The produced molecular-scale pores in porous structures have a number of desirable characteristics, including low density, high surface area, and high porosity. When determining the structure of MOFs, crystallinity and porosity should be considered essential characteristics. The ability to deliberately design and choose organic and inorganic molecular building blocks allows MOFs to establish a wide variety of topologies and structures, making them superior to other porous materials like zeolites and porous carbons.[26,27] Additionally, because MOFs are synthesized under pretty normal conditions, various delicate functions can be added to the framework. Creating MOFs requires careful consideration in choosing secondary building blocks (SBU) and relies on reticular chemistry. The organic linker defines the number of nodes that will be coupled, necessitating at least the usage of a ditopic linker (linear connector). In contrast, the inorganic SBU specifies the node connectivity (typically as a polyhedron where the vertices are the connection points). Several MOF structure examples and their corresponding SBUs are shown in Figure 1.7.[28] The coordination chemistry of the metal atom determines how stable the SBU and, by extension, the entire framework will be. The size and d-electron configuration of a metal atom and other factors dictated by coordination chemistry determine its preferred or typical coordination geometry. MOFs have been identified as interesting candidates for various possible applications, including gas sorption, gas separation and storage, catalysis photocatalysis, sensing, drug delivery, optical applications, and heat transformation. However, most of the previously described MOFs are sensitive to water content, because of the lability of ligand-metal bonds. Given that water or moisture is typically present in many industrial processes, as previously indicated, the MOFs' instability in water has severely restricted their further application and commercialization. Consequently, there has been a massive need for water-stable MOFs in the scientific community.

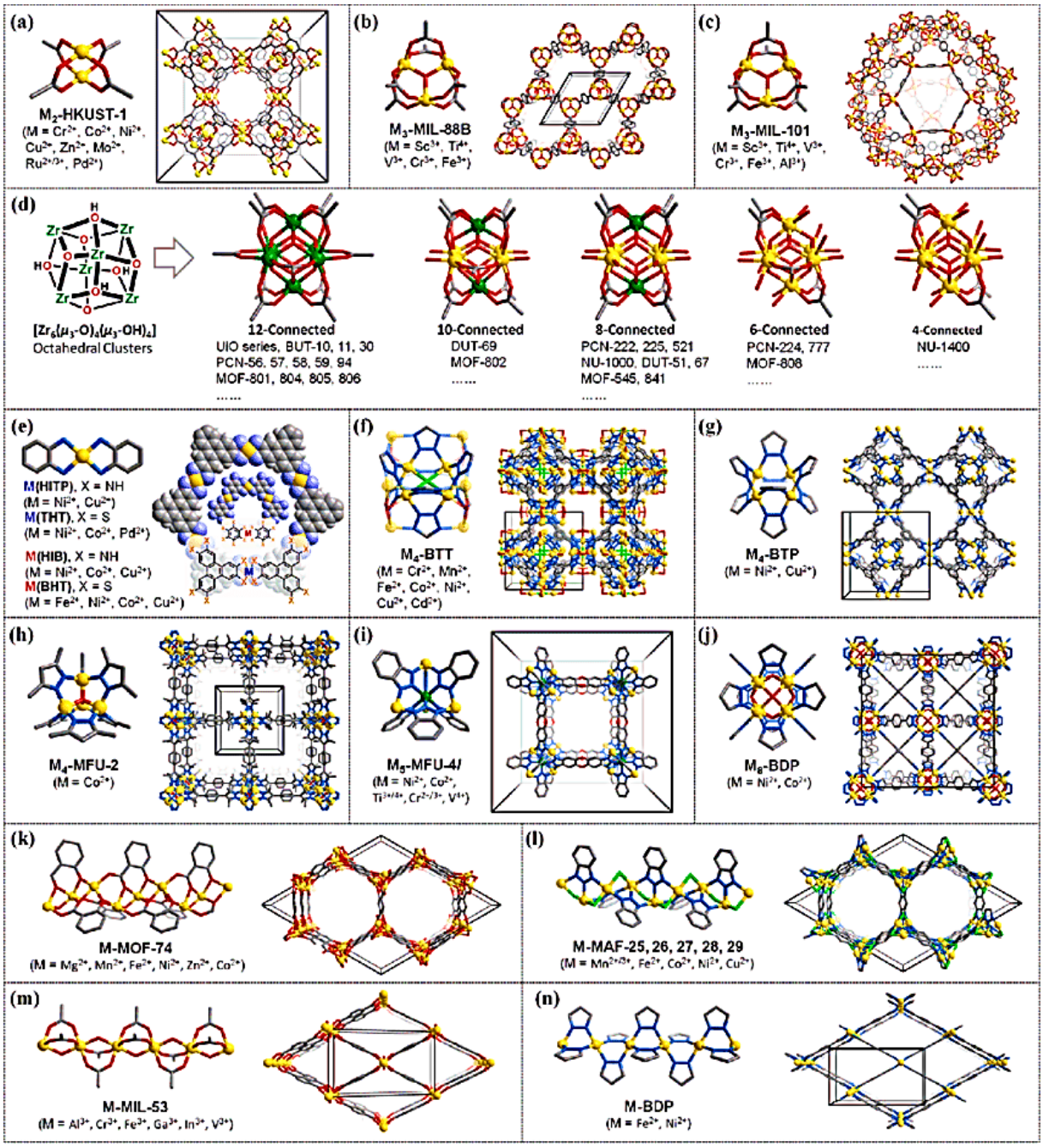

Figure 1.7. Typical MOFs constructed by high-symmetry metal clusters/chains as SBUs and organic carboxylate/azolate ligands as linkers. Ligands: Benzene-1,3,5-tricarboxylic acid (H_3BTC) for HKUST-1; terephthalic acid (H_2BDC) for MIL-88B, MIL-101, and MIL-53; 1,3,5-tri(2H-tetrazol-5-yl)benzene (H_4BTT) for M_4-BTT; 1,3,5-tri(1H-pyrazol-4-yl)benzene (H_4BTP) for M_4-BTP; 1,4-bis(3,5-dimethyl-1H-pyrazol-4-yl)benzene for MFU-2; 1,7-dihydrodibenzo[b,e][1,4]dioxino[2,3-d:7,8-d′]bis([1,2,3]triazole) for MFU-4l; 1,4-di(1H-pyrazol-4-yl)benzene(H2BDP) for M_8-BDP and M-BDP; 2,5-dihydroxyterephthalic acid for MOF-74; 1,5-dihydrobenzo[1,2-d:4,5-d′]bis([1,2,3]triazole) for MAF-25. Color code: open metal sites, yellow; inactive metal cations, green; N, blue; O, red; C, gray; Cl, light green.[28]

1.3.1 The most stable family of MOFs: Zr-based MOFs

Much work has been devoted into the development of MOFs with increased stability.[29-32] Post-treatments or post-synthetic adjustments have shown to be successful.[33-36] For example, IRMOF-1 (MOF-5) demonstrated improved moisture resistance after thermal modification and the formation of an amorphous carbon coating on the MOF particle surfaces, or after thermal vapor deposition of a thin hydrophobic polydimethylsiloxane (PDMS) layer on the MOF surface.[35,36] However, enhanced MOF stability following post-treatment always comes at the expense of reduced micropore surface areas or functioning. Furthermore, many post-treatment experimental procedures or physical approaches are labor and resource intensive. It has been suggested that several variables, including the pKa of the ligands, the oxidation state, reduction potential, and ionic radius of the metal ions, metal-ligand coordination geometry, the hydrophobicity of the pore surface, etc., influence the stability of MOFs.[37,38] The nature of both the metal ion and the ligand influences the metal-ligand bond strength, which is thought to be critical for determining the hydrothermal stability of MOFs. As a result, it is not easy to compare the bonding strength of MOFs with various metals and ligands. However, it is well known that the oxidation state, ionic radius, or charge density of the metal ions significantly impact the metal-ligand bond interactions in MOFs with a specific ligand. Generally, three types of MOFs are stable in water. 1) specific carboxylated MOFs with high valence ions in the metallic center, 2) metal ion holes shielded by hydrophobic moieties in MOFs, and 3) metallic isolated networks linked to ligands that include nitrogen.[39]

Cavka et al. discovered $Zr_6(\mu_3\text{-}O)_4(\mu_3\text{-}OH)_4(BDC)_6$ (UiO-66, UiO stands for the University of Oslo) with 12-coordinated $Zr_6(\mu_3\text{-}O)_4(\mu_3\text{-}OH)_4(CO_2)_{12}$ clusters, which was a significant step forward in this direction.[40] The structure of UiO-66 demonstrated exceptional stability, particularly hydrothermal stability, exceeding that of most previously described MOFs.[41-43] Since then, the discovery of MOFs based on Zr(IV) ions (Zr-MOFs), principally Zr(IV)

carboxylates, has resulted in the publication of novel structural types, the use of various ways to change their structures and characteristics, and the investigation of multiple functions and applications. The high oxidation state of Zr(IV) in comparison to M(I), M(II), and M(III)-based MOFs (M stands for metal element) is a significant property of Zr-MOFs. Due to high charge density and bond polarization, most carboxylate-based Zr-MOFs have a considerable affinity between Zr(IV) and carboxylate O atoms.[44] This corresponds to Pearson's hard/soft acid/base idea.[45] Zr(IV) ions and carboxylate ligands are hard acids and bases, respectively, with solid coordination bonds. As a result, most Zr-MOFs are stable in organic solvents and water and even tolerate acidic aqueous solutions. It should be noted, however, that the Zr-MOFs are still less stable in very basic aqueous solution, which may be described well by natural bond orbital (NBO) theory.[46] The NBO charge of O atoms in OH^- (-1.403) is substantially more significant than that of O atoms in the carboxylate group (-0.74), implying that OH^- can make a stronger bond with Zr(IV) than a carboxylate O atom, causing Zr-MOFs to decompose under very basic circumstances.

Enhancing the durability of MOFs can expand their potential uses and enhance their significance in critical fields like catalysis, adsorption, separation, and biomedicine.[47-50] Zirconium, owing to its abundance in nature and presence in biological systems, is especially suitable for advancing and utilizing Zr-MOFs, due to its high concentration and minimal toxicity. Although the Zr-MOF class is only a subset of the larger MOF family, Zr-MOFs have attracted extensive interest since the key discovery of the UiO-66 series, due to its superior chemical and physical characteristics. Furthermore, the tunability and possibility of adding other materials to the Zr-MOFs allows for the design of materials with specific properties tailored for various applications.

1.4 Water Treatment: MOF-based Adsorbents

1.4.1 Challenges and Solutions for Water Treatment

Water treatment has become more complex in recent years, due to a rise in pollutant species from various sources.[51] This has led to a significant increase in water contamination, making it one of the most challenging global issues. By the end of 2025, desert residents are expected to face a water crisis. While obtaining freshwater or groundwater from seawater is a viable solution, it is not an option for rural populations or those with limited resources.[52] A large amount of wastewater is released annually into freshwater and flowing water bodies, which raises continuous concerns regarding water contamination.[53] Therefore, there is a growing emphasis on drinkable water, filtration, and reuse to solve the issue of water scarcity (Fig. 1.8).

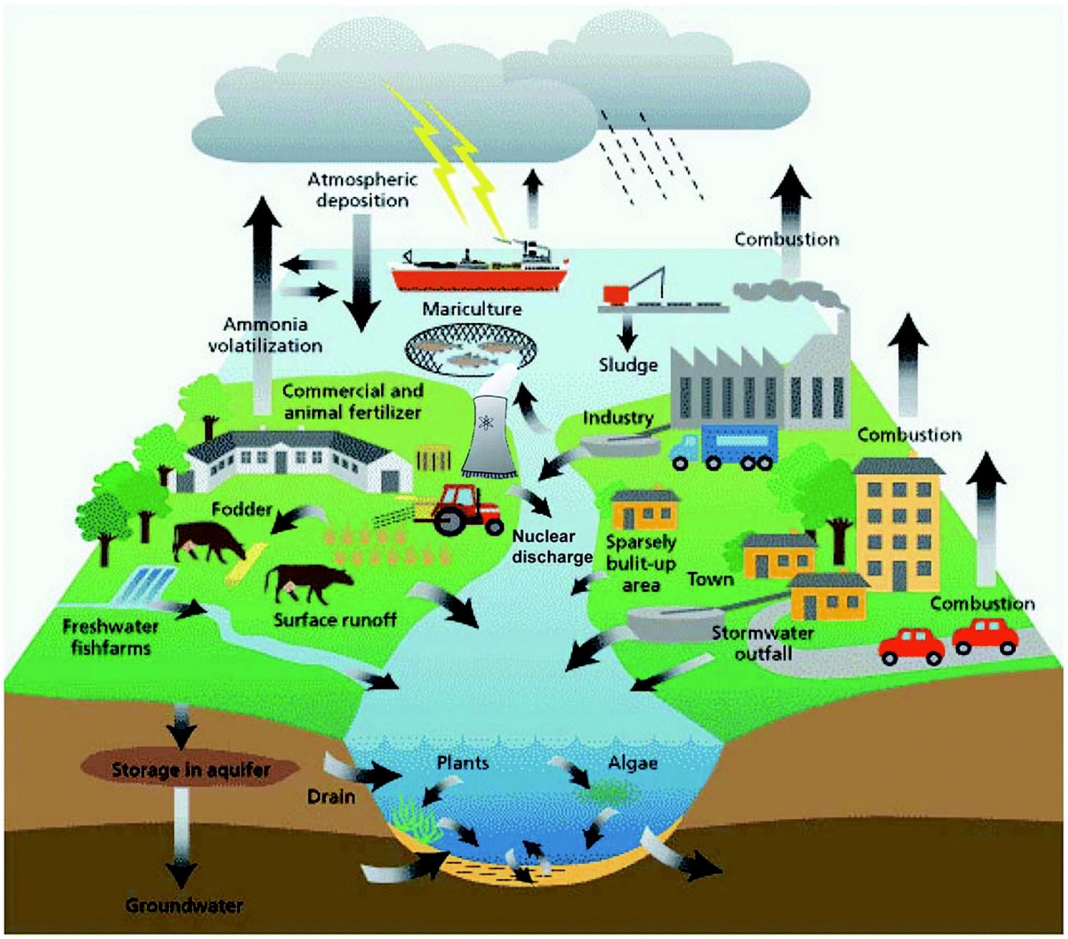

Figure 1.8. Sources of groundwater contamination in the hydrologic cycle.[54]

The existence of heavy or radioactive inorganic pollutants, such as oxyanions/cations and metal ions, poses a significant environmental threat.[55] Inorganic contaminants tend to persist in the environment longer than organic pollutants. Their charged nature makes them highly soluble in water, easily mobile, and readily taken up by living organisms. Additionally, they accumulate swiftly in the human body and food chain,[56] with a narrow margin between deficiency and toxicity. Inorganic contaminants are highly toxic and can be deadly even at low concentrations, making their elimination a top priority in water remediation processes.

A wide range of contaminants fall under the category of organic pollutants, surpassing the scope of inorganic contaminants.[57] These pollutants can stem from multiple sources and pose significant threats to the environment. Waterways, in particular, are often tainted with organic pollutants such as dyes, detergents, oils, polyaromatic hydrocarbons, pesticides, insecticides, herbicides, and personal care products and pharmaceuticals (PPCPs).[57] Many industries, farms, and households release sewage into bodies of water. Although organic pollutants may not linger as long as inorganic ones, their constant generation in contemporary societies makes them appear almost permanent in our environment. The number of dyes released into the environment by the printing and dyeing industries has dramatically increased during the past century. Organic dyes are commonly used to colour fabrics, paper, rubber, leather, printing, plastic, and other materials.[58] Among the top three contemporary polluters, the textile sector uses more than 700,000 metric tonnes of dye annually. Organic chemicals, which are teratogenic and carcinogenic, make up most of the colours used.[59] Aromatic organic dyes are one of the most prevalent organic contaminants found in industrial effluents. Scientists have devoted significant efforts to overcoming this challenge since learning about the dangers associated with dyeing materials, and as a result, several chemical, biological, and physical solutions for wastewater treatment have been developed (Fig. 1.9).

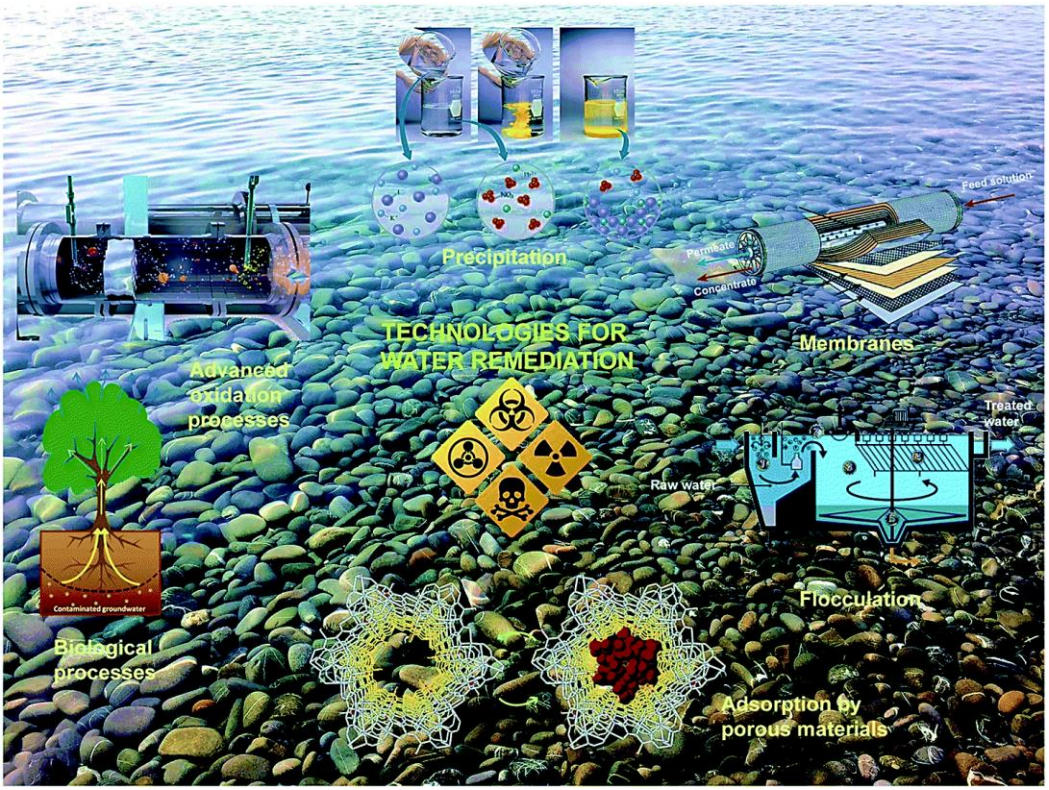

Figure 1.9. Current technologies and processes for water decontamination.[55]

These methods include membrane separation, advanced oxidation processes, ion exchange, flocculation, adsorption, photocatalysis, biodegradation, coagulation, and electrochemical processes. Table 1.1 displays the key benefits and drawbacks of various techniques. Biological approaches are eco-friendlier and more straightforward than other methods. Microorganisms may decolorize dyes, but only under controlled environmental circumstances. A bioreactor must be built, which takes time and requires a specialized site.[60] Because of their durability and inflexible structure, biological techniques are inefficient at degrading dyes. Disposing of a substantial volume of sludge is a fundamental problem with biological processes. While the chemical method is advantageous and practicable, but the mud deposition raises the procedure's cost. The most significant disadvantage of chemical technology is that it requires many chemicals and electricity.[61] Because of its great oxidizing characteristics, advanced oxidation processes have received a lot of attention. However, while these processes are efficient, they

are expensive, and the production of oxide intermediates are harmful to organisms.[62,63] As a result of the preceding, it is evident that these procedures are economically unfavorable. Traditional approaches include membrane separation and adsorption technology. Membrane separation is a very effective method that comprises nanofiltration, ultrafiltration, microfiltration, and reverse osmosis.[64] However, membrane technology in wastewater treatment is not a typical practice, and while utilizing membranes is cost-effective, they can contaminate the water.[65] According to the literature, the adsorption method is the most often utilized technology for the remediation of dye wastewater, due to its flexibility, low-cost treatment and overall efficacy.[66] Furthermore, even though several issues must be addressed, the adsorption mode does not produce any dangerous pollutants.[67]

Table 1.1 The advantages and disadvantages of different dye removal technologies.

Technology	Disadvantages	Advantages
Biodegradation	Occupies a particular land area Requires strict external environmental conditions Slow process	Economically attractive Simple
Membrane separation	Short lifetime Economically unfeasible	High efficiency Reuses salts
Electrochemical process	High electricity consumption Economically unfeasible	High efficiency Rapid
Ion exchange	Economically unattractive Ineffective for certain dyes	No loss of sorbents
Coagulation/Flocculation	High sludge production Disposal issues	Simple Economically attractive
Photochemical process	Formation of by-products Power consumption	No sludge production Rapid
Adsorption	Ineffective for certain dyes Costly regeneration Disposal of adsorbent residue Loss of adsorbents	High efficiency Simple operation process Low cost Does not form hazardous substances

Adsorption using porous materials has emerged as one of the most promising techniques for water purification during the last few decades.[68,69] Porous materials, such as zeolites, activated

carbon, silica, polymeric materials and hybrid materials[70,71] (Fig. 1.10) have piqued the interest of scientists for adsorption processes, because they may be good candidates to overcome the obstacles (i.e., low capacity, weak interaction, and difficulty in regeneration) for contaminant removal in water purification.[72] Nonetheless, aside from surface size, the number of active sites is an unavoidable issue that must be considered. Therefore, to reliably and efficiently access clean water in a cost-effective way, superior adsorbents with a high number of active sites and surface areas are desirable.

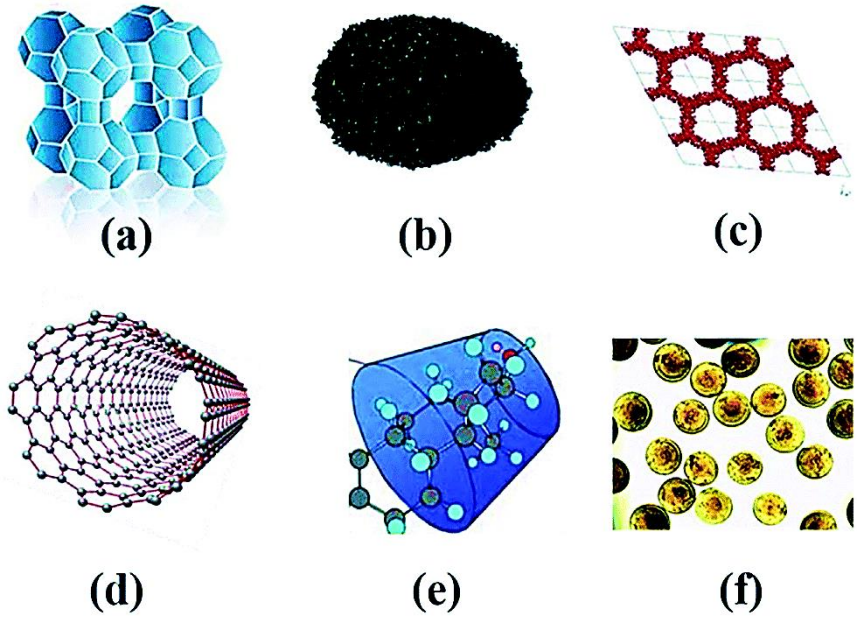

Figure 1.10. Different types of adsorbents used for the removal of Emerging contaminants: (**a**) zeolites, (**b**) activated carbon, (**c**) mesoporous silica, (**d**) carbon nanotubes, (**e**) cyclodextrins, and (**f**) chitosan beads.[73]

1.4.2 Characteristics of MOFs as Adsorbents

In recent years, highly ordered and porous crystalline MOFs have been recognized as a potential alternative to overcome the technical limitations of conventional porous and nano-based materials for environmental applications. MOFs offer a fascinating alternative platform for use in water remediation applications as adsorbents. As mentioned, MOFs are porous and structurally diverse materials made up of metal nodes bridged by organic linkers. MOFs can be effectively tailored to yield materials with precisely ordered structures,[74] abundant active

metal sites.[75] enhanced surface area,[76] and tuneable functional groups.[77] Nowadays, MOFs can be synthesized on a large scale through low-price and simple synthetic methods. These exceptional characteristics make MOFs and MOF-based composites auspicious next-generation adsorbent materials with remarkably high adsorption efficiencies for removing toxic waste-related metal ions[78] and organic contaminants[79] from wastewater.

When it comes to using MOFs for water purification, the focus is on four main factors: water stability, adsorption capacity, interaction, and regeneration. Water stability is crucial for the practical application of MOFs in water purification.[80,81] It is the most critical factor to consider since it directly impacts the efficacy of the filtration process. Another essential factor that demonstrates the substantial performances of MOFs is adsorption capacity (including selectivity), which is primarily impacted by interactions between pollutants and MOFs (active sites or functional groups). Finally, regeneration determines the ability of MOFs to operate continuously.

Substantial progress has been made in using MOFs for liquid-phase adsorption and separation. This progress began with investigating phenomena, followed by the goal-oriented design of task-specific MOFs and, finally, the implementation of device applications. The key to this progress lies in a deep understanding of host-guest interactions and rational framework design. Organic ligands, metal ions/clusters, and architectural diversity are crucial elements in the design of task-specific frameworks for liquid-phase adsorption and separation.[82] Figure 1.11 illustrates that the framework can be rationally designed before synthesis or post-modified by various means, allowing for the rational tuning of the inner surface and architectural properties.

MOFs have been widely studied for their application in liquid phase adsorption and separation, as they can be used for a wide range of objectives. MOFs, such as the NUs (short for Northwestern University),[83] MIL series (short for Materials from Institute Lavoisier),[84] ZIFs

(short for Zeolitic Imidazolate Frameworks),[85] UiOs (short for University of Oslo),[86] and PCNs (short for Porous Coordination Network).[87] have been extensively investigated for their ability to uptake/separate various chemicals. Furthermore, the intrinsic mechanisms of molecular recognition have become increasingly apparent, allowing researchers to perform goal-directed design on MOFs in this area.

The rational design of the physical and chemical properties of frameworks is highly effective for adsorbing and separating different molecules. This is because such properties determine the interactions between the host and guest molecules and their size matching, mobility, and recognition within the pores.[88,89] Chemical properties include charge states, acid-base properties, polarity, and even stability in different solvents, while physical properties include window size, channel diameter, porosity, morphology, dimensions, and flexibility.[90] The functional strategies depend on the specific guest molecules that must be separated or adsorbed.

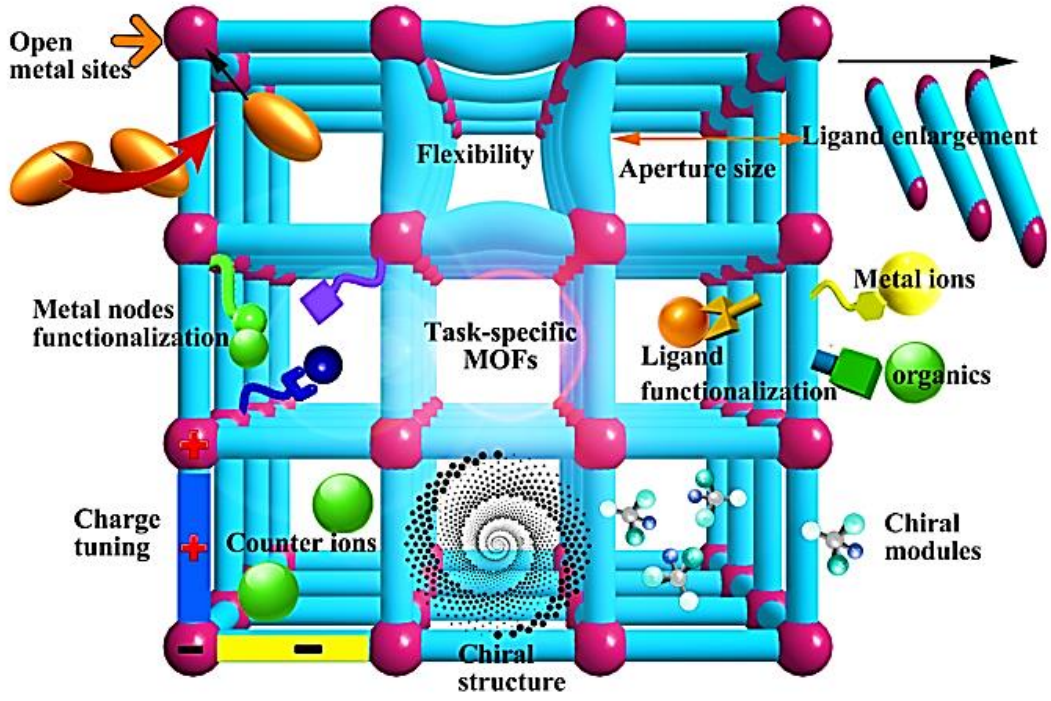

Figure 1.11. Design methodologies of task-specific MOFs for the adsorption/separation of various chemicals in the liquid phase.[91]

1.5 Solar to Fuel Conversion: Photocatalytic Nitrogen Fixation by MOFs

1.5.1 Photocatalysis for Solar Fuel Production

The consumption of fossil fuels has resulted in significant environmental problems, including dramatic changes in the Earth's climate. To address these issues and the energy crisis, there is a growing need for sustainable and clean energy alternatives. Solar fuel is a promising solution, which can be produced in the form of hydrogen, hydrocarbons, or other high-energy carriers by converting solar energy into chemical energy.[92,93] Photocatalysis is an attractive and straightforward method for producing solar fuel from solar energy utilization. The most promising approaches for solar fuel production include photocatalytic water splitting that generates hydrogen (H_2),[94] photocatalytic carbon dioxide (CO_2) reduction that produces hydrocarbon fuels (such as carbon monoxide (CO), methanol (CH_3OH), methane (CH_4), formic acid (HCOOH)),[95] and photocatalytic nitrogen fixation that forms hydro nitrogen compounds (such as ammonia (NH_3)).[96] The process of photocatalytic solar-to-fuel conversion in artificial photosynthetic systems involves a three-step procedure. Initially, light-harvesting chromophores absorb photons, followed by the spatial migration and separation of carriers. Finally, the photogenerated charges are utilized to drive redox reactions.[97] The overall efficacy of the system is determined by the collective efficiency of these three steps.

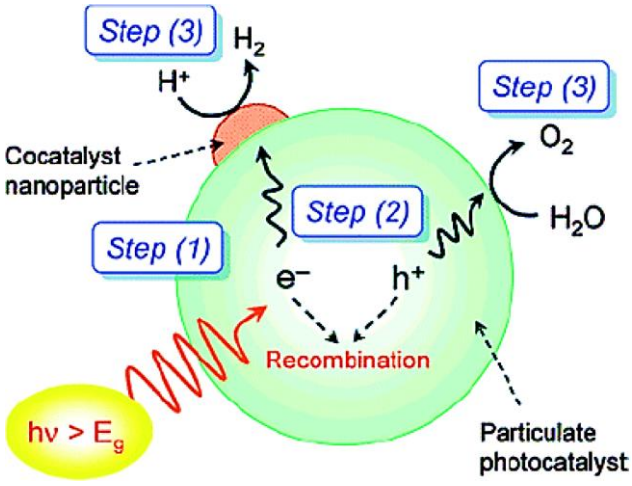

Figure 1.12. The significant processes in classic photocatalysis system.[97]

To initiate solar energy conversion into fuel, it is essential to match the photon energy uptake with the band gap energy, enabling thermodynamically uphill transformations.[99,100] Sunlight can be categorized into three groups based on their wavelengths: ultraviolet light (UV, $\lambda < 400$ nm, $E > 3.20$ eV, accounting for approximately 4% of the total solar energy), visible light (vis, 400 nm $< \lambda <$ 800 nm, $3.20 > E > 1.60$ eV, accounting for approximately 43%), and near-infrared light (NIR, $\lambda >$ 800 nm, $E < 1.60$ eV, accounting for about 53%).[101] In a study conducted by Prof. Domen,[94] it was noted that the solar-to-hydrogen conversion efficiency (STH) cannot exceed 2% if only the UV part of sunlight is utilized. However, by extending the light absorption edges to 700 or 1000 nm, the ideal STH can reach 25% or 47%, respectively. This means that for efficient artificial photosynthetic systems to be constructed, light harvesters must absorb most sunlight (>400 nm). Therefore, research has focused on designing photocatalysts that can efficiently operate under visible light.

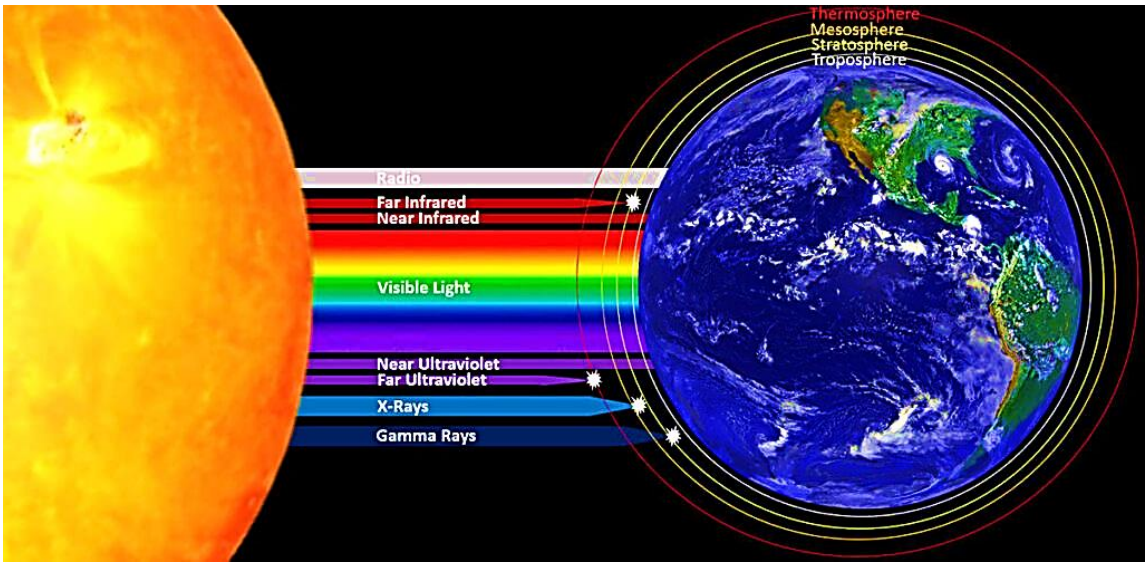

Figure 1.13. Absorption of solar radiation in the atmosphere.

Up to date, research has concentrated on creating photocatalysts that operate well when exposed to visible light. However, most inorganic semiconductor photocatalysts do not react to visible light. Additionally, increasing the visible light collecting capability is not accessible

by only changing their architecture. The most popular method for reducing band gap is to dope ultraviolet-active metal oxides with foreign elements. Because organic dye molecules may be tailored, another idea is to use organic chromophores as visible light-collecting antennas.[102,103] However, because organic dye molecules move inexorably, self-quenching and photobleaching are inescapable issues. Therefore, the ongoing objective for solar-to-fuel conversion is the development of novel photocatalyst materials to improve the catalytic efficiency under visible-light irradiation. Functional nanomaterials have been widely used as photocatalysts for energy conversion systems. These materials include metal oxides, metal phosphides, metal sulfides, and carbon-based composites.[104] However, these photocatalysts still face various challenges, such as low electronic conductivity and poor apparent quantum efficiency of the metal oxides-based photocatalysts, rapid recombination of the charge carriers of the metal phosphides-based photocatalysts, poor chemical stability of the metal sulfides-based photocatalysts, and poor cycling stability of the carbon materials-based photocatalysts.[105] Therefore, it is highly desirable to construct superior functional materials that exhibit outstanding overall photocatalytic performances.

1.5.2 MOF-based Photocatalysis for Solar Fuel Production

MOFs are typically constructed from semiconducting quantum dots that are regularly distributed throughout the architecture and separated by customizable organic linkers. Due to their semiconductor-like characteristics, MOFs have attracted much attention for their prospective application in photocatalysis.[106] The frameworks' metal-organic linkages, which give rise to the highest occupied molecular orbital (HOMO) and lowest unoccupied molecular orbital (LUMO), are the cause of these characteristics. The bandgap—the difference in energy between these two states—can be managed by picking the suitable multidentate metal ions and organic ligands.[107] Generally, the two efficient techniques of metal substitution and ligand post-synthetic modification/exchange yield MOFs adjustable structures, pore properties, and band

edge positions, demonstrating a tailorable semiconducting behaviour. The semiconducting behaviour of MOFs can be controlled in several ways to modify their bandgap. Firstly, the linkers can be functionalized with suitable groups, which increases the HOMO energy. Secondly, the metal nodes can be selected based on their electron-rich character, which reduces the LUMO energy. Finally, MOF-composite photocatalysts can be fabricated to introduce a new electron transport channel, which improves the separation and transfer efficiency of electrons and holes.

In a study conducted by Kuc et al.,[108] the bandgaps of several MOFs were calculated, and it was concluded that all of them exhibited semiconductor behaviour with bandgaps ranging from 1.0-5.5 eV. It was also observed that the bandgap values can be adjusted by manipulating the degree of conjugation in the organic ligands.[109] For example, increasing the length of the linkers can result in a smaller bandgap, but this may cause the MOF system to lose stiffness due to ligand distortion, resulting in lower crystalline symmetry.[108] Some MOFs have both catalyst and semiconductor properties, making them potential heterogeneous photocatalysts. In a recent study, Nasalevich et al. outlined the different roles of MOFs in photocatalytic engineering: (1) as photocatalysts, where the organic ligands of MOFs function as light-harvesting antennae and media for transferring photo-induced electrons to the metal clusters; (2) as containers to encapsulate other photocatalysts, and (3) as electron-transferring media, facilitating the transfer of charge carriers between MOFs and encapsulated photocatalysts, as illustrated in Figure 1.14.[110]

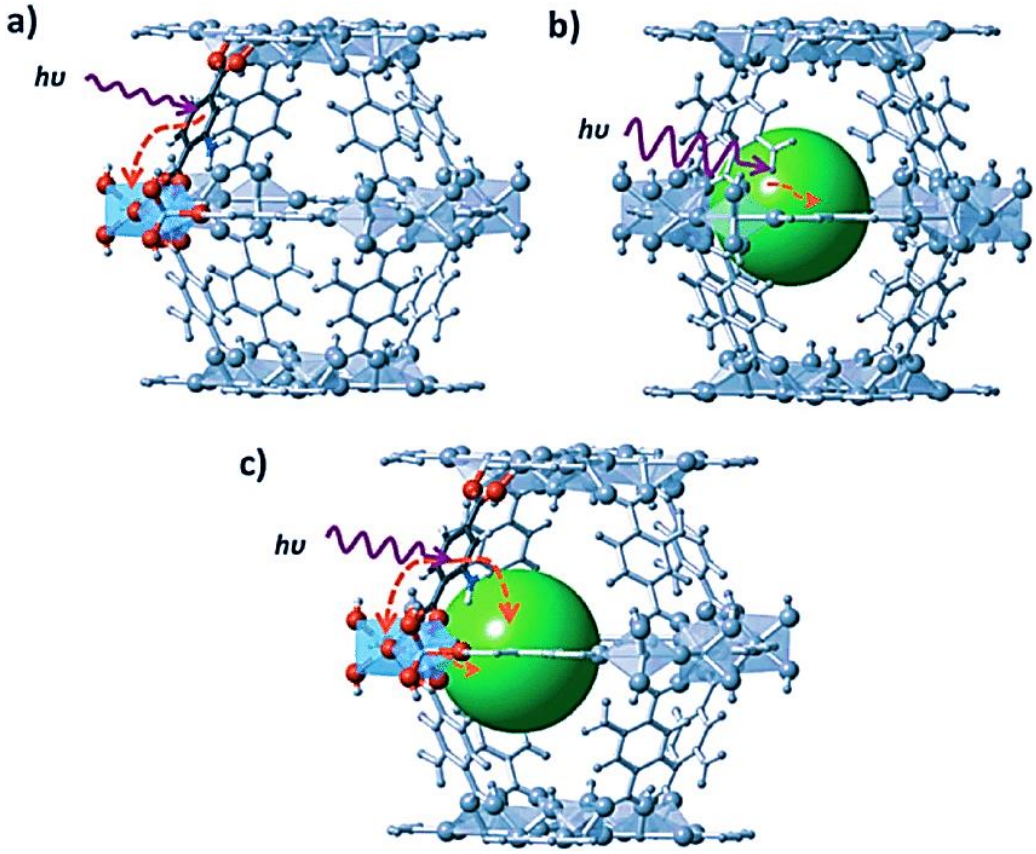

Figure 1.14. Various roles of MOFs in photocatalytic engineering: (**a**) MOFs as photocatalysts; (**b**) MOFs as a container to encapsulate other photocatalysts; (**c**) MOFs as an electron-transferring medium.[110]

Two approaches are commonly applied to prepare MOFs able to absorb visible light, which accounts for over 42% of total solar radiation. The first strategy involves the introduction of functionalized organic ligands, such as porphyrins,[111] nitro and amino terephthalate,[112] into MOFs. Notably, the bandgap of MOFs can be adjusted by varying the degree of conjugation or functional group modification in the ligands.[113] In 2015, Hen-Drickx et al. synthesized UiO-66 using different ligands, including H_2BDC, H_2BDC-OH, H_2BDC-2,5OH, H_2BDC-NH_2, H_2BDC-2,5NH_2 and H_2BDC-2,5SH, respectively. These various MOFs showed strong visible light absorption and exhibited different colours based on the "push–pull" effect caused by the electron-donating ability of the additional substituents.[114] The second strategy involves introducing metal-oxo complexes as dopants into MOFs, which can also change their absorption ability,[115] similar to the doping method in semiconductors.

The active centres within MOFs play a crucial role in their effectiveness as catalysts for chemical reactions, particularly in photocatalytic redox reactions.[116,117] Unfortunately, pure MOFs typically feature unsaturated metal or metal oxide clusters as active centres, which suffer from limited photocatalytic activity due to electron and hole recombination. However, the photocatalytic activity of MOFs can be enhanced by introducing additional vibrant centres through post-synthetic modification strategies or by creating MOF-based composites with integrated cocatalysts.[118,119] For instance, a potential solution to the challenge of rapid recombination of active species in pure MOF is to implement a semi-conductor p-n heterojunction. This approach entails separating photogenerated electrons and holes by directing electrons toward n-type semiconductors and holes toward p-type semiconductors. The resulting electric field across the heterointerface facilitates the longevity of active species, allowing them to interact with the substrate for the photoreduction reaction. Subudhi et al. developed a heterojunction architecture of cobalt titanate integrated UiO-66-NH_2 ($CoTiO_3$/UiO-66-NH_2 p–n junction), displaying enhanced photocatalytic activities toward norfloxacin degradation and H_2 production.[120]

In summary as it shown in Figure 1.15, there are five strategies that can help enhance the photocatalytic performance of MOFs: (i) Utilizing longer linkers to intensify the degree of conjugation and lower the bandgap energy. (ii) Creating structural defects that lead to meso/macro pores in MOFs, thereby facilitating the capture of photogenerated electrons for subsequent redox reactions at surface active sites. (iii) Using porphyrins, nitro, and amino functional linkers. (iv) Post-synthetic functionalization of the metal nodes. (v) Constructing MOF-based composite photocatalysts, such as heterojunction, homojunction or Schottky junctions (Fig. 1.21), to introduce additional catalytic centers into the MOF system. This approach enhances the utilization efficiency of active sites.

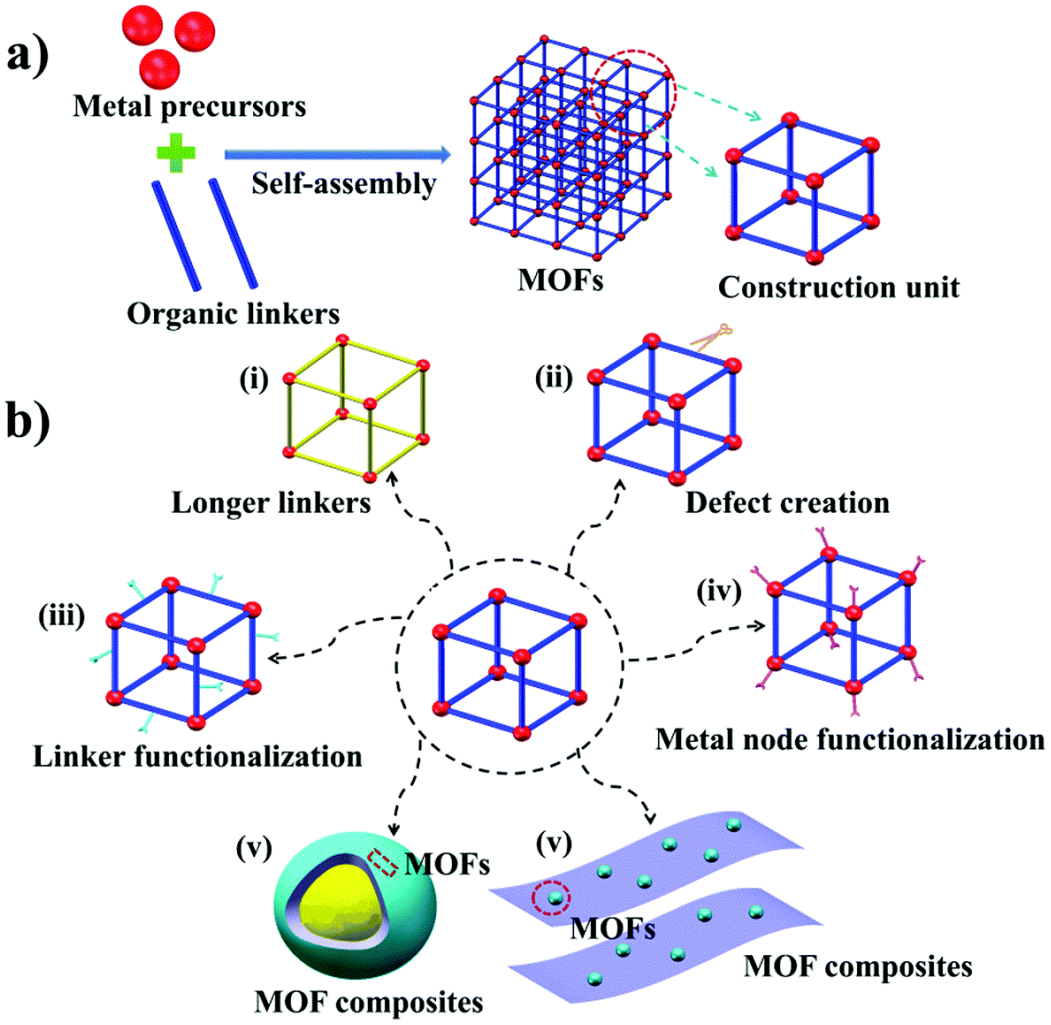

Figure 1.15. Graphical representation of MOFs and strategies for boosting the photocatalytic performance of MOFs.

1.5.3 Photocatalytic N_2 Fixation: Sustainable Ammonia Synthesis Method

Nitrogen (N) is a necessary element in the periodic table. It makes up 78% of the atmosphere of the blue planet in the form of N_2, and, more importantly, it serves as the basis for the development of a variety of bio-macromolecules, including proteins and nucleic acids, as well as nitrogenated compounds from sectors that connect the agricultural and food cycle.[121,122] However, it is of little direct value because of the difficulty in breaking and hydrogenating the N≡N triple bond, which is required to make various vital organic and inorganic chemicals.[123] Therefore, the considerable form of N_2 molecules like ammonia and nitrate is necessary for the complete community of living species, including those in the plant, animal, and microbial

realms, to meet their needs.[124] Since then, the scientific community has given considerably greater emphasis and attention to converting nitrogen into its fully hydrogenated form, which is ammonia and other nitrate-based compounds. Ammonia is regarded as one of the most valuable resources in the economy, and carbon-free fuels like H_2 (18% H_2 and easily liquefied at 10 atm and ambient temperature) are what is bringing the world into a new era of prosperity and sustainability.[125] Ammonia is also used in agriculture to make nitrogenous fertilizers to meet the growing population's demand for food. Ammonia can be viewed as a potentially renewable alternative to non-renewable fuels to address the energy needs of a future civilized society, because of its high energy potential (15.3 MJ/L), easy handling, transportation and storage facilities.[126] Natural nitrogen fixation was caused by a geochemical (lightning flash) and biological (nitrogenase enzyme) mechanism. However, because the conversion ratio is so much lower, it cannot meet the demands of human society to increase food production.[127] In summary, Figure 1.16 shows the nitrogen cycle and the numerous mechanisms that lead to dinitrogen fixation. However, the energy-intensive Haber-Bosch (HB) method for ammonia synthesis was discovered in the 19th century, and it sparked a revolution in the agricultural industry by boosting crop yields and the global economy.[128] Additionally, the HB process makes it possible to commercialize ammonia, contributing about 150 metric tonnes of NH_3 annually, of which 80% are used in agricultural production. This has the potential to satisfy the demand of the expanding industry.[129] The Haber-Bosch process has been the main method used for industrial-scale production and management of the global ammonia market. Ammonia synthesis is reversible and exothermic, meaning lower temperatures are more favourable, according to Le Chatelier's principle. However, despite this fact, the production rate is often prolonged and does not meet industrial requirements.[130]

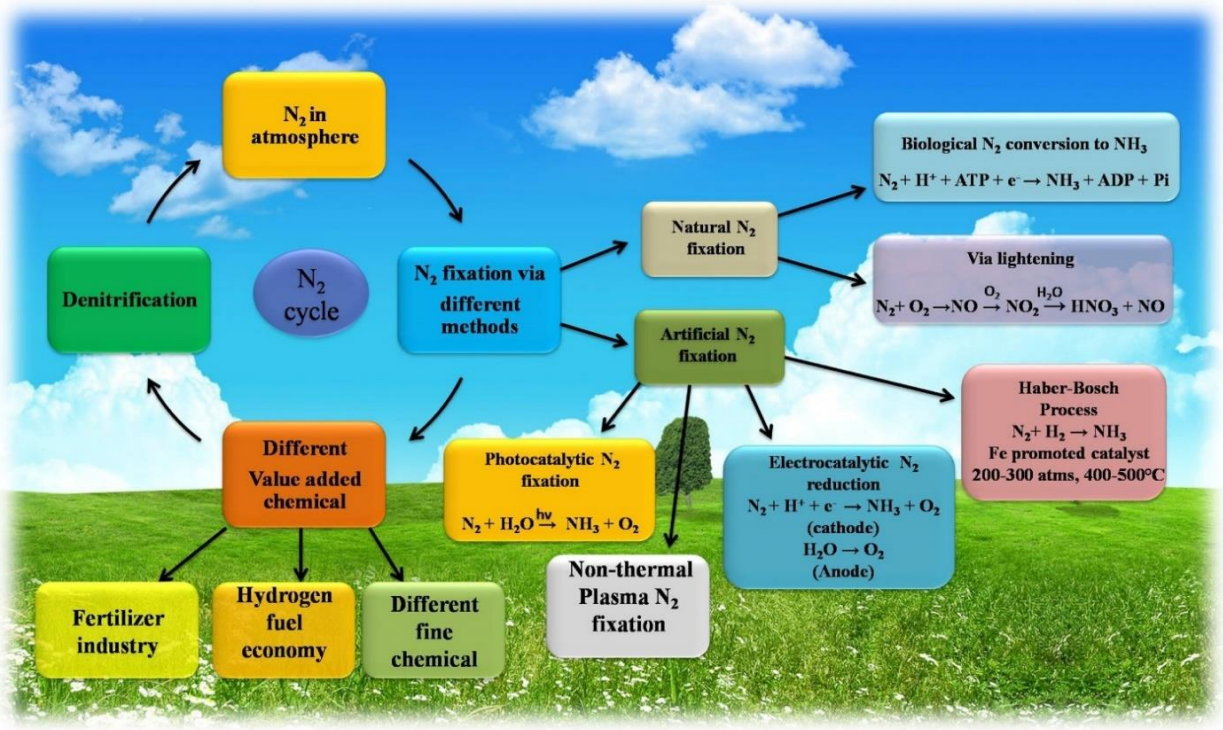

Figure 1.16. Scheme of the nitrogen cycle, different methods for ammonia synthesis, and various applications of NH_3.

The Haber-Bosch process is responsible for 1-2% of the world's annual energy consumption and uses 3-5% of natural gas and 1-3% of global electrical energy.[131] While the process relies heavily on non-renewable fossil fuels and harms the environment and living beings, it remains the most widely used method for ammonia production. Creating a green, sustainable, and affordable way for ammonia production to keep up with the increasing demand is a significant challenge for the scientific community. Multiple approaches have been explored to address this issue, including electrocatalysis, bio-catalysis, photocatalysis, and photo(electro)catalysis. Nevertheless, these techniques are presently limited to small-scale production in a laboratory setting and are insufficient to satisfy worldwide requirements.[131] It is widely known that producing one gram of ammonia through industrial processes requires considerable energy, ranging from 3.5×10^4–5×10^4 J, and can cause environmental damage. However, By achieving a Faradic efficiency exceeding 50% via electrocatalysis and a conversion efficiency

of 10% through photocatalysis, we can safely produce one gram of NH_3 from water with minimal environmental impact, requiring only 1.9×10^5 J and 2×10^5 J of energy respectively. Unfortunately, these methods are not yet efficient enough to meet industrial standards for ammonia production. Still, researchers are working on improving the efficiency of photocatalytic and electrocatalytic N_2 fixation techniques through catalyst modification strategies.[132]

Naturally, the nitrogenase enzyme (FeCo, FeFe, or FeV co-factor) present in Azotobacter uses an energy transporter (ATP) to produce ammonia by transferring multiple protons and electrons.[133]

$$N_2 + 16ATP + 8H^+ + 8e^- \rightarrow 2NH_3 + H_2 + 16ADP + 16Pi \quad (1\text{-}1)$$

ADP: adenosine diphosphate and Pi: inorganic phosphate

($\triangle G_0 = -248$ kJ/mol at pH 7.0 and 310 K)

This beautiful concept from a natural phenomenon has inspired a new method of ammonia synthesis using photocatalytic reduction of nitrogen. This process can produce carbon-free and sustainable ammonia under ambient conditions using renewable sources, such as sun and water. In this green synthesis, nitrogen molecules from the atmosphere are used as nitrogen sources, while water is the source of protons. The process occurs under normal conditions and offers a promising solution to achieving clean and sustainable ammonia production. However, the low yield of ammonia is a concern as the formed NH_3 may get oxidized to its corresponding nitrate form.

1.5.3.1 Fundamental Aspects of N_2 Fixation to NH_3

While theoretically possible, dinitrogen fixation is not an easy process to achieve under normal conditions. The reason for this is due to several factors, including the short and robust N≡N bond (measuring at 109 pm), the high bond energy (at 945.33 kJ/mol), the high ionization value

(at 15.85 eV), the low proton affinity (at 1.90 eV), the absence of a dipole moment or non-polarity character, the negative electron affinity (at -1.8 eV), and a wide HOMO (σ_g2p)-LUMO ($^*\pi_g2p$) gap (at 22.9 eV).[122,132]

$$N_2(g) + 3H_2(g) \rightarrow 2NH_3(g) \qquad \triangle H^\circ = -92.22 \text{ kJ/mol}, \triangle S^\circ = -99 \text{ J/mol}*\text{K} \qquad (1\text{-}2)$$

$$N_2(g) + 6e^- + 6H^+ \rightarrow 2NH_3 \qquad E_0 = -0.148\text{V } \textit{vs.}\text{ RHE} \qquad (1\text{-}3)$$

The first equation pertains to the overall thermodynamic equation, while the second equation pertains to the ionic equation for NH_3 formation in an aqueous environment. Unfortunately, the creation of high-energy intermediates like diazene ($\triangle H_f^\circ$ = +212.9 kJ/mol) and hydrazine ($\triangle H_f^\circ$ = +95.35 kJ/mol) in a water medium hinders the nitrogen reduction reaction NRR process. The process of N_2 fixation comprises three stages. Initially, nitrogen is adsorbed onto the catalytic surface. Subsequently, hydrogenation takes place, followed by cleavage, or vice versa. Finally, ammonia is produced and released from the catalyst. In essence, N_2 is chemically adsorbed onto the reactive site and activated through electron gain from the catalyst, resulting in the reduction of N_2 to NH_3. Transition metal-based catalysts are deemed superior, due to their vacant and occupied d-orbitals that facilitate the robust binding of nitrogen and metal centers.[126] During this process, the metal's vacant orbital receives lone-pair electrons of N_2, and, in turn, donates its electrons to the π-antibonding orbital of nitrogen. This donation, known as π back-donation, results in the weakening of the triple bond of dinitrogen.[125] The concept of back-donation can be quite complicated for main group compounds, but it is beneficial for p-block sp^2 and sp^3 (as shown in Fig. 1.17).[126]

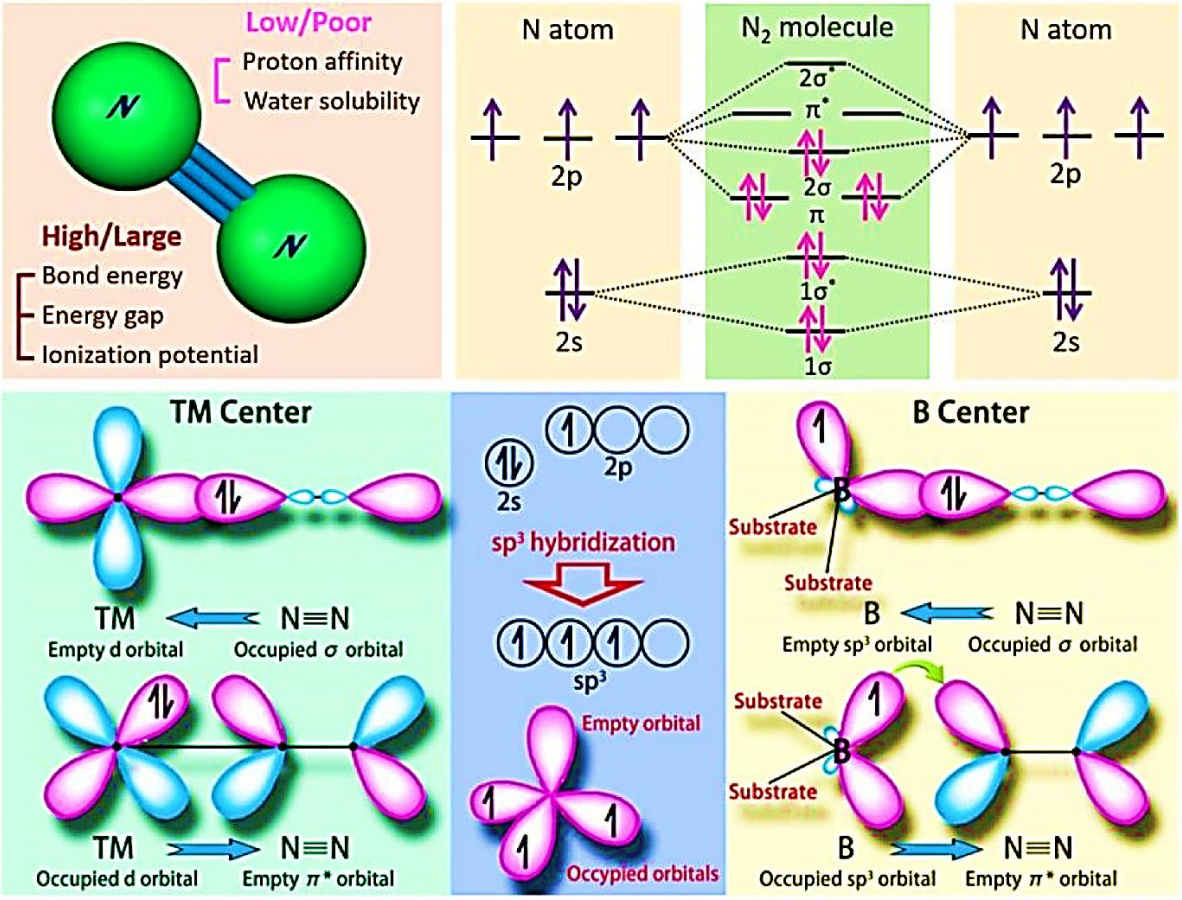

Figure 1.17. Representation of the molecular orbital diagram of N_2 along with transition metal and dinitrogen orbital interaction *via* the back donation concept.[126]

1.5.3.2 Reaction Pathways of Nitrogen Fixation

For nitrogen reduction reaction (NRR) to be effective, dinitrogen must chemisorb onto the catalyst. Based on the mode of nitrogen adsorption and hydrogenation, NRR mechanisms can be classified into two pathways: dissociation and association pathways, as illustrated in Figure 1.18.[134] In the dissociation pathway, N_2 molecules undergo dissociation into N radicals or N atoms, which then bind to the catalyst surface. Subsequently, these radicals or atoms undergo hydrogenation and reduction, eventually producing ammonia. This pathway is particularly pertinent to the Haber-Bosch process. The association pathway involves the adsorption of N_2 molecules on the catalyst's surface, which can occur in two modes: "side-on" or "end-on". Nitrogenase enzymes generally use the "side-on" mode for N_2 fixation. In this mode, both N

atoms in the N_2 molecule form weak bonds with the catalyst, making them chemically equivalent. The N≡N triple bond is then broken, and the N atoms undergo alternating hydrogenation to ultimately form NH_3. When N_2 molecule binds to the catalyst surface in the "end-on" mode, only one N atom binds. Since the two N atoms are not the same, there are two pathways for the hydrogenation process: the alternative pathway and the distal pathway. In the alternative pathway, the two N atoms are hydrogenated alternatively, similar to the "side-on" mode. In the distal pathway, the uncoordinated N atom is hydrogenated and released first. Then, the other N atom (coordinated with the catalyst) is gradually hydrogenated to transform to NH_3, like the "dissociation pathway". The actual reaction pathway of NRR is complicated and may involve multiple reaction pathways mentioned above. Moreover, the coordination environment around the metal ions on the catalyst's surface will also impact the reduction pathways of NRR.

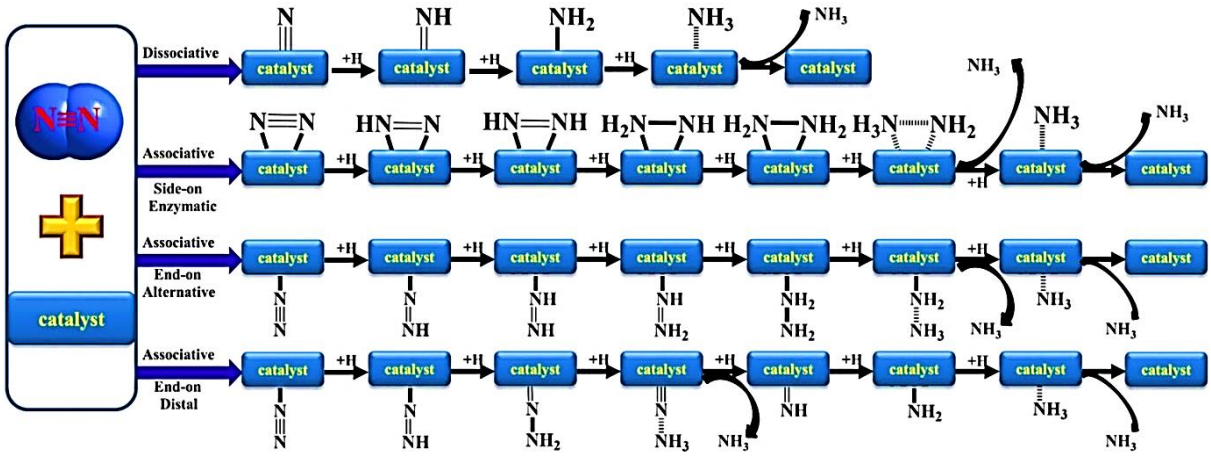

Figure 1.18. Schematic diagrams of different reaction pathways of nitrogen fixation.

Yao and his team proposed an associative pathway for di-nitrogen reduction over Au surface. They used SEIRS (surface-enhanced infrared absorption spectroscopy) characterization to study the process. The N_2H_y species, formed during NRR, exhibits trademark IR bands at 1453, 1298, and 1109 cm^{-1} corresponding to N-H bending, -NH_2 wagging, and N-N stretching vibration respectively. These bands indicate the above associative route, as proposed by Yao

and his team.[135] *In situ* FTIR is a useful technique for characterizing the adsorption, activation, and reaction pathways during dinitrogen reduction in the presence of N_2 gas and water vapor. The IR band observed at 1655 cm^{-1} represents chemisorbed N_2, and over time, the intensity of this peak gradually increases. Upon exposure to light, the system detects two distinct and robust infrared peaks at 1460 and 1740 cm^{-1}. These peaks signify the H-N-H bending mode of vibration, indicating the generation of either ammonia or ammonium ion. Additionally, an asymmetric deformation vibrational band of NH_4^+ is observed at 1648 cm^{-1}, along with two asymmetric stretching modes of the N-H bond at 3246 and 3555 cm^{-1}, respectively.[128,136]

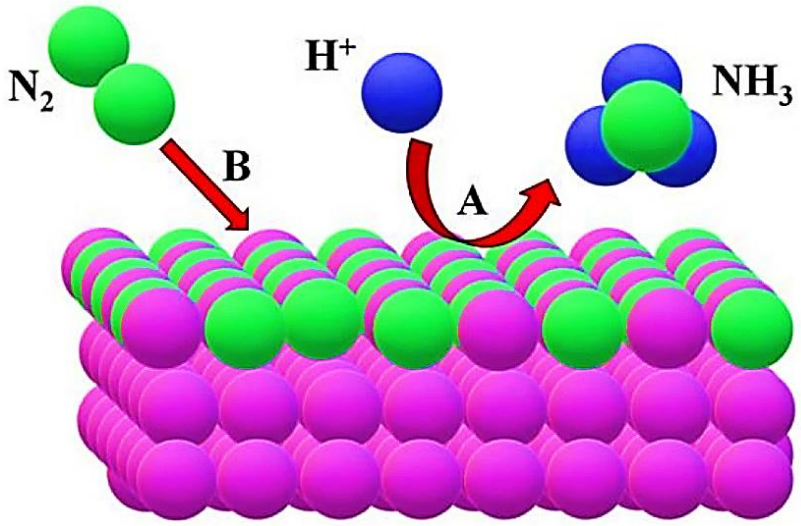

Figure 1.19. Schematic representation of Mars-van Krevelen reaction mechanism for N_2 reduction over the surface of transition metal nitrides (TMN) (* A: the surface of TMN reduced N_2 to ammonia and B: Regeneration of the vacancy by gaseous N_2).[128]

Apart from the mechanism described for NH_3 generation, the Mars-van Krevelen (Mvk) N_2 reduction pathway over transition metal nitride (TMN) is also a highly accepted way of generating NH_3 (shown in Figure 1.19).[128] In this process, the nitrogen atom of TMN is reduced to NH_3, and the N-vacancy is simultaneously refilled by the supplied N_2 gas to restore the catalyst.[137] According to computational calculation, the Mvk pathway for N_2 fixation over TMNs is more feasible than the stereotypical associative and dissociative pathways, because

(i) N_2 isolation from TMNs catalyst surface *via* dissociative route is quite frustrating due to the large activation energy barrier and endothermic nature, and (ii) there is a high overpotential value for N_2 reduction in the associative mechanism.[138] Li. et al. reported Mvk type mechanism for N_2 reduction over KOH etched g-C_3N_4.[128]

1.5.3.3 Techniques to Boost the Catalytic Efficiency in N_2 Fixation

In order to overcome the challenges associated with the industrial-scale production of NH_3 *via* light-driven dinitrogen fixation, researchers worldwide have been working on various photocatalyst and material modification techniques. These include doping with metal or non-metal, adding noble metal to semiconductors, creating hetero/homo-junctions between semiconductors, implementing double or Z/S-scheme charge transfer dynamics, leveraging defect/vacancy chemistry, facet/edge engineering, and tuning via carbon-allotropes (such as graphene, C-dot, CNT, etc.). Among these techniques, vacancy or defect chemistry - specifically oxygen vacancies (OVs), nitrogen vacancies (NVs), and sulphur vacancies (SVs) - have shown promise in improving the NRR catalytic efficiency of materials, as shown in Figure 1.20.[139,140] Various types of vacancies found in a catalyst have the potential to impact its characteristics, including adsorption, charge separation, migration, and electronic structure. More significantly, they can lower the activation energy necessary for reactions to proceed smoothly, which makes them highly valuable. These defect sites can also function as photoexcited electron-hole pair traps, hindering the rate of recombination. Furthermore, N_2 molecules can be adsorbed on these vacancies and undergo back-donation, which weakens the strong triple bond in N_2, making the cleavage and protonation process more accessible.[139] In a different method, the catalyst's lattice structure is doped with foreign or heteroatoms, cha nging the catalyst's surface texture, electrical characteristics, chemical composition, adsorptio n and desorption behavior, and optical response.

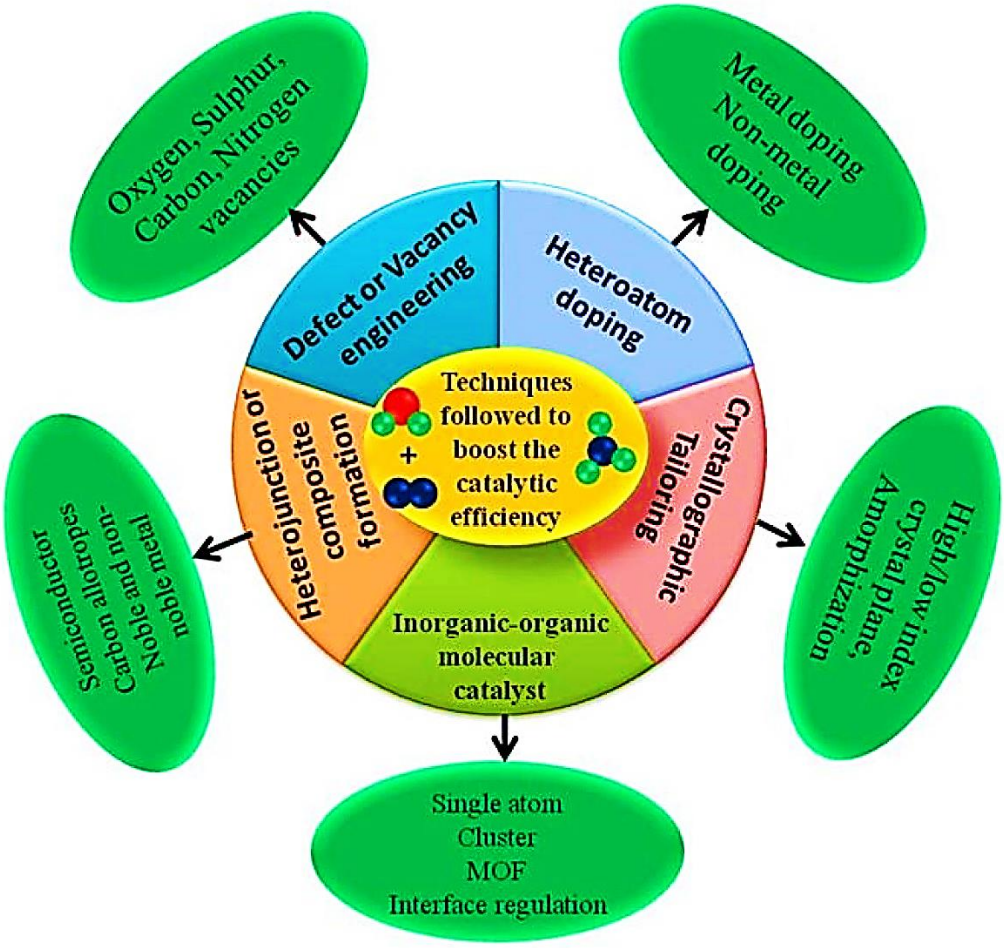

Figure 1.20. Schematic representation of different catalyst modification techniques.

The formation of an impurity or subenergy band within the material's bandgap as a result of d oping metal (transition elements) or nonmetal (S, C, O, P, etc.) results in a widening of the lig ht absorption range (redshift or decrease in the bandgap) and an increase in the charge transfe r process.[141,142] Edge engineering, which adds heterogeneity to the edge site, electrical configuration, and functions of the specimen, is another technique for adjusting the catalytic performance of 2D-based photocatalytic materials. Because this region (edge) has more active sites with a higher energy density than the basal plane, it has been found that graphene's edge carbon atoms are more catalytically active than basal plane C-atoms. For 2D metal chalcogenides, such as MoS_2, similar forms of edge chemistry have also been found.[143] According to the computational work on MXene, metal-containing terminal sites are more

capable of activating N_2 and exhibit higher NRR activity than the oxygen-functional groups (directly related to metal atoms) that compose the terminal surface. Furthermore, because of its poor N_2 binding capacity, the basal plane has a low nitrogen reduction efficiency.[144] The single-atom catalyst is another intriguing heterogeneous catalysis approach, with the source of increased activity being the maximal availability of atomic sites. In this case, metal atoms are bonded to a support material, resulting in unique physio-chemical properties.[145] Facet engineering of crystals is gaining popularity, because it allows for introducing a specific facet or crystal plane at the atomic level (i.e., arrangement of atoms on distinct lattice planes) that improves the material's catalytic behaviour. According to computer studies, intermediates produced during NRR are more tightly bound to step atoms than terrace atoms, because they provide more active sites for adsorption and activation.[146] Numerous aspects and surfaces of nanomaterials, such as the (001) plane of BiOCl NSs, the (411) facet of Pt, and the (111) facets of octahedral Pd NPs, have demonstrated promising results in photocatalysis.[147]

Carbon derivatives, including CNTs, rGO, graphene, activated carbon, and carbon dots, are commonly utilized in conjunction with semiconductors to construct highly effective photocatalytic systems. Carbon plays a crucial role in the heterojunction for several reasons: it acts as an electron sink, accepting and directing charge carriers; it functions as a support; it inhibits nanoparticle aggregation; it adsorbs substrate to promote better interaction; it acts as a mediator, and it contributes to shaping the material's morphology during preparation, which affects its adsorption and light absorption capabilities.[148] Cluster catalysts and bio-memetic nitrogenase-type catalytic systems are another intriguing class of catalysts for enhancing NRR performance.[149] The catalytic response of the material is, technically speaking, magnified many times when cocatalysts (reduction, oxidation, and plasmonic type) are loaded over a photocatalyst. This method is widely used to boost a semiconducting photocatalyst's ability to split water molecules, reduce CO_2, and fix nitrogen dioxide. Cocatalyst often lowers the

activation energy barrier, prevents excitons from recombining, and shields the materials from photo-corrosion. The cocatalyst is unique due to these distinguishing characteristics, and as a result, its presence boosts the system's catalytic potential.[150]

A further promising and doable method to improve the catalytic efficiency of the photocatalysts towards NRR and other photocatalytic reactions is the construction of a semiconductor-semiconductor heterojunction (binary or multijunction)-based photocatalytic system. The integration of two or more semiconducting materials, where an internal electric field is generated at the interface or junction point, can best achieve the two most demanding properties of the photocatalyst—light absorption and charge carrier separation ability—because this slows down the recombination process and raises charge carrier densities. The heterojunction system boasts superior catalytic efficiency thanks to a specific mechanism. This mechanism can be classified in two ways: double charge transfer, which falls into categories 1 or 2, or Z-scheme, which may or may not require a mediator (Fig. 1.21). With double charge transfer, electrons that are photoexcited jump from the conduction band (CB) of one semiconductor (A) with a more negative potential to the CB of another semiconductor (B) with a less harmful potential. Meanwhile, holes migrate from the valency band (VB) of a semiconductor with a higher positive potential to the VB of another semiconductor with a lower potential. In contrast, with the Z or S scheme-type charge migration pathway, electrons from the CB of one photocatalyst combine with the holes from the VB of other semiconductors *via* a mediator or without a mediator. This way, the photogenerated electrons are available in the CB of one catalyst to carry out reduction, and holes are available in the VB of another catalyst to bring about oxidation.[151] After exposure to the appropriate amount of light, photoexcited electron-hole pairs were generated. Strong interfacial contact and junction creation prevent charge carrier recombination, prolonging the lifetime of excitons, and promote catalysis in the catalytic system.

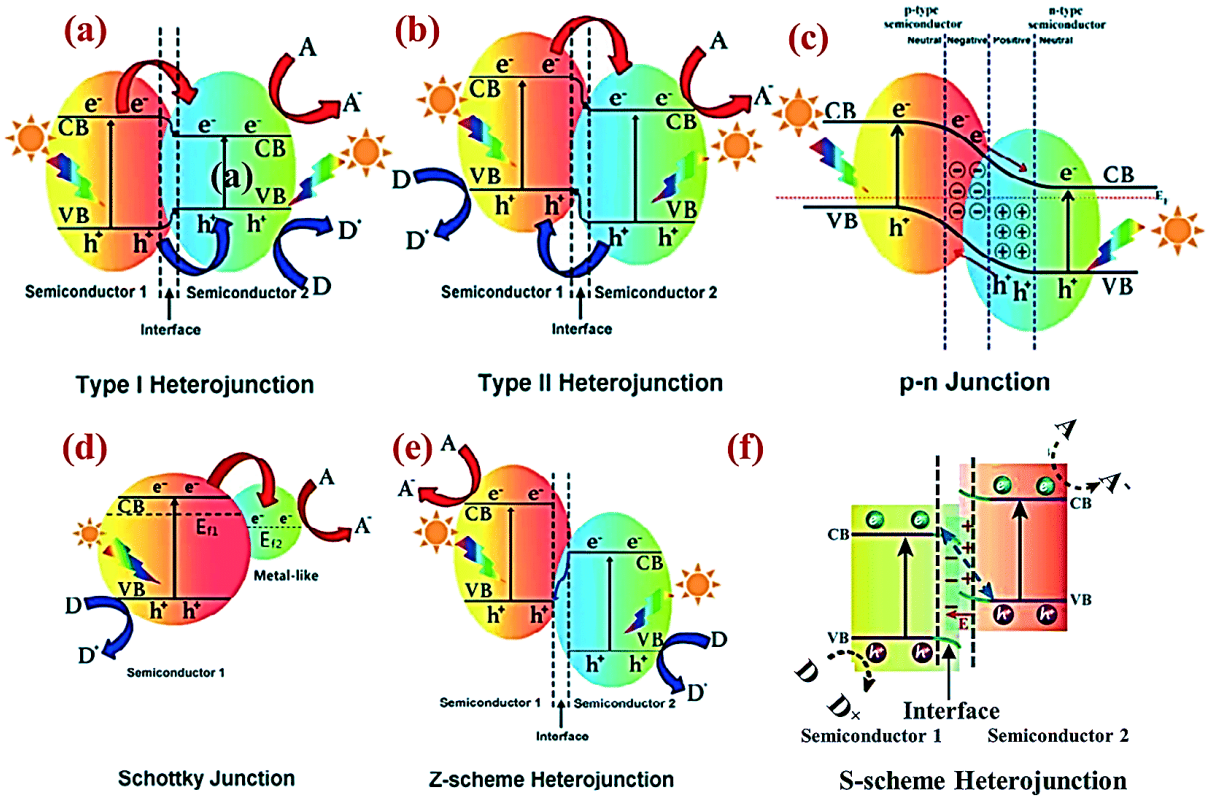

Figure 1.21. Band structure of various types of heterojunctions in a photocatalytic hybrid nanocomposite: (a) type I heterojunction, (b) type II heterojunction, (c) p–n junction, (d) Schottky junction, (e) Z-scheme heterojunction, and (f) S-scheme heterojunction. A, D and E_f represent electron acceptor, electron donor and Fermi level, respectively.[152]

Amorphous nanocatalyst is another intriguing modification method that is attracting a lot of interest in NRR and other catalytic applications in ambient settings. Due to the large concentration of active centres, or, in this phase, unsaturated coordination sites associated to dangling bonds, these nanomaterials with irregular atomic ordering exhibit exceptional catalytic capabilities.[153] To create an effective NRR photocatalytic system that can meet the established standard and turn the photon irradiated N_2 conversion to NH_3 reaction into a commercial and industrial process, the aforementioned modification techniques or approaches are frequently used.

1.5.4 Ammonia Production from MOF-Based Photocatalytic N_2 Fixation

In comparison to natural N_2 fixation methods that are energy-intensive, such as the Haber-Bosch process and the Fe/Mo-dependent nitrogenase process, as well as the energy-saving electrocatalytic reduction route, solar-driven photocatalytic N_2 fixation is considered a more environmentally and economically friendly approach to NH_3 fuel production. However, despite the high energy needed to break the N-N triple bond, there have been few studies on MOF-based photocatalysis for N_2 fixation. Therefore, this section provides an overview of recent research on MOF-based photocatalysts for N_2 fixation, categorizing them based on the types of active catalytic sites they use.

1.5.4.1 Active Sites on MOF Structures

Building photocatalysts with effective light absorption and prolonged electron-hole recombination is extremely desirable for increasing the photocatalytic N_2 reduction rate, which is encouraged by the three essential photocatalytic processes. In their work, Hu et al. described the creation of a new 2D viologen-based reactor that contained the MOF Gd-IHEP-7 ([Gd(bcbp)(H_2O)$_2$]) and its 3D counterpart, Gd-IHEP-8, which was created via a single crystal to single crystal transition from Gd-IHEP-7 (Figure 1.22a).[154] Both MOFs exhibit excellent photocatalytic activity when exposed to long-lived radicals, which results in broad-spectrum absorption in the 200–2500 nm region. In this study, Gd-IHEP-8 was found to have a higher solar-driven N_2-to-NH_3 efficiency of 220 mol g^{-1} h^{-1} towards sacrificial agent-free N_2 reduction with water under ambient temperature and simulated solar light irradiation than Gd-IHEP-7 (128 mol g^{-1} h^{-1}), due to stabilized intermediates attributed to enhanced H_2 bonding upon modification of the Gd^{3+} coordination environment through crystal transformation. The Gd^{3+} cation at the Gd-oxo cluster works as the N_2 activation centre and the N_2 photoreduction centre via alternate routes (Figure 1.22b). This research will help to guide the development of new

MOF-based N_2-fixing photocatalysts with a focus on the effect of metal nodes on enhancing effective light absorption.

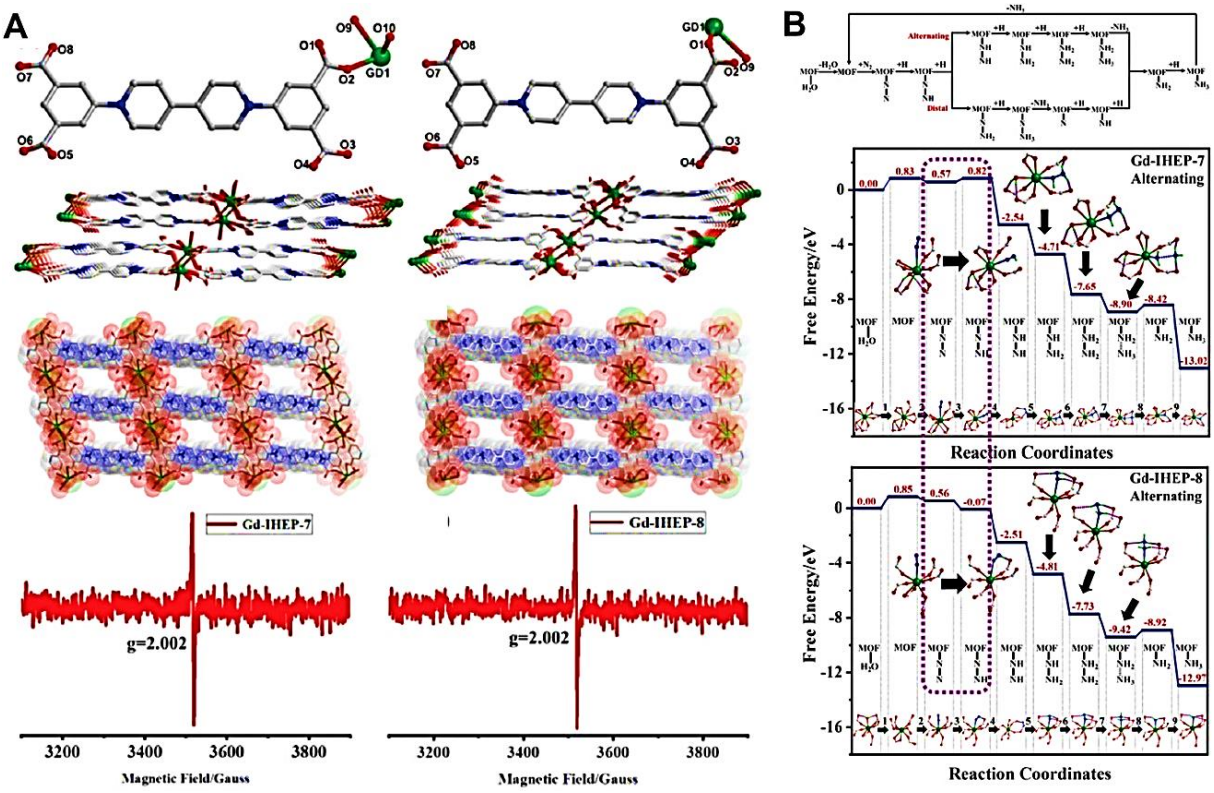

Figure 1.22. A) The asymmetric units, 3D porous structures and the EPR spectra of Gd-IHEP-7 and Gd-IHEP-8. **B**) The energy diagrams for the photocatalytic N_2 reduction alternating pathway of Gd-IHEP-7 and Gd-IHEP-8 to produce NH_3. Gd: green; C: gray; O: red; N: blue; H: light green.[154]

To boost the rate of photocatalytic N_2 reduction, scientists have employed ligand functionalization to expand the light-harvesting ability of MOF. Huang et al. employed Ti-based MIL-125(Ti) to catalyse photocatalytic N_2 fixation, where the Ti^{3+} species, produced by the ligand-to-metal cluster electron transfer process, serve as reactive sites for N_2 reduction.[155] This has yielded a variety of MOF catalysts that are active under visible light, such as CH_3-MIL-125(Ti), OH-MIL-125(Ti), and NH_2-MIL-125(Ti). Of these, NH_2-MIL-125(Ti) functionalized with amines has demonstrated the highest N_2-to-NH_3 rate of 12.3 μmol $g^{-1}h^{-1}$

in visible-light-assisted photocatalytic N_2 fixation, as it has the broadest light absorption range from 200 to 500 nm.

According to Figure 1.22, an increase in N-H bond generation can significantly improve the efficiency of photocatalytic N_2 reduction. Promising results have been observed with Fe-based MOFs, such as MIL-101(Fe), MIL-100(Fe), and MIL-88(Fe), which feature Fe^{3+} as catalytic centres. These centres possess high electron density and a lower reaction activation energy, leading to the formation of a greater number of N-H bonds.[156]

Designing bimetal active sites in a photocatalyst, inspired by biogenic nitrogenase, can enhance N_2 activation by enabling the simultaneous coupling of electron acceptance and donation processes. A series of bimetallic organic framework (BMOF) photocatalysts were created by Zhao et al. by choosing a hard acid metal node as the electron acceptor and a soft acid metal node as the electron donator.[157] The photocatalysts BMOF(Sr)-Fe, BMOF(Sr)-Co, BMOF(Sr)-Ba, BMOF(Ru)-Fe, BMOF(Co)-Fe and BMOF(Co)-Zn were fabricated, and the optimal BMOF(Sr)-0.2Fe was found with an ionization potential difference (ΔI_n between Fe and Sr) of $\geq$ 6 eV and a proportion of hard acid metal reaching ≈20%. This photocatalyst exhibited the highest N_2-to-NH_3 conversion rate of 780 μmol $g^{-1}h^{-1}$ due to the bimetal synergistic effect, which reduced the potential activation energy barrier (as shown in Figure 1.23a). This study provides a generic strategy for boosting solar-driven N_2 activation and highlights the potential of bimetallic photocatalysts for efficient N_2 fixation, based on the theory of hard and soft acids and bases.

Other researchers synthesized a UiO-66-based MOF, called (Zr-Hf)-X, for photocatalytic N_2 fixation using visible light.[158] This MOF has bimetallic nodes and functionalized ligands (X) that are modified with thiol groups (-SH) to enhance light absorption in the visible region. The Hf species acts as an electron buffer tank, optimizing the electron transfer to the catalytic active

Zr centres to enable efficient photocatalytic N_2 fixation. The optimized rate of conversion from N_2 to NH_3 is 116.1 μmol $g^{-1}h^{-1}$, due to the synergistic effect of visible-light assistance and the modified ligands.

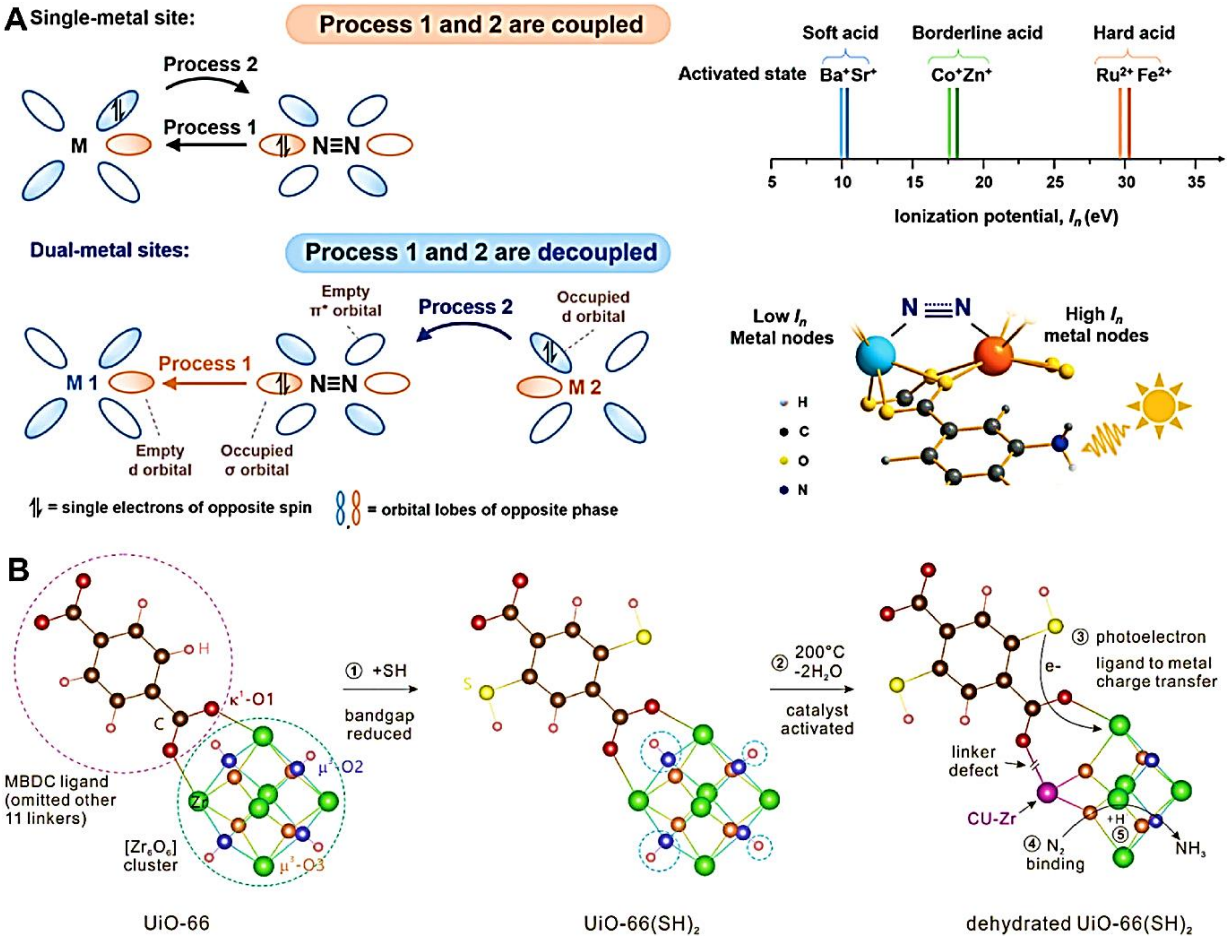

Figure 1.23. Schematic illustration showing the construction of MOF-based catalysts for photocatalytic N_2 fixation inspired by biogenic nitrogenase. **A)** N_2 bonding to the single-metal or dual-metal sites and the designed BMOF with dual-metal structure.[157] **B)** The synthesis of the dehydrated UiO-66(SH)$_2$ with the Zr–O cluster mimicking the biological N_2 fixation.[159]

Furthermore, recent studies have uncovered the exceptional visible-light-driven photocatalytic properties of dehydrated UiO-66(SH)$_2$, which closely mimics the biological N_2 fixation process, akin to the enzyme nitrogenase.[159] The -SH group introduction has resulted in an absorption edge in the visible region (500 nm) for dehydrated UiO-66(SH)$_2$. Dehydration has

modified the local structures surrounding Zr and the linker defects, creating an entrance for N_2 molecules into the [Zr_6O_6] cluster, as illustrated in Figure 1.23b. The robust N≡N bond was gradually broken down, and the photocatalytic N_2-to-NH_3 conversion efficiency was remarkably as high as 32.4 μmol $g^{-1}h^{-1}$. This was propelled by the photoelectrons supported by protonation. The research highlights the UiO-66$(SH)_2$ photocatalyst's similarity to the MoFe nitrogenase in its N_2 fixation mechanism, thus providing a promising avenue for comprehending the catalytic mechanism for MOF-based solar light-driven N_2 fixation modelled after the biological system.

1.5.4.2 Active Sites Supported on MOFs

A porphyrin-based MOF (PMOF) called Al-PMOF was created, inspired by the biological chlorophyll found in green leaves with porphyrin structure. Enzyme nitrogenase features Fe or Mo as favourable active sites for N_2 activation via π-back bonding. The PMOF had Al as the metal node and was carefully fabricated to anchor the atomically dispersed Fe active centres by post-synthetic modification.[160] This resulted in Al PMOF(Fe), which can be used for photocatalytic N_2 fixation. At the heart of the porphyrin, Fe atoms were found with full occupancy, indicating a high density of potential Fe-N catalytic sites with a valence state of Fe^{3+}. As a result, Al-PMOF(Fe) exhibited stable photocatalytic activity, significantly boosting N_2-to-NH_3 production (127 μg $h^{-1}g_{cat.}^{-1}$) compared to pristine Al-PMOF. The N_2 activation towards Fe-N catalytic sites is the rate-determining step. The potential activation pathway adopted in this Al-PMOF(Fe) photocatalyst is proposed as the associative alternating pathway (Figure 1.24a). This study boosts confidence in employing porphyrin-based MOF for artificial photosynthesis towards N_2 fixation.

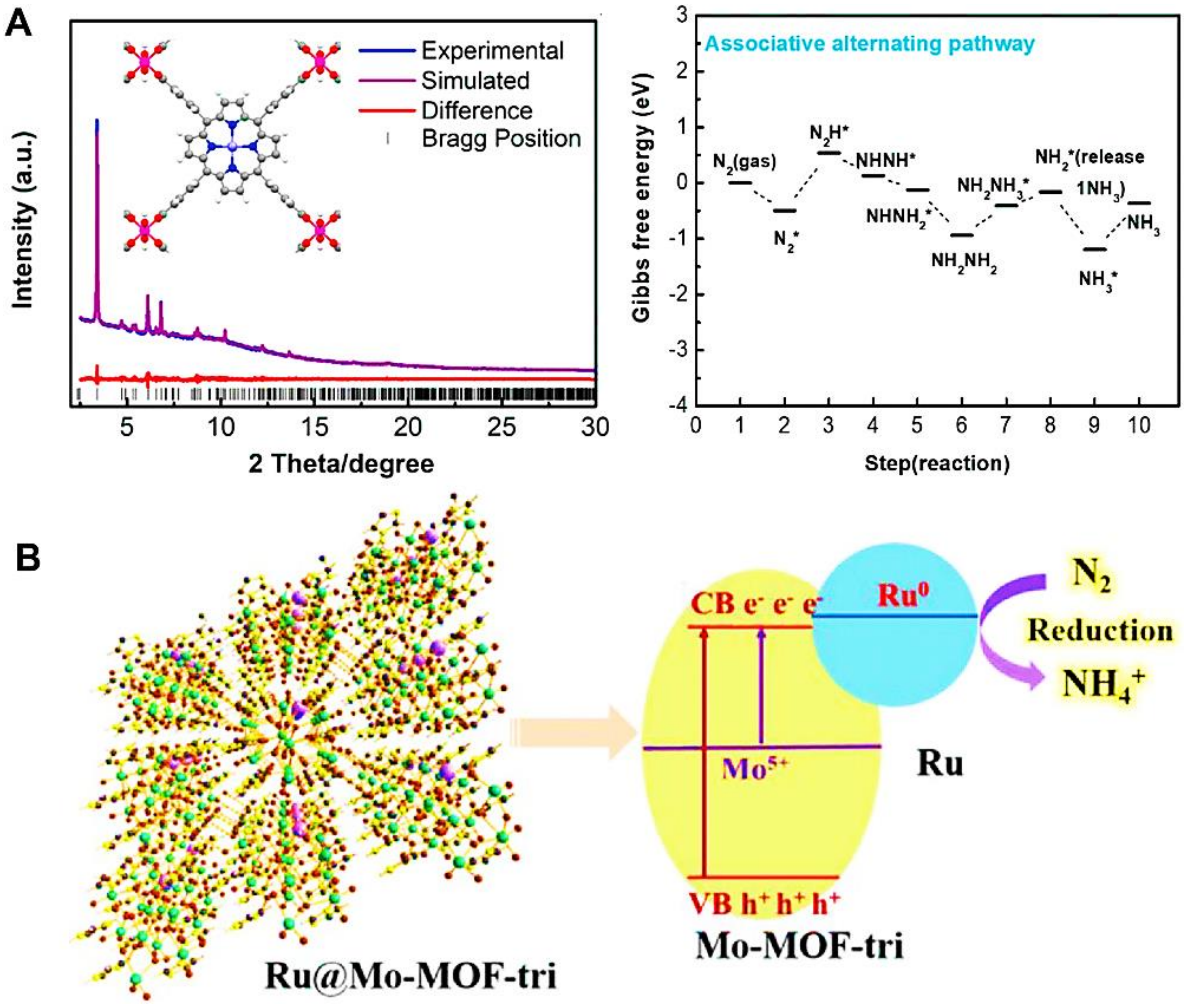

Figure 1.24. Schematic illustration showing the synthesis of MOF-based photocatalysts with active sites supported on MOFs for N_2 fixation. **A**) The structure of Al-PMOF(Fe) with Fe active sites and the proposed associative alternating pathway for photocatalytic N_2 fixation.[160] **B**) The crystal structure of Ru@Mo-MOF-tri and the possible photocatalytic mechanism toward N_2 fixation inspired by the biological enzyme nitrogenase.[161]

Furthermore, the nitrogenase MoFe cluster enzyme [Fe_7MoCS_9] has been identified as a crucial component. To develop effective photocatalysts for photocatalytic N_2 fixation, two meticulously crafted Mo-MOFs featuring $[Mo_8O_{26}(im)_2]^{4-}$ structures were designed to integrate isolated Ru SAs.[161] These Mo-MOFs were then utilized to form $Ru^{\delta+}$–O_3–Mo_3 single-site heterojunctions. The energy level of both Mo^{5+} and Ru was regulated to enable the Mo-MOF semiconductors to absorb solar light up to 700 nm, as depicted in Figure 1.24b. The NH_4^+ yield was higher in Ru@Mo-MOF-tri compared to Ru@Mo-MOF-mono. This was attributed

to the increased number of active sites for N_2 activation, specifically the $Ru^{\delta+}$–O_3–Mo_3 sites. Additionally, the adjacent $Ru^{\delta+}$–O_3–Mo_3 single site, neighbouring Mo^{5+}, decreased the energy barrier required to produce the critical intermediate NNH*. These results emphasize the significance of constructing MOF-based single-site heterojunctions with adjustable energy band structures as biomimetic photocatalysts for effective solar-driven N_2 fixation.

To enhance the separation and transmission of photogenerated electrons, a novel type of graphene-embedded Ce-based UiO-66 photocatalyst (GSCe) is studied for photocatalytic N_2 fixation.[162] When Ce-UiO-66 was exposed to UV light, while submerged in water, active sites developed and benzene-C bonds broke. In order to achieve visible light absorption and activation, the graphene embedding technique resorted to exporting electrons in a timely manner, protecting structural integrity, and pushing the band alignment of Ce-UiO-66. With a rate of 3.06 mmol L^{-1} in 24 hours and a stunning AQE of 9.25% at 365 nm, GSCe—which has a graphene ratio of 0.35—performed the best N_2-to-NH_3 photoactivity. Furthermore, GSCe performed well as a solar ammonia fertilizer, and for the first time, it was successfully used in crop cultivation.

Plasmonic metal nanoparticles, such as gold (Au) and palladium (Pd), show great potential as photosensitizers for converting nitrogen (N_2) to ammonia (NH_3) through photocatalysis under ambient conditions.[163,164] This is achieved through their synergistic localized surface plasmon resonance (LSPR) effect, which includes electron transfer (eT), energy transfer (ET), and localized electric-field polarization (EF-polarization). By utilizing these effects, the activation of the surface adsorbed N_2 molecules is promoted, resulting in an increased capability to harvest solar light, generate hot electrons, and reduce the activation energy barrier. This enhances the overall reaction of N_2 reduction, as shown in Figure 1.25a.

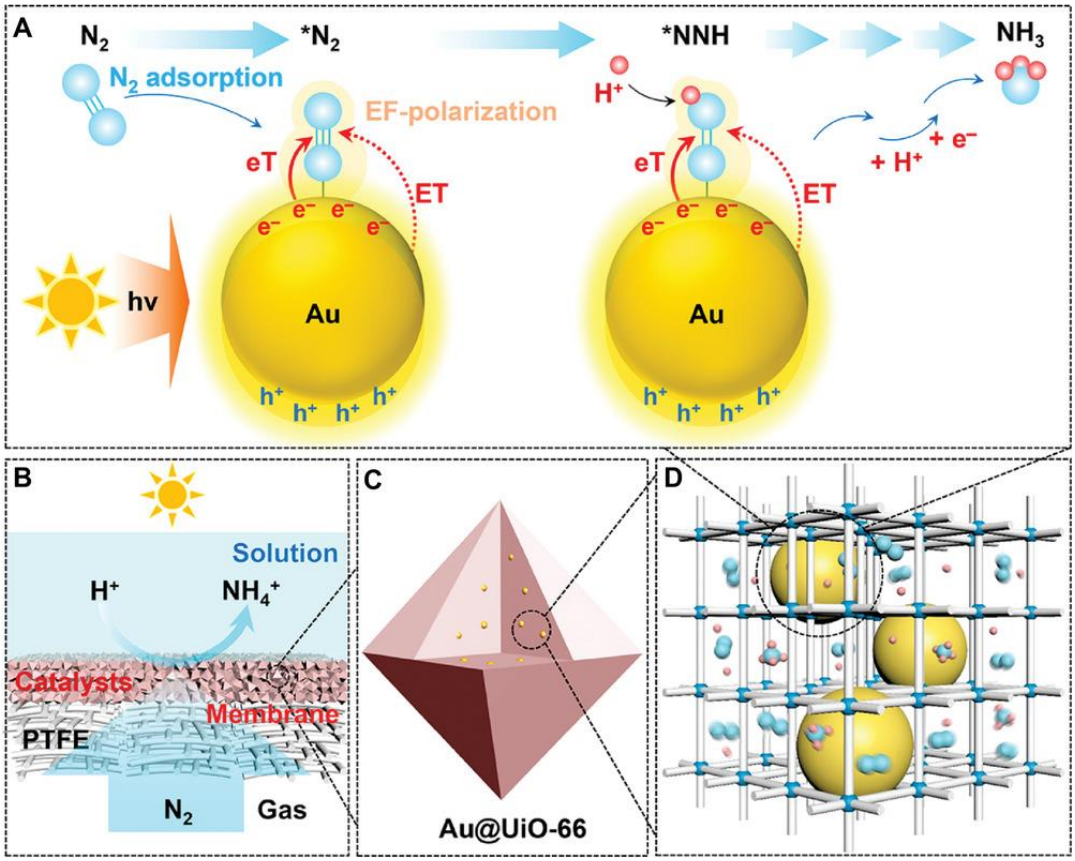

Figure 1.25. A) Schematic illustration of the direct N_2 photoreduction on AuNPs encapsulated in UiO-66 matrix by the synergistic LSPR effects, including hot electron generation, eT, ET, and EF-polarization effects. **B**) Schematic illustration of the N_2 directly diffused in high flux through the gas-permeable Au@UiO-66 membranes supported by porous PTFE films, and **C, D**) the dispersion of AuNPs within the cavities of MOFs matrix. Reproduced with permission.[165]

Chen and colleagues have presented a method for synthesizing highly dispersed plasmonic AuNPs.[165] These nanoparticles are embedded in a porous UiO-66 support, producing Au@MOF particles that can directly reduce N_2. Additionally, they have created gas-permeable Au@MOF membranes by mixing the catalysts with polytetrafluoroethylene (PTFE). This results in numerous interconnected nanoreactors, which ensure the dispersity and stability of AuNPs. Each AuNP in the MOF matrix can act as a photosensitizer and an active centre for the photocatalyst design. Meanwhile, the MOF substrates serve as a stable matrix to confine AuNPs with a porous nature, providing accessibility of these AuNPs to both N_2 molecules and protons (Fig. 1.25b, c, and d). The gas membrane-solution interface has been crafted to

optimize the transmission of N_2 molecules and protons, leading to enhanced photocatalytic reactions. Notably, this system has yielded a noteworthy NH_3 evolution rate of 18.9 mmol g_{Au}^{-1} h^{-1} under visible light, as well as an AQE of 1.54% at 520 nm, for the photocatalytic N_2 fixation under ambient conditions. These findings underscore the potential of plasmonic photocatalysis.

It has been discovered that MOFs can serve as useful supports for activating photocatalytic N_2 by anchoring active foreign species. By combining $Bi_4O_5Br_2$ with ZIF-8 (30%), with $Bi_4O_5Br_2$ as the activation centres, the photocatalytic N_2-to-NH_3 production rate was increased by 3.6 times (327.338 μmol L^{-1} h^{-1} g^{-1}), compared to $Bi_4O_5Br_2$ alone. This improvement was primarily due to the hydrophobic nature of ZIF-8, which allowed for forming a hydrophilic-hydrophilic structure at the gas-liquid-solid triphase reaction interface. This structure facilitated direct delivery of N_2 to the interface, promoting charge separation and ultimately leading to improved photocatalytic performance.[166]

1.6 Objective of This Thesis

The increasing global challenges of water scarcity and energy security have necessitated the development of innovative solutions for sustainable water treatment and solar-to-fuel conversion. Metal-organic frameworks (MOFs), with their exceptional properties and versatile architectures, have emerged as promising materials for addressing these challenges. In this thesis titled "Synthesis and Characterization of Zr-MOFs for Adsorption of Water Pollutants and N_2 Photoreduction," the focus is on the synthesis and characterization of Zr-based MOFs, specifically TMU-66 for water treatment, and MOF-808, TMU-34-(-2H), and their composites based on g-C_3N_4, for solar fuel production with focus on N_2 photoreduction.

To achieve the objectives of this research, a solvothermal and vial synthesis approach was employed to fabricate the Zr-MOFs and MOF-based composites with high crystallinity and

controlled morphologies. The resulting materials were characterized using various techniques, such as X-ray diffraction (XRD) and scanning electron microscopy (SEM) to determine their structural properties and surface morphology. Furthermore, thorough adsorption studies were conducted to investigate the adsorption isotherms, kinetics, and thermodynamics of water pollutants over the Zr-MOFs. The results showcased the impressive adsorption capacities and efficient removal of various water contaminants, highlighting the potential of Zr-MOFs as effective adsorbents for water treatment.

In addition, the MOF@g-C_3N_4 were subjected to photocatalytic experiments for nitrogen (N_2) photoreduction, aiming to produce ammonia (NH_3) as a sustainable fuel source. The photocatalytic activity of the MOF-based composites was evaluated, and the resulting ammonia yields were measured and analysed. By exploring the reaction pathways and employing techniques to enhance catalytic efficiency, this research provides insights into the potential of MOF@g-C_3N_4 composites for solar fuel production and the active sites present on the MOF structures. These findings contribute to the development of MOF-based photocatalytic systems and offer prospects for advancing the field of sustainable ammonia synthesis. The limitations and future directions of this research are discussed in the concluding section, along with the implications and potential applications of Zr-MOFs and their composites in addressing water pollution and energy demands.

1.7 References

(1) Beer, P. D.; Gale, P. A.; Smith, D. K., *Supramolecular chemistry*. Oxford University Press: **1999**.

(2) Atwood, J. L., *Comprehensive supramolecular chemistry II*. Elsevier: **2017**.

(3) Aronsson, Christopher. *Tunable and modular assembly of polypeptides and polypeptide-hybrid biomaterials*. Diss. Linköping University Electronic Press, **2016**.

(4) Lehn, J.-M., *Science* **1993,** *260* (5115), 1762-1764.

(5) Fyfe, M. C.; Stoddart, J. F., *Accounts of chemical research* **1997,** *30* (10), 393-401.

(6) Steed, J. W.; Turner, D. R.; Wallace, K., *Core concepts in supramolecular chemistry and nanochemistry*. John Wiley & Sons: **2007**.

(7) Lehn, J.-M., *European Review* **2009,** *17* (2), 263-280.

(8) Lehn, J. M. Makromolekulare Chemie. Macromolecular Symposia, Wiley Online Library: 1993; pp 1-17.

(9) Huang, F.; Anslyn, E. V., *Chemical reviews* **2015,** *115* (15), 6999-7000.

(10) Kolesnichenko, I. V.; Anslyn, E. V., *Chemical Society Reviews* **2017,** *46* (9), 2385-2390.

(11) Ishiwari, Fumitaka, Yoshiaki Shoji, and Takanori Fukushima. *Chemical Science* **2018**, 2028-2041.

(12) Lawrance, G. A., *Introduction to coordination chemistry*. John Wiley & Sons: 2013.

(13) Batten, S. R.; Neville, S. M.; Turner, D. R., *Coordination polymers: design, analysis and application*. Royal Society of Chemistry: **2008**.

(14) Kitagawa, S.; Kitaura, R.; Noro, S. i., *Angewandte Chemie International Edition* **2004,** *43* (18), 2334-2375.

(15) Kitagawa, S.; Matsuda, R., *Coordination Chemistry Reviews* **2007,** *251* (21-24), 2490-2509.

(16) Hong, M.-C.; Chen, L., *Design and construction of coordination polymers*. John Wiley & Sons: **2009**.

(17) Janiak, C., *Dalton Transactions* **2003,** (14), 2781-2804.

(18) Kitagawa, S.; Uemura, K., *Chemical Society Reviews* **2005,** *34* (2), 109-119.

(19) Rowsell, J. L.; Yaghi, O. M., *Microporous and mesoporous materials* **2004,** *73* (1-2), 3-14.

(20) Uemura, K.; Matsuda, R.; Kitagawa, S., *Journal of Solid State Chemistry* **2005,** *178* (8), 2420-2429.

(19) Tomic, E. A. *J. Appl. Polym. Sci.* **1965**, 9, 3745−3752.

(20) Hoskins, B. F.; Robson, R. *J. Am. Chem. Soc.* **1990**, 112, 1546−1554. (21) Yaghi, O. M.; Li, H. J. Am. Chem. Soc. **1995**, 117, 10401−10402.

(22) Li, H.; Eddaoudi, M.; O'Keeffe, M.; Yaghi, O. M. Nature 1999, 402, 276−279. (23) Ferey, G.; Mellot-Draznieks, C.; Serre, C.; Millange, F.; Dutour,́ J.; Surble, S.; Margiolaki, I. Science 2005, 309, 2040−2042.

(24) Xuan, W.; Zhu, C.; Liu, Y.; Cui, Y., Mesoporous metal–organic framework materials. *Chemical Society Reviews* **2012,** *41* (5), 1677-1695.

(25) Liu, Tianyu, et al. *Journal of Materials Chemistry A* **2017**, 17705-17733.

(26) Stock, N.; Biswas, S., *Chemical reviews* **2012,** *112* (2), 933-969.

(27) Zhou, H.-C.; Long, J. R.; Yaghi, O. M., *Chemical reviews* **2012,** *112* (2), 673-674.

(28) Wei, Yong-Sheng, et al. *Chemical reviews* **2020**, 12089-12174.

(29) J. J. Low, A. I. Benin, P. Jakubczak, J. F. Abrahamian, S. A. Faheem and R. R. Willis, *J. Am. Chem. Soc.* **2009**, 131, 15834–15842

(30) S. S. Iremonger, J. Liang, R. Vaidhyanathan, I. Martens, G. K. H. Shimizu, T. D. Daff, M. Z. Aghaji, S. Yeganegi and T. K. Woo, *J. Am. Chem. Soc.* **2011**, 133, 20048–20051.

(31) C. Montoro, F. Linares, E. Quartapelle Procopio, I. Senkovska, S. Kaskel, S. Galli, N. Masciocchi, E. Barea and J. A. R. Navarro, *J. Am. Chem. Soc.* **2011**, 133, 11888–11891.

(32) X. Liu, Y. Li, Y. Ban, Y. Peng, H. Jin, H. Bux, L. Xu, J. Caro and W. Yang, *Chem. Commun.* **2013**, 49, 9140–9142.

(33) J. G. Nguyen and S. M. Cohen, *J. Am. Chem. Soc.* **2010**, 132, 4560–4561.

(34) J. B. Decoste, G. W. Peterson, M. W. Smith, C. A. Stone and C. R. Willis, *J. Am. Chem. Soc.* **2012**, 134, 1486–1489.

(35) 5 S. J. Yang and C. R. Park, *Adv. Mater.*, **2012**, 24, 4010–4013.

(36) W. Zhang, Y. Hu, J. Ge, H.-L. Jiang and S.-H. Yu, *J. Am. Chem. Soc.* **2014**, 136, 16978–16981.

(37) Devic and C. Serre, *Chem. Soc. Rev.* **2014**, 43, 6097–6115.

(38) P. Lu, Y. Wu, H. Kang, H. Wei, H. Liu and M. Fang, *J. Mater. Chem. A.* **2014**, 2, 16250–16267

(39) M. Bosch, M. Zhang and H.-C. Zhou, *Adv. Chem.* **2014**, 2014, 1

(40) J. H. Cavka, S. Jakobsen, U. Olsbye, N. Guillou, C. Lamberti, S. Bordiga and K. P. Lillerud, J. *Am. Chem. Soc.* **2008**, 130, 13850–13851

(41) M. Kandiah, M. H. Nilsen, S. Usseglio, S. Jakobsen, U. Olsbye, M. Tilset, C. Larabi, E. A. Quadrelli, F. Bonino and K. P. Lillerud, *Chem. Mater*. **2010**, 22, 6632–6640.

(42) J. B. DeCoste, G. W. Peterson, H. Jasuja, T. G. Glover, Y.-g. Huang and K. S. Walton*, J. Mater. Chem. A* **2013**, 1, 5642–5650.

(43) X. Liu, N. K. Demir, Z. Wu and K. Li, *J. Am. Chem. Soc.* **2015**, 137, 6999–7002

(44) M. Zhang, Y.-P. Chen, M. Bosch, T. Gentle, K. Wang, D. Feng, Z. U. Wang and H.-C. Zhou, *Angew. Chem., Int. Ed.* **2014**, 53, 815–818.

(45) R. G. Pearson, *J. Am. Chem. Soc.*, **1963**, 85, 3533–3539.

(46) S. Wang, J. Wang, W. Cheng, X. Yang, Z. Zhang, Y. Xu, H. Liu, Y. Wu and M. Fang, *Dalton Trans.*, **2015**, 44, 8049–8061.

(47) P. S. Ba´rcia, D. Guimara˜es, P. A. P. Mendes, J. A. C. Silva, V. Guillerm, H. Chevreau, C. Serre and A. E. Rodrigues, *Microporous Mesoporous Mater.* **2011**, 139, 67–73.

(48) S. Chavan, J. G. Vitillo, D. Gianolio, O. Zavorotynska, B. Civalleri, S. Jakobsen, M. H. Nilsen, L. Valenzano, C. Lamberti, K. P. Lillerud and S. Bordiga, *Phys. Chem. Chem. Phys.* **2012**, 14, 1614–1626. 49. Q. Yang, V. Guillerm, F. Ragon, A. D. Wiersum, P. L. Llewellyn, C. Zhong, T. Devic, C. Serre and G. Maurin, *Chem. Commun.* **2012**, 48, 9831–9833.

(50) D. B. N. Lee, M. Roberts, C. G. Bluchel and R. A. Odell, *ASAIO J.* **2010**, 56, 550–556.

(51) D. Seckler, R. Barker and U. Amarasinghe, Int. *J. Water Resour. D* **1999**, 15, 29–42

(52) S. Malato, P. Fernandez-Ibanez, M. I. Maldonado, J. Blanco and W. Gernjak, *Catal. Today* **2009**, 147, 1–59.

(53) M. Rafatullah, O. Sulaiman, R. Hashim and A. Ahmad, *J. Hazard. Mater.* 2010, 177, 70–80.

(54) Mon, Marta, et al. *Journal of materials chemistry A* **2018**, 4912-4947.

(55) P. B. Tchounwou, C. G. Yedjou, A. K. Patlolla and D. J. Sutton, EXS, 2012, 133–164.

(56) H. Galal-Gorchev, Food Addit. Contam., 1993, 10, 115–128.

(57) Organic Pollutants in Water, ed. I. H. Suffet and M. Malaiyandi, *American Chemical Society, Washington, DC* **1986**, vol. 214.

(58) J. S. Gajda, H. S. Freeman and A. Reife, *Dyes Pigm. 1996*, 30, 1–20.

(59) S.F. Yang, C.-G. Niu, D.-W. Huang, H. Zhang, C. Liang and G.-M. Zeng*, Environ. Sci. Nano* **2017**, 4, 585–595.

(60) T. Ngulube, J. R. Gumbo, V. Masindi and A. Maity*, J. Environ. Manage* **2017**, 191, 35–57.

(61) M. A. Jamal, M. Muneer and M. Iqbal, *Chem. Int.* **2015**, 1, 2–6.

(62) M. Ismail, W. Zheng, L. Zhang, J. Ma, Y. Jia, Y. Hu and Y. Wang, *Chemosphere,* **2019**, 228, 212–218. 63. Y. Zhou, X. Liu, Y. Xiang, P. Wang, J. Zhang, F. Zhang and L. Tang, *Bioresour. Technol.* **2017**, 245, 266–273.

(64) U. Shamraiz, R. A. Hussain, A. Badshah, B. Raza and S. Saba, *J. Photochem. Photobiol. B* 2016, 159, 33–41.

(65) X. Jiang, J. Shen, S. Lou, Y. Mu, N. Wang, W. Han and L. Wang, *Bioresour. Technol.* **2016**, 216, 645–652.

(66) G. Crini, *Bioresour. Technol.* **2006**, 97, 1061–1085.

(67) J. R. Long and O. M. Yaghi*, Chem. Soc. Rev.* **2009**, 38, 1201–1507.

(68) Rafatullah, M.; Sulaiman, O.; Hashim, R.; Ahmad, A. *J. Hazard. Mater.* **2010**, 177, 70.

(69) Comotti, A.; Bracco, S.; Yamamoto, A.; Beretta, M.; Hirukawa, T.; Tohnai, N.; Miyata, M.; Sozzani, P. *J. Am. Chem. Soc.* **2014**, 136, 618.

(70) S. B. Wang and Y. L. Peng, *Chem. Eng. J.* **2010**, 156, 11–24.

(71) M. S. Khan, M. Khalid, M. S. Ahmad, M. Shahid and M. Ahmad, *Res. Chem. Intermed*. **2020**, 46, 2985–3006.

(72) Yavuz, C. T.; Mayo, J. T.; Yu, W. W.; Prakash, A.; Falkner, J. C.; Yean, S.; Cong, L. L.; Shipley, H. J.; Kan, A.; Tomson, M.; Natelson, D.; Colvin, V. L. *Science* **2006**, 314, 964.

(73) S. Dhaka , R. Kumar, A. Deep , M. B. Kurade , S. W. Ji and B. H. Jeon , *Coord. Chem. Rev.*, 2019, **380** , 330 —352.

(74) Eddaoudi, M.; Moler, D. B.; Li, H. L.; Chen, B. L.; Reineke, T. M.; O'Keeffe, M.; Yaghi, O. M. Acc. Chem. Res. 2001, 34, 319.

(75) Furukawa, H.; Cordova, K. E.; O'Keeffe, M.; Yaghi, O. M. *Science* **2013**, 341, 974.

(76) Koh, K.; Wong-Foy, A. G.; Matzger, A. J. *J. Am. Chem. Soc.* **2009**, 131, 4184.

(77) Deng, H. X.; Doonan, C. J.; Furukawa, H.; Ferreira, R. B.; Towne, J.; Knobler, C. B.; Wang, B.; Yaghi, O. M. *Science* **2010**, 327, 846.

(78) Kobielska, Paulina A., et al. *Coordination Chemistry Reviews* **2018**, 92-107.

(79) Dias, Elton M., and Camille Petit. *Journal of Materials Chemistry A* **2015**, 22484-22506.

(80) Colombo, V.; Galli, S.; Choi, H. J.; Han, G. D.; Maspero, A.; Palmisano, G.; Masciocchi, N.; Long, J. R. *Chem. Sci.* **2011**, 2, 1311.

(81) Galli, S.; Maspero, A.; Giacobbe, C.; Palmisano, G.; Nardo, L.; Comotti, A.; Bassanetti, I.; Sozzani, P.; Masciocchi, N. *J. Mater. Chem., A* **2014**, 2, 12208.

(82) S.-T. Zheng, X. Zhao, S. Lau, A. Fuhr, P. Feng, X. Bu*, J. Am. Chem. Soc.* **2013**, 10270.

(83) T.C. Wang, W. Bury, D.A. Gómez-Gualdrón, N.A. Vermeulen, J.E. Mondloch, P. Deria, K. Zhang, P.Z. Moghadam, A.A. Sarjeant, R.Q. Snurr, J.F. Stoddart, J.T. Hupp, O.K. Farha, *J. Am. Chem. Soc.* **2015**, 3585.

(84) G. Mouchaham, L. Cooper, N. Guillou, C. Martineau, E. Elkaïm, S. Bourrelly, P.L. Llewellyn, C. Allain, G. Clavier, C. Serre, T. Devic, *Angew. Chem. Int. Ed.* **2015**, 13297.

(85) G. Aromí, L.A. Barrios, O. Roubeau, P. Gamez, *Coord. Chem. Rev.* **2011**, 485.

(86) M.J. Katz, Z.J. Brown, Y.J. Colón, P.W. Siu, K.A. Scheidt, R.Q. Snurr, J.T. Hupp, O. K. Farha, *Chem. Commun*. **2013**, 9449.

(87) S. Yuan, Y.P. Chen, J.S. Qin, W. Lu, L. Zou, Q. Zhang, X. Wang, X. Sun, H.C. Zhou, *J. Am. Chem. Soc.* **2016**, 8912.

(88) X. Zhao, X. Bu, T. Wu, S.-T. Zheng, L. Wang, P. Feng, *Nat. Commun*. **2013**, 2344.

(89) S.-C. Xiang, Z. Zhang, C.-G. Zhao, K. Hong, X. Zhao, D.-R. Ding, M.-H. Xie, C.-D. Wu, M.C. Das, R. Gill, K.M. Thomas, B. Chen, *Nat. Commun.* **2011**, 204.

(90) G. Cai, H.-L. Jiang*, Angew. Chem. Int. Ed.* **2017**, 563.

(91) Zhang, Qi, Yuanjing Cui, and Guodong Qian. *Coordination Chemistry Reviews* **2019**, 310-332.

(92) H. Zhang, G. Liu, L. Shi, H. Liu, T. Wang, J. Ye, *Nano Energy* **2016**, 149–168.

(93) A. Kubacka, M. Fernández-García, G. Colón, *Chem. Rev.* **2012**, 1555–1614.

(94) Q. Wang, K. Domen, *Chem. Rev.* **2020**, 120, 919.

(95) Y. Zhang, B. Xia, J. Ran, K. Davey, S. Z. Qiao, *Adv. Energy Mater.* **2020**, 10, 1903879.

(96) S. E. Saji, H. Lu, Z. Lu, A. Carroll, Z. Yin, *Small Methods* **2021**, 5, 2000694.

(97) Sun D, et al. *Chem. Eur. J.* **2014**, 20:4780–4788.

(98) R.V. Kumar, M. Coto, Wiley-VCH Verlag GmbH & Co., *Weinheim* **2018**, pp. 499–526.

(99) D.L. Ashford, M.K. Gish, A.K. Vannucci, M.K. Brennaman, J.L. Templeton, J.M. Papanikolas, T.J. Meyer, *Chem. Rev.* **2015**, 13006–13049.

(100) C.-C. Hou, Q. Xu, *Adv. Energy Mater.* **2019**, 1801307.

(101) H. Wang, L. Zhang, Z. Chen, J. Hu, S. Li, Z. Wang, J. Liu, X. Wang, *Chem. Soc. Rev.* **2014**, 5234.

(102) J. Kou, C. Lu, J. Wang, Y. Chen, Z. Xu, R.S. Varma, *Chem. Rev.* **2017**, 1445–1514.

(103) B.o. Weng, M.-Y. Qi, C. Han, Z.-R. Tang, Y.-J. Xu, *ACS Catal.* **2019**, 4642–4687.

(104) Baig, Nadeem, Irshad Kammakakam, and Wail Falath. *Materials Advances* **2021**, 1821-1871.

(105) Nautiyal, Rashmi, et al, *Science and Technology of Advanced Materials* **2022**, 866-894.

(106) É. Whelan, F. W. Steuber, T. Gunnlaugsson, W. Schmitt, *Coord. Chem. Rev.* **2021**, 437, 213757.

(107) N. Kolobov, M. G. Goesten, J. Gascon*, Angew. Chem., Int. Ed.* **2021**, 60, 26038.

(108) A. Kuc, A. Enyashin and G. Seifert, *J. Phys. Chem. B* **2007**, 111, 8179–8186.

(109) M. Alvaro, E. Carbonell, B. Ferrer, F. X. Labr´es i Xamena and H. Garcia, *Chem.–Eur. J.* **2007**, 13, 5106–5112.

(110) M. Nasalevich, M. Van der Veen, F. Kapteijn and J. Gascon*, CrystEngComm*. **2014**, 16, 4919–4926.

(111) A. Fateeva, P. A. Chater, C. P. Ireland, A. A. Tahir, Y. Z. Khimyak, P. V. Wiper, J. R. Darwent and M. J. Rosseinsky, *Angew. Chem., Int. Ed.* **2012**, 51, 7440– 7444.

(112) C. Gomes Silva, I. Luz, F. X. Llabr´es i Xamena, A. Corma and H. Garc´ıa, *Chem.–Eur. J.*, **2010**, 16, 11133–11138.

(113) J. K. Gao, J. W. Miao, P. Z. Li, W. Y. Teng, L. Yang, Y. L. Zhao, B. Liu and Q. C. Zhang*, Chem. Commun.* **2014**, 50, 3786– 3788.

(114) K. Hendrickx, D. E. Vanpoucke, K. Leus, K. Lejaeghere, A. Van Yperen-De Deyne, V. Van Speybroeck, P. Van Der Voort and K. Hemelsoet, *Inorg. Chem.* **2015**, 54, 10701– 10710.

(115) T. H. Zhou, Y. H. Du, A. Borgna, J. D. Hong, Y. B. Wang, J. Y. Han, W. Zhang and R. Xu, *Energy Environ. Sci.,* **2013**, 6, 3229–3234.

(116) X.-S. Wang, L. Li, D. Li, J. Ye, *Sol. RRL* **2020,** 4, 1900547.

(117) Y. Deng, Y. Wang, Z. Di, M. Xie, F. Dai, S. Zhan, Z. Zhang, *Small Methods* **2022**, 6, 2200265.

(118) A. E. Platero-Prats, A. Mavrandonakis, J. Liu, Z. Chen, Z. Chen, Z. Li, A. A. Yakovenko, L. C. Gallington, J. T. Hupp, O. K. Farha, C. J. Cramer, K. W. Chapman, *J. Am. Chem. Soc.* **2021**, 143, 20090.

(119) G. Ji, L. Zhao, J. Wei, J. Cai, C. He, Z. Du, W. Cai, C. Duan, *Angew. Chem., Int. Ed.* **2022**, 61, e202114490

(120) S. Subudhi, L. Paramanik, S. Sultana, S. Mansingh, P. Mohapatra, K. Parida, *J. Colloid Interface Sci.* **2020**, 568, 89.

(121) H.P. Jia, E.A. Quadrelli, *Chem. Soc. Rev.* **2014**, 547–564.

(122) X. Xue, R. Chen, C. Yan, P. Zhao, Y. Hu, W. Zhang, S. Yang, Z. Jin, *Nano Res.* **2019**, 1229–1249.

(124) T.A. Bazhenova, A.E. Shilov, *Coordn. Chem. Rev.* **1995**, 69–145.

(125) L. Shi, Y. Yin, S. Wang, H. Sun, *ACS Catal.* **2020**, 6870–6899.

(126) J. John, D.K. Lee, U. Sim, *Nano Converg.* **2019**, 15.

(127) B.K. Burgess, D.J. Lowe, *Chem. Rev.* **1996**, 2983–3012.

(128) K. Wang, D. Smith, Y. Zheng, *Carbon Resour. Convers*. **2018**, 2–31.

(129) M.H. Vu, M. Sakar, S.A. Hassanzadeh-Tabrizi, T.O. Do, *Adv. Mater. Interfaces* **2019**, 1900091.

(130) R. Manjunatha, A. Karajic, ´ M. Liu, et al., A review of Composite/Hybrid electrocatalysts and photocatalysts for nitrogen reduction reactions: advanced materials, mechanisms, challenges and perspectives, Electrochem. Energy Rev. 3 (2020) 506–540.

(131) J.W. Erisman, M.A. Sutton, J. Galloway, Z. Klimont, W. Winiwarter, *Nat. Geosci.* **2008**, 636–639.

(132) M. Li, H. Huang, J. Low, C. Gao, R. Long, Y. Xiong, *Small Methods* **2019**, 1800388.

(133) B.M. Hoffman, D. Lukoyanov, Z.Y. Yang, D.R. Dean, L.C. Seefeldt, *Chem. Rev.* **2014**, 4041–4062.

(134) Fan, Linkun, et al. *Catalysts* **2022**, 1005.

(135) Y. Yao, S. Zhu, H. Wang, H. Li, M. Shao, *J. Am. Chem. Soc.* **2018**, 1496–1501.

(136) N. Zhang, A. Jalil, D. Wu, S. Chen, Y. Liu, C. Gao, W. Ye, Z. Qi, H. Ju, C. Wang, X. Wu, *J. Am. Chem. Soc.* **2018**, 9434–9443.

(137) C.D. Zeinalipour-Yazdi, J.S. Hargreaves, C.R.A. Catlow, *J. Phys. Chem. C* **2016**, 21390–21398.

(138) Y. Abghoui, A.L. Garden, J.G. Howalt, T. Vegge, E. Skúlason, *ACS Catal.* **2016**, 635–646

(139) V. Rosca, M. Duca, M.T. de Groot, M.T. Koper, *Chem. Rev.* **2009**, 2209–2244.

(140) D.E. Canfield, A.N. Glazer, P.G. Falkowski, *science* **2010**, 192–196.

(141) A. Le Duy, R. Samson, *Biotechnol. Lett.* **1982**, 303–306.

(142) C. Mao, J. Wang, Y. Zou, H. Li, G. Zhan, J. Li, J. Zhao, G. Zhan, *Green Chem.* **2019**, 2852–2867.

(143) J. Kibsgaard, Z. Chen, B.N. Reinecke, T.F. Jaramillo, *Nat. Mater.* **2012**, 963–969.

(144) Y. Luo, G.F. Chen, L. Ding, X. Chen, L.X. Ding, H. Wang, *Joule* **2019**, 279–289.

(145) H. Zhang, G. Liu, L. Shi, J. Ye, *Adv. Energy Mater.* **2018**, 1701343.

(146) K. Zhou, Y. Li, *Angew. Chemie Int. Ed.* **2012**, 602–613.

(147) J. Jiang, K. Zhao, X. Xiao, L. Zhang, *J. Am. Chem. Soc.* **2012**, 4473–4476.

(148) C. Guo, J. Ran, A. Vasileff, S.Z. Qiao, *Energy Environ. Sci.* **2018**, 45–56.

(149) S.L. Foster, S.I.P. Bakovic, R.D. Duda, S. Maheshwari, R.D. Milton, S.D. Minteer, M.J. Janik, J.N. Renner, L.F. *Nat. Catal.* **2018**, 490–500.

(150) J. Ran, J. Zhang, J. Yu, M. Jaroniec, S.Z. Qiao, *Chem. Soc. Rev.* **2014**, 7787–7812.

(151) J.S. Steckel, J.P. Zimmer, S. Coe-Sullivan, N.E. Stott, V. Bulovic, ´ M.G. Bawendi, *Angew. Chemie* **2004**,116 (16) 2206–2210.

(152) Zhong, Yi, et al. "Interface engineering of heterojunction photocatalysts based on 1D nanomaterials." *Catalysis Science & Technology* **2021**, 27-42.

(153) C. Li, T. Wang, Z.J. Zhao, W. Yang, J.F. Li, A. Li, Z. Yang, G.A. Ozin, J. Gong, *Angew. Chemie Int. Ed.* **2018**, 57 (19) 5278–5282.

(154) K.-Q. Hu, P.-X. Qiu, L.-W. Zeng, S.-X. Hu, L. Mei, S.-W. An, Z.-W. Huang, X.-H. Kong, J.-H. Lan, J.-P. Yu, Z.-H. Zhang, Z.-F. Xu, J. K. Gibson, Z.-F. Chai, Y.-F. Bu, W.-Q. Shi, *Angew. Chem., Int. Ed.* **2020**, 59, 20666.

(155) H. Huang, X.-S. Wang, D. Philo, F. Ichihara, H. Song, Y. Li, D. Li, T. Qiu, S. Wang, J. Ye, *Appl. Catal., B* **2020**, 267, 118686.

(156) G. Li, F. Li, J. Liu, C. Fan, J. *Solid State Chem.* **2020**, 285, 121245.

(157) Z. Zhao, H. Ren, D. Yang, Y. Han, J. Shi, K. An, Y. Chen, Y. Shi, W. Wang, J. Tan, X. Xin, Y. Zhang, Z. Jiang, *ACS Catal.* **2021**, 11, 9986.

(158) K. An, H. Ren, D. Yang, Z. Zhao, Y. Gao, Y. Chen, J. Tan, W. Wang, Z. Jiang*, Appl. Catal. B* **2021**, 292, 120167.

(159) B. Guo, X. Cheng, Y. Tang, W. Guo, S. Deng, L. Wu, X. Fu, *Angew. Chem., Int. Ed*. **2022**, 61, e202117244.

(160) S. Shang, W. Xiong, C. Yang, B. Johannessen, R. Liu, H. Y. Hsu, Q. Gu, J. Shang, *ACS Nano* **2021**, 15, 9670.

(161) S. Wang, J.-J. Zhang, M.-Y. Zong, J. Xu, D.-H. Wang, X.-H. Bu, *ACS Catal.* **2022**, 12, 7960.

(162) S. Liu, Z. Teng, H. Liu, T. Wang, G. Wang, Q. Xu, X. Zhang, M. Jiang, C. Wang, W. Huang, H. Pang, *Angew. Chem., Int. Ed.* **2022**, 61, e202207026.

(163) J. Yang, Y. Guo, R. Jiang, F. Qin, H. Zhang, W. Lu, J. Wang, J. C. Yu, *J. Am. Chem. Soc.* **2018**, 140, 8497.

(164) C. Hu, X. Chen, J. Jin, Y. Han, S. Chen, H. Ju, J. Cai, Y. Qiu, C. Gao, C. Wang, Z. Qi, R. Long, L. Song, Z. Liu, Y. Xiong*, J. Am. Chem. Soc.* **2019**, 141, 7807.

(165) L.-W. Chen, Y.-C. Hao, Y. Guo, Q. Zhang, J. Li, W.-Y. Gao, L. Ren, X. Su, L. Hu, N. Zhang, S. Li, X. Feng, L. Gu, Y.-W. Zhang, A.-X. Yin, B. Wang*, J. Am. Chem. Soc.* **2021**, 143, 5727.

(166) J. Liu, R. Li, X. Zu, X. Zhang, Y. Wang, Y. Wang, C. Fan, *Chem. Eng. J.* **201**9, 371, 796.

Chapter 2

Materials and methods

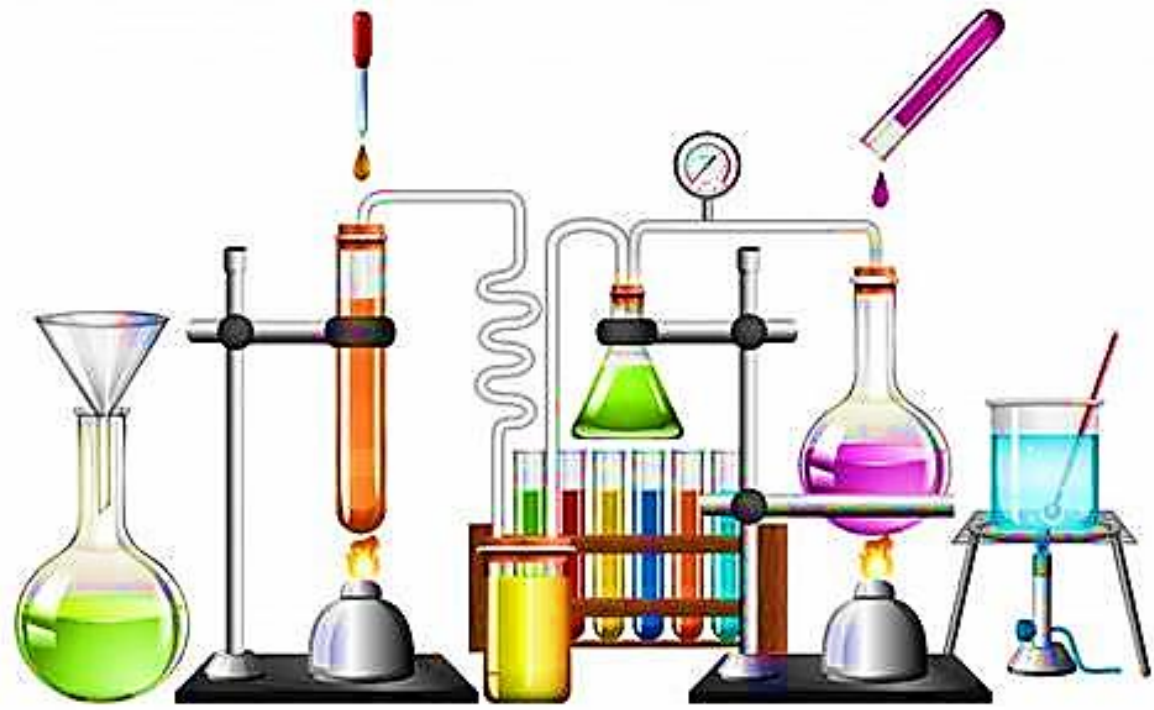

2. Experimental Section

This chapter presents the materials, equipment, and methods utilized in the preparation and characterization of metal-organic frameworks (MOFs) and their application in batch adsorption and N_2 photoreduction processes. Additionally, the synthesis method employed for the preparation of MOF@g-C_3N_4 composites, as well as the investigation of solid and solution state reactions, are described: the solvothermal and vial synthesis methods, the characterization methods, the batch experiments and equilibrium concentration measurements, and the photocatalytic experiments and ammonia yield analyses. The chapter aims to provide a comprehensive overview of the experimental procedures employed in this study, ensuring reproducibility and clarity in understanding the subsequent results and findings. The subsequent sections delve into the specific procedures employed for the aspect of the research, highlighting the techniques and analytical tools utilized.

2.1. Materials

Table 2.1 summarizes the names, purity percentages, and origin of the materials employed in this thesis's experiments. Zirconium (IV) chloride and zinc acetate dihydrate to produce the central metals and isonicotinic acid N-oxide (INO), benzene-1,3,5-tricarboxylic acid (BTC), 5-nitro isophthalic acid (NIP), 4,4'-Oxybisbenzoic acid (OBA) and (3,6-di(pyridine-4-yl)-1,2,4,5-tetrazine (DPT) as the linkers were used for the synthesis of MOFs and melamine as an initial source for the synthesis of g-C_3N_4. Formic acid and benzoic acid were used as modulators for the preparation of crystalline structures, and HCl was used as a defective factor. Potassium iodide, sodium hydroxide, and mercury (II) chloride were utilized for Nessler's reagent preparation as a colorimetry method for the determination of the amount of produced NH_3 in N_2 photoreduction experiments. Also, eight dyes were used for batch adsorption studies.

Table 2.2 The names, purity percentages, and origin of materials.

Name	Formula	Purity level (%)	Company	Country
Zirconium (IV) chloride	$ZrCl_4$	≥99.0%	Sigma-Aldrich	France
Zinc acetate dihydrate	$Zn(CH_3CO_2)_2 \cdot 2H_2O$	≥99.0%	Merck	Germany
Isonicotinic acid N-oxide	HINO	≥99.0%	Sigma-Aldrich	France
Benzene-1,3,5-tricarboxylic acid	BTC	≥98.0%	Sigma-Aldrich	France
5-Nitro isophthalic acid	NIP	≥98.0%	Sigma-Aldrich	France
4,4'-Oxybisbenzoic acid	H_2OBA	≥99.0%	Merck	Germany
(3,6-Di(pyridine-4-yl)-1,2,4,5-tetrazine	DPT	≥96.0%	Sigma-Aldrich	Germany
Dimethylformamide	DMF	≥99.0%	Fisher Scientific	France
Acetonitrile	CH_3CN	≥99.0%	Sigma-Aldrich	Germany
Methanol	CH_3OH	≥99.0%	Fisher Scientific	France
Hydrochloric acid 37 w %	HCl	99.0%	Merck	Germany
Formic acid	CH_2O_2	≥99.0%	Sigma-Aldrich	France
Benzoic acid	C_6H_5COOH	≥98.0%	Merck	Germany
Sodium sulfate anhydrous	Na_2SO_4	≥99.0%	Sigma-Aldrich	France
Potassium iodide	KI	≥99.0%	Sigma-Aldrich	France
Sodium hydroxide	NaOH	≥99.0%	Merck	Germany
Mercury (II) chloride	$HgCl_2$	≥99.0%	Sigma-Aldrich	France
Potassium sodium tartrate	$KNaC_4H_4O_6$	≥98.0%	Sigma	France
Sulfuric acid	H_2SO_4	≥98.0%	Fisher Scientific	France
Melamine	$C_3H_6N_6$	≥98.0%	Sigma-Aldrich	France
Congo red	$C_{32}H_{22}N_6Na_2O_6S_2$	≥75.0%	Merck	Germany
Rose Bengal	$C_{20}H_4Cl_4I_4O_5$	≥95.0%	Merck	Germany
Methyl orange	$C_{14}H_{14}N_3NaO_3S$	85.0%	Merck	Germany
Crystal violet	$C_{25}N_3H_{30}Cl$	90.0%	Merck	Germany
Malachite green	$C_{23}H_{25}ClN_2Cl$	~90.0%	Merck	Germany
Naphthol green B	$C_{30}H_{15}FeN_3Na_3O_{15}S_3$	80.0%	Merck	Germany
Rhodamine B	$C_{28}H_{31}ClN_2O_3$	97.0%	Merck	Germany
Methyl red	$C_{15}H_{15}N_3O_2$	95.0%	Merck	Germany

2.2 Synthesis Methods

In general, for the synthesis of Zr-MOFs and MOF@g-C_3N_4 structures, the vial method, solvothermal, and ultrasonic methods were used.

2.2.1 Synthesis of g-C_3N_4 powder. Bulk g-C_3N_4 was prepared following the most common method.[1] In the typical procedure, 2 g of melamine were dissolved in the 60 mL of water and stirred for 20 min at 100 °C. Afterward, the solution was gradually cooled down to room temperature to recrystallize melamine. The mixture was further dried at 100 °C. Finally, the dried product was calcinated in a ceramic-covered crucible, heated at 2.3 °C min^{-1} to 550 °C, and maintained for 4 h in air. After cooling to room temperature, the reacted mass was ground to obtain a raw g-C_3N_4 powder.

2.2.2 Synthesis of MOFs and MOF@g-C_3N_4 composites

Vial method

2.2.2.1 Synthesis of TMU-66 with modulators. 0.8 mL of formic acid or 3g of benzoic acid in 10 mL DMF was used as a solvent to dissolve 0.24 g of $ZrCl_4$ under 5 min sonication. Isonicotinic acid N-oxide (INO) (0.278 g, 2 mmol) was added, and the mixture was sonicated for another 5 min. The resulting solution was distributed in several vials and placed into a 120°C preheated oven for 1 day. The precipitate was filtered, washed with DMF (4 times) and acetone (4 times) over 12 hours, then placed into a 120°C preheated oven for 24 h. To eliminate solvent molecules from the structure, the obtained materials were soaked in fresh methanol for three days and then dried at 100°C for 24 h.

2.2.2.2 Synthesis of TMU-66 with HCl. 1 mmol of $ZrCl_4$ was dissolved in a 15 mL glass tube containing 5 mL of DMF and 69 µL of concentrated HCl by sonication for 5 min. Then, 2 mmol of INO ligand in 5 mL of DMF were added, and the mixture was sonicated for

another 5 min. Afterwards, the glass tube was heated on a thermal plate at 120 °C for 18 h. The resulting white crystalline solid was separated by filtration and washed three times with DMF. To eliminate solvent molecules from the structure, the resulting materials were soaked in fresh methanol for three days and then dried at 100°C for 24 h.

Solvothermal method

2.2.2.3 Synthesis of MOF-808/NIP and MOF/g-C_3N_4 composite. A mixture of $ZrCl_4$ (1 mmol), BTC (0.5 mmol) and 5-nitro isophthalic acid (NIP) (0.5 mmol) linkers, 15 mL formic acid, and dimethylformamide (DMF) (45 mL) was sonicated, and then transferred into a 125 mL Teflon-lined stainless-steel autoclave, and heated on a heating plate (Agitemp) at 120 °C for 24 h. After cooling naturally to room temperature, the solid product was separated by centrifugation and washed several times with DMF to ensure the removal of unreacted materials. In order to remove the solvent molecules from the MOF structural holes, the synthetic materials were soaked in fresh methanol for three days and then dried at 120 °C for 24 h. For the synthesis of MOF/g-C_3N_4 composite, 10 mg g-C_3N_4 was added to the synthesis medium, following an hour of sonication, then the autoclave was stirred during heating.

Sonication method

2.2.2.4 Synthesis of TMU-34(-2H) frameworks

The powder sample of TMU-34(-2H) was synthesized using the following procedure in an ultrasonic bath at room temperature and atmospheric pressure. First, zinc acetate dihydrate (0.22 g, 1 mmol) and 1 mmol of linkers (0.26 g for H_2OBA and 0.24 g for DPT) were mixed in 30 mL of DMF/acetonitrile (1:1 v/v). Then, the mixture was sonicated for 1 h at room temperature. Finally, the MOF was separated by centrifugation (6000 rpm, 2 min), and washed with DMF (3 × 5 mL) to remove the unreacted ligand and metal ions. Finally, the powder was dried in a preheated oven at 80 °C for 48 h.

2.2.2.5 Synthesis of TMU-34(-2H)@g-C_3N_4 composite

TMU-34-(-2H) @g-C_3N_4 composite was prepared by dispersing 24 mg of g-C_3N_4 powder (10 wt% based on DPT) in the synthesis medium of TMU-34-(-2H), according to the procedure mentioned above in an ultrasonic bath at room temperature and atmospheric pressure.

2.3 Instruments and Characterizations Methods

2.3.1 Structural characterization methods

In this part, the instruments and structural characterization methods that were used to analyze the Zr-MOFs and MOF-based composites are described. Each technique's purpose, principle, and procedure are explained, along with the instruments, settings, and samples used.

X-ray diffraction (XRD), **powder X-ray diffraction (PXRD)**, **and Rietveld and Lebail refinements** were used to analyze the structural properties of crystalline materials. XRD and PXRD are methods that measure the diffraction patterns of X-rays that interact with a material's crystal lattice.[2,3] The diffraction patterns can reveal information, such as the material's phase composition, crystal structure, unit cell dimensions, and lattice parameters. Rietveld and Lebail refinements fit a theoretical model to the experimental diffraction data, using various parameters to minimize the difference between the observed and calculated patterns.[4,5] These methods can refine the structural parameters of the material, such as the atomic positions and occupancies. They can also determine the phase fractions and background contributions of the material. These techniques help to identify and characterize the Zr-MOFs and MOF-based composites synthesized and applied in this research.

A two-step method consisting of single crystal analysis and simulation method was applied to analyze the structure of TMU-66. The PXRD patterns and Lebail refinements were used to validate the synthesis and modification process of MOF-808 to MOF-808/NIP. The PXRD patterns were also used to verify the synthesis of MOF@g-C_3N_4 composites.

Powder X-ray diffraction (XRD) patterns of the as-prepared materials were collected on a high flux Rigaku Smartlab rotated anode, operated with a copper Kα radiation (1.5418 ang) at an applied voltage of 45 kV and an anode current of 200 mA in the 2θ range of 5° to 80° at a scan rate of 5° min^{-1} in France.

Details for crystal structure refinement of TMU-66

The **synchrotron X-ray powder diffraction data** were obtained on the undulator beamline 8.0.1 at Advanced Light Source (ALS), Lawrence Berkeley National Laboratory. The position and orientation of Zr-clusters in TMU-66-formic acid crystals were recognized using synchrotron X-ray powder diffraction data (**Figure 2.1**). These data were considered as a starting point for modeling with the Materials Studio package (Accelrys Inc.), and the resulting model was solved by Rietveld refinement.[6] The refinement results were in reasonable agreement with experimental data and led us to the proposed formula and structure of TMU-66.

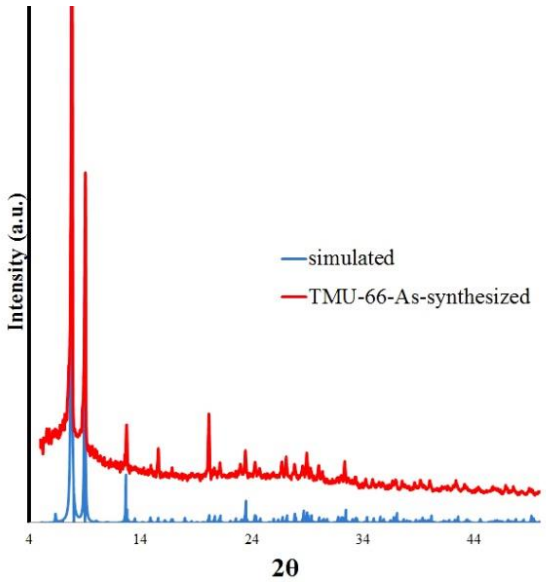

Figure 2.1. Comparison of the simulated PXRD pattern obtained from synchrotron X-ray with PXRD patterns of TMU-66.

data_TMU-66
_audit_creation_date 2018-04-04

```
_audit_creation_method            'Materials Studio'
_symmetry_space_group_name_H-M    'PA-3'
_symmetry_Int_Tables_number       205
_symmetry_cell_setting            cubic
loop_
_symmetry_equiv_pos_as_xyz
  x,y,z
  -x+1/2,-y,z+1/2
  -x,y+1/2,-z+1/2
  x+1/2,-y+1/2,-z
  z,x,y
  z+1/2,-x+1/2,-y
  -z+1/2,-x,y+1/2
  -z,x+1/2,-y+1/2
  y,z,x
  -y,z+1/2,-x+1/2
  y+1/2,-z+1/2,-x
  -y+1/2,-z,x+1/2
  -x,-y,-z
  x+1/2,y,-z+1/2
  x,-y+1/2,z+1/2
  -x+1/2,y+1/2,z
  -z,-x,-y
  -z+1/2,x+1/2,y
  z+1/2,x,-y+1/2
  z,-x+1/2,y+1/2
  -y,-z,-x
  y,-z+1/2,x+1/2
  -y+1/2,z+1/2,x
  y+1/2,z,-x+1/2
_cell_length_a                    19.6716
_cell_length_b                    19.6716
_cell_length_c                    19.6716
_cell_angle_alpha                 90.0000
_cell_angle_beta                  90.0000
_cell_angle_gamma                 90.0000
loop_
_atom_site_label
_atom_site_type_symbol
_atom_site_fract_x
_atom_site_fract_y
_atom_site_fract_z
_atom_site_U_iso_or_equiv
_atom_site_adp_type
_atom_site_occupancy
Zr1   Zr   0.12040   0.00000   0.00000   0.00000  Uiso   1.00
O2    O    0.17260   0.00000   0.09600   0.00000  Uiso   1.00
O3    O    0.05610   0.94390   0.94390   0.00000  Uiso   1.00
O4    O    0.09600   0.00000   0.17260   0.00000  Uiso   1.00
O5    O    0.36299  -0.00118   0.36088   0.00000  Uiso   1.00
```

```
C13   C    0.73570   0.50000   0.31590   0.00000  Uiso   1.00
C15   C    0.85270   0.50000   0.35270   0.00000  Uiso   1.00
C16   C    0.79810   0.50000   0.29810   0.00000  Uiso   1.00
C17   C    0.81590   0.50000   0.23570   0.00000  Uiso   1.00
N19   N    0.70190   0.50000   0.20190   0.00000  Uiso   1.00
C20   C    0.68410   0.50000   0.26430   0.00000  Uiso   1.00
C21   C    0.76430   0.50000   0.18410   0.00000  Uiso   1.00
O205  O    0.94390   0.94390   0.94390   0.00000  Uiso   1.00
loop_
_geom_bond_atom_site_label_1
_geom_bond_atom_site_label_2
_geom_bond_distance
_geom_bond_site_symmetry_2
_ccdc_geom_bond_type
Zr1   O2     2.150   .    S
Zr1   O4     2.150   5    S
Zr1   O205   2.009   13_666 S
Zr1   O3     2.009   1_544 S
Zr1   Zr1    3.350   5    S
Zr1   Zr1    3.350   9    S
Zr1   Zr1    3.350   17   S
Zr1   Zr1    3.350   21   S
Zr1   O3     2.009   17_656 S
Zr1   O5     2.720   18_545 S
Zr1   O3     2.009   21_665 S
Zr1   O5     2.756   2_554 S
O2    C15    1.125   3_645 S
O3    Zr1    2.009   1_566 S
O3    Zr1    2.009   21_566 S
O3    Zr1    2.009   17_566 S
O4    Zr1    2.150   9    S
O4    C15    1.125   3_645 S
O5    Zr1    2.720   24   S
O5    N19    1.776   3_645 S
O5    Zr1    2.756   2    S
C13   C16    1.276   .    S
C13   C20    1.436   .    S
C15   C16    1.519   .    S
C15   O4     1.125   3_655 S
C15   O2     1.125   3_655 S
C16   C17    1.276   .    S
C17   C21    1.436   .    S
N19   C21    1.276   .    S
N19   C20    1.276   .    S
N19   O5     1.776   3_655 S
O205  Zr1    2.009   13_666 S
O205  Zr1    2.009   17_666 S
O205  Zr1    2.009   21_666 S
```

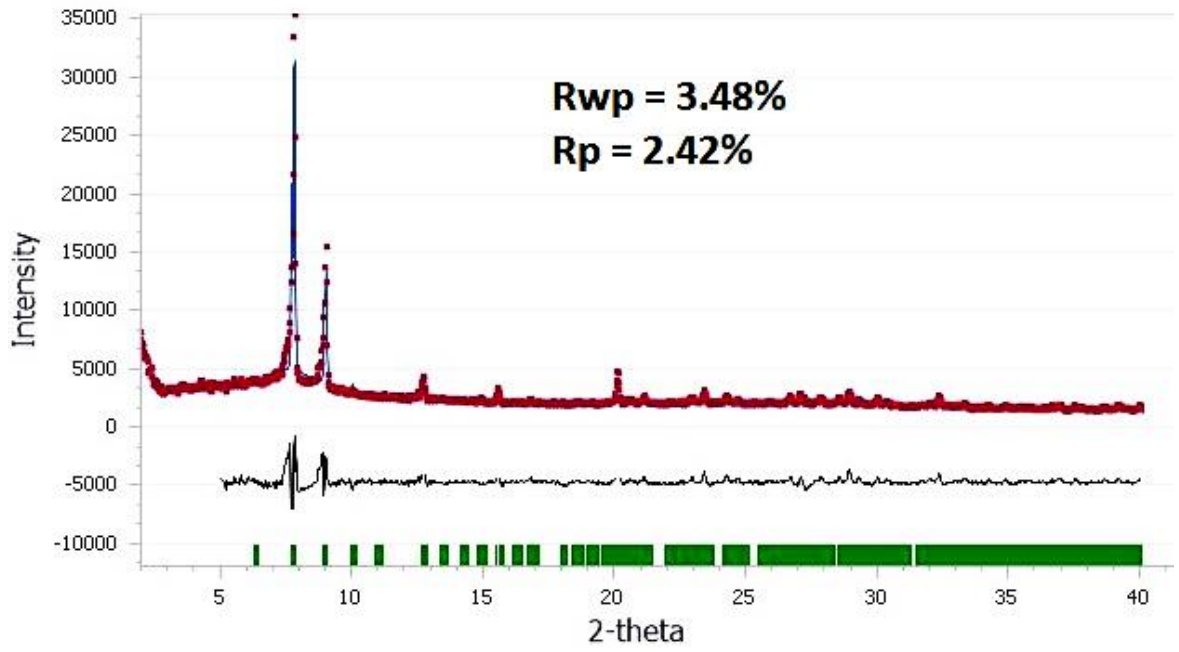

Figure 2.2. Rietveld plot of TMU-66; red: experimental pattern; blue: calculated pattern; green: Bragg peaks; and black: the difference between the experimental and calculated data.

N_2 adsorption-desorption isotherms were measured at 77 K using a Micromeritics Instrument Corporation (TriStar II), and BET and BJH methods were applied to the adsorption branch of isotherms. N_2 adsorption-desorption isotherms are curves that display the amount of nitrogen gas adsorbed and desorbed by a material at different relative pressures at a constant temperature. The shape and features of the isotherms can indicate the type and size of pores present in the material and the adsorption mechanism and hysteresis behavior.[7] BET and BJH are two methods that can calculate the material's pore size distribution and surface area from the isotherm data. **BET** stands for **Brunauer-Emmett-Teller**, a method that allows to estimate the surface area of a material by assuming that the gas molecules form a monolayer on the surface.[8] **BJH** stands for **Barrett-Joyner-Halenda**, a method that permits to assess the pore size distribution of the material by assuming that the gas molecules fill the pores by capillary condensation.[9]

Fourier-transform infrared (FT-IR) spectra were obtained by preparing a mix sample-KBr (about 1 to 2 % of the sample) pellet and using a Thermo Scientific Nicolet IR100 (Madison, WI) Fourier-transform infrared (FT-IR) spectrometer. FT-IR is a technique that measures a sample's absorption or emission of infrared radiation. The infrared spectrum gives information about the molecular structure and composition of the sample and the presence of impurities or contaminants.[10] FT-IR can also be used to monitor the changes in the chemical bonds and functional groups of the sample during reactions or modifications. FT-IR is a fast and reliable technique for solid, liquid, or gas samples.[11]

Scanning electron microscopy (SEM) imaging was conducted using ULTRA 55 (Zeiss) equipped with a thermal field emission emitter and an **energy-dispersive X-ray spectroscopy (EDS)** mapping detector. Also, **transmission electron microscopy (TEM)** imaging was performed by a TECNAI-G_2 equipped with an EDS spectrometer at a working voltage of 200 kV. SEM and EDS are techniques that allow to observe the surface features and elemental distribution of the samples at a nanometer resolution. SEM uses a beam of electrons to scan the sample and produce an image based on the secondary electrons emitted from the sample.[12] EDS uses a detector to collect the X-rays generated by the interaction of the electron beam and the sample atoms. The X-rays have characteristic energies that correspond to the elements present in the sample. By analyzing the X-ray spectrum, we can identify and quantify the elements in the sample.[13]

TEM and chemical mapping allow us to examine the samples' atomic arrangement and chemical bonding at an angstrom resolution. TEM uses a beam of electrons to transmit through a sample and produce an image based on the shared electrons. Chemical mapping uses various methods to collect the signals from different regions of the sample and generate a map that shows the spatial distribution of elements or compounds in the sample. For example, energy-filtered TEM (EFTEM) uses an energy filter to select electrons with specific energies

corresponding to certain elements or bonds. By scanning the electron beam across the sample, we can obtain a map showing where those elements or bonds are located.[14] These techniques complement each other and provide valuable information about the morphology, structure, and composition of the Zr-MOFs and MOF-based composites we synthesized and applied in this research.

X-ray photoelectron spectroscopy (XPS) measurements were acquired on a Thermo-Scientific ESCALAB Xi+ spectrometer with a spherical energy analyzer (constant analyzer energy) electromagnetic lens mode. The spectra were recorded using a monochromatic Al Kα X-ray source (1486.6 eV) at an operating power of 25 W (15 kV). The peak deconvolution and the decomposed spectra into their components were carried out using CasaXPS processing software. XPS was used to analyze the synthesized material's chemical state and electronic structure. XPS is a technique that can identify the elements and their oxidation states on the surface of a material by measuring the kinetic energy and number of electrons that are emitted when the material is irradiated with X-rays. XPS can also provide information about the bonding environment and electronic configuration of the atoms in the material.[15]

Thermogravimetric analysis (TGA) data were recorded on a Thermal Analyzer (TG 209 F3 Tarsus, Netzsch) instrument under a nitrogen atmosphere (20 mL min^{-1}), and the heating rate was adjusted to 10 °C min^{-1} from 30 to 980 °C. TGA is a technique that measures the change in mass of a sample as a function of temperature or time under a controlled atmosphere. TGA can be applied to study materials' thermal stability, decomposition, and composition. For example, TGA can help to understand:

• The amount and type of defects in MOFs, such as missing linkers or metal clusters, by comparing the mass loss of the defective MOF with the ideal MOF.[16]

• The ratio and distribution of mixed linkers in MOFs by analyzing the mass loss steps corresponding to the decomposition of different linkers.[17]

• The loading and interaction of g-C_3N_4 with MOFs by observing the mass loss of the composite and the individual components.[18]

2.3.2 Characterization of the Optical and Electrochemical Behaviour of Photocatalysts

2.3.2.1 Photochemical methods

Ultraviolet-visible (UV-vis) spectra and Tauc plot are methods that can be used to determine the band gap energy of semiconductors. The band gap energy is the minimum energy required to excite an electron from the valence band to the conduction band of a material. The band gap energy affects the optical and electronic properties of the material, such as the absorption and emission of light, the photocatalytic activity, and the conductivity.[19]

UV-vis spectroscopy is a technique that measures how much ultraviolet and visible light is absorbed or transmitted by a material. The absorption spectrum indicates the amount of light that is absorbed by the material at different energies or wavelengths, while the transmission spectrum allows to determine the amount of light that passes through the material at different energies or wavelengths. This data can be used to determine the band gap energy of the material, which is revealed by the onset of either absorption or transmission.[20]

The Tauc plot is a useful method for estimating the band gap energy of a material. It works by transforming the absorption or transmission spectrum into a linear function. The plot assumes that the absorption coefficient of the material follows a power law with respect to photon energy and band gap energy. By plotting a function of the absorption coefficient and the photon energy, a linear region can be obtained, such as $(\alpha h\nu)^2$ *vs.* $h\nu$ for direct band gap materials or $(\alpha h\nu)^{1/2}$

vs. hν for indirect band gap materials. This linear region can then be extrapolated to zero absorption coefficient to give an estimate of the material's band gap energy.[21]

Ultraviolet-visible (UV-vis) spectra were recorded using Safas Bio-UVmc² spectrophotometer using a quartz cell (1 cm path length) and a tungsten-halogen source. Absorption spectra were acquired from 200 to 800 nm at 25 ± 1 ºC**.**

The **Tauc plot** was used to determine the band gap of the samples using Tauc's relation:

$$[(\alpha h\nu)^{1/n} = C \times (h\nu - E_g)] \qquad (2.1)$$

Where hν is the incident photon energy, C is the proportionality constant, E_g is the band gap energy, and n = ½ and 2 for direct and indirect band gap, respectively.

2.3.2.2 Photo-electrochemical measurements

Electrochemical and photoelectrochemical experiments were performed with an Autolab PGSTAT204 (Metrohm, France) using a custom-made three-electrode cell with a quartz glass window. **Cyclic voltammetry (CV)**, **Nyquist**, and **Mott-Schottky plots** were acquired using a glassy carbon electrode (3 mm diameter). A saturated calomel ($Hg/HgCl_2$, 3M KCl) electrode was used as a reference electrode, and a Pt mesh was applied as a counter electrode.

To create a homogeneous catalyst ink, the as-prepared sample (10 mg) was uniformly dispersed in 1 mL of ethanol/water (1:1) and 10 µL of 5% Nafion binder and the mixture was subsequently ultrasonicated for 30 min. 5 µL of the same catalyst slurry was dropped slowly on the GC electrode surface and dried at room temperature. During the cyclic voltammetry, the potential was scanned between 1 and -1 V *versus* SCE at a scan rate of 30 mV s^{-1} for three cycles. **Electrochemical impedance spectroscopy (EIS)** was performed at an AC amplitude of 10 mV in a frequency range from 1 kHz to 0.1 Hz at open circuit potential value.

For **photocurrent measurements,** a 150W Xenon Arc Lamp (L8253 Hamamatsu, Japan) was used with a light at 400 to 700 nm cut-off filter at 420 nm. The electrolyte was Na_2SO_4 (0.5M) saturated with Ar gas for at least 30 min to remove dissolved oxygen. Current densities under illumination and in the dark were measured by mechanically chopping the light every 20 s.

Cyclic voltammetry (CV) is a technique used to measure the current response of a material when exposed to a varying potential. This method provides important insights into the redox potentials, reaction mechanisms, electron transfer kinetics, and diffusion coefficients of the material. Additionally, CV can be utilized to monitor changes in the current response of the material under various lighting conditions, such as dark, visible, or UV light. This information is crucial in evaluating the photocatalytic activity and efficiency of the material, specifically for N_2 photoreduction.[22]

Nyquist plot is a type of impedance spectroscopy used to measure the complex impedance of a material as a function of frequency. It provides valuable information, such as the charge transfer resistance, double layer capacitance, and equivalent circuit model of the material. Through Nyquist plot, we can also compare the impedance of the material under different light conditions including dark, visible, or UV light, which can help to understand the effect of light on the charge transfer and accumulation processes of the material for N_2 photoreduction.[23]

The Mott-Schottky analysis is a technique used to measure the capacitance of a material as a function of potential. This plot can provide essential information regarding the flat band potential, the density of donor or acceptor atoms, and the type of semiconductor present in the material. Additionally, it can help determine the band gap energy and conduction band position of the material. By matching the material's band structure with the light source and the redox potential of N_2, the Mott-Schottky plot can be used to optimize the material for N_2 photoreduction.[24]

Photocurrent measurements play a crucial role in studying the photoelectrochemical properties and performance of materials used in N_2 photocatalysis. These measurements are the primary tool for investigating the light absorption, charge generation, and charge transfer processes of photocatalysts. Photocurrent measurements can provide information about important parameters, such as photocurrent density, onset potential, fill factor, and conversion efficiency of the photoelectrodes. Moreover, these measurements can be used to monitor changes in the photocurrent response of the photoelectrodes under different light conditions, such as dark, visible, or UV light. This helps to evaluate the photocatalytic activity and stability of photoelectrodes for N_2 photocatalysis.[25]

2.4 Batch adsorption experiments

To make a stock solution of Congo red (CR, 696.665 g mol^{-1}) with a concentration of 1000 mg L^{-1}, 100 mg of Congo red was dissolved in 100 mL of deionized water. To create different solutions, the stock solution was diluted accordingly. During all experiments, 10 mg of solid adsorbent was used.

2.4.1 Effect of pH on the adsorption process

The impact of pH on the adsorption of Congo red was tested within a pH range from 1.0 to 10.0. The pH was adjusted by adding 0.1 M HCl or 0.1 M NaOH while maintaining a constant initial concentration of 150 mg L^{-1} for all samples. The efficiency of Congo red adsorption (% adsorption) was determined by:

$$\%adsorption = [(C_0 - C_e)/C_0] \times 100 \qquad (2.2)$$

where C_0 and C_e represent the starting and equilibrium concentrations of Congo red in mg L^{-1}, respectively.

2.4.2 Kinetics for the Congo red adsorption

To prepare ten samples, a fixed concentration of Congo red (150 mg L^{-1}) was added to 50 mL falcon conical tubes containing 10 mg of TMU-66 at 298 K. The adsorption process was halted at intervals ranging from 1 to 120 min. Subsequently, the mixture was centrifuged at 14000 rpm for 3 min and then analyzed using a UV–vis spectrophotometer (Shimadzu UV 2100). The amount of Congo red adsorbed was determined using the following calculation (Eq. 2.3):

$$q_t = [(C_0 - C_t)/m] \times V \quad (2.3)$$

Where q_t and C_t are the amount of Congo red adsorbed per unit mass of adsorbent (mg g^{-1}) and the Congo red concentration (mg L^{-1}) at time t (min), respectively; m is the adsorbent mass (g), and V is the volume of the sample (L).

The pseudo-second-order model can be described by equation (2.4):

$$\frac{t}{q_t} = \frac{1}{k_{ad} q_e^2} + \frac{t}{q_e} \quad (2.4)$$

Where q_t (mg g^{-1}) is the adsorption capacity of TMU-66 at time t (min), q_e (mg g^{-1}) is the adsorption capacity at equilibrium, and k_{ad} (g mg^{-1} min^{-1}) is the rate constant of adsorption. The values of q_e and k_{ad} were calculated from the slope and intercept of the t/q_t *vs.* t plot.

2.4.3 Adsorption isotherms and thermodynamic evaluations

To study the adsorption isotherm, 50 mL of Congo red aqueous solution (the initial Congo red concentrations varying from 5 to 120 mg L^{-1}) were poured into a falcon conical tube with 10.0 mg of TMU-66 and stirred for 2 h at 298 K. The mixture was then centrifuged at 12000 rpm for 2 min, and the concentration of remaining Congo red was determined by a UV–vis spectrophotometer (Shimadzu UV 2100). The equilibrium adsorption capacity was calculated using Eq. 3:

$$q_e = [(C_0 - C_t)/m] \times V \quad (2.5)$$

where q_e is the equilibrium amount of Congo red adsorbed per mass unit of adsorbent (mg g^{-1}) and C_0 and C_t are initial and equilibrium concentrations of Congo red, respectively.

The equation represents the dual-site Langmuir model:[26]

$$q_{total} = \frac{q_1^{max}.K_1.C_e}{1+K_1.C_e} + \frac{q_2^{max}.K_2.C_e}{1+K_2.C_e} \qquad (2.6)$$

q_{total}: total amount adsorbed at a given adsorbate concentration.
q_1^{max}: maximum capacity of site type 1 (mg g^{-1})
q_2^{max}: maximum capacity of site type 2 (mg g^{-1})
K_1: equilibrium (affinity) constant of site type 1 (L mg^{-1})
K_2: equilibrium (affinity) constant of site type 2 (L mg^{-1})

Every sentence of this model is represented by equation:

$$\frac{C_e}{q_e} = \frac{C_e}{q_m} + \frac{1}{k_L q_m} \qquad (2.7)$$

where q_m (mg g^{-1}) and k_L (L mg^{-1}) are the maximum adsorption capacity of the adsorbent and Langmuir constant, respectively. The values of q_m and k_L were calculated from the slope and the intercept of C_e/q_e *vs.* C_e plot.

Thermodynamic parameters were investigated at 283−325 K. The adsorption equilibrium constant (K_0), the changes in free energy (ΔG°, kJ mol^{-1}), enthalpy (ΔH°, kJ mol^{-1}), and entropy (ΔS°, kJ mol^{-1} K^{-1}) were calculated based on equations 2.8- 2.10:

$$K_0 = \frac{q_e}{C_e} \qquad (2.8)$$

$$\Delta G° = -RT \ln K_0 \qquad (2.9)$$

$$\ln K_0 = \frac{\Delta S°}{T} - \frac{\Delta H°}{RT} \qquad (2.10)$$

Where R and T are the universal gas constant (8.314 J mol^{-1} K^{-1}) and absolute temperature (K), respectively, ΔS° and ΔH° values are determined by drawing a linear plot of ln K_0 *vs.* 1/T.

2.5 Nitrogen Photocatalytic Experiments

2.5.1 General photocatalytic process

The nitrogen (N_2) photoreduction experiments were performed in a glass tube. 10 mg of the photocatalyst were added to 10 mL of water containing 333.3 µL of H_2SO_4. The mixture was dispersed using an ultrasonicator for 1 min, and the resulting suspension was saturated with N_2 for 30 min. After that, the solution was stirred in the dark for 30 min. During the photoreduction under visible irradiation using a 150W Xenon arc lamp (400 to 700 nm, cut-off filter at 420 nm L8253 and power (P) = 0.2 W), a balloon full of nitrogen was utilized to keep the tube under a positive pressure of N_2. At certain time intervals, 0.6 µL of the reaction mixture was collected and immediately centrifuged to separate the liquid sample from the solid catalyst. NMR and Nessler's reagent methods were used to determine the NH_4^+ ion concentration.

Determination of NH_3 by Nessler's reagent method: 10 µL of the aqueous solution of potassium tartrate ($KNaC_4H_6O_6$, 0.5 mL, 500 g L^{-1}) and 10 µL Nessler's reagent was added to the 0.6 mL of the ammonia-containing solution. After 10 min, the solution was pipetted into a quartz cuvette. Absorbance measurement was performed at λ= 420 nm.

Determination of NH_3 (^{1}H NMR): 550 µL of the ammonia-containing solution and 50 µL of DMSO-d6 were added to the NMR tube. NMR measurements were performed on an Agilent 600-MHz system.

2.5.2 Nessler's Reagent

Nessler's reagent is a solution that contains K_2HgI_4 and KOH. Under alkaline conditions, iodide and mercury ions react with ammonia to produce a reddish-brown complex. This complex strongly absorbs light at 420 nm (Eq. (2.11)), and its absorbance is directly

proportional to the concentration of ammonia in the absence of interferents. To minimize interference from other ions (such as Fe^{3+}, Co^{2+}, Ni^{2+}, Cr^{3+}, Ag^{+}, and S^{2-}), Rochelle salt ($KNaC_4H_4O_6$) is often added during the detection process.

$$2[HgI_4]^{2-} + NH_3 + 3OH^- \rightarrow Hg_2ONH_2I + 7I^- + 2HO_2 \qquad (2.11)$$

When utilizing Nessler's reagent, it is crucial to keep in mind the following: firstly, the reagent contains mercury ions that are potentially hazardous, so it is necessary to use it with caution. Secondly, the reagent's shelf life is only about three weeks. Thirdly, the water used to create the Nessler's reagent solution should be devoid of ammonia, and ultrapure water is the optimal choice. Finally, the precision of NH_3 quantification can be influenced by the duration of the ammonia reaction with Nessler's reagent, which should ideally fall between 10 and 30 minutes.[27]

2.5.2.1 Procedure for the preparation of Nessler's reagent

The preparation of Nessler’s reagent was performed as following: 1) 2 g of potassium iodide was weighed and added to a clean container. 2) 5 milliliters of water were added to the container with the potassium iodide. 3) the solution was stirred until the potassium iodide was completely dissolved. 4) 3 grams of mercury (II) iodide were weighed separately and added to the solution of potassium iodide and water. 5) the solution was stirred until the mercury (II) iodide was completely dissolved. 6) enough water was added to bring the total volume of the solution up to 20 mL. 7) 40 grams of 30% potassium hydroxide were added to the solution of mercury (II) iodide and potassium iodide. 8) the solution was stirred until the potassium hydroxide was completely dissolved. 9) The resulting solution was Nessler’s reagent with a pale orange colour.

2.5.3 Computational details

The Vienna Ab initio Simulation Package (VASP) code[28] was utilized for all calculations, within the framework of density functional theory (DFT) approach. The generalized gradient approximation (GGA) in the form of Perdew-Burke-Ernzerhof (PBE)[29] was used to consider the electron correlation functional, while the pseudopotentials were generated using the projector augmented wave (PAW) method.[30] The kinetic cut-off energy was set to 450 eV, and the force and energy convergence thresholds of 0.01 eV/Å and 10^{-5} eV per atom, respectively, were used for self-consistent optimizations. A Γ-centered Monkhorst-Pack grid[31] is utilized for performing Brillouin zone integration. The pairwise additive dispersion correction (DFT+D3), proposed by Grimme,[32] is applied to account for van der Waals interactions. MOF-808 cluster model used in the MOF-808/g-C_3N_4 configuration is constructed from $Zr_6O_4(OH)_4(HCOO)_6$ metal nodes and 1,3,5-benzene tricarboxylate (BTC^{3-}) linker, as shown in Figure 2.3. A vacuum space of 15 Å is established along the z-direction, ensuring that the periodic images of the system did not interact with each other. The adsorption energy of the adsorbates on the substrate surface is calculated using the following equation:

$$E_b = E_{Total} - E_{sub} - E_{ads}$$

Where E_{Total} corresponds to the energy of the adsorbed species on the substrate, while E_{sub} and E_{ads} are the energies of the isolated substrate and adsorbates, respectively.

The Gibbs free energy change of the NRR process was computed using the following equation:

$$\Delta G = \Delta E_{DFT} + \Delta E_{ZPE} - T\Delta S$$

Where E_{DFT} is the DFT computed total energy difference. ΔE_{ZPE} and $T\Delta S$ correspond to zero-point energy change and entropy change between reactants and products, respectively, at a temperature of 298.15 K.

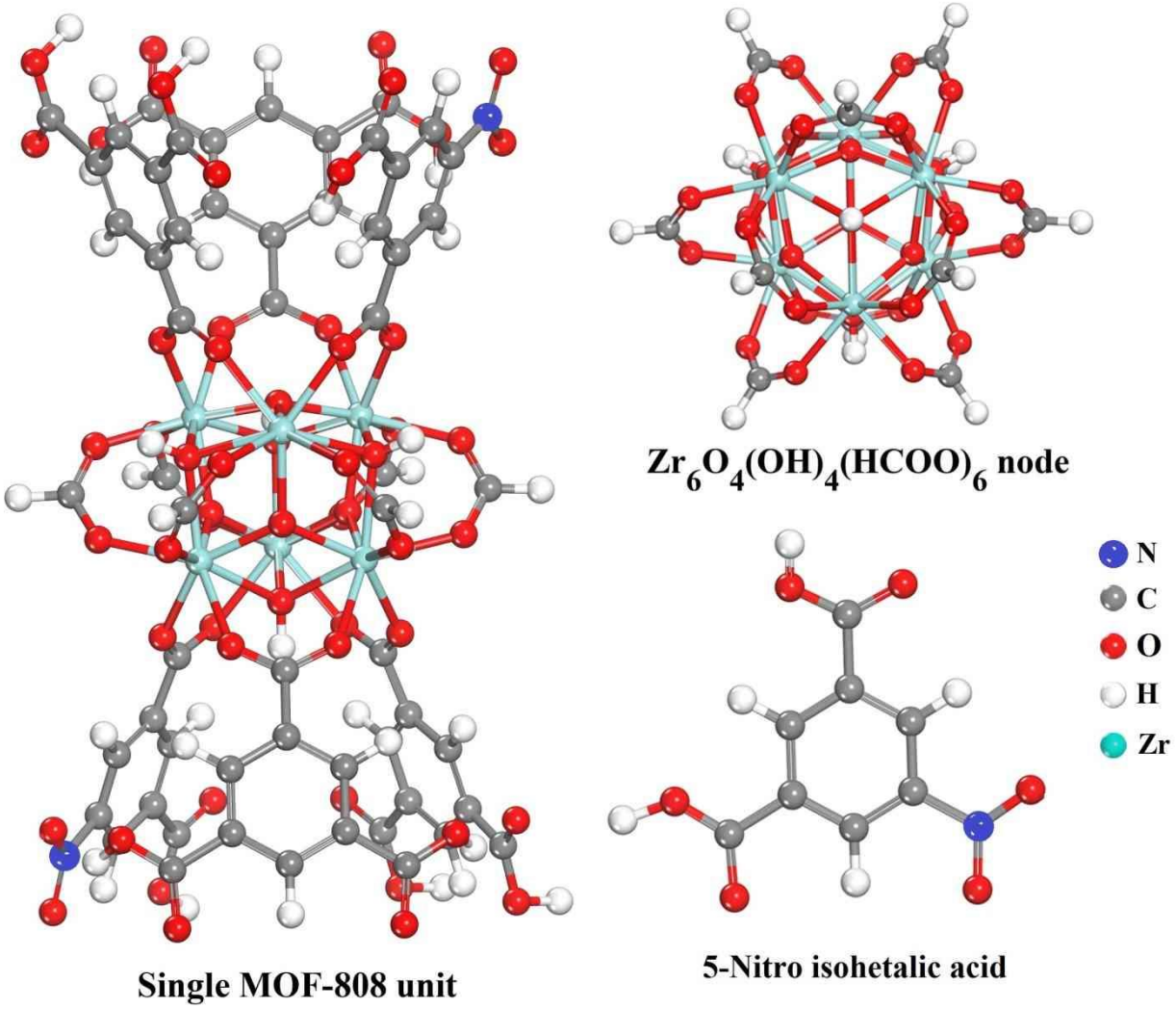

Figure 2.3. The single MOF-808 unit structure constructed from $Zr_6O_4(OH)_4(HCOO)_6$ metal nodes and 1,3,5-benzene tricarboxylate (BTC^{3-}) linker.

2.6 References

(1) Wang, Z.; Wang, H.; Zeng, Z.; Zeng, G.; Xu, P.; Xiao, R.; Huang, D.; Chen, X.; He, L.; Zhou, C.; Yang, Y.; Wang, Z.; Wang, W.; Xiong, W. *Appl. Catal. B Environ.* **2020**, *267*, 118700.

(2) Holder, Cameron F., and Raymond E. Schaak. *Acs Nano* **2019**, 7359-7365.

(3) Bunaciu, Andrei A., Elena Gabriela UdriŞTioiu, and Hassan Y. Aboul-Enein. *Critical reviews in analytical chemistry* **2015**, 289-299.

(4) Evans, John SO, and Ivana Radosavljevic Evans. *Journal of Chemical Education* **2020**, 495-505.

(5) Pecharsky, Vitalij K., and Peter Y. Zavalij. *Fundamentals of Powder Diffraction and Structural Characterization of Materials* **2003**, 599-701.

(6) Rapti, Sofia, et al. *Journal of Materials Chemistry A* **2017**, 14707-14719.

(7) Ravikovitch, Peter I., and Alexander V. Neimark. *Colloids and Surfaces A: Physicochemical and Engineering Aspects* **2001**, 11-21.

(8) Naderi, Majid. *Progress in filtration and separation*. Academic Press **2015**. 585-608.

(9) Bardestani, Raoof, Gregory S. Patience, and Serge Kaliaguine. *The Canadian Journal of Chemical Engineering* **2019**, 2781-2791.

(10) Stuart, Barbara. *Analytical Techniques in Forensic Science* **2021**, 145-160.

(11) McClelland, J. F., et al. *Practical sampling techniques for infrared analysis*. CRC Press **2020**. 107-144.

(12) Zhou, Weilie, et al. *Scanning Microscopy for Nanotechnology: Techniques and Applications* **2007**, 1-40.

(13) Newbury, Dale E., and Nicholas WM Ritchie. *Journal of Analytical Atomic Spectrometry* **2013**, 973-988.

(14) Inkson, Beverley J. *Materials characterization using nondestructive evaluation (NDE) methods*. Woodhead publishing **2016**, 17-43.

(15) Chastain, Jill, and Roger C. King Jr. *Perkin-Elmer Corporation* **1992**, 221.

(16) Karimia, Meghdad, et al. *New Journal of Chemistry* **2021**, 6671-6681.

(17) Zhao L, Zhao Z, Li Y, Chu X, Li Z, Qu Y, Bai L, Jing L. *Nanoscale.* **2020**, 10010-8.

(18) Jiang, Jing-Jing, Feng-Jun Zhang, and Ying-Rui Wang. *New Journal of Chemistry* **2023**, 1599-1609.

(19) Haryński Ł, Olejnik A, Grochowska K, Siuzdak K. Optical Materials **2022**, 112205.

(20) Shard, Alexander G., Robert C. Schofield, and Caterina Minelli. *Characterization of Nanoparticles*. Elsevier, **2020**. 185-196.

(21) Makuła, Patrycja, Michał Pacia, and Wojciech Macyk. *The journal of physical chemistry letters* **2018**, 6814-6817.

(22) Kissinger, Peter T., and William R. Heineman. *Journal of chemical education* **1983**, 702.

(23) Instruments, Gamry. "Basics of electrochemical impedance spectroscopy." *G. Instruments, Complex impedance in Corrosion* **2007**, 1-30.

(24) Gelderman, K., L. Lee, and S. W. Donne. "Flat-band potential of a semiconductor: using the Mott–Schottky equation." *Journal of chemical education* **2007**, 685.

(25) van de Krol, Roel. *Photoelectrochemical hydrogen production*. Boston, MA: *Springer US* **2011**. 69-117.

(26) VanDer Kamp, Kirk A., Dongmei Qiang, Aktham Aburub, and Dale Eric Wurster. *Langmuir* **2005**, 217-224.

(27) Zhao, Yunxuan, Run Shi, Xuanang Bian, Chao Zhou, Yufei Zhao, Shuai Zhang, Fan Wu et al. *Advanced Science* **2019**, 1802109.

(28) Kresse, G.; Furthmüller, J. Efficient Iterative Schemes for Ab Initio Total-Energy Calculations Using a Plane-Wave Basis Set. Phys. Rev. B **1996**, 11169–11186.

(29) Perdew, J. P.; Burke, K.; Ernzerhof, M. Generalized Gradient Approximation Made Simple. Phys. Rev. Lett. **1996**, 3865–3868.

(30) Blöchl, P. E. Projector Augmented-Wave Method. Phys. Rev. B **1994**, 17953–17979.

(31) Monkhorst, H. J.; Pack, J. D. Special Points for Brillouin-Zone Integrations. Phys. Rev. B **1976**, 5188–5192.

(32) Grimme, S.; Antony, J.; Ehrlich, S.; Krieg, H. A Consistent and Accurate Ab Initio Parametrization of Density Functional Dispersion Correction (DFT-D) for the 94 Elements H-Pu. J. Chem. Phys. **2010**, 154104.

Chapter 3

Adsorption as a Gateway to Structural Characterization

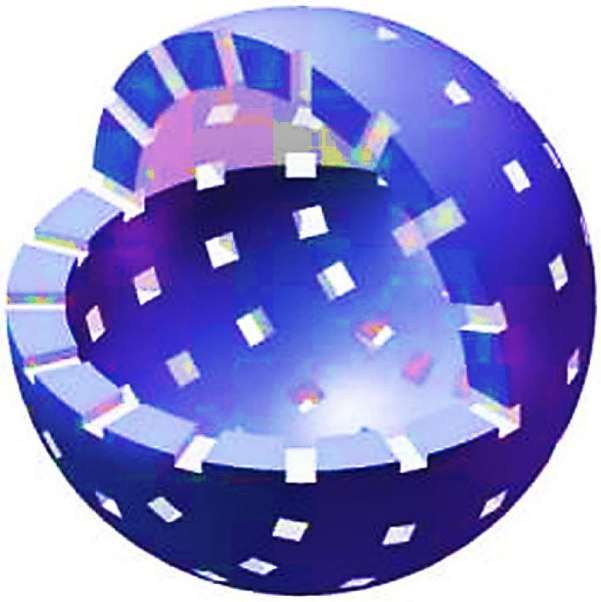

3. Adsorption as a Gateway to Structural Characterization

3.1 Introduction

In the fascinating realm of materials science, the investigation of highly porous components has long challenged researchers.[1,2] Yet, advancements in characterization methods have paved the way for a deeper understanding of these intricate materials. Among these methods, adsorption has emerged as a valuable tool for unraveling the complexities of porous materials by examining the behavior of substances that adhere to their surfaces.[3] Through exploring the adsorption process, scientists gain valuable insights into the unique properties, structures, and applications of such materials.[4]

An area of significant research interest lies in the adsorption of anionic dyes, particularly those used in critical industries, such as textiles and water treatment. Anionic dyes, widely used in industries like textiles, printing and dyeing, pose a significant environmental challenge due to their persistence, toxicity, and color.[5] The effective removal of anionic dyes from wastewater is crucial to prevent water pollution and ensure the safety of aquatic ecosystems. Congo Red (CR) is a synthetic dye with anionic properties that is frequently employed among these dyes. Even at low concentrations, it can pose significant risks to human health and aquatic ecosystems, such as plant growth inhibition, carcinogenicity, and kidney disease. CR's complex and stable aromatic molecular structure makes it difficult to break down naturally, necessitating the immediate development of effective methods for removing it from aqueous solutions.[6,7] Numerous technologies have been implemented for water treatment, encompassing electroflocculation, membrane filtration, ultrafiltration, photodegradation, and adsorption.[8] Among these, adsorption shines for its cost-effectiveness, superior performance, user-friendliness, and minimal secondary pollution. Carbon-based materials, like activated carbon, biochar and carbon nanotubes, are commonly used.[9,10] However, their inconsistent performance and inability to be tailored lead to subpar adsorption capabilities.

One intriguing class of porous materials that has garnered considerable attention is Metal-Organic Frameworks (MOFs).[11,12] These compounds consist of metal ions coordinated with organic ligands, resulting in intricate and highly ordered structures. The remarkable feature of MOFs lies in their interconnected pores and channels, which endows them with exceptional versatility for various purposes. MOFs present an array of benefits compared to traditional adsorbents. These include extensive surface area, substantial pore volume, customizable chemical properties, and effortless modification. MOFs can efficiently adsorb CR via interactions like hydrogen bonding, electrostatic attraction, coordination bonding, and π–π stacking.[13] Among various MOF types, Zr-based MOFs (Zr-MOFs) have demonstrated outstanding potential in adsorbing and removing different pollutants from aqueous solutions.[14,15] Certain MOFs exhibit a unique hollow sphere morphology, enhancing their adsorption capability and rendering them particularly promising for environmental remediation, gas storage, and separation processes.[16]

In this chapter, our focus rests on an in-depth investigation of TMU-66,[17] a novel MOF-based on zirconium, and isonicotinic acid N-oxide as a linker with noteworthy hollow sphere morphology, which measures over 1.4 micrometers in size. Using adsorption as a powerful analytical tool, we aim to comprehensively understand TMU-66's structure, functionality, and adsorption properties. By conducting meticulous experimental studies and rigorous data analysis, we seek to elucidate the intricate mechanisms that underlie its adsorption behavior, thereby shedding light on the immense potential of MOFs for a wide range of practical water treatment applications.

3.2.1 Comparison of TMU-66 synthesized with HCl and modulator

TMU-66 was synthesized using two different methods: 1) modulator-controlled synthesis[18], $Zr_6O_4(OH)_4(INO)_6(BzO)_4(OH)_2(DMF)_2$, (BzO = benzoate), and 2) synthesis through addition

of HCl to reaction mixture[19], $Zr_6O_4(OH)_4(INO)_6(Cl)_4(OH)_2(DMF)_3(H_2O)_4$. To ascertain the chemical formula of the synthesized materials, the crystalline powders of TMU-66 underwent various analytical tests. CHN elemental analysis and inductively coupled plasma optical emission spectrometry (ICP-OES) assisted in determining the percentage of elements present in the compounds (Table 3.1). Also, Energy-dispersive X-ray spectroscopy (EDS) and X-ray photoelectron spectroscopy (XPS) to identify the presence of elements, especially Cl, in the materials. Finally, thermal gravimetric analysis (TGA) before and after activation was utilized to determine the quantity of DMF and H_2O in the structures (Figure 3.1).

Table 3.1. Elemental analysis of TMU-66.

Complex	%C	%H	%N	%Zr
Observed HCl-synthesized TMU-66	27.57	3.04	6.01	27.35
Calculated for $Zr_6O_4(OH)_4(INO)_6(Cl)_4(OH)_2(DMF)_3(H_2O)_4$	27.35	2.99	6.38	27.72
Observed benzoic acid (BzO) -synthesized TMU-66	38.63	3.52	5.33	25.76
Calculated for $Zr_6O_4(OH)_4(INO)_6(BzO)_4(OH)_2(DMF)_2$	38.69	2.95	5.16	25.20

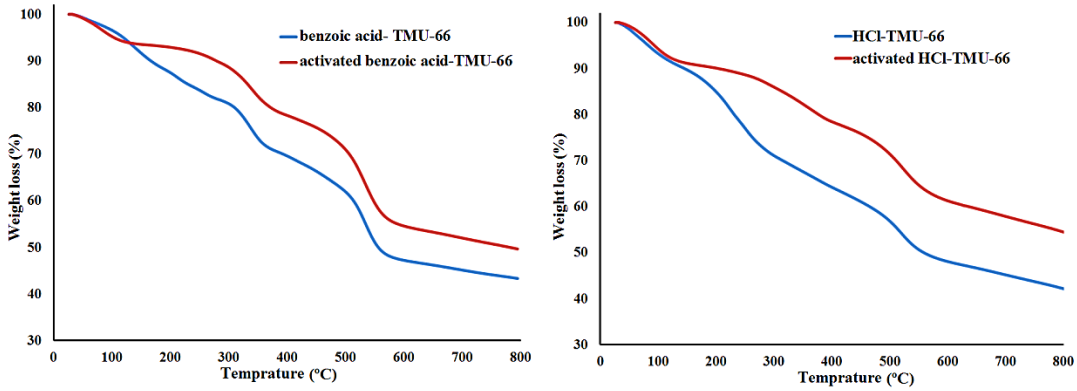

Figure 3.1. TGA plots of HCl- and benzoic acid-synthesized TMU-66.

The modulator-controlled synthesis method produces MOF material with higher crystallinity, as evidenced by sharper and more intense peaks in PXRD patterns compared to the second method (Figure 3.1). Benzoic acid tunes TMU-66 crystal growth as a modulator in the synthesis. This modulator could terminate the framework and participate in the framework

formation as a partial substitute for INO, because of the similar coordination mode. Unlike INO, benzoate can only connect to one Zr_6 cluster, and it is much more likely to detach from frameworks. Therefore, defects in the frameworks can be generated, which not only expand the pore size by combining neighboring pores but also result in coordinately unsaturated Zr sites.[20] The existence of defects in the frameworks was confirmed by N_2 adsorption isotherms at 77 K, as shown in Figure 3.2-a in comparison with HCl-synthesized TMU-66 (Figure 3.2-b). BET surface area of TMU-66 increased from 79 to 384 m^2/g using a benzoic acid modulator instead of HCl.

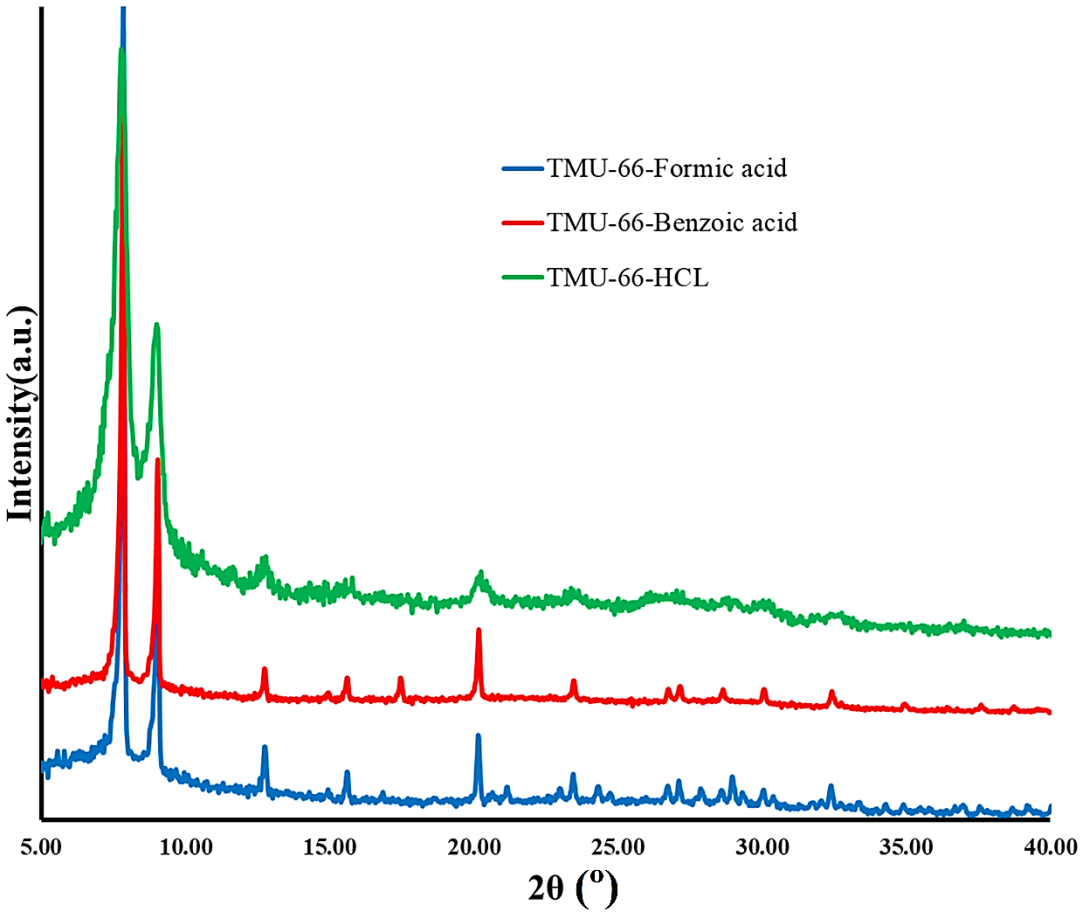

Figure 3.2. Comparison of the PXRD patterns of the synthesized TMU-66 with modulators and HCl.

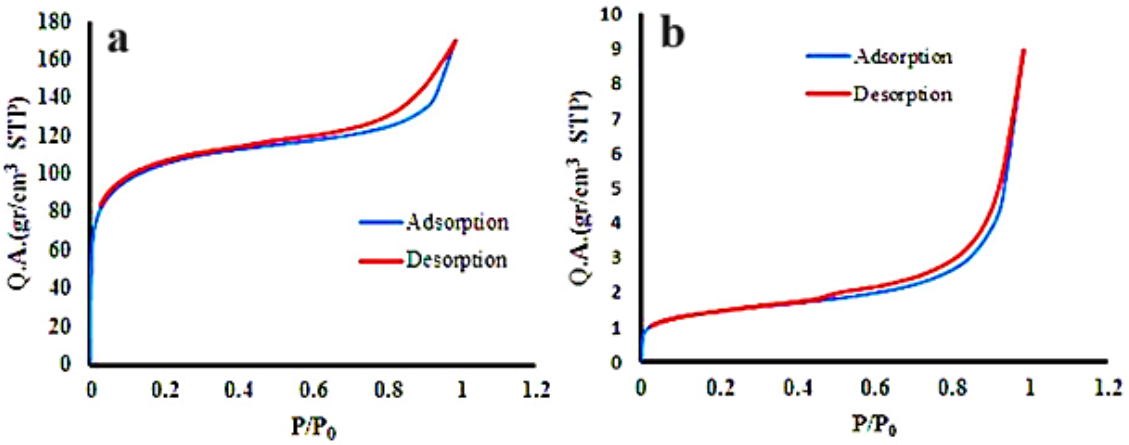

Figure 3.3. Nitrogen gas adsorption-desorption isotherms: (**a**) benzoic acid-synthesized TMU-66, and (**b**) HCl-synthesized TMU-66.

3.2.2 Structural description of TMU-66

According to the crystal structure refinement of TMU-66 mentioned in Chapter 2, TMU-66 crystallizes in the cubic lattice space group $\boldsymbol{Pa\bar{3}}$ (No. 205) with the cell parameter a = 19.6716 Å. The IBU consists of a hexanuclear cluster $[Zr_6O_4(OH)_4]$. Each Zr^{4+} center is coordinated by four face-capped oxygen atoms (μ_3–O and μ_3–OH), two oxygen atoms from N-oxide groups (μ_2–O), and two oxygen atoms from carboxylate groups (μ_2-η^1:η^1) (Figure 3.4).

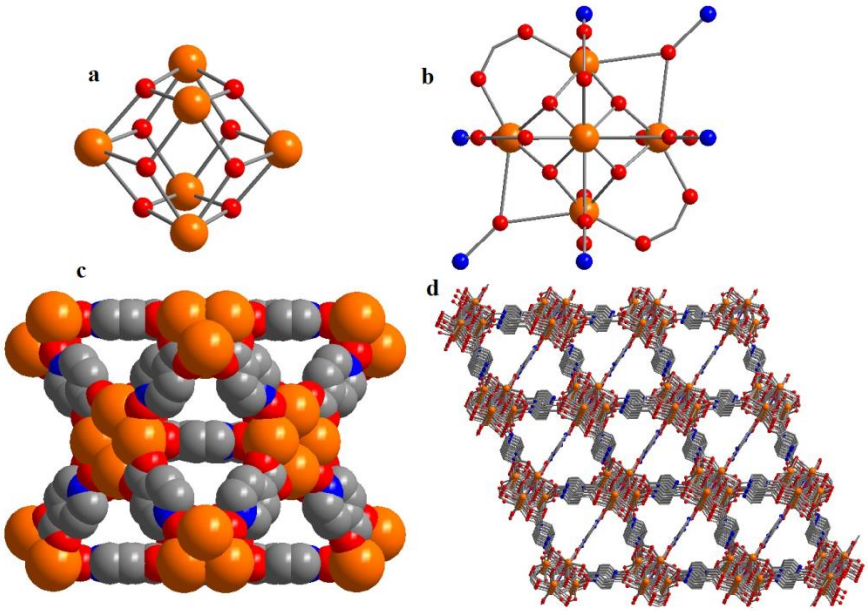

Figure 3.4. Structural and topological representation of TMU-66: (**a**) $[Zr_6O_4(OH)_4]$ cluster; (**b**) coordination environment around Zr_6 cluster in TMU-66; (**c**) and (**d**) 3-dimensional structures; orange, Zr; red, O; blue, N; and grey, C atoms.

Each Zr_6-cluster is surrounded by 12 INO ligands (Figure 3.5-a), which create a 3D structure with two types of octahedral (10.5 Å) and tetrahedral (7 Å) pores that are connected to each other through triangular windows (5 Å) (Figure 3.5 -b, c, and d). TGA analysis indicated that the pores are occupied with water and DMF molecules (Figure 3.11). XPS and EDS proved the existence of chlorine atoms in the structure. The characteristic peak of Cl^- anions in XPS spectra was deconvoluted into Cl $2p_{3/2}$ and Cl $2p_{1/2}$ located at 197.89 and 199.38 eV (Figure 3.12-f). Therefore, chloride ions can be located near Zr_6 nodes through ionic interactions.

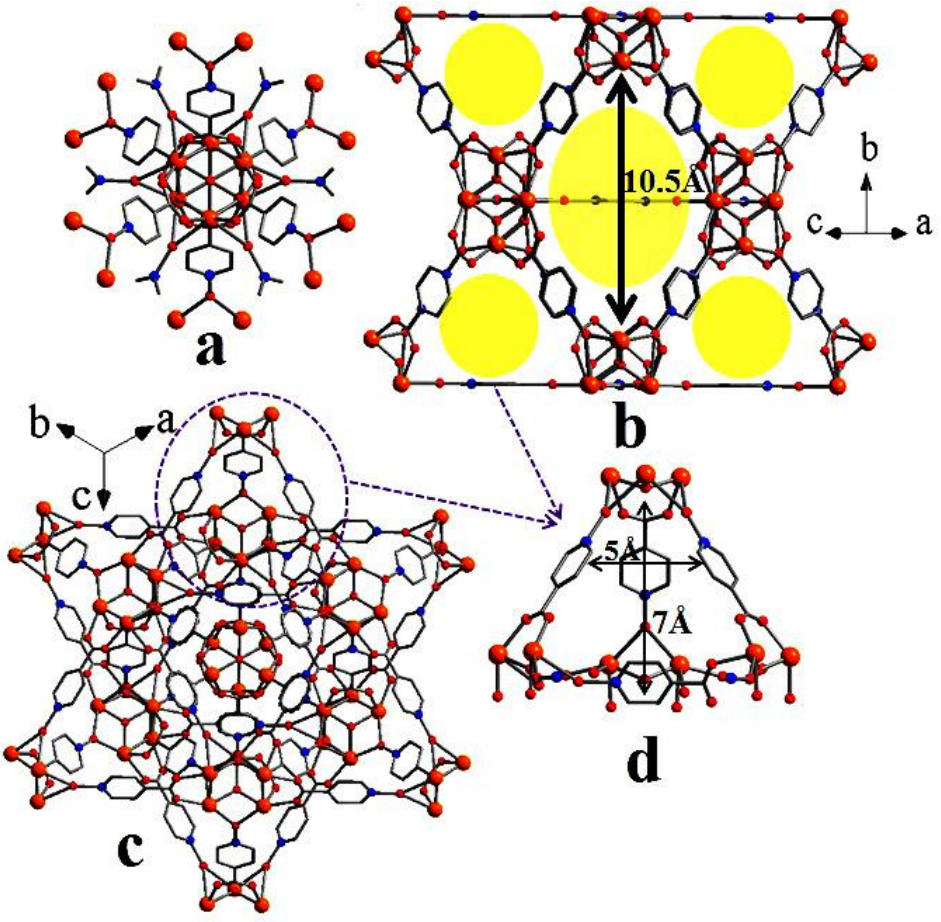

Figure 3.5. (**a**) Representation view of TMU-66 with 12-coordinated cluster $[Zr_6O_4(OH)_4(ON)_6(CO_2)_6]$; (**b**) Representation of octahedral pore (10,5 Å) of TMU-66; (**c**) One unit cell of TMU-66 in the [111] direction; d); Representation of tetrahedral pore (7 Å) with a triangular window (5 Å) of TMU-66; Color code: orange, Zr; red, O; blue, N; grey, C atoms.

The synthesized MOFs were assessed for their adsorption of Congo Red (CR). The primary results indicated that HCl-synthesized TMU-66 has a higher adsorption capacity. Therefore, this sample was used for further characterization and adsorption studies. In Figure 3.2, we can see the PXRD pattern of the HCl-synthesized TMU-66, which displays various peaks at 2θ values of 7.8°, 8.9°, 12.7°, 15.6°, 20.1°, and 23.4° corresponding respectively to the (111), (200), (222), (400), (420), and (600) reflections of the cubic $Pa\bar{3}$ space group. As shown, TMU-66-HCl and TMU-66-formic are in good agreement with each other (Figure 3.2).

The Fourier transform infrared (FT-IR) spectrum of TMU-66 is depicted in Figure 3.6. In the 1800-800 cm^{-1} region, INO displays characteristic ν(C=O) (1720-1708 cm^{-1}), ν(C−O) (1400-1439 cm^{-1}), ν(N−O) (1220-1290 cm^{-1}) and δ(N−O) (877-852 cm^{-1}) vibrations.[21,22] In this study, two characteristic peaks at 872 and 1235 cm^{-1} are attributed to the bending and stretching vibrations of the N-O bond, respectively, which indicates that the N-O group is coordinated to Zr-nodes. The two intense bands at around 1604 and 1411 cm^{-1} are associated with the OCO asymmetric and symmetric stretching vibrations of the carboxylate group in INO, respectively. The band at around 560 cm^{-1} belongs to the Zr–(OC) asymmetric stretch and the bands at about 640 and 462 cm^{-1} are assigned to the μ_3-O and the μ_3-OH stretchings in Zr-nodes, respectively.[23] The small shoulder at 1658 cm^{-1} in the TMU-66 before adsorption corresponds to the C=O asymmetric stretching of the residual DMF within the pores. The hetero-aromatic structure shows the presence of the C–H stretching vibration in the 2933–3110 cm^{-1} range, which is the characteristic region for ready identification of C–H stretching vibrations.[24] Also, OH stretching vibration with a broad band at 3401 cm^{-1} is observed.

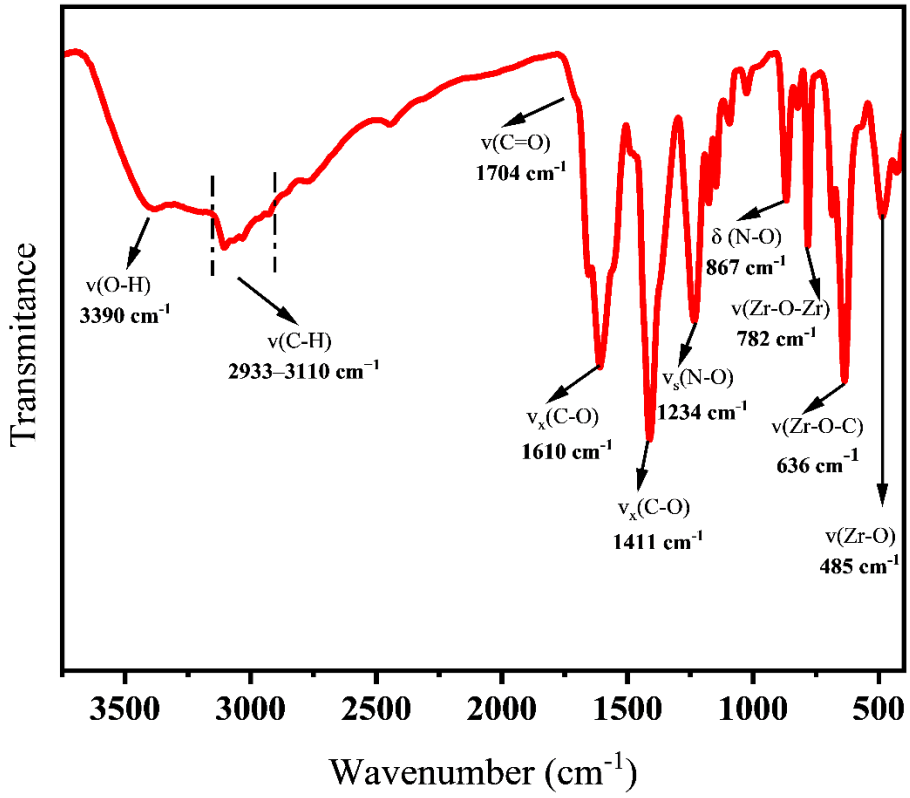

Figure 3.6. FT-IR spectrum of TMU-66.

The surface area and pore distribution were determined by using the BET and BJH methods through N_2 adsorption/desorption at 77 K. Figure 3.7-a depicts the nitrogen adsorption/desorption isotherm of hollow TMU-66 spheres, with a BET surface area of 66.76 m^2/g. Based on this figure, it could be seen that the adsorption branch adheres to an isotherm that falls between types I and IV. This suggests that the material is micro-mesoporous and undergoes capillary condensation.

Capillary condensation is a phenomenon that occurs after multilayer adsorption and is the reason behind the second upward trend seen in Type IV isotherms that display an S-shaped curve. At a relative pressure of 1 atm, the isotherm of Type IV exhibits a plateau once all pores are filled. However, incomplete filling may occur in macroporous materials with more prominent pores like TMU-66, leading to a hysteresis loop. The vapor pressure of the adsorptive sets the maximum threshold for pore size where capillary condensation can occur.

Any pressure surpassing this limit leads to complete bulk condensation. As a result, it is impossible to measure pores larger than 50-100 nm in diameter (macropores) using the N_2 adsorption technique. The desorption branch displays a type H4 hysteresis loop featuring a narrow loop that initiates and concludes at active pressure. This hysteresis loop relates to tiny slit-like pores, particles with internal voids, or hollow spheres.

Based on the BJH method, illustrated in Figure 3.7b, it was noticed that as the pore volume increases, the pore size decreases. This indicates that the walls of the hollow TMU-66 spheres are composed of an orderly mesoporous structure with an average pore size of 43.707 Å and a pore volume of 0.22412 cm^3 g^{-1}.

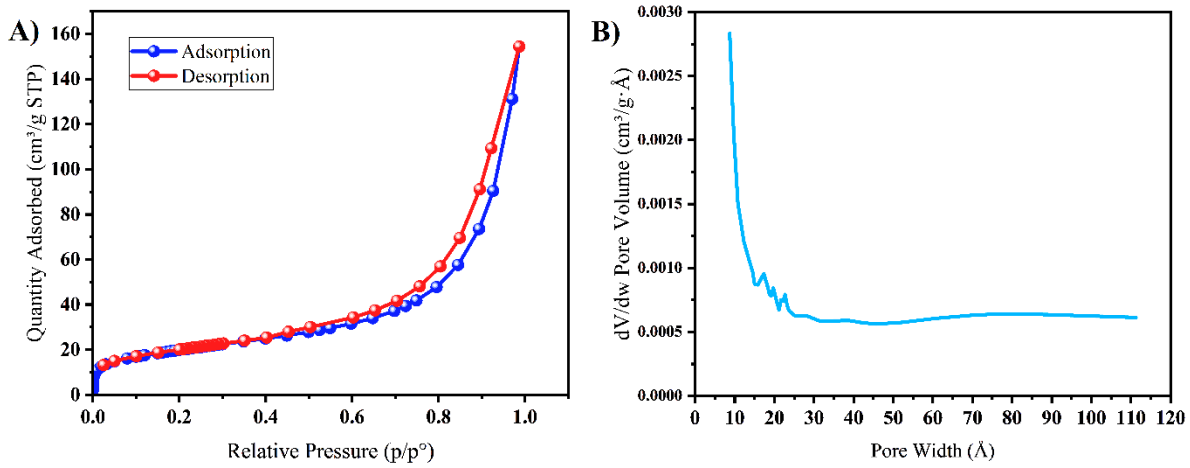

Figure 3.7. (A) Nitrogen adsorption/desorption isotherm and **(B)** pore size distribution of the TMU-66 by BJH method.

Through the use of field-emission scanning electron microscopy (FESEM), we have examined the morphology of TMU-66. Figure 3.8-a&b displays a sphere-like structure of TMU-66 with a smooth surface and a diameter of > 1.5 µm, which could provide a large contact area for adsorption. The compound possesses a hollow structure, as evidenced by the broken spheres (Fig. 3.8-c&d), with a shell thickness ranging from 160 to 210 nm. Additionally, energy-dispersive spectroscopy (EDS) elemental mapping images of TMU-66 (Figs. 3.9 & 3.10)

revealed a uniform distribution of Zr, C, O, N, and Cl elements throughout the Zr-MOF hollow sphere, which correspond to the metal nodes and organic linkers of the framework. Unfortunately, TEM analysis cannot be employed for characterization due to the particle size exceeding the expected range of 100-150 nm.

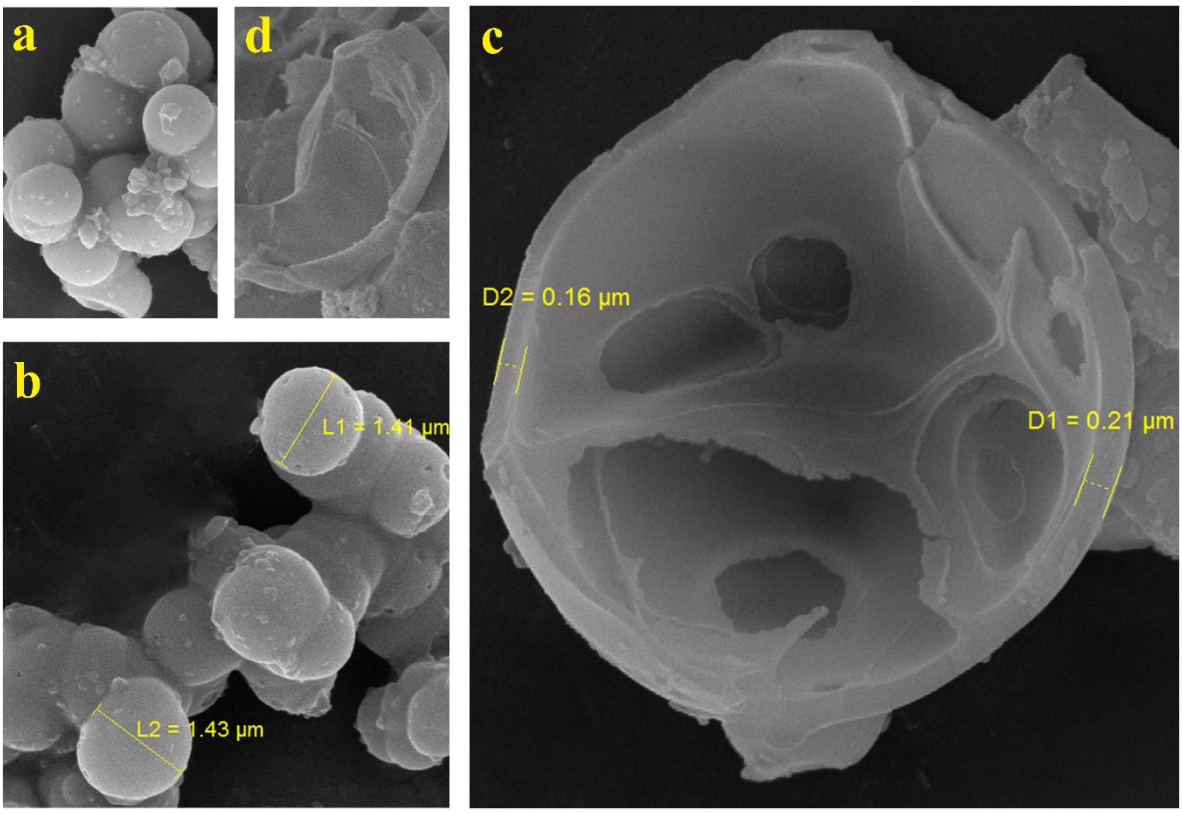

Figure 2.8. SEM images of TMU-66. (**a**) spherical structure, (**b**) diameters of micro-spheres, (**c**) shell thickness of the broken spheres, and (**d**) broken spheres.

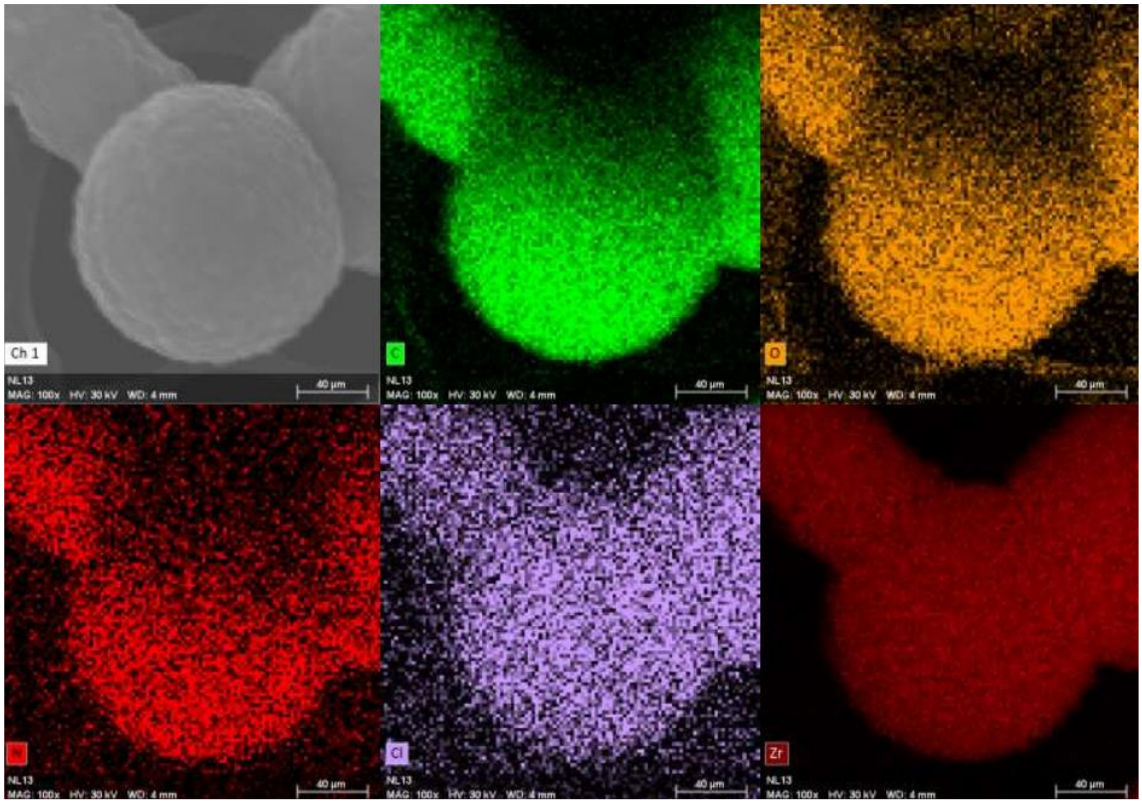

Figure 3.9. SEM image and elemental mapping of C, O, N, Cl and Zr in TMU-66.

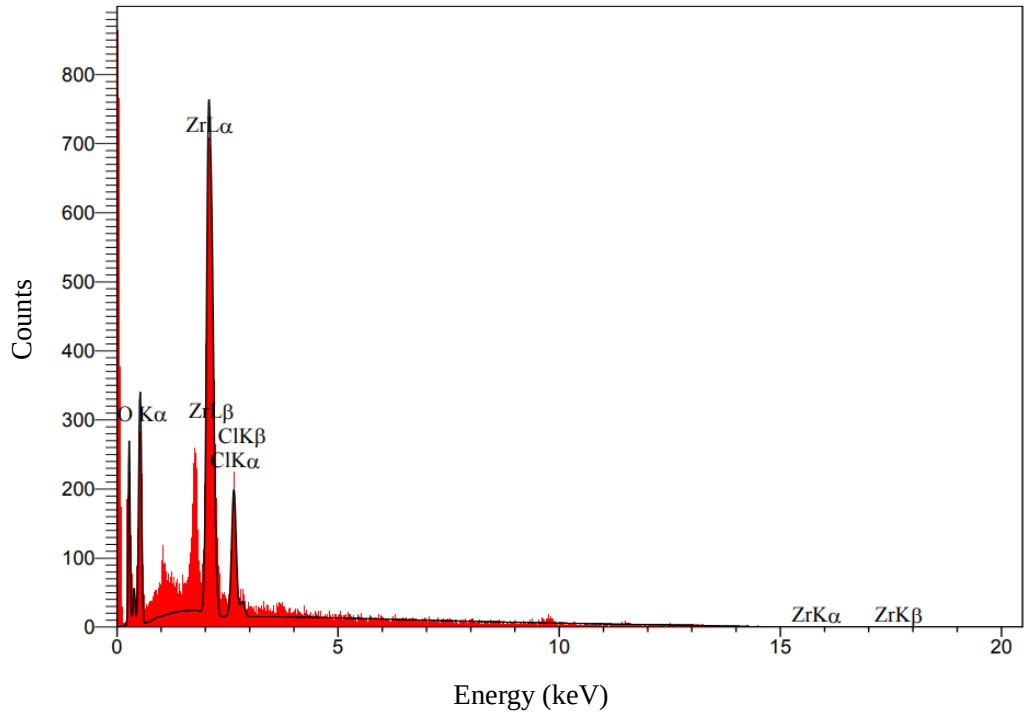

Figure 3.10. Energy dispersive X-ray spectroscopy (EDS) spectrum of TMU-66.

Table 3.2. Quantitative data of energy dispersive X-ray spectroscopy (EDS) of TMU-66.

Elt	Line	Int	Error	K	Kr	Wt%	At%	ZAF	Pk/Bg
C	Ka	42.5	21.3874	0.2178	0.0767	28.35	40.34	0.2707	31.60
N	Ka	8.0	21.3874	0.0557	0.0196	12.55	15.31	0.1564	6.24
O	Ka	83.2	21.3874	0.2128	0.0749	36.22	38.69	0.2069	60.46
Cl	Ka	78.0	11.0278	0.1038	0.0366	4.68	2.25	0.7814	13.93
Zr	La	230.3	11.0278	0.4099	0.1444	18.21	3.41	0.7930	33.94
				1.0000	0.3522	100.00	100.00		

Figure 3.11 shows the TGA and DTG curves of TMU-66, which can be divided into three distinct regions.[25] From room temperature to 220 °C, the first region exhibits two mass losses of roughly 7.02% and 5.02%, respectively. These losses are attributed to the removal of physically adsorbed water and residual solvent molecules from the material's pores. The DTG curve indicates two peaks at approximately 100 and 180 °C corresponding to these steps. The second region, ranging from 220 to 420 °C, shows a mass loss of about 6.62% due to evaporation of chemically bonded water molecules from the zirconium oxide clusters. Additionally, a mass loss of 7.65% remains even after MOF activation, which may be attributed to trapped water molecules inside the hollow spheres' central hole. The DTG curve depicts peaks at around 300 and 400 °C, corresponding to these steps. The third and final stage spans from 500 to 1000 °C and exhibits a mass loss of approximately 19.45%. This loss is due to the decomposition of the INO linkers, followed by the formation of ZrO_2 and NO_x, resulting in a final mass loss of around 10.47%. The DTG curve features a sharp peak at about 500 °C and a broad small peak at around 850 °C, corresponding to this step.

One notable feature of the hollow spheres that could be detected through TGA is the increase in mass caused by the adsorption of water vapor or other gases within the pores or cavities of

the hollow structure. The TGA curve of TMU-66 reveals a rise in mass at low temperatures due to the adsorption of water molecules on the surface or inside the material's pores.[26]

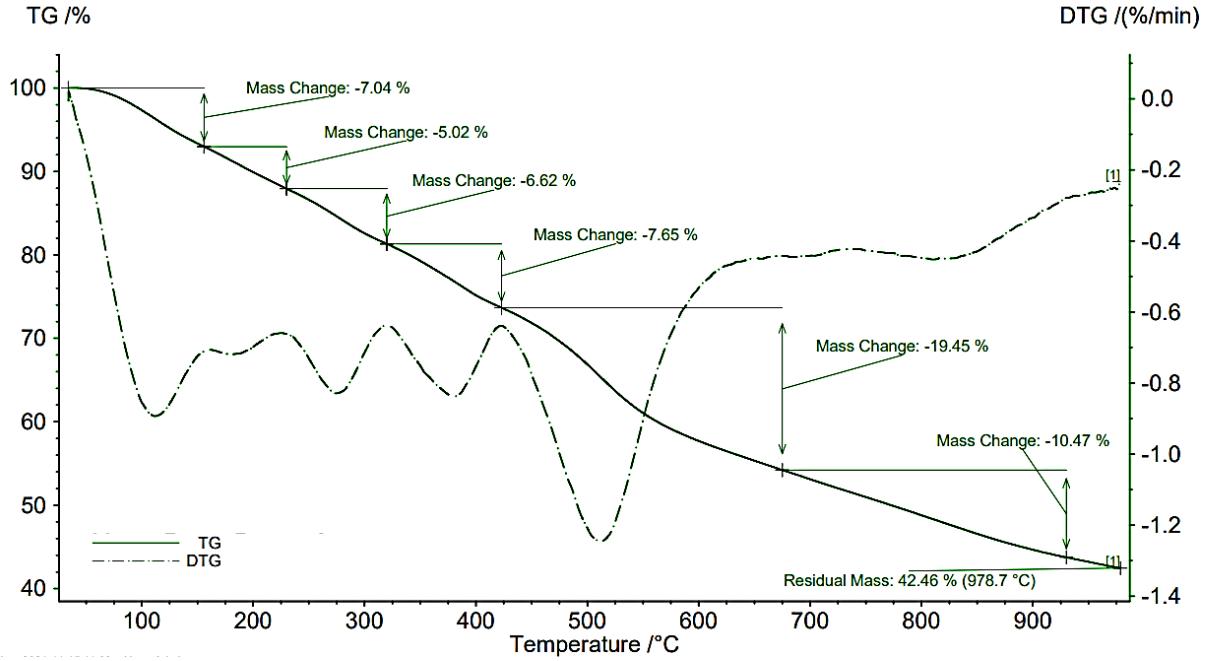

Figure 3.11. Thermogravimetry analysis (TGA) and differential thermogravimetric (DTG) of TMU-66.

The hierarchical hollow spheres were analyzed using X-ray photoelectron spectroscopy (XPS) to identify the surface species and chemical states. The XPS survey spectrum reveals the presence of carbon, nitrogen, oxygen, zirconium, and chlorine in the sample, as depicted in Figure 3.12-a and Table 3.3.

Table 3.3. Atomic concentration of elements on the surface determined by XPS.

Sample	Surface Atomic Score Levels (%)				
	C 1s	N 1s	O 1s	Zr 3d	Cl 2p
TMU-66	74.85	2.32	18.74	3.03	1.06

The high-resolution XPS spectrum of the C 1s (Figure 3.12b) is fitted with three distinct peaks at 284.63, 285.92, and 288.59 eV, respectively. These peaks correspond to the C–C, C–N, and C=O bonds, characteristic of the INO linker in TMU-66. The N 1s spectrum is deconvoluted

into two peaks: C-N (399.12 eV) and N-O (403.04 eV), indicating the presence of nitrogen species from INO linkers. The Zr 3d core level spectrum in Figure 3.12-d is curve-fitted with two significant peaks at approximately 182.53 and 184.92 eV, which are ascribed to the Zr $3d_{5/2}$ and Zr $3d_{3/2}$ energy levels, respectively. These peaks indicate the presence of zirconium species in the sample, and their bonding energy aligns with the values reported in the literature for Zr-nodes coordinated with linkers in Zr-MOFs.[27] In Figure 3.12-e, the O 1s spectrum of TMU-66 is deconvoluted into several bands at 529.92, 531.77, and 533.31 eV attributed to Zr-O, C-O, and N-O, respectively. These oxygen species are characteristic of the bonding energy between Zr nodes and INO linker in TMU-66. The characteristic peak of Cl^- anions in the Cl 2p core level XPS spectrum was deconvoluted into Cl $2p_{3/2}$ and Cl $2p_{1/2}$ located respectively at 197.89 and 199.39 eV (Figure 3.12-f).

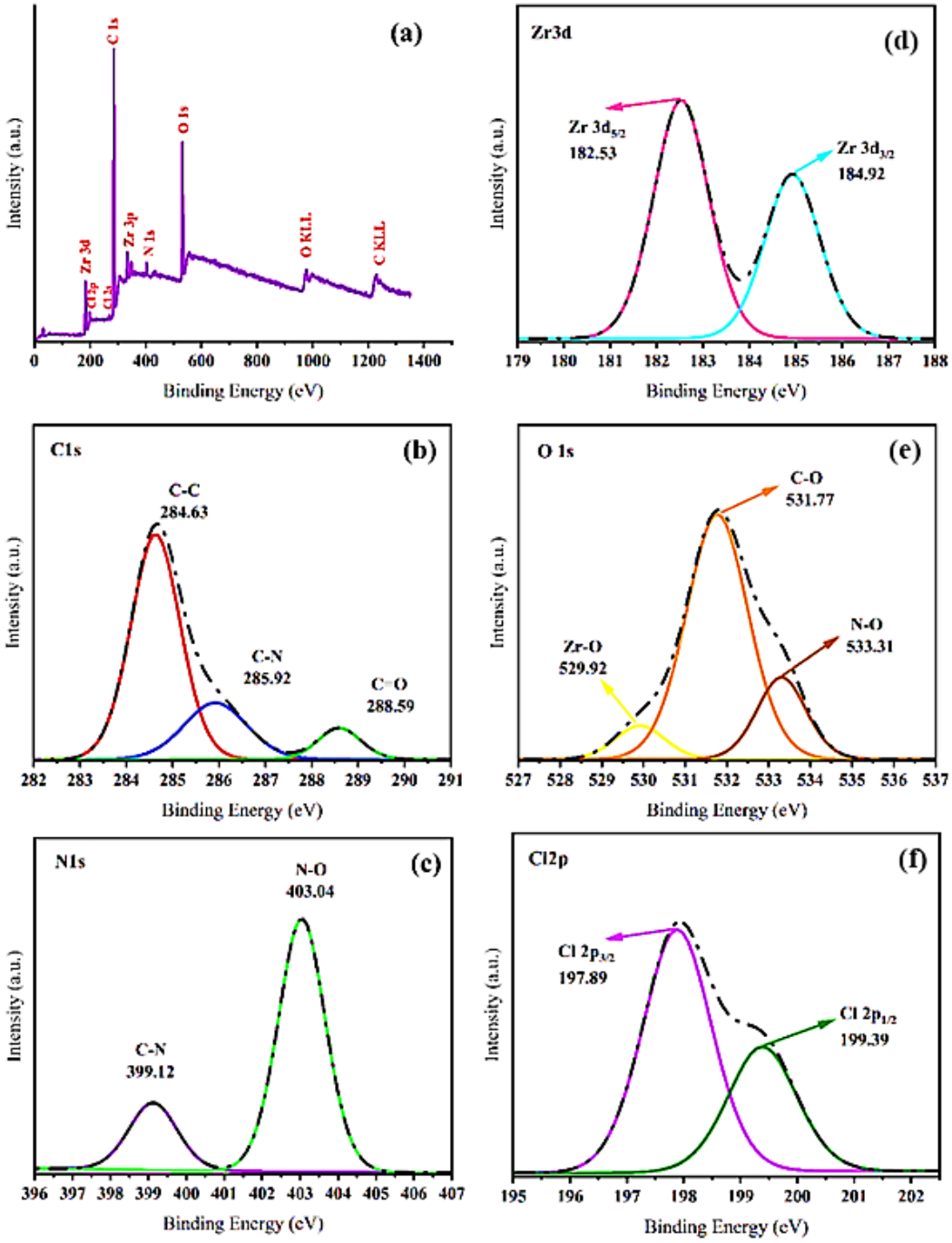

Figure 3.12. (**a**) The full-scan and core-level XPS scans of (**b**) C 1s, (**c**) N 1s, (**d**) Zr 3d, (**e**) O1s, and (**f**) Cl 2p atoms of TMU-66.

3.3. Adsorption studies

3.3.1. Selective adsorption of organic dyes

The selectivity of the Zr-MOF hollow spheres with the isonicotinic acid N-oxide (TMU-66) for different organic dyes was investigated by comparing the adsorption capacities of eight dyes with different structures and charges at pH around 7 (Fig. 3.13). The results revealed that TMU-66 exhibits high selectivity for anionic dyes, especially those with multiple sulfonic or carboxylic acid groups, such as Congo red (CR) and Rose Bengal (RB) (Figs. 3.14 & 3.15). The adsorption capacities for CR and RB are 98.91% (148.36 mg g^{-1}) and 94.95% (142.42 mg g^{-1}), respectively, which are much higher than those of other anionic dyes, such as naphthol green B (NGB) (Fig. 3.16), methyl orange (MO) (Fig. 3.17), and methyl red (MR) (Fig. 3.18). The adsorption capacities of NGB, MO, and MR are 82.22% (123.33 mg g^{-1}), 71.01% (106.52 mg g^{-1}), and 14.46% (21.69 mg g^{-1}), respectively, lower than those of CR and RB, probably due to their smaller molecular sizes and lower negative charges. On the other hand, TMU-66 showed negligible or deficient adsorption capacities for cationic dyes, such as Crystal violet (CV), Malachite green (MG), and Rhodamine B (RhB). The adsorption capacities of CV, MG, and RhB are 1.98%, 0%, and 0%, respectively, which indicates that hollow spheres have a strong repulsion for positively charged dyes.

The high selectivity of TMU-66 for anionic dyes can be attributed to its unique structure and surface properties. TMU-66 comprises hollow spheres with a micro-mesoporous shell and a hollow core. The shell is formed by coordinating Zr ions with INO ligands with oxygen atoms as donors. The oxygen atoms on the surface of Zr-MOF-INO can act as Lewis base sites, which can interact with the Lewis acid sites on the anionic dyes, such as the sulfonic acid groups.[28] This interaction can enhance the adsorption of anionic dyes by TMU-66 through chemical bonding or electrostatic interaction.[29] Moreover, the hollow core of Zr-MOF-INO can provide ample void space for accommodating large dye molecules, such as CR and RB.[30] The micro-

mesoporous shell can also facilitate the diffusion and penetration of dye molecules into the core.[31] Therefore, TMU-66 can achieve high adsorption capacities for anionic dyes with large molecular sizes and high negative charges.

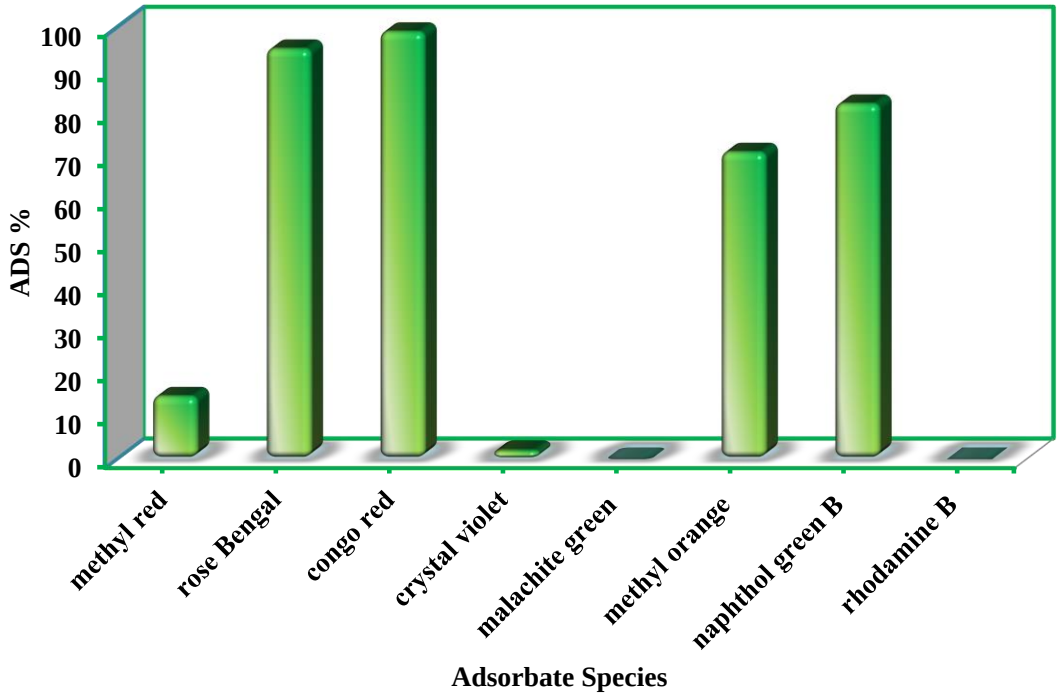

Figure 3.13. Adsorption of various cationic and anionic dyes on TMU-66.

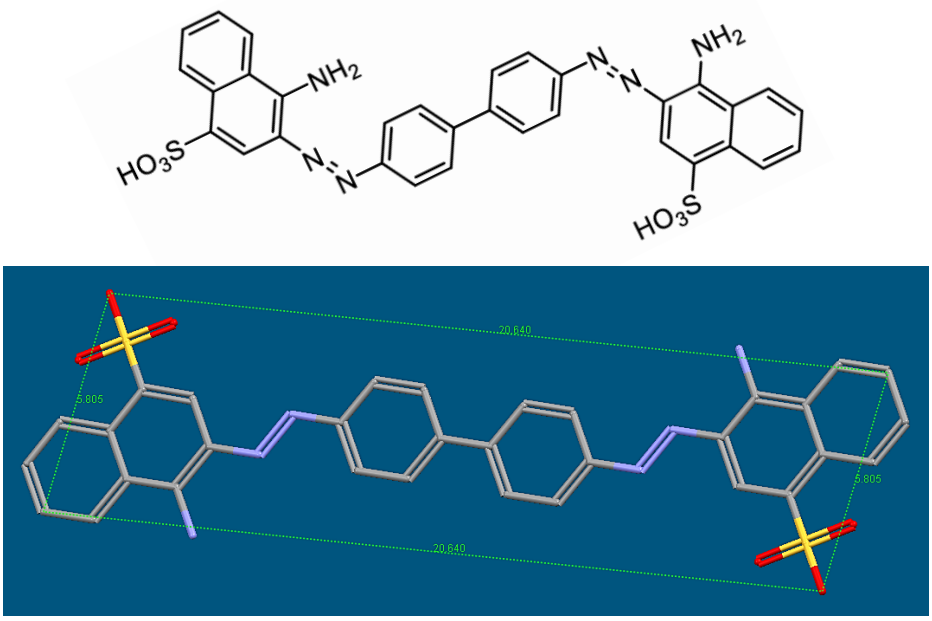

Figure 3.14. Structure and size of Congo red molecules.

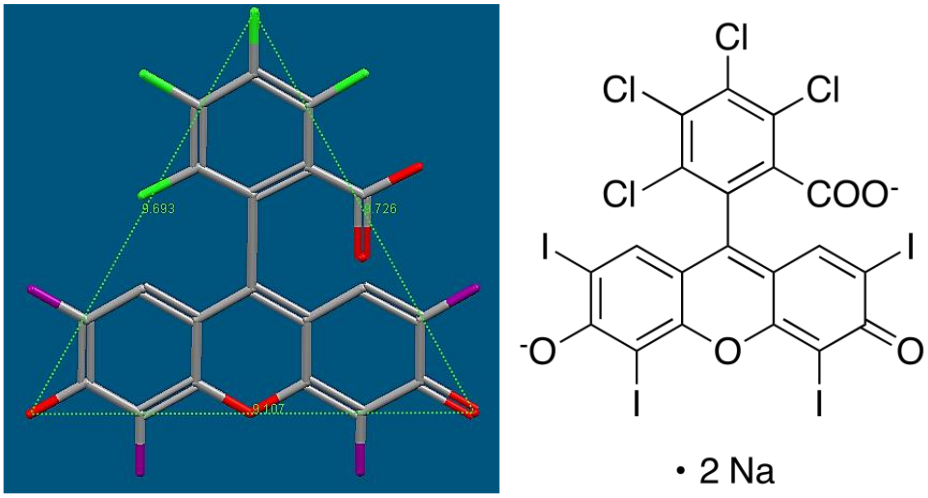

Figure 3.15. Structure and size of Rose Bengal molecule.

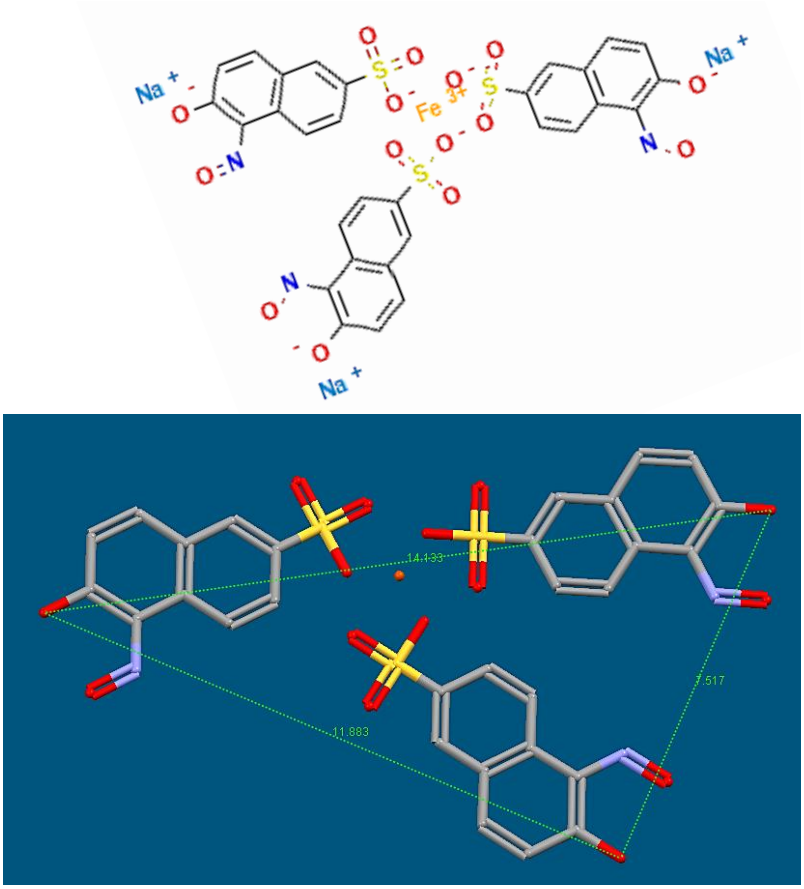

Figure 3.16. Structure and size of Naphthol green B molecule.

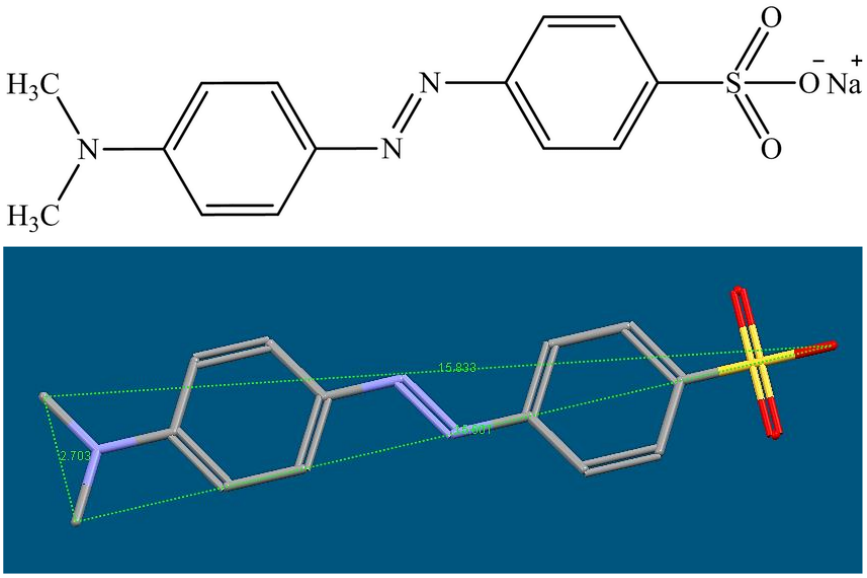

Figure 3.17. Structure and size of Methyl orange molecule.

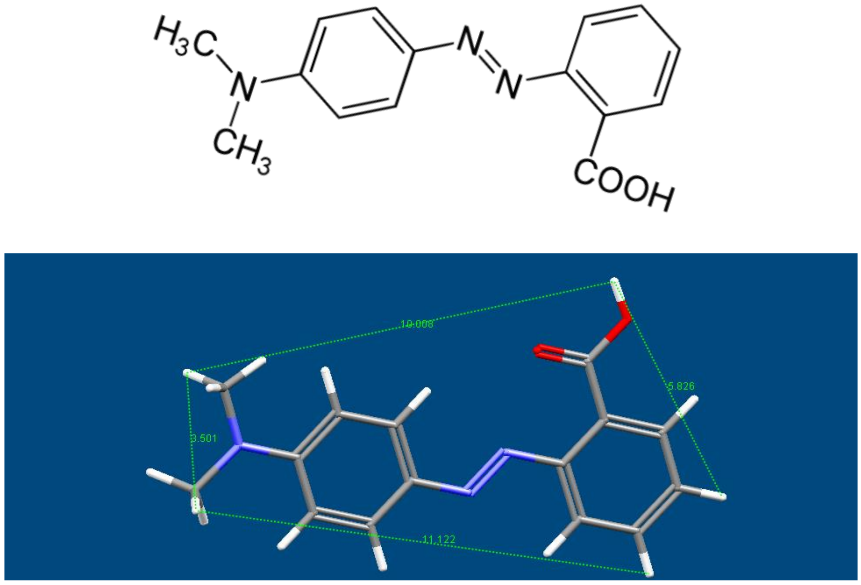

Figure 3.18. Structure and size of Methyl red molecule.

3.3.2. Effect of pH

The adsorption of CR was studied over a pH range of 1.0-10.0 (Fig. 3.19). The original pH levels of the CR solution, MOF, and deionized water are 8.5, 3.8, and 6.86, respectively. Figure 7 demonstrates that the highest adsorption (more than 98%) occurs at pH values greater than 3, with the maximum (around 100%) at pH 8-10. TMU-66 can adsorb all forms of CR over a

wide pH range of 3 to 10, unlike typical adsorbents with specific pH values for maximum adsorption. The structure of the dye molecule at different pH levels is depicted in Scheme 1. CR is an azo dye with two sulfonic acid and two amino groups, and its form varies depending on the pH. At acidic pH (below 3), CR is protonated, with one positive charge on each amino group and each sulfonic acid group carrying a negative charge (Scheme 1a). The overall charge of CR in this form is neutral. At neutral pH (around 6.8), CR is partially protonated, with both amino groups having a neutral charge alongside the negative charge on each sulfonic acid group (Scheme 1b). The overall charge of CR in this form is -2. CR is deprotonated at alkaline pH (above 8), resulting in both amino and sulfonic acid groups carrying negative charges (Scheme 1c). The overall charge of CR in this form is -4. Additionally, at pH below 2.2, the solubility of CR decreases in the solution.[32,33]

On the other side, at pH 6.8 (selected pH for all experiments), the zeta potential of TMU-66 in water is +50.5 mV, indicating that the hollow spheres have a net positive charge and efficiently disperse in water. The zeta potential distribution of TMU-66 is so broad from 0 to 100 mV with two maxima at 45 and 70 mV at this pH, because it has a heterogeneous surface with different functional groups and charges (Fig. 3.20). The zeta potential distribution of a MOF can be influenced by the type and amount of metal ions, organic linkers, defects, and adsorbed species on the MOF surface.[34] These factors can create different regions or domains on the MOF surface with different zeta potentials. Therefore, TMU-66 may have two dominant regions or domains with different zeta potentials at 45 and 70 mV, respectively. The pH of the suspension can also affect the zeta potential distribution of MOF by changing the protonation or deprotonation state of the functional groups and charges on the MOF surface. Based on this information, TMU-66 would attract CR molecules with a negative charge through electrostatic interactions with N-O groups or chemical bonding with Zr-nodes. However, if the pH becomes too low, CR molecules may become protonated, losing their negative charge and weakening

the attraction. Conversely, if the pH becomes too high, CR molecules may be deprotonated, increasing their negative charge and strengthening the attraction. Therefore, TMU-66 exhibits the highest adsorption capacity for CR at alkaline pH, when CR molecules carry the highest negative charge and solubility. In contrast, the adsorption capacity is lowest at acidic pH when CR molecules carry zero or common negative charge and have lower solubility.

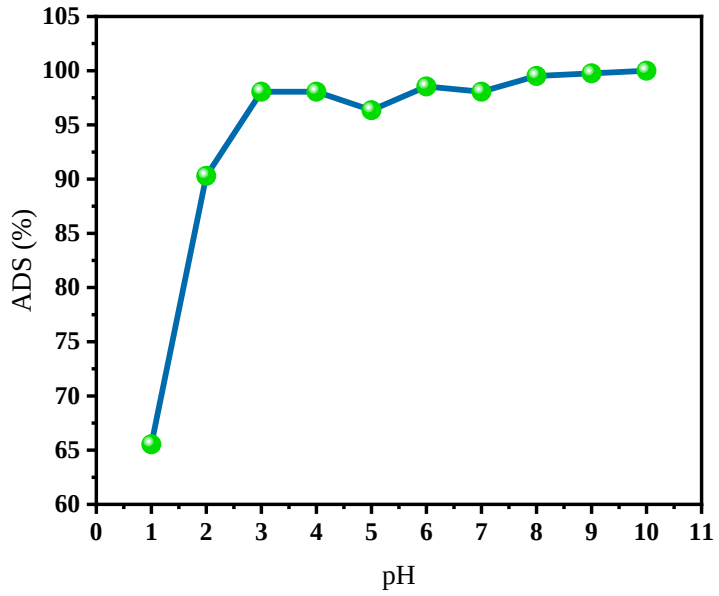

Figure 3.19. The effect of pH on adsorption of CR by TMU-66. Initial CR concentration=150 mg L^{-1}, the amount of adsorbent=10 mg, sample volume=10 mL, T=298 K.

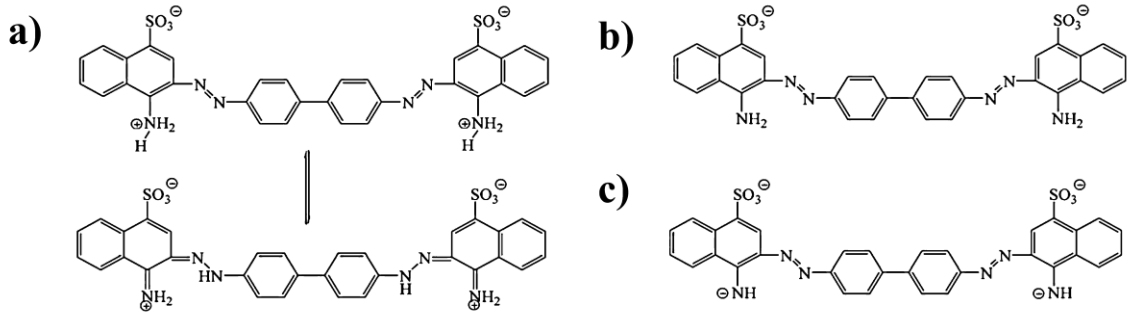

Scheme 1. Structure of Congo red at (**a**) pH < 3, (**b**) around 6.8, and (**c**) pH > 8.

Temperature (°C):	25.0		Zeta Runs:	15
Count Rate (kcps):	121.0		Measurement Position (mm):	4.50
Cell Description:	Zeta dip cell		Attenuator:	6

		Mean (mV)	Area (%)	St Dev (mV)
Zeta Potential (mV):	50.5	Peak 1: 39.3	52.7	11.1
Zeta Deviation (mV):	16.2	Peak 2: 63.6	47.3	7.35
Conductivity (mS/cm):	0.477	Peak 3: 0.00	0.0	0.00

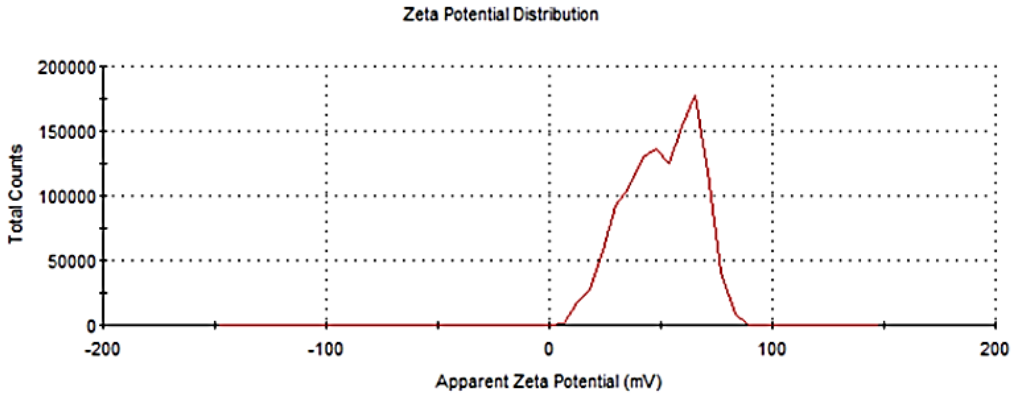

Figure 3.20. Zeta potential distribution of TMU-66 in water (pH 6.8).

3.3.3. Effect of contact time and concentration of CR

3.3.3.1. Adsorption kinetics

The time-dependent behavior of CR adsorption over TMU-66 is achieved at room temperature. The results show that the hollow sphere structure has a fast and high adsorption rate for CR (Fig. 3.21). In 30 s, TMU-66 achieved 86% of the adsorption capacity, indicating a high affinity and accessibility for CR molecules. After 10 min, TMU-66 reached 90% of the adsorption capacity, which can be attributed to micro-mesopores shell structure and N-oxide functional groups on TMU-66 hollow spheres to accommodate CR molecules (Fig. 3.21b). However, after 30 min, the adsorption capacity starts to increase again up to 2 h, which implies that there is some secondary or tertiary adsorption process occurring on TMU-66.

One possible explanation for this phenomenon is that TMU-66 has a hollow sphere morphology, meaning it has an empty space inside the sphere. This space can act as a reservoir

for the adsorbate molecules, which can diffuse from the outer surface to the inner core of the sphere. This diffusion process may take longer than the initial adsorption process on the outer surface. Another possible explanation is that TMU-66 has some active sites like Zr-nodes and N-oxide functional groups on its surface or inside its pores, which can interact with the adsorbate molecules through chemical bonding or electrostatic attraction. These interactions may require more energy or time to form than the physical adsorption process, so an increase in the adsorption capacity was observed after the first plateaus from 10 to 30 min.

The adsorption rate of TMU-66 is accurately fitted to the kinetic results using semiempirical kinetic models, pseudo-second order, with the highest correlation coefficient ($R^2 = 0.999$) (Fig. 3.22). The equilibrium adsorption capacity (q_e) from this model is calculated to be 179.53 mg/g, and the value of k_2 is found to be 0.0041 min^{-1}, indicating that TMU-66 has a fast adsorption rate for CR.

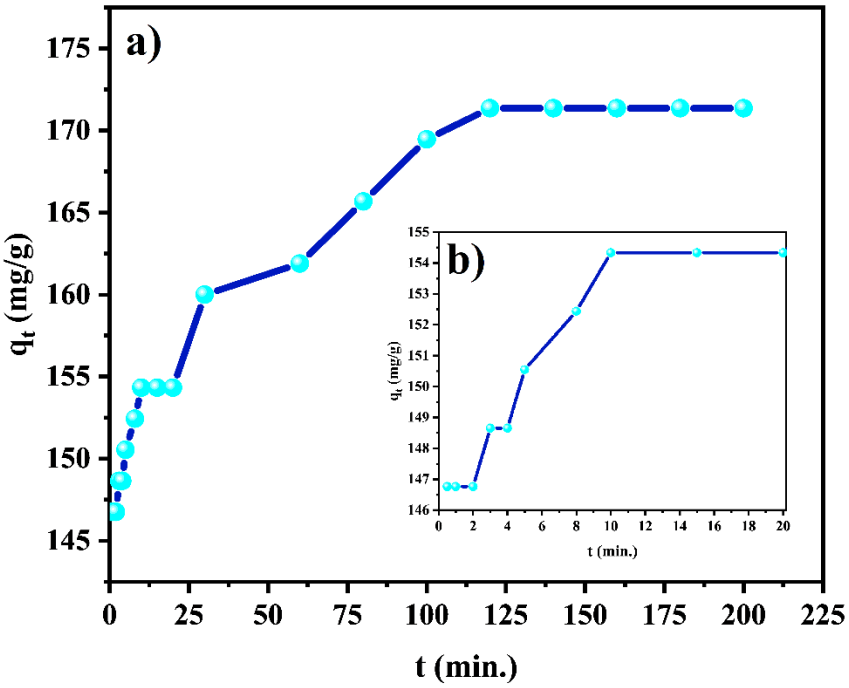

Figure 3.21. Effect of the contact time on CR adsorption by 10 mg of TMU-66 with an initial concentration of 50 ppm; q_t: the amount of CR adsorbed at different times.

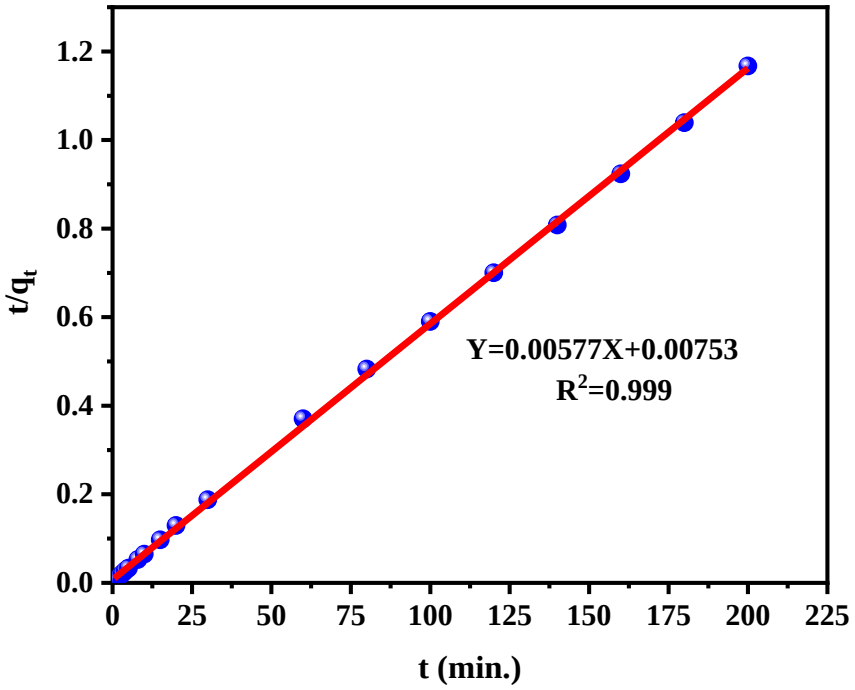

Figure 3.22. Linear pseudo-second-order kinetic model for adsorption of CR on TMU-66 (initial CR concentration=50 mg/L, amount of adsorbent=10 mg, sample volume=50 mL, and T=298 K).

3.3.3.2. Adsorption isotherm

The design of an adsorption system, analysis of its mechanism, assessment of the affinity between adsorbents and adsorbates, and determination of the maximum adsorption capacity rely heavily on adsorption isotherms. The adsorption isotherm is the curve showing the solute distribution between fluid and solid phases at adsorption equilibrium.

To assess the impact of initial CR concentration on the adsorption process, a graph of q_e versus C_e is generated, and the representative isotherm is illustrated in Figure 3.23. Unlike typical dye adsorption isotherms, this plot comprises two distinct steps. Initially, the adsorption on TMU-66 increases rapidly with an increase in initial CR concentration until the plot reaches a semi-plateau. Then, adsorption increases to another level, but this time more slowly than the first step.

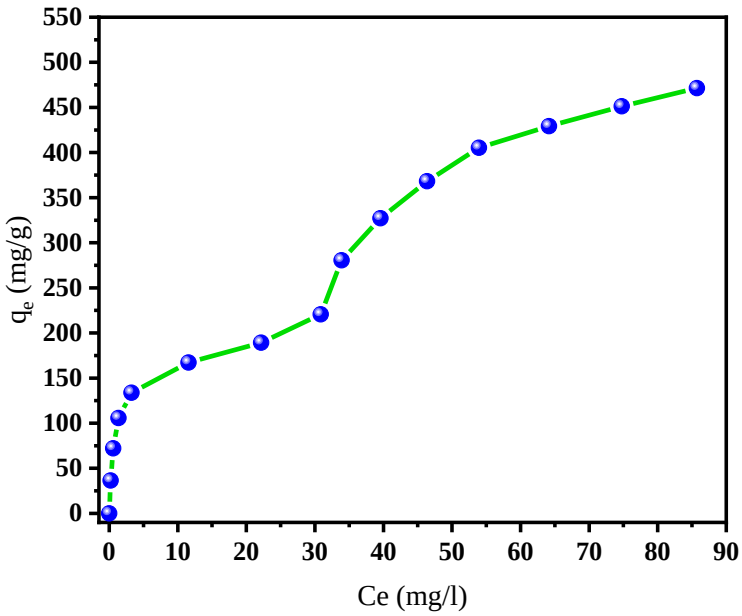

Figure 3.23. Effect of initial CR concentration on adsorption by 10 mg of TMU-66; C_e, the equilibrium concentration of adsorbate; q_e, the adsorbed amount of CR.

The two-step adsorption phenomenon could be explained by two types of sites on TMU-66, which have different affinities and capacities for CR molecules. Site 1 has a high affinity and a low capacity, while site 2 has a low affinity and a high capacity. In Region I, most of the CR molecules are adsorbed on site 1, which results in a fast and linear increase in q_e. In Region II, site 1 is saturated, and most of the CR molecules are adsorbed on site 2, which results in a slow and nonlinear increase in q_e.[35,36]

To establish an appropriate correlation between experimental and theoretical data, we used a qualitative approach to identify the isotherm class, subgroup, and sorption model proposed by Christoph Hinz.[37] As he suggested, we considered three plots: 1) q_e *vs.* C_e (Fig.3.23), 2) q_e/C_e *vs.* q_e (Fig. 3.24-a), 3) log (q_e/C_e) *vs.* Log (q_e) (Fig. 3.24-b) and corroding to his method, we reach the L4-type adsorption isotherm. It is one of the categories of adsorption isotherms in the Giles classification,[38-40] which is based on the shape and slope of the curve. L4-type adsorption

isotherm has a concave downward or L-shaped curve, which indicates the adsorption process involved a monolayer formation of CR molecules on the surface of TMU-66.

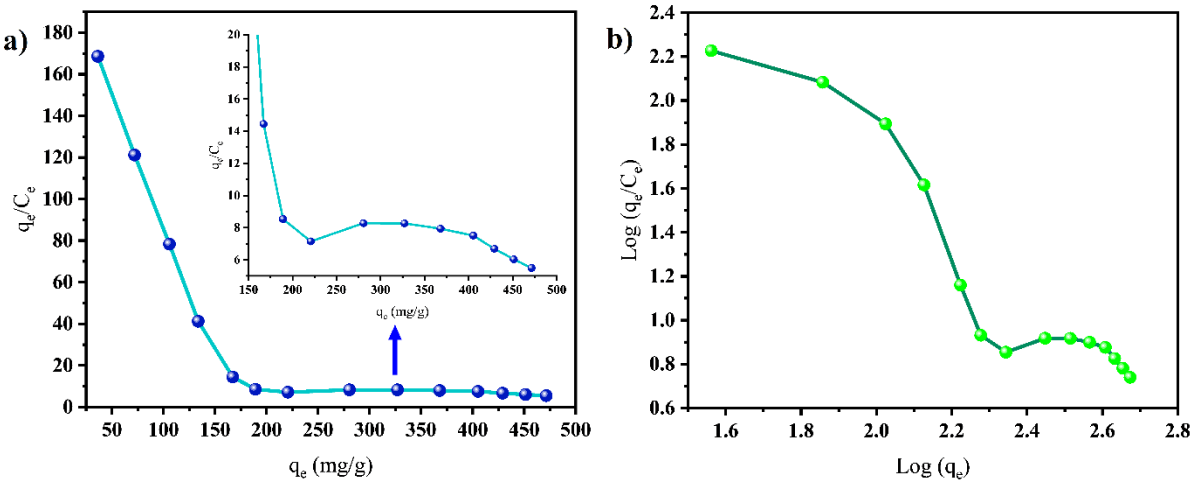

Figure 3.24. Isotherm classification, according to Giles et al. 1974 shown with differently transformed coordinates.[37]

To fit the experimental data, the two-site Langmuir model (see the chapter 2) is used, which is a mathematical equation that describes the adsorption isotherm of an adsorbate on a solid surface that has two types of sites with different affinities and capacities for the adsorbate. The values of q_1^{max} and q_2^{max}, K_1 and K_2 are obtained by fitting the experimental data with this model using a nonlinear regression and linear regression analysis for each step (Table 3.4). The correlation coefficients are 0.998, 0.999, and 0.999, respectively, which indicates that the two-site Langmuir model is well-fitted with the experimental data (Fig. 3.25).

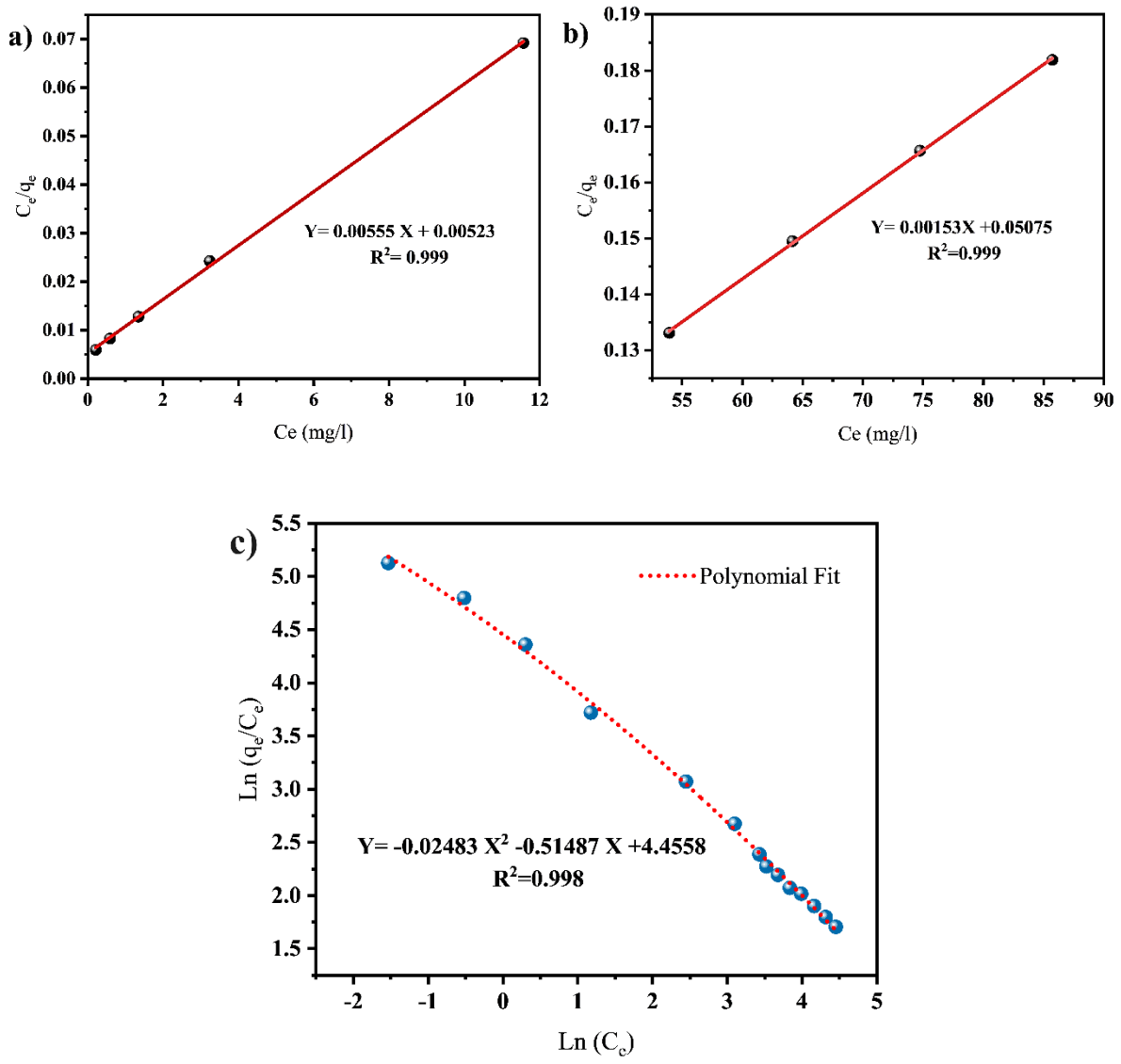

Figure 3.25. Two-step Langmuir (**a**) linear plot step 1, (**b**) linear plot step 2, and (**c**) two-site Langmuir nonlinear fit for adsorption of CR on TMU-66 (amount of adsorbent=10 mg, contact time=2 h, sample volume=50 mL, pH=6.8 and T=298 K).

Table 3.4. The values of parameters of the two-site Langmuir model.

Sample	q_1^{max}	q_2^{max}	K_1	K_2
TMU-66	180.18	473.41	0.94	0.03

Table 3.5. Adsorption capacities for CR on Various MOFs.

Adsorbent	Maximum Congo Red Adsorption Capacity (mg/g)	Reference
Fe_3O_4@ZTB-1	458.0	[41]
[Cd (5-aip) (bpy)]	211.0	[42]
ZT-MOF@Ag@C	416.6	[43]
$Zr_6O_4(OH)_4(BDC)_6$	340.0	[44]
TMU-66	473.5	This work

3.3.4. Thermodynamic Studies

Table 3.6 displays the thermodynamic parameters for CR adsorption on TMU-66. Briefly, the adsorption capacity increases with increasing temperature. During the adsorption process, the enthalpy change (ΔH) is positive, indicating that heat is required from the surroundings, making the process endothermic. Furthermore, the entropy change (ΔS) is positive, implying that the adsorption process increases the disorder or randomness of the system. This shows that the adsorption process is entropy-driven or favors disorder. Lastly, the Gibbs free energy change (ΔG) of the adsorption process is negative, which makes the adsorption process thermodynamically favorable and spontaneous.

Table 3.6. Thermodynamic parameters for CR adsorption on TMU-66.

T (K)	ΔG° (kJ mol^{-1})	ΔH° (kJ mol^{-1})	ΔS°, (kJ mol^{-1} K^{-1})	R^2
283	-5.713	+16.870	+79.843	0.995
297	-6.830			
305	-7.468			
315	-8.266			
325	-9.064			

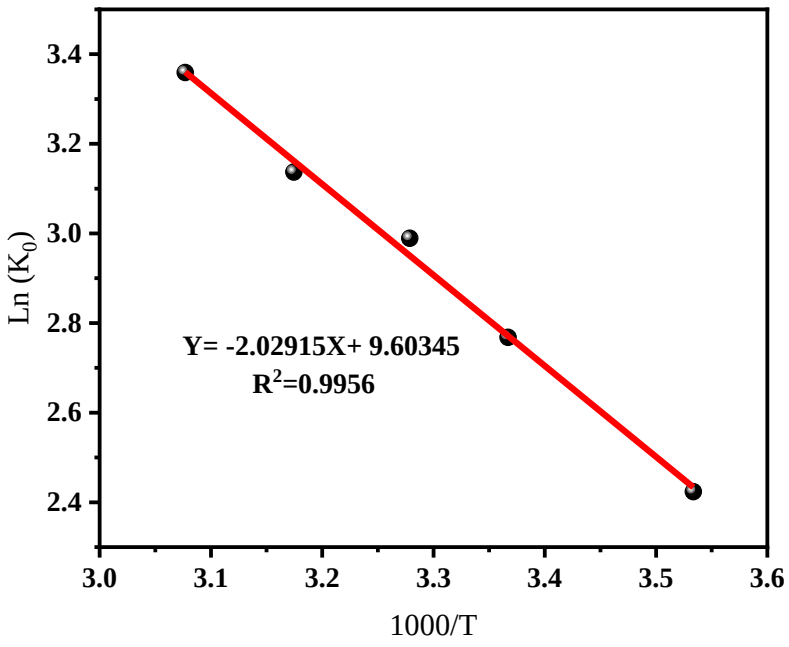

Figure 3.26. The plot of lnK_0 *vs.* 1/T.

3.3.5. Adsorption mechanism

To further understand the interaction between CR and TMU-66, we performed FTIR spectroscopy, PXRD analysis, N_2 adsorption/desorption, EDS, and SEM of TMU-66 before and after adsorption. Characteristic peaks of Congo red, according to Figure 3.27, are N=N stretching (1583 cm^{-1}), N-H stretching (1446 cm^{-1}), C-N bending (1363 cm^{-1}), SO_3^- stretching (1178 and 1226 cm^{-1}), S=O stretching (1122 cm^{-1}), and C-N vibration of aliphatic amines (1062 cm^{-1}). The FTIR spectrum of TMU-66 after adsorption, Figure 3.28, shows the characteristic peaks of the dye, confirming the presence of CR on TMU-66. However, the peaks related to the amine and sulfonic acid groups exhibit a redshift to 1432 and 1020 cm^{-1} (N-H stretching and C-N vibration of aliphatic amines) and 1206, 1157 and 1103 cm^{-1} (SO_3^- and S=O stretching and other peaks like N=N, C-N, and C-H bending appear in the same place without any shift. It could be proof of the interaction between hollow spheres and dye from these two functional groups. Figure 3.29 presents the FTIR spectra of TMU-66 at four different times of adsorption (t = 0, 30 min, 1 h, 2 h) to better understand the mechanism behind the appearance of peaks.

The peaks related to the μ_3-O and the μ_3-OH stretchings in Zr nodes feature a blue shift from 640 to 667 cm^{-1} and 462 to 485 cm^{-1}, respectively, with increased adsorption time. This suggests that Zr nodes play an important role in the adsorption process. The band at 1235 cm^{-1}, ascribed to N–O stretching vibration coordinates to the Zr nodes at 1235 cm^{-1}, gradually decreases as the adsorption time increases and redshifts to 1226 cm^{-1}. This indicates that this group has weak interactions with CR molecules. Additionally, as the adsorption time increases, two new peaks appear in the FTIR plot of TMU-66. A shoulder at 1300 cm^{-1} and another at 1704 cm^{-1} corresponding respectively to the N-O and C=O related to the INO linker. However, inductively coupled plasma optical emission spectrometry (ICP-OES) analysis of the solution after adsorption illustrates a zero percentage of Zr, indicating no leaching or significant release of Zr into the solution during the adsorption process.

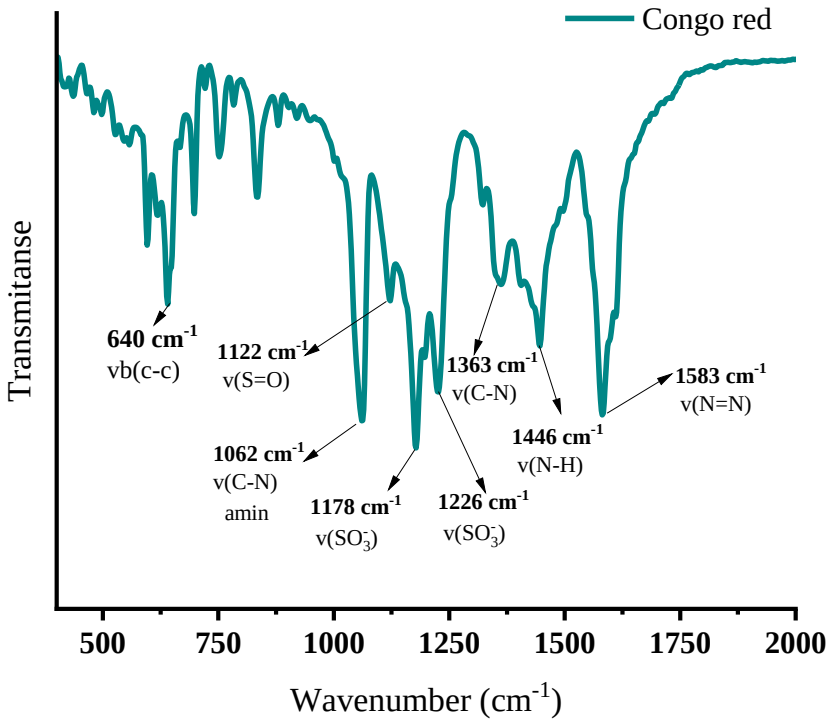

Figure 3.27. FT-IR spectrum of Congo red.

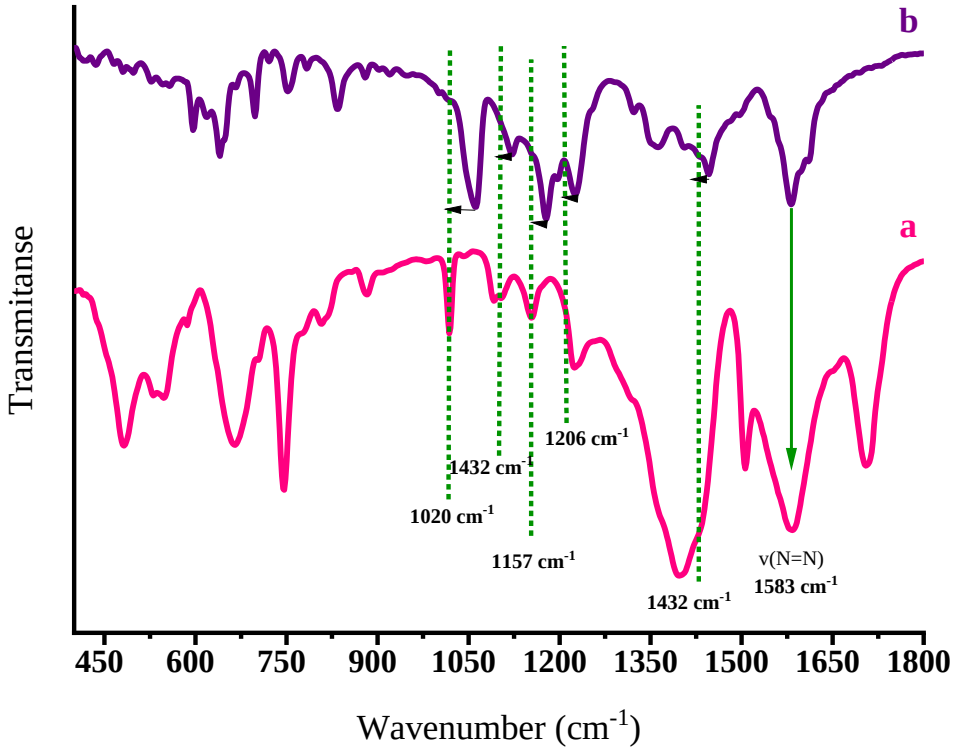

Figure 3.28. FT-IR spectra of (**a**) TMU-66 after CR adsorption and (**b**) CR.

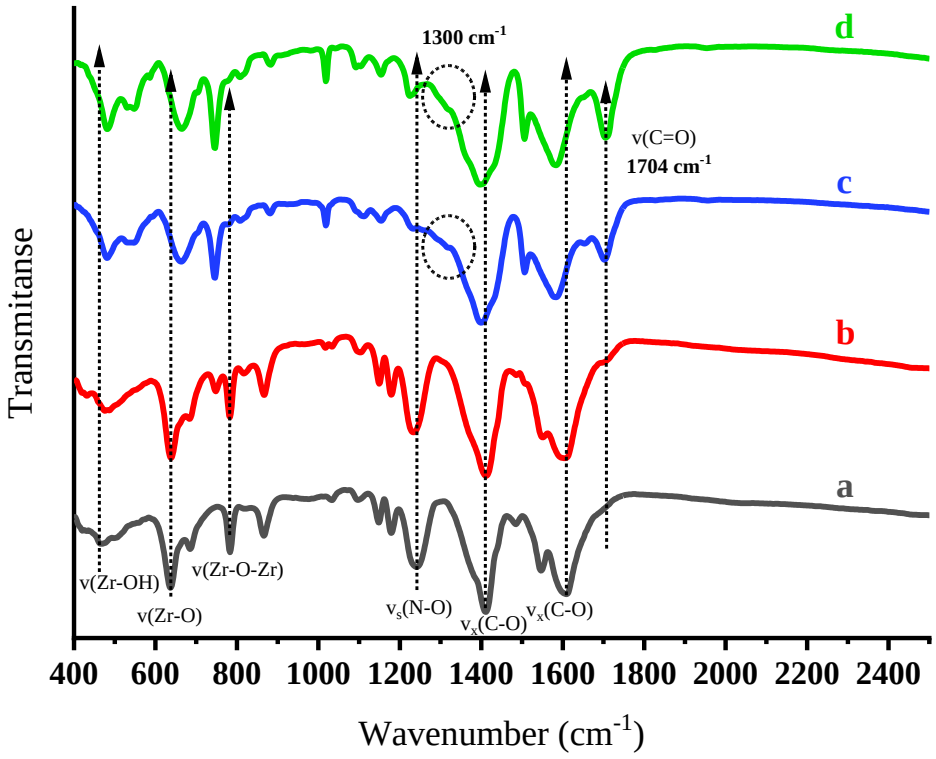

Figure 3.29. FT-IR spectra of TMU-66 after CR adsorption at different times: (**a**) t= 0, (**b**) t= 30 min, (**c**) t= 1 h, (**d**) t= 2 h.

To ensure the stability of the structure, we analyzed the sample by PXRD following adsorption. The PXRD patterns (Fig. 3.30) show that after adsorption, the main peak of TMU-66 shifts to the smaller 2θ angles, indicating that the lattice parameters of TMU-66 increased due to the insertion of CR molecules into the pores.

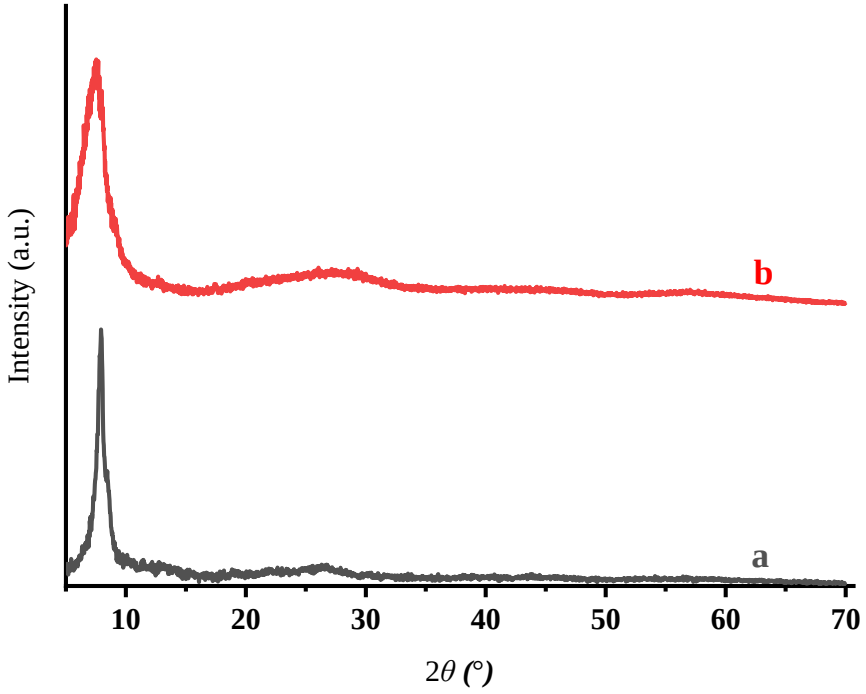

Figure 3.30. PXRD patterns of TMU-66 (**a**) before and (**b**) after CR adsorption (initial CR concentration=150 mg L^{-1}, the amount of adsorbent=10 mg, sample volume=10 mL, t= 2hr, T=298 K).

Figure 3.31 shows that the morphology of TMU-66 after CR adsorption is not altered. The unchanged morphology of the Zr MOF suggests that the overall physical appearance of the material remains unaffected by the adsorption. Still, it seems the size of spheres is increased from 1.5 to 2 μm, and the smooth surface before adsorption turns to a rough surface after adsorption, indicating the attachment of CR molecules on the framework. The EDX plot also reveals an increase in the peak intensity corresponding to the S element, which could be attributed to the sulfonic acid groups of CR molecules. The EDX mapping images exhibited a uniform distribution of Zr, O, C, and Cl elements on the surface of the hollow Zr-MOF sphere,

suggesting a homogeneous framework structure. However, the distribution of the S and N elements was more heterogeneous, indicating selective adsorption of CR molecules on some sites of the hollow Zr-MOF sphere. Also, EDS analysis of TMU-66 after adsorption (Figs. 3.32) featured an increase in wt% of C and especially N; it can prove the presence of CR on the structure. A decrease in the wt% of O could be a sign of removing the OH and H_2O on Zr-nodes.

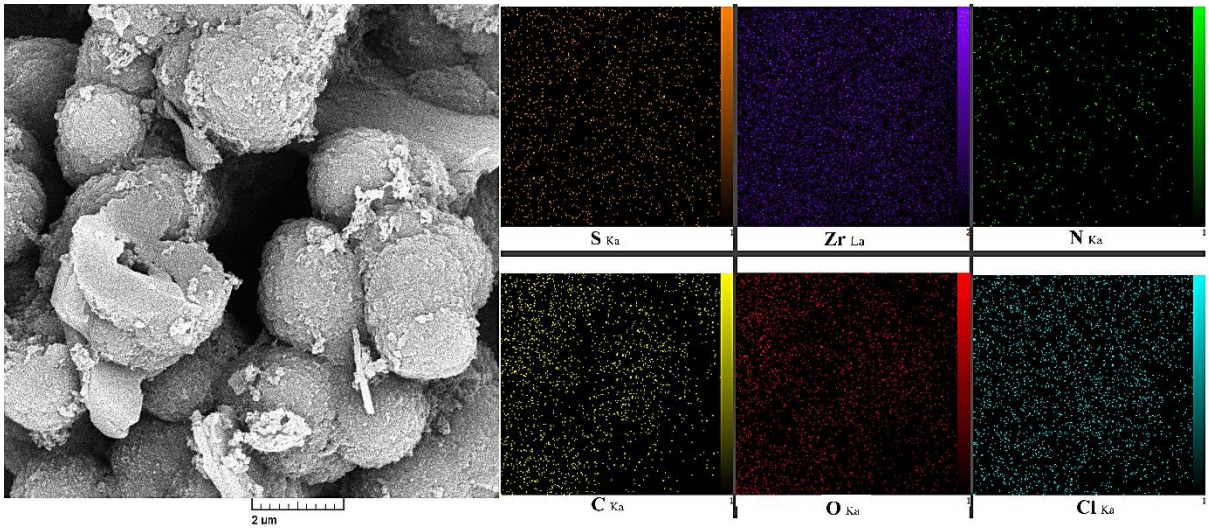

Figure 3.31. SEM image and EDX mapping images of TMU-66 after CR adsorption (initial CR concentration=150 mg L^{-1}, the amount of adsorbent=10 mg, sample volume=10 mL, t= 2hr, T=298 K).

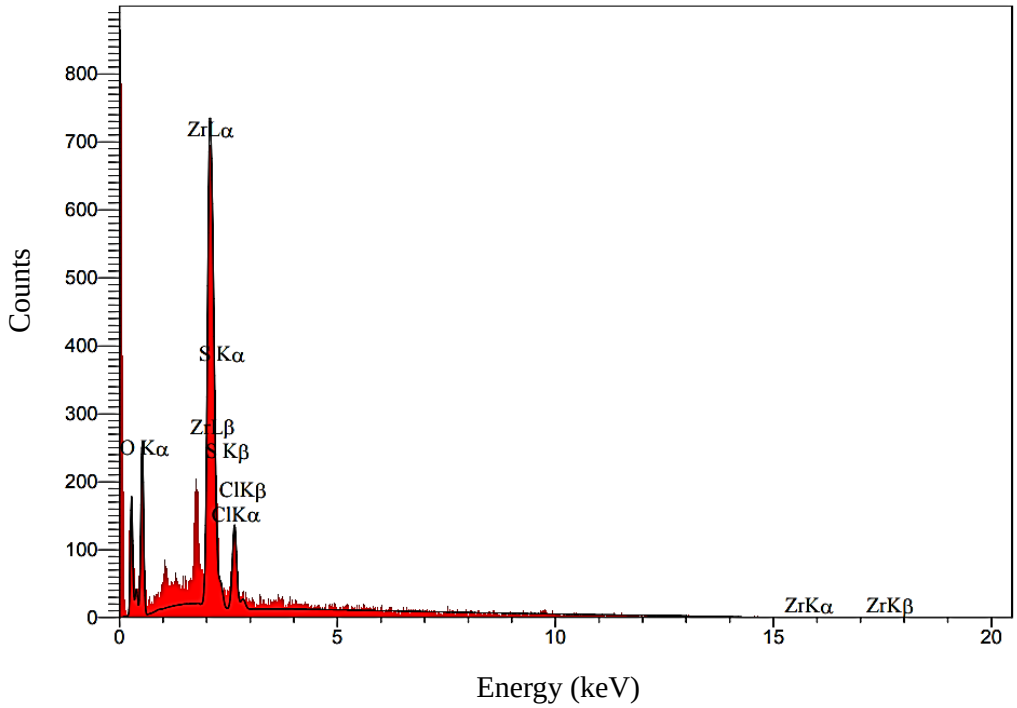

Figure 3.32. EDS spectrum of TMU-66 after CR adsorption (initial CR concentration=150 mg L^{-1}, the amount of adsorbent=10 mg, sample volume=10 mL, t= 2hr, T=298 K).

Table 3.7. Quantitative results of EDS of TMU-66 after CR adsorption.

Elt	Line	Int	Error	K	Kr	W%	A%	ZAF	Pk/Bg
C	Ka	37.1	10.4425	0.2115	0.0763	28.64	41.45	0.2665	22.94
N	Ka	7.5	10.4425	0.0579	0.0209	13.70	17.01	0.1525	5.18
O	Ka	62.7	10.4425	0.1782	0.0643	32.59	35.41	0.1973	52.86
S	Ka	13.6	7.2716	0.0181	0.0065	0.80	0.44	0.8141	6.83
Cl	Ka	51.5	7.2716	0.0761	0.0275	3.56	1.74	0.7713	11.79
Zr	La	231.5	7.2716	0.4582	0.1653	20.70	3.94	0.7988	37.86
				1.0000	0.3609	100.00	100.00		

XPS analysis of TMU-66 after adsorption displays two significant peaks at 182.08 and 184.57 eV, indicating a peak shift to lower binding energy (Fig. 3.33). This shift indicates that Zr has a lower oxidation state and a lower coordination number after dye adsorption, which means that Zr transfers some electrons to the oxygen atoms of isonicotinic acid or the dye molecules.

This transfer of electrons reduces the charge and the size of Zr, which in turn reduces its binding energy and its coordination number.[45]

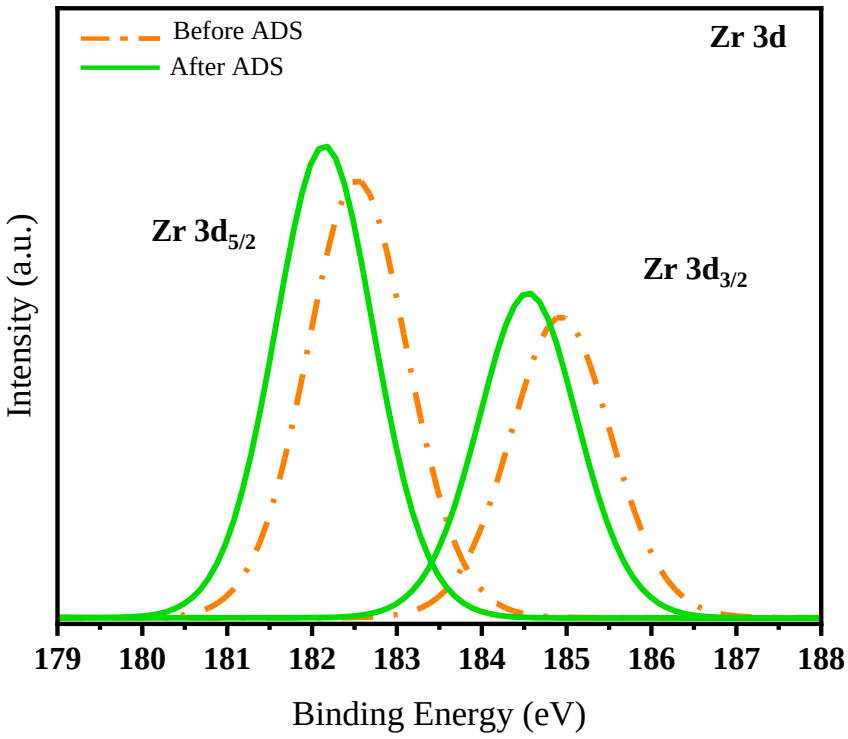

Figure 3.33. High-resolution XPS spectra of Zr 3d for TMU-66 before (red) and after (green) CR adsorption (initial CR concentration=150 mg L^{-1}, the amount of adsorbent=10 mg, sample volume=10 mL, t= 2hr, T=298 K).

Based on these results and analyses, we propose the following mechanism for CR adsorption on TMU-66. The adsorption process consists of two steps: (1) a fast and primary adsorption of CR molecules on the surface of TMU-66 through electrostatic and π-π stacking interactions, and (2) a slow and secondary adsorption of CR molecules into the pores of TMU-66 through interactions with the linker C=O and N-O groups and Zr-nodes. The adsorption process is favored by high temperature and high initial concentration of CR. The adsorption process results in a monolayer formation of CR molecules on TMU-66 with a high adsorption capacity.

3.4. Conclusion

In conclusion, the adsorption studies on TMU-66, a hollow Zr-MOF sphere with isonicotinic acid N-oxide, have unveiled its remarkable capability as an efficient adsorbent for anionic dyes, particularly those with multiple sulfonic or carboxylic acid groups, and high negative charges. The pH-dependent adsorption behavior of CR onto TMU-66 showcases its highest adsorption capacity at the pH between 5 and 10 when CR molecules carry the highest negative charge and solubility. Notably, the time-dependent behavior reveals rapid initial adsorption, followed by a slower process indicative of the involvement of micro-mesopores shell structure and N-oxide functional groups on TMU-66 hollow spheres. The adsorption isotherm and analysis of FT-IR, PXRD, and XPS data support the formation of a monolayer of CR molecules on the surface of TMU-66, showcasing key interactions, such as electrostatic attraction, π-π stacking, and interactions with linker and Zr-nodes. These findings provide key insights into the mechanism of CR adsorption on TMU-66 and highlight its potential for effective dye removal in environmental applications.

3.5. References

(1) Sing, Kenneth SW. *Colloids and Surfaces A: Physicochemical and Engineering Aspects* **2004**, 241.1-3, 3-7.

(2) Boucher, E.A. *J Mater Sci*. **1976**, 11, 1734–1750.

(3) Roszak, Rafal, et al. *Colloids and Surfaces A: Physicochemical and Engineering Aspects* **2016**, 496, 69-76.

(4) Burhan, M., Shahzad, M. & Ng, K. *Sci Rep* **2019**, 9, 8773.

(5) Al-Zoubi, H., Zubair, M., Manzar, M.S. *et al. Arab J Sci Eng* **2020**, 45, 7275–7287.

(6) Bafana, Amit, Sivanesan Saravana Devi, and Tapan Chakrabarti. *Environmental Reviews* **2011**, 19.NA, 350-371.

(7) Wagner, Matthias, et al. *Frontiers in Materials* **2020**, 7, 567130.

(8) Ghanavati Nasab, S., Semnani, A., Teimouri, A. *et al. J Polym Environ* **2018**, 26, 3677–3697.

(9) Jabar, J.M., Odusote, Y.A., Alabi, K.A. *et al.* Kinetics and mechanisms of congo-red dye removal from aqueous solution using activated *Moringa oleifera* seed coat as adsorbent. *Appl Water Sc* **2020**, 10, 136.

(10) Sabzehmeidani, Mohammad Mehdi, et al. *Materials Advances* **2021**, 2 (2), 598-627.

(11) Zhou, Hong-Cai, Jeffrey R. Long, and Omar M. Yaghi. "Introduction to metal–organic frameworks." *Chemical reviews* **2012**, 112 (2), 673-674.

(12) Kitagawa, Susumu. *Chemical Society Reviews* **2014**, 43 (16),5415-5418.

(13) Gangu, Kranthi Kumar, and Sreekantha B. Jonnalagadda. *Frontiers in Chemistry* **2021**, 9, 747615.

(14) Bůžek, Daniel, et al. *Inorganic Chemistry Frontiers* **2021**, 8 (3), 720-734.

(15) Liu, Peijia, et al. *Chemical Communications* **2021**, 57 (47), 5822-5825.

(16) Wanigarathna, Darshika KJA, Jiajian Gao, and Bin Liu. *Materials Advances* **2020**, 1 (3), 310-320.

(17) Shokouhfar, Nasrin, Leila Aboutorabi, and Ali Morsali. *Dalton Transactions* **2018**, 47 (41), 14549-14555.

(18) Schaate, P. Roy, A. Godt, J. Lippke, F. Waltz, M. Wiebcke and P. Behrens, Chemistry-A European Journal, **2011**, 17, 6643-6651.

(19) M. J. Katz, Z. J. Brown, Y. J. Colón, P. W. Siu, K. A. Scheidt, R. Q. Snurr, J. T. Hupp and O. K. Farha, Chem. Commun., **2013**, 49, 9449-9451.

(20) Wasson, Megan C., et al. *CrystEngComm* **2020**, 22 (47), 8182-8188.

(21) Atac, Ahmet, et al. *Spectrochimica Acta Part A: Molecular and Biomolecular Spectroscopy* **2012**, 85 (1) 145-154.

(22) Arivazhagan, R., C. Sridevi, and A. Prakasam. *Journal of Molecular Structure* **2022**, 1250, 131895.

(23) Han, Yitong, et al. *CrystEngComm* **2015**, 17 (33), 6434-6440.

(24) Silverstein, Robert M., and G. Clayton Bassler. *Journal of Chemical Education* **1962**, 39 (11), 546.

(25) Healy, Colm, et al. *Coordination Chemistry Reviews* **2020**, 419, 213388.

(26) Wang, Jingjing, et al. *Materials letters* **2015**, 142, 269-272.

(27) Shen, Lijuan, et al. *Nanoscale* **2013**, 5 (19), 9374-9382.

(28) Li, Huijie, et al. *Dalton Transactions* **2021**, 50 (9), 3348-3355.

(29) Liu, B., Liu, M., Xie, Z. *et al. J Mater Sci* **2022**, 57, 5438–5455.

(30) Au, Vonika Ka-Man *Frontiers in Chemistry* **2020**, 8, 708.

(31) Li, Huijie, et al. *Dalton Transactions* **2021**, 50 (9), 3348-3355.

(32) Mera, S.L., Davies, J.D. *Histochem J* **1984**, 16, 195–210.

(33) Pigorsch, E., A. Elhaddaoui, and S. Turrell *Spectrochimica Acta Part A: Molecular Spectroscopy* **1994**, 50 (12),2145-2152.

(34) Zhang, Xuan, et al. *Journal of materials chemistry A* **2020**, 8 (16) 7569-7587.

(35) Kalam, Shams, et al. *ACS omega* **2021**, 6 (48), 32342-32348.

(36) Han, Li-Juan, et al. *Dalton Transactions* **2019**, 48 (1), 4650-4656.

(37) Hinz, Christoph. "Description of sorption data with isotherm equations." *Geoderma* **2001**, 99 (3-4), 225-243.

(38) Giles, Charles H., David Smith, and Alan Huitson. *Journal of colloid and interface science* **1974**, 47(3) 755-765.

(39) Giles, Charles H., Anthony P. D'Silva, and Ian A. Easton. *Journal of colloid and interface science* **1974**, 47(3), 766-778.

(40) Gauden, Piotr, et al. *Carbon Materials: Theory and Practice*. Research Signpost, **2008**, 517-570.

(41) Han, Li-Juan, et al. *Dalton Transactions* **2019**, 48 (14) 4650-4656.

(42) Ghosh, Shankhamala, et al. *Journal of Solid State Chemistry* **2021**, 296, 121929.

(43) Obayomi, Kehinde Shola, et al. *Microporous and Mesoporous Materials* **2023**, 355, 112568.

(44) Farhadi, Saeed, Faranak Manteghi, and Reza Tondfekr. *Monatshefte für Chemie-Chemical Monthly* **2019**,150, 193-205.

(45) Lackner, Peter, et al. *Physical Chemistry Chemical Physics* **2019**, 21.32, 17613-17620.

Chapter 4

Solar-driven ammonia production through engineering of the electronic structure of MOF-808

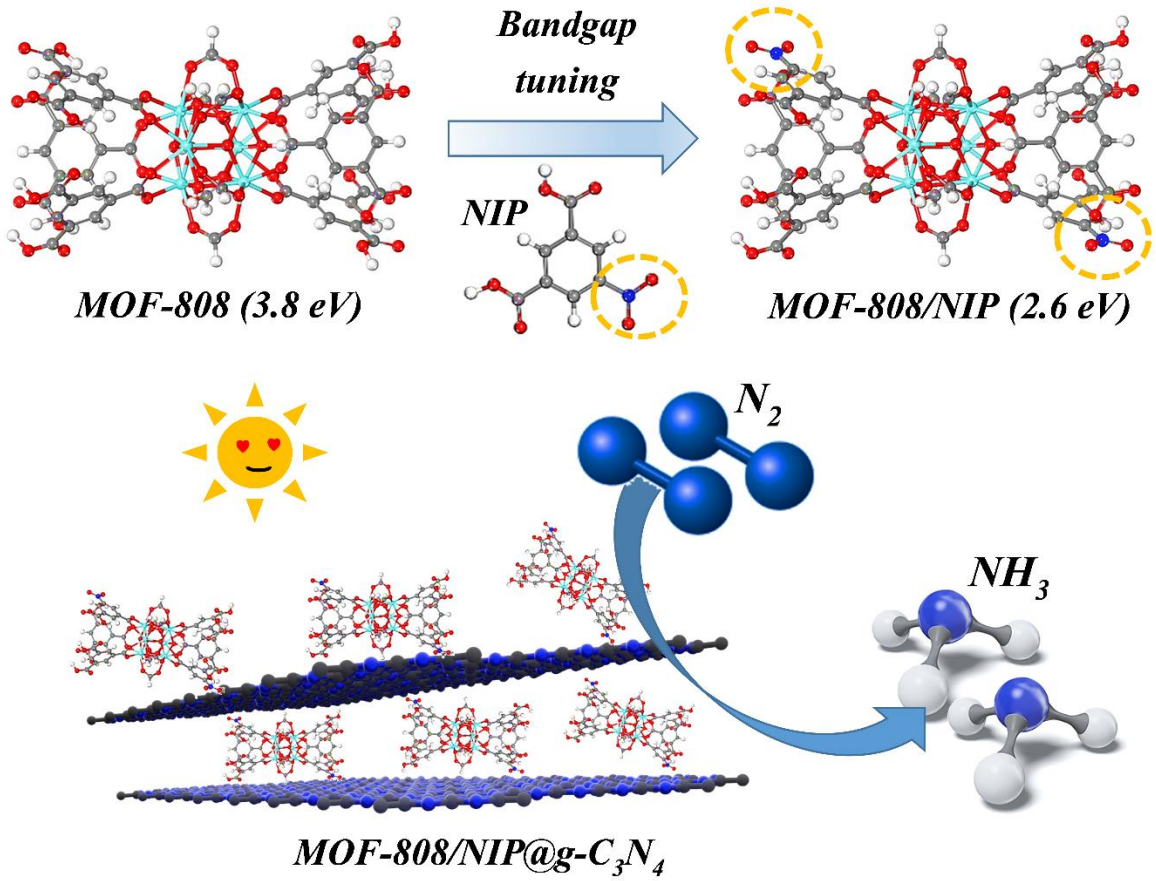

4. Solar-driven ammonia production through engineering of the electronic structure of MOF-808

4.1 Introduction

Ammonia (NH_3) is an essential component in multiple industries, including fertilizers and pharmaceuticals.[1,2] Moreover, it is widely recognized as a significant energy source and commonly referred to as "the other hydrogen" in the fuel sector.[3] One potential solution to the problem of hydrogen storage is to use NH_3 as a hydrogen carrier, as it is relatively inexpensive and has a simple decomposition process.[4] The Haber-Bosch approach is one of the most frequently utilized methods for generating NH_3. Unfortunately, this industrial process for nitrogen fixation demands extreme conditions, such as high pressure and temperature, to overcome significant activation energy. In addition, this method faces several drawbacks, including significant energy usage and emission of substantial amounts of carbon dioxide (CO_2).[5,6] Consequently, exploring more cost-effective and environmentally-friendly methods for NH_3 production is of uttermost importance.

The use of solar energy provides a potential answer to problems related to energy and environment. The effective transformation of sustainable and clean energy into chemical energy makes the process extremely attractive.[7,8] Currently, efforts have been made on developing photocatalysts that can function efficiently under visible light exposure. Unfortunately, several inorganic semiconductor photocatalysts cannot operate under visible light.[9] Thus, several approaches have been developed for enhancing the ability to harness visible light through structural modifications. The prevalent technique for narrowing band gaps is foreign element doping of ultraviolet-active metal oxides. One practical approach can be through the use of organic chromophores as receptors to capture visible light. The reason behind this approach lies in the fact that organic dye molecules are highly customizable. However, the uncontrollable movements of these molecules can cause self-quenching and

photobleaching, which are unavoidable issues.[10,11] The ongoing goal in solar-to-fuel conversion is to enhance catalytic efficiency when exposed to visible light by creating new photocatalyst materials.

Recently, photocatalytic nitrogen (N_2) fixation has gained significant attention, owing to its simple reaction conditions and eco-friendly nature.[12] This process has a significant advantage over traditional industrial methods, because it can activate molecular N_2 under normal conditions and replace H_2 with H_2O as the hydrogen source. However, several factors restrict the process, including the limited range of light absorption, frequent charge recombination, and the difficulty of activating highly stable N_2 molecules.[13,14] Therefore, developing photocatalysts for N_2 fixation can be a huge challenge. It requires creating semiconductor materials that can supply the high energy requirements of N_2, while exhibiting a short band gap to allow the use of optimal visible light exposure.[15]

The combination of inorganic and organic photocatalysts in metal-organic frameworks (MOFs) holds immense potential in developing innovative materials for solar fuel production. MOFs offer an extensive range of choices, including different metal nodes, organic linkers, and flexible coordination modes. Their high porosity and compatibility have made them a popular subject of study in photocatalysis in recent years.[16,17] One of the advantages of MOFs is their compatibility with various catalysts, which makes them an ideal choice for the fabrication of novel composite materials.[18] Zr-MOFs undoubtedly stand out as one of the most viable MOF materials for real-world implementation, owing to their remarkable porosity, extensive range of structure types, excellent water and thermal stabilities, and simple post-modification.[19,20] However, they have limited absorption in the visible region, which results in restricted charge transfer for excitation and facilitates the recombination of electrons and holes generated by light.[21] Thus, they require modification or combination with different effective substances to enhance their photocatalytic function. In the past few decades, there have been numerous

articles about using Zr-MOFs in photocatalysis. However, only a handful of papers have specifically explored band gap engineering through both experimental and theoretical approaches.[22]

There are three ways to reduce the energy required for photons to excite the outer shell electrons of an atom (band gap) in MOFs. These methods include enhancing the conjugation of linkers, choosing ligands and metal nodes that are electron-rich, and incorporating amino and nitro groups into linkers.[23] A group of researchers led by Duan provided a comprehensive overview on how MOFs can enhance photoelectronic performance for efficient photocatalysis.[24] Their study examined three strategies for modifying the band gap of MOF-based semiconductors by analysing the energy systematization of photocatalysis. According to Zeng et al., organic linkers together with metal doping reduce the band gap and can improve photocatalytic performance.[25] There is currently a lack of understanding regarding how electronic properties, such as optical absorption and band levels, can be effectively modulated. It is worth noting that the energy levels of MOF bands are crucial in determining their capacity to transform solar energy into fuel, because the proper band energy levels are essential for the target reactions to take place successfully from a thermodynamic perspective.[21]

Polymeric graphitic carbon nitride (g-C_3N_4) is a well-known substance for solar-to-fuel applications, because its band structure is ideal for visible light excitation.[26] Also, there have been reports on g-C_3N_4 exhibiting commendable photocatalytic N_2 fixation performance.[27,28] The chemical stability, simple synthesis process, and adjustable electronic structure make g-C_3N_4 a promising material for photocatalytic applications. However, its major disadvantage is the significant occurrence of electron-hole pair recombination, as well as low efficiency in terms of quantum yield and surface area.[29] To enhance photocatalytic performance and surpass the restrictions of MOFs and g-C_3N_4, it is useful to produce g-C_3N_4/MOF heterostructure composites. The organic ligands in MOFs form π-π interactions with the triazine rings of g-

C_3N_4, resulting in strong electrostatic interactions and efficient electron transfer. This enables the construction of a heterojunction and close contact between the two materials.[30] According to the research conducted by Ding and colleagues, utilizing nano-MOF and a flawed layer of C_3N_4 could significantly enhance the capability of N_2 fixation in photocatalysis under visible light through the Z-scheme method. This improvement was observed compared to the performance of pure flawed film of C_3N_4. They utilized a sol-gel technique to disperse nano-size MOF-74 particles (less than 20 nm) onto a nitrogen-defective C_3N_4 thin film (4 nm) and then subjected it to calcination at 200 ºC.[31]

Herein, a Zr-based MOF, MOF-808/NIP@g-C_3N_4, composite was prepared as a suitable photocatalyst for N_2 photoreduction with the aim of proper catalytic performance under visible light irradiation. First, introducing a linker containing a nitro group similar to the primary linker of the MOF-808 was used to reduce the band gap energy of the framework. Then, to reach a suitable photocatalytic performance for NH_3 production, it was combined with g-C_3N_4, which has a confirmed performance for this reaction and band gap energy close to that of the modified MOF-808 structure. The obtained composite recorded higher photocurrent than both its constituent materials and is also able to absorb light in the entire UV-visible region. Our comprehensive literature review revealed that MOF-808/NIP@g-C_3N_4 exhibited one of the highest performances for N_2 photoreduction under visible light, surpassing other MOFs studied so far.

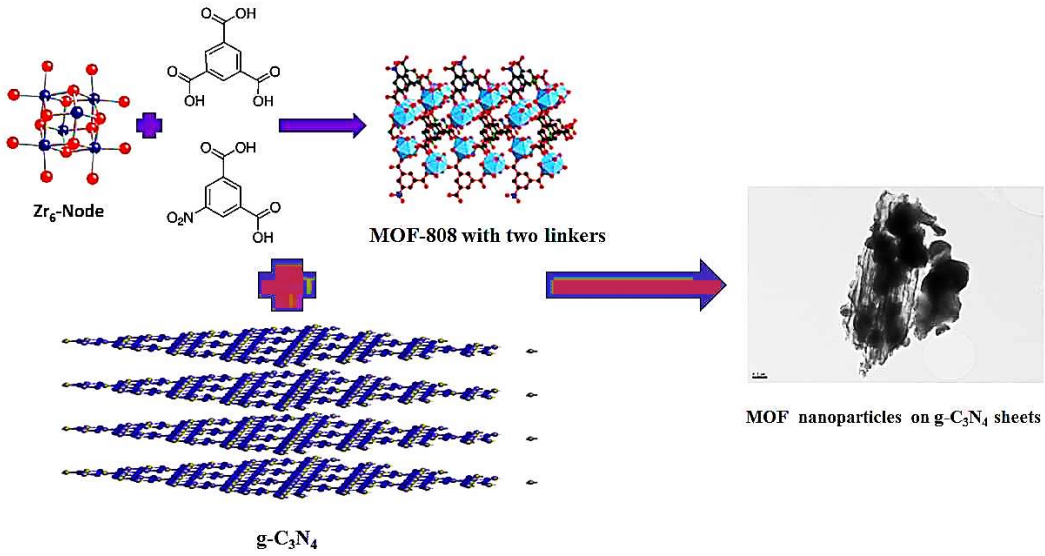

Scheme 4.1. Schematic illustration of the preparation of MOF-808/NIP@g-C_3N_4.

4.3.1 Characterization of photocatalysts

The mixed linker method was used to incorporate specific amounts of the 5-nitro isophthalic acid (NIP) ligand into the structure of MOF-808, a method proven for decreasing Zr-based MOFs' bandgap energy.[23,33] Thus, 10 mg of g-C_3N_4 were added to prepare MOF hetero-composites during the synthesis of MOF-808 with NIP linker (**Scheme 4.1**). Characterization of the formed compounds was comparatively carried out using various techniques, such as FT-IR, ^{1}H-NMR, PXRD, XPS, and Brunauer-Emmett-Teller (BET) adsorption-desorption isotherms.

The FT-IR spectrum of MOF-808 (**Fig. 4.2-b**) shows bands at 647, 763, 1375, 1617 and 1707 cm^{-1} assigned to the vibrations of Zr-O, Zr-O-Zr and various stretching modes of Zr-carboxylate bonds related to the MOF-808, respectively.[34] The stretching vibrations of the nitro group at 1537 and 1346 cm^{-1} confirmed the incorporation of the NIP ligand into the mix-linker structure and composite (**Fig. 4.2-c**).[35] In the spectrum of MOF-808/NIP, there are two peaks at 737 and 1452 cm^{-1} related to Zr-O-N and N=O, respectively.[36,37] The presence of these peaks suggests that a small portion of nitro groups may be interacting with zirconium nodes from one end. Also, the bands at 805 cm^{-1} (breathing mode of the triazine unit) and 1250-1700 cm^{-1}

(stretching vibrations of conjugated CN rings) are characteristic of g-C_3N_4 in the hetero-composite (**Fig. 4.2-d&a**).[38] In the MOF composite spectrum (**Fig. 4.2-d**), in addition to the presence of the characteristic peaks of both components, the peaks at 1020, 1205, and a doublet at 1452 and 1465 cm^{-1} are also seen, which are related to the N–O bond stretching characteristic of the nitrito (ONO) group, the N–N stretching, and the N=O stretching frequency, respectively.[39,40] Considering these new peaks, it seems that the connection of the two components in this composite is through the NO_2 functional group on the NIP linker inserted in the MOF-808 structure and the nitrogen atoms on the graphitic carbon.

Verification of the BTC: NIP ratio (1.33) in the structure was done by digestion of the mixed-linker structure in D_2SO_4/D_2O solution, followed by ^{1}H-NMR spectroscopy analysis. One doublet peak at 9.02 ppm and one triplet peak at 8.92 ppm are related to the NIP ligand, and a singlet peak at 8.78 ppm is attributed to the BTC linker (**Fig. 4.3**).

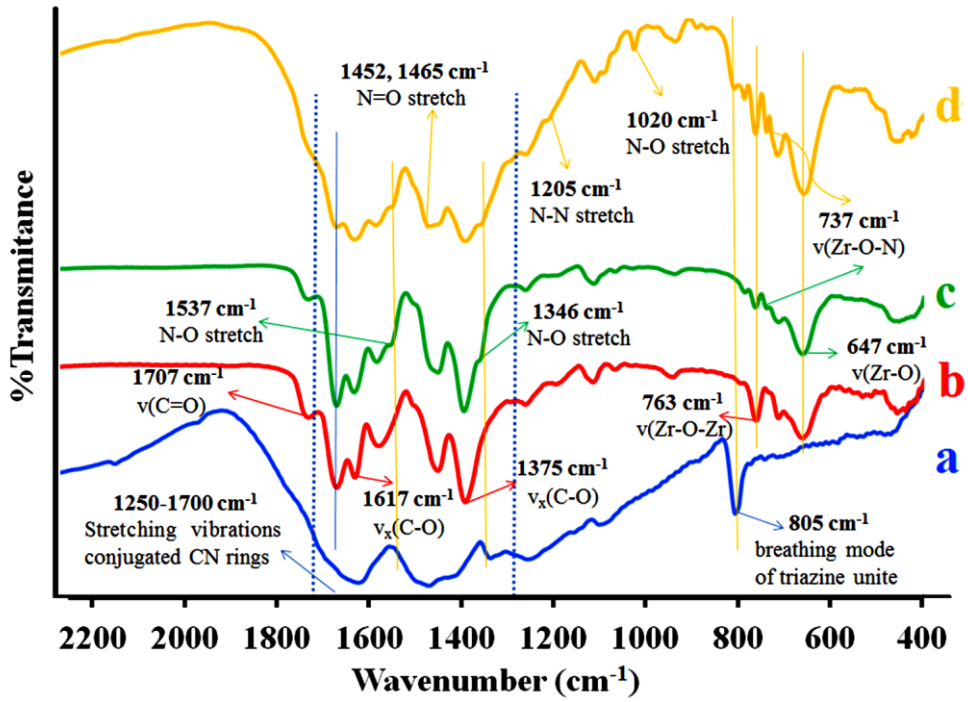

Figure 4.2. FT-IR spectra of (a) g-C_3N_4, (b) MOF-808, (c) MOF-808/NIP, (d) MOF-808/NIP@g-C_3N_4.

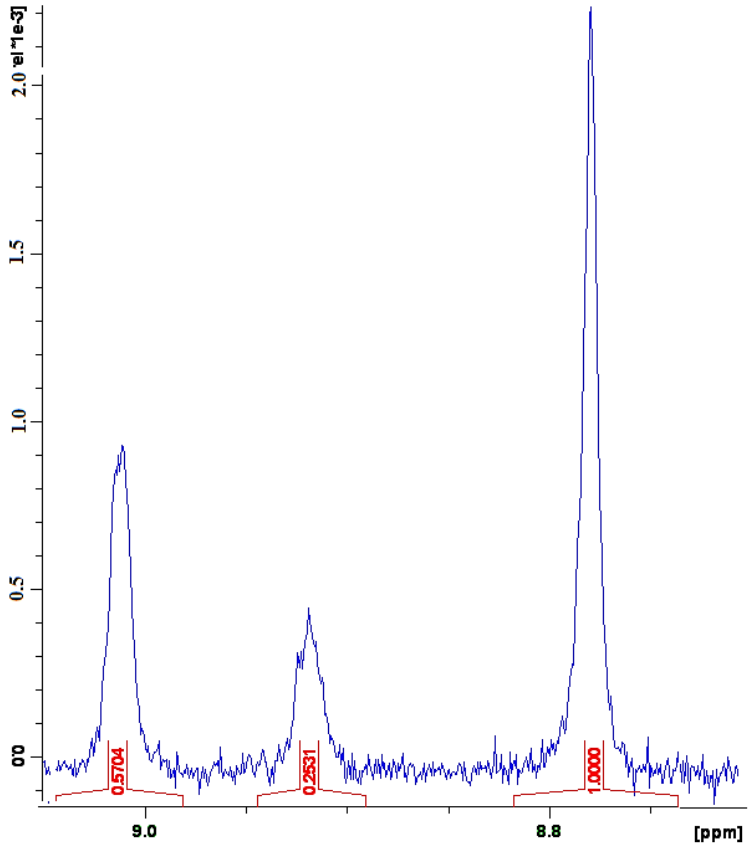

Figure 4.3. ^{1}H NMR spectrum of the MOF-808/ NIP.

PXRD analyses revealed that all compounds synthesized have crystalline structure (**Fig. 4.4**). The similarity of the diffraction patterns of the synthesized structures proved that they are isostructural with MOF-808.[41] The first six primary peaks in PXRD patterns of the mixed-linker MOF and MOF composite, related to the (3,1,1), (2,2,2), (3,3,1), (4,2,0), and (4,2,2) diffraction plans and showed a minor shift (0.06°), towards smaller 2θ values. This shift could be related to defects in the network due to the introduction of the second linker. Furthermore, the single peak related to g-C_3N_4 at 2θ= 27.5° (**Fig. 4.6**) overlaps with the peaks related to the MOF structure. The structural peaks in the MOF composite are located on a broad peak in the 2θ range of 25° - 35°. This broad peak is associated with g-C_3N_4 in the composite material.

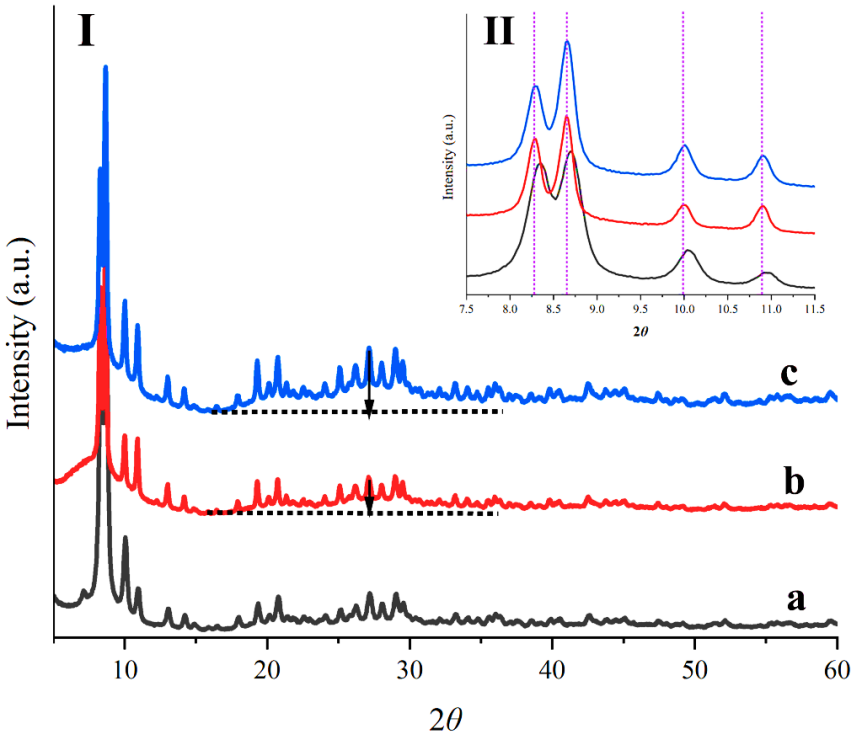

Figure 4.4. I) PXRD patterns of (a) MOF-808, (b) MOF-808 with NIP, and (c) MOF composite. II) Peak shift in mixed-linker structures.

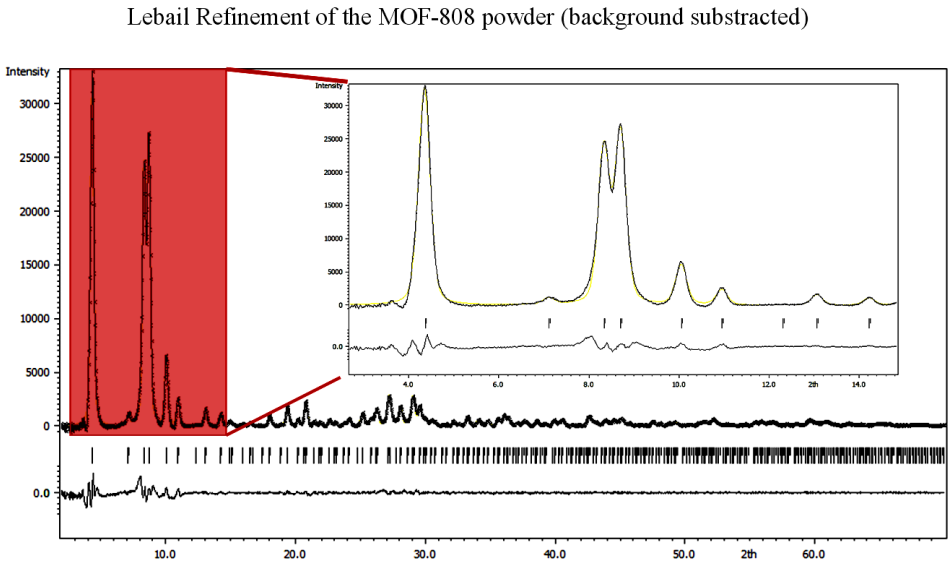

Cell parameter a=35.286(9) V=43934(12), space group: Fd-3m (n°227)

Profile R factors for 3326 points and 16 parameters, GOF = 2.28, Rp = 2.69, wRp = 4.19

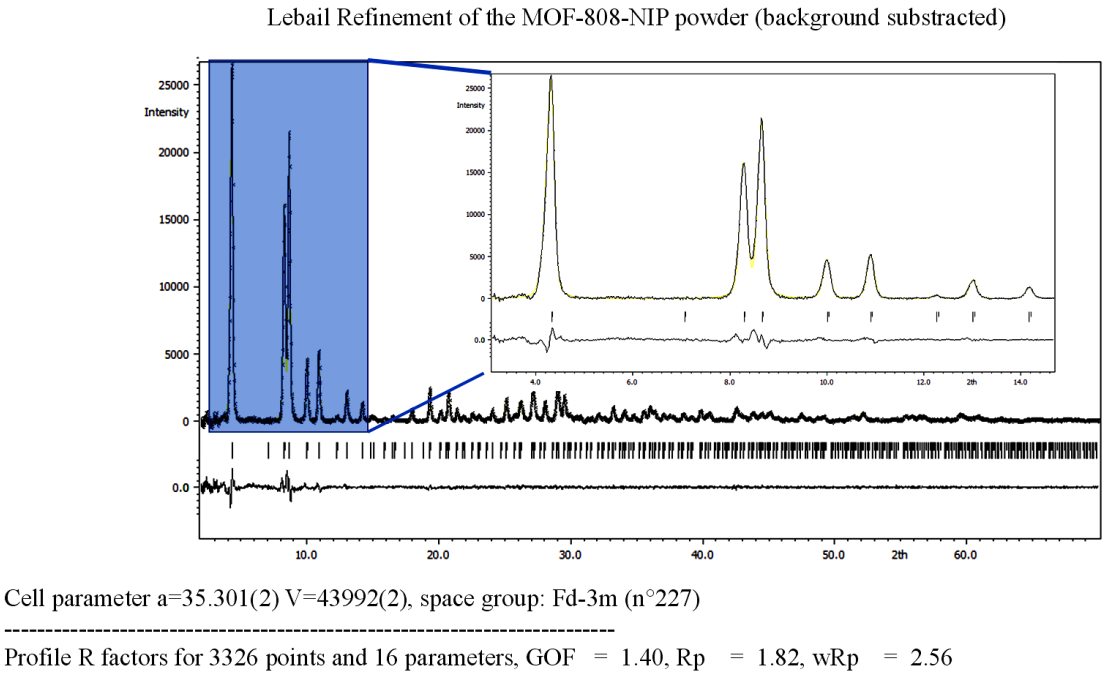

Figure 4.5. Lebail refinement and lattice parameters of the MOF-808 and MOF-808-NIP.

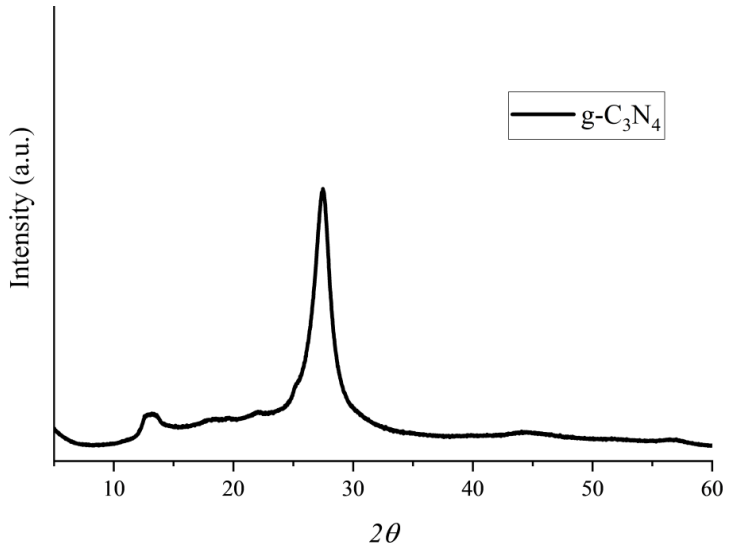

Figure 4.6. PXRD pattern of g-C_3N_4.

Pore structure analysis was performed by nitrogen gas adsorption-desorption studies. As shown in **Fig. 4.7-a**, the shape of N_2 adsorption isotherms of prepared materials are between types I and IV based on the most recent IUPAC classification.[42] For all three synthesized materials, the adsorption capacity of nitrogen significantly increases at very low relative pressures. This

behavior is characteristic of microporous systems with a narrow pore size distribution. Based on the pore size distribution plot presented in **Fig. 4.7-b**, it is evident that, besides the microporous distribution, there is a wide range of mesopores distribution between 15 to 50 nm in the mixed-linker structures, especially in the MOF/g-C_3N_4 composite. This may be related to the roughness of the crystal surface, the MOF−g-C_3N_4 interface, and the particle sizes that are all responsible for an increase in the external surface area. These experiments showed that, by inserting the NIP linker in the network, the BET surface area of MOF-808 (1303 m^2/g) decreased to 577 m^2/g; this is mainly because the pores of MOF-808 contain NIP linkers that are connected to the Zr clusters through carboxylate sites. The specific surface areas of g-C_3N_4 and MOF composite were 3.8 and 570 m^2/g, respectively.

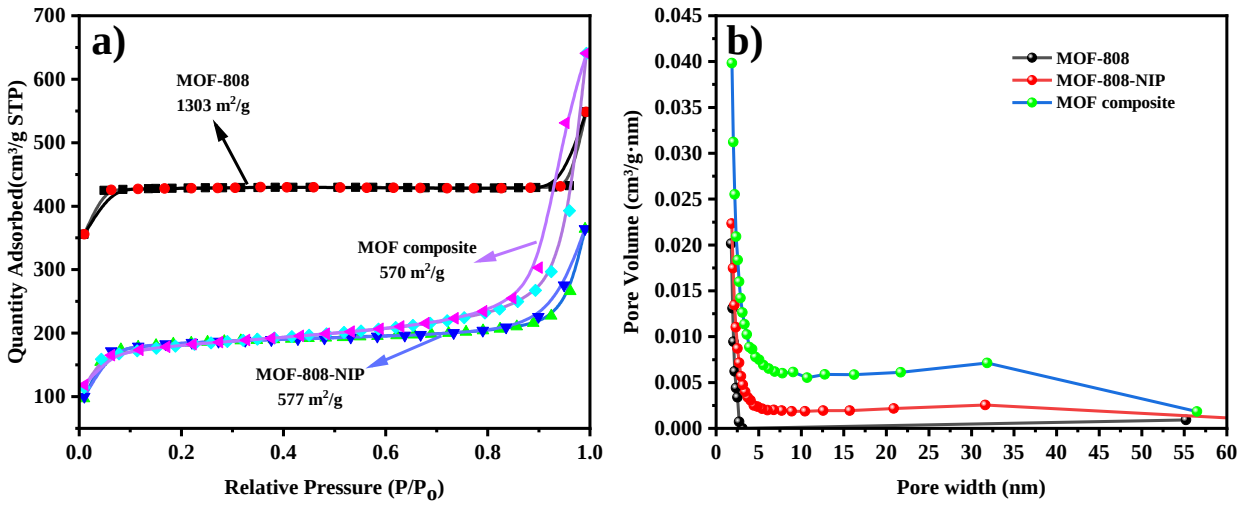

Figure 4.7. (a) Nitrogen adsorption/desorption isotherms, and (b) Pore size distribution of the prepared materials by BJH method.

Scanning and transmission electron microscopies were used to investigate the morphologies of synthesized samples. As expected, 2D g-C_3N_4 nanosheets are seen in **Fig. 4.8**. MOF-808 displayed a nanoparticulate shape with a size of about 100-200 nm (**Fig. 4.9-a**). Upon insertion of the second linker in the structure, the size of the nanoparticles decreased to 50-100 nm. In addition, particle aggregation of the mixed-linker MOF was significantly reduced compared to the MOF-808 (**Fig. 4.9-b**). As shown in **Fig. 4.9-c** and **4.10**, the composite material consisted

of nanoparticles of mixed-linker structure placed on the surface of g-C_3N_4 nanosheets. The elemental analysis confirmed the presence of both components in the composite. The g-C_3N_4 is rich in nitrogen, and the MOF structure contains Zr and Cl. In the TEM image (**Fig. 4.10**), the 2D sheet edges are indicated by yellow dots. Focusing on the yellow dots makes it possible to observe the 2D sheet edges of g-C_3N_4 in the nitrogen and carbon chemical map, but not in the chemical maps of zirconium, chlorine, and oxygen. This light sheet is associated with g-C_3N_4 and linked to the darker particles corresponding to MOF nanoparticles.

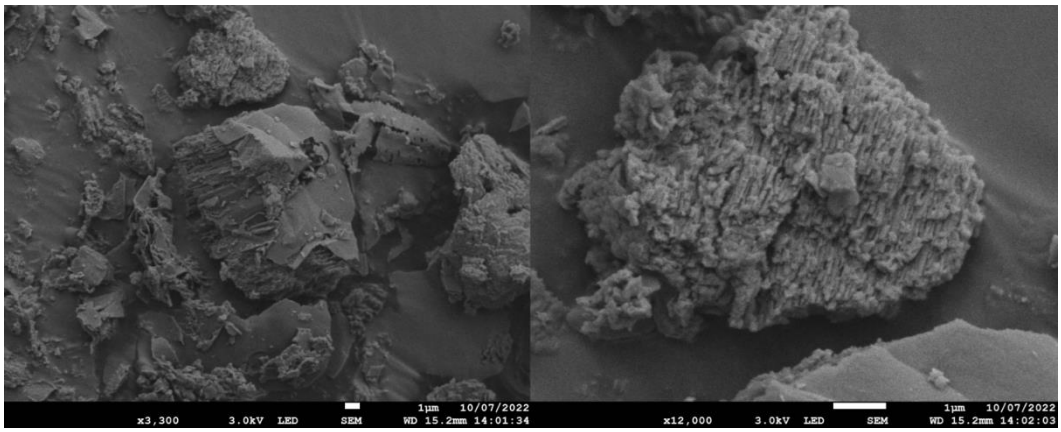

Figure 4.8. SEM images of g-C_3N_4.

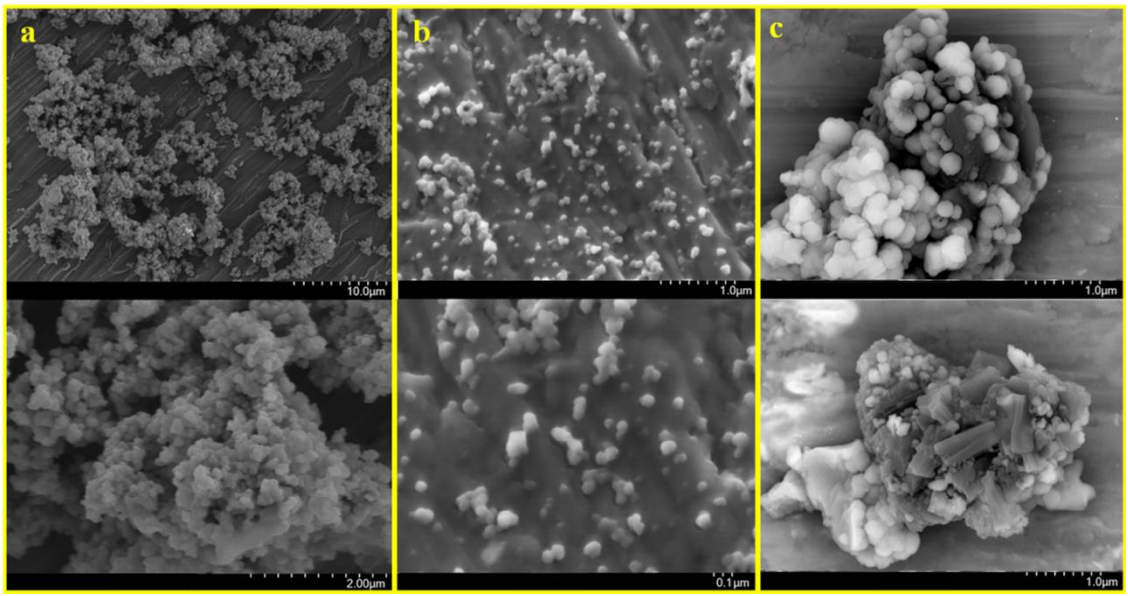

Figure 4.9. SEM images at different magnifications of (a) MOF-808, (b) MOF-808/NIP, and (c) MOF-808/NIP@g-C_3N_4-composite.

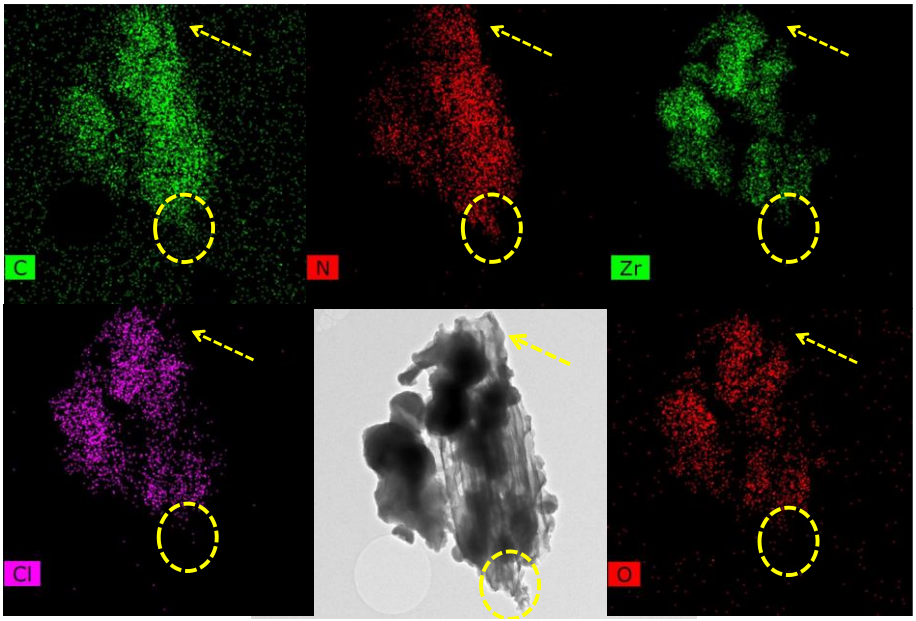

Figure 4.10. TEM image and chemical elemental mappings of C, Zr, Cl, N, and O in MOF-808/NIP@g-C_3N_4.

Thermogravimetry analysis (TGA) was recorded to evaluate the thermal stability of g-C_3N_4, MOF, and its composite. As shown in **Fig 4.11-A, C**, the TGA curves for the MOF and its composite exhibit similar shapes, with two significant decomposition stages occurring at approximately 300 and 420 °C. The two primary steps before these two significant decomposition stages are related to the loss of water and solvent inside the structure.[43] In **Fig 4.11-B**, a slow decomposition between 520 and 620 °C declines sharply from 675 °C, ending at 760 ºC and material turning into carbon and nitrogen-containing gases. Based on the TGA plot, it can be concluded that the prepared g-C_3N_4 is thermally stable and almost pure according to the literature.[44] It exhibits remarkable robustness and can maintain stability even at high temperatures of around 600 °C. These features are attributed to the stable construction of the material, which is based on heptazine-based units. The difference in the weight loss observed in the last stage for composite material compared to MOF-808 is evidence for the presence of g-C_3N_4 in the composite.

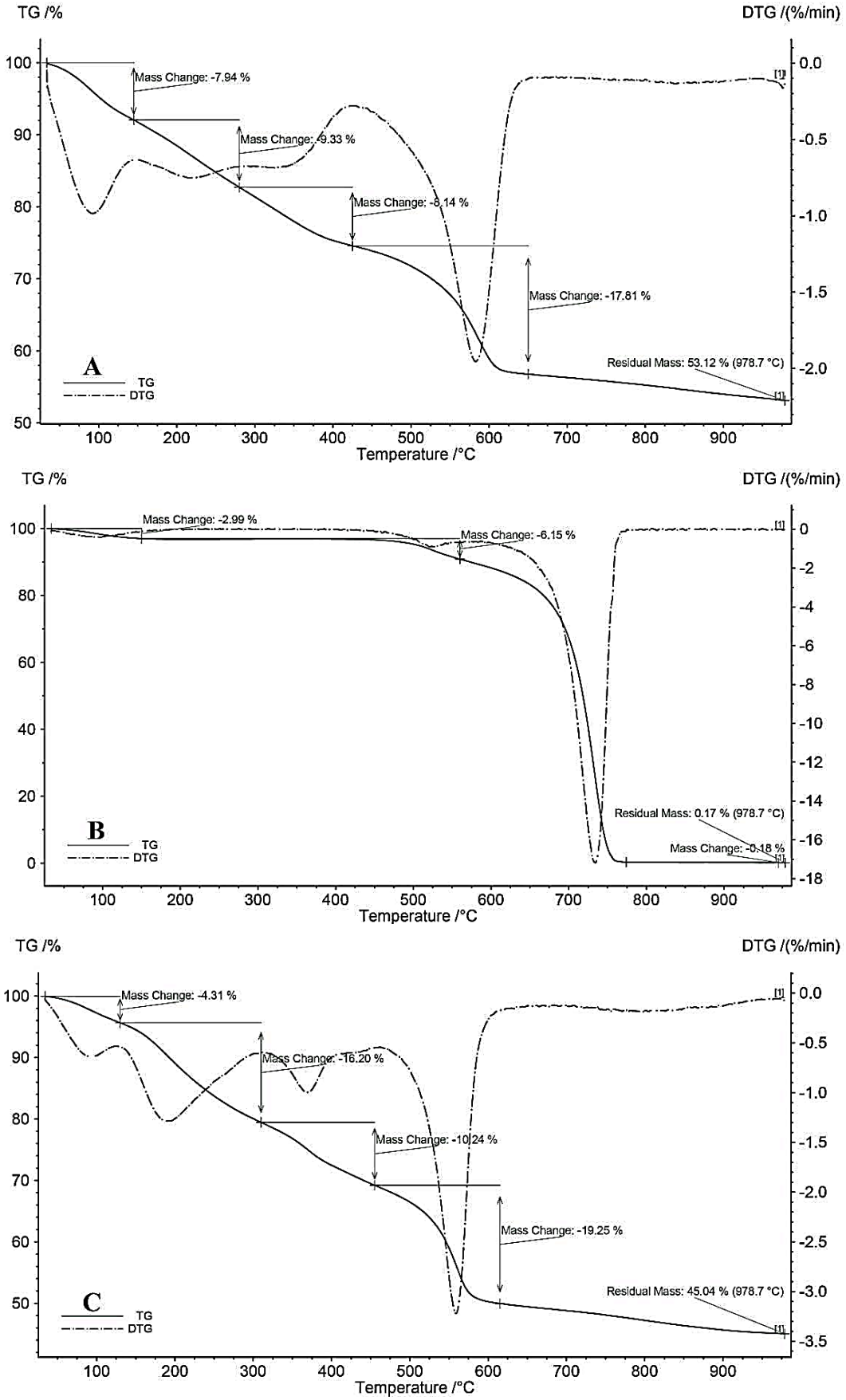

Figure 4.11. Thermogravimetry analysis (TGA) and differential thermogravimetric (DTG) of (A) MOF-808, (B) g-C_3N_4, and (C) MOF-808/NIP@g-C_3N_4 composite.

X-ray photoelectron spectroscopy (XPS) was used to assess the elemental composition and surface properties. XPS spectra are, for the most part, quantified in terms of peak intensities and peak positions. The peak intensities measure how much of a material is at the surface, while the peak positions indicate the elements' oxidation state and local chemical environment. The full scan spectrum in **Fig. 4.12** shows that the MOF-808, MOF-808/NIP and MOF-808/NIP@g-C_3N_4 comprise C, O, Zr, and N atoms. **Table 4.1** displays the surface element compositions following background subtraction and fitting. The MOF composite spectrum displays a stronger peak related to N 1s compared to MOF-808/NIP, indicating the presence of g-C_3N_4 in its structure.

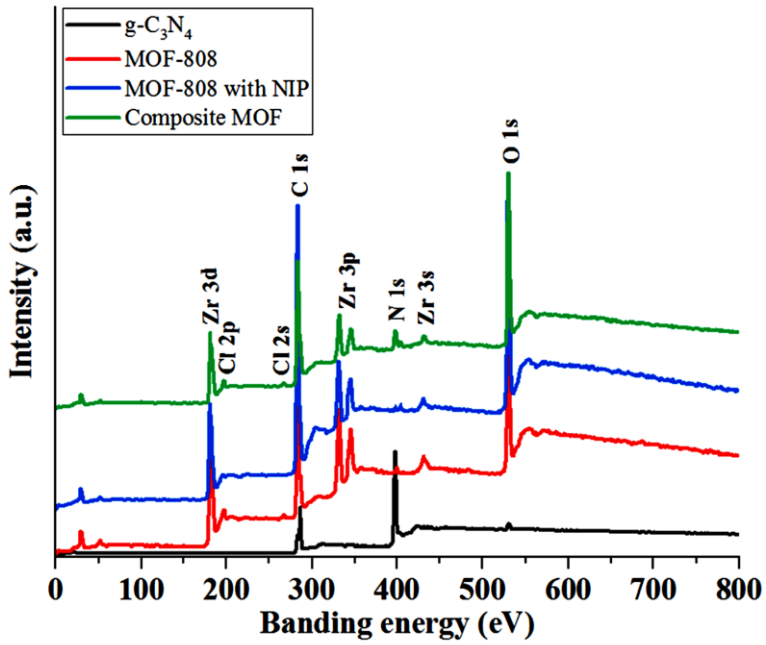

Figure 4.12. The full-scan XPS spectra of MOF-808 [red], MOF-808/NIP [blue], g-C_3N_4 [black] and MOF-808/NIP@g-C_3N_4 [green].

Table 4.4. Atomic concentration of elements on the surface determined by XPS.

Sample	Surface Atomic Score Levels (%)			
	C 1s	N 1s	O 1s	Zr 3d
g-C_3N_4	49.99	48.70	1.30	-
MOF-808	57.05	0.97	32.31	9.65
MOF-808/NIP	74.29	1.73	20.21	3.75
Fresh MOF-808/NIP@g-C_3N_4	61.72	5.20	28.10	4.96
Recovery MOF-808/NIP@g-C_3N_4	62.12	5.56	27.58	4.72

The core-level scans of the C 1s of the prepared samples are illustrated in **Fig. 4.13-A**. The bands at 284.68 and 288.10 eV, assigned to C-C and sp^2 N=C–N bonds, respectively, are the characteristic carbon species in g-C_3N_4 (**Fig. 4.13-A-I**). Two small peaks at 285.42 and 288.86 eV are attributed to the sp N-C=N and C=O originating from the surface functional groups, respectively.[45–47] The C 1s XPS spectrum of MOF-808/NIP (**Fig. 4.13-A-II**) could be curve-fitted with four peaks at 284.51, 285.06, 285.98 and 288.57 eV, which are ascribed to the sp^2 C=C, C-N, C–O, and O–C=O, respectively.[48,49] The appearance of the C-N peak alongside the other three peaks can be attributed to the presence of the NIP linker within the MOF-808 structure. The C 1s spectrum of the MOF-808/NIP@g-C_3N_4 sample is deconvoluted into six peaks (**Table 4.2**, **Fig. 4.13-A-III**). In this sample, there is a slight shift to the lower binding energy for following peaks: sp^2 N-C=N at 287.89 eV, which is associated with g-C_3N_4, the C-N peak at 284.89 eV, which is related to MOF-808/NIP and the C=C/C-C at 284.37 eV. This means that these groups play an active role in the interaction between the g-C_3N_4 structure and MOF-808/NIP in the composite MOF structure.

Table 4.2. The fitting parameters of the high-resolution XPS spectrum of the C 1s of the synthesized materials.

C 1s		XPS parameters		
Sample	Assignments	Binding energy (eV)	FWHM	% Area
g-C_3N_4	C=C/C-C/C-H	284.68	1.17	19.88
	sp N(C≡N)	285.42	1.62	9.27
	sp_2 N-C=N	288.10	1.13	59.40
	C=O	288.86	1.28	11.45
MOF-808/NIP	C=C/C-C/C-H	284.51	1.22	56.64
	C-N	285.06	1.12	17.42
	C-O-C	285.98	1.61	14.35
	O-C=O	288.57	1.37	11.59
MOF-808/NIP@g-C_3N_4	C=C/C-C/C-H	284.37	1.27	44.98
	C-N	284.89	0.98	16.14
	sp N(C≡N)	285.41	0.85	4.27
	C-O-C	285.94	1.41	13.15
	sp_2 N-C=N	287.89	1.41	7.8
	C=O	288.57	1.36	13.21

In the high-resolution XPS spectrum of the N 1s of the mixed-linker structure (**Fig. 4.13-B-II**), two peaks are observed and can be split into four smaller peaks at 398.33, 399.74, 404.64, and 405.45 eV corresponding to the Zr-O-N, C-N, N=O bounds and -NO_2 group in the NIP linker, respectively.[50–52] These peaks confirm the presence of the second linker in the MOF-808/NIP structure. It seems that part of the NO_2 groups on the NIP linker is connected to the zirconium nodes at least from one end, and another part is present in the structure as free NO_2. Regarding the g-C_3N_4 sample (**Table 4.3**, **Fig. 4.13-B-I**), it is worth noting that the N 1s XPS peak can be fitted with bands at C-N=C (398.83 eV), N-$(C)_3$ (399.61 eV), $(C)_2$-NH (401.11 eV), and π-excitation (404.69 eV) [47]. The N 1s spectrum of the composite sample (**Table 4.3**, **Fig. 4.13-B-III**) is deconvoluted into peaks corresponding to C-N=C (398.85 eV), N-$(C)_3$ (399.98 eV), and $(C)_2$-NH (401.10 eV) associated with g-C_3N_4 and the peaks Zr-O-N (398.19 eV), C-N (399.45 eV), N=O (404.26 eV), NO_2 (406.28 eV) are related to MOF-808/NIP. Furthermore, the band at 402.9 eV is believed to be due to N-N=O species.[36,53,54] Additionally, the electron density of the nitrogen in N-$(C)_3$, Zr-O-N, C-N, and N=O peaks has increased and shifted to lower binding energies. In comparison, electron density of the nitrogen in NO_2 peak has experienced a decrease and shifted to higher binding energies (**Fig. 4.13-B-III**).

The O 1s XPS spectrum of g-C_3N_4 in **Fig. 4.13-C** suggests the presence of oxygen atoms of different chemical environments. In **Fig. 4.13-C-I**, the bands at binding energies of 531.83 and 533.21 eV can be assigned to N–C=O and C–OH, respectively as the characteristic oxygen species in g-C_3N_4.[48] In addition, MOF-808/NIP displays a distinct XPS O 1s spectrum with six different peaks at 530.01, 531.04, 531.84, 532.39, 533.03, and 533.86 eV corresponding to Zr-O_2, Zr-O-N, C=O, N=O, Zr–OH and O-N=O peaks, respectively (**Fig. 4.13-C-II**).[51,55] Upon analysing the composite sample, it was found that the O 1s spectrum can be divided into eight peaks (**Table 4.4**). These peaks correspond to Zr-O_2 (530.35 eV), Zr-O-N (531.24 eV), N–C=O (531.67 eV), N=O (531.95 eV), C=O (532.19 eV), Zr-OH (533.14 eV), and O-N=O (533.93

eV) with an additional band at 532.61 eV (N-N=O).[54,55] Interestingly, all the components showed a slight shift towards higher binding energy except N-C=O associated to g-C_3N_4 and N=O in MOF-808/NIP, which shifted towards lower binding energies (**Fig. 4.13-C-III**).

Table 4.3. The fitting parameters of the high-resolution XPS spectrum of the N 1s of the synthesized materials.

N 1s		XPS parameters		
Sample	Assignments	Binding energy (eV)	FWHM	% Area
g-C_3N_4	sp_2 C-N=C	398.83	1.17	52.89
	N-$(C)_3$	399.61	1.37	28.02
	$(C)_2$-NH	401.11	1.69	15.62
	π-excitations	404.69	1.73	3.47
MOF-808/NIP	Zr-O-N	398.33	1.74	16.56
	C-N	399.74	2.05	34.42
	N-O	404.64	1.29	19.61
	NO_2	405.45	1.58	29.41
MOF-808/NIP@g-C_3N_4	Zr-O-N	398.19	1.03	8.37
	sp_2 C-N=C	398.85	1.10	24.30
	C-N	399.45	0.93	6.06
	N-$(C)_3$	399.98	1.52	20.53
	$(C)_2$-NH	401.10	1.57	17.40
	N-N=O	402.09	2.06	11.59
	N-O	404.26	1.38	1.15
	NO_2	406.28	1.73	10.05

Table 4.4. The fitting parameters of the high-resolution XPS spectrum of the O 1s of the synthesized materials.

O 1s		XPS parameters		
Sample	Assignments	Binding energy (eV)	FWHM	% Area
$g\text{-}C_3N_4$	N-C=O	531.83	1.86	71.19
	O-H	533.21	1.75	28.81
MOF-808/NIP	$Zr\text{-}O_2$	530.01	1.41	11.67
	Zr-O-N	531.04	1.44	20.13
	C=O	531.84	1.19	27.12
	N=O	532.39	1.00	7.89
	Zr-OH	533.03	1.58	26.38
	NO_2	533.86	1.34	6.80
MOF-808/NIP@$g\text{-}C_3N_4$	$Zr\text{-}O_2$	530.35	1.29	9.93
	Zr-O-N	531.24	1.19	18.22
	N-C=O	531.67	0.83	14.98
	N=O	531.95	0.61	1.42
	C=O	532.19	0.88	21.72
	N-N=O	532.61	0.98	14.88
	Zr-OH	533.14	1.17	14.01
	NO_2	533.93	1.16	4.84

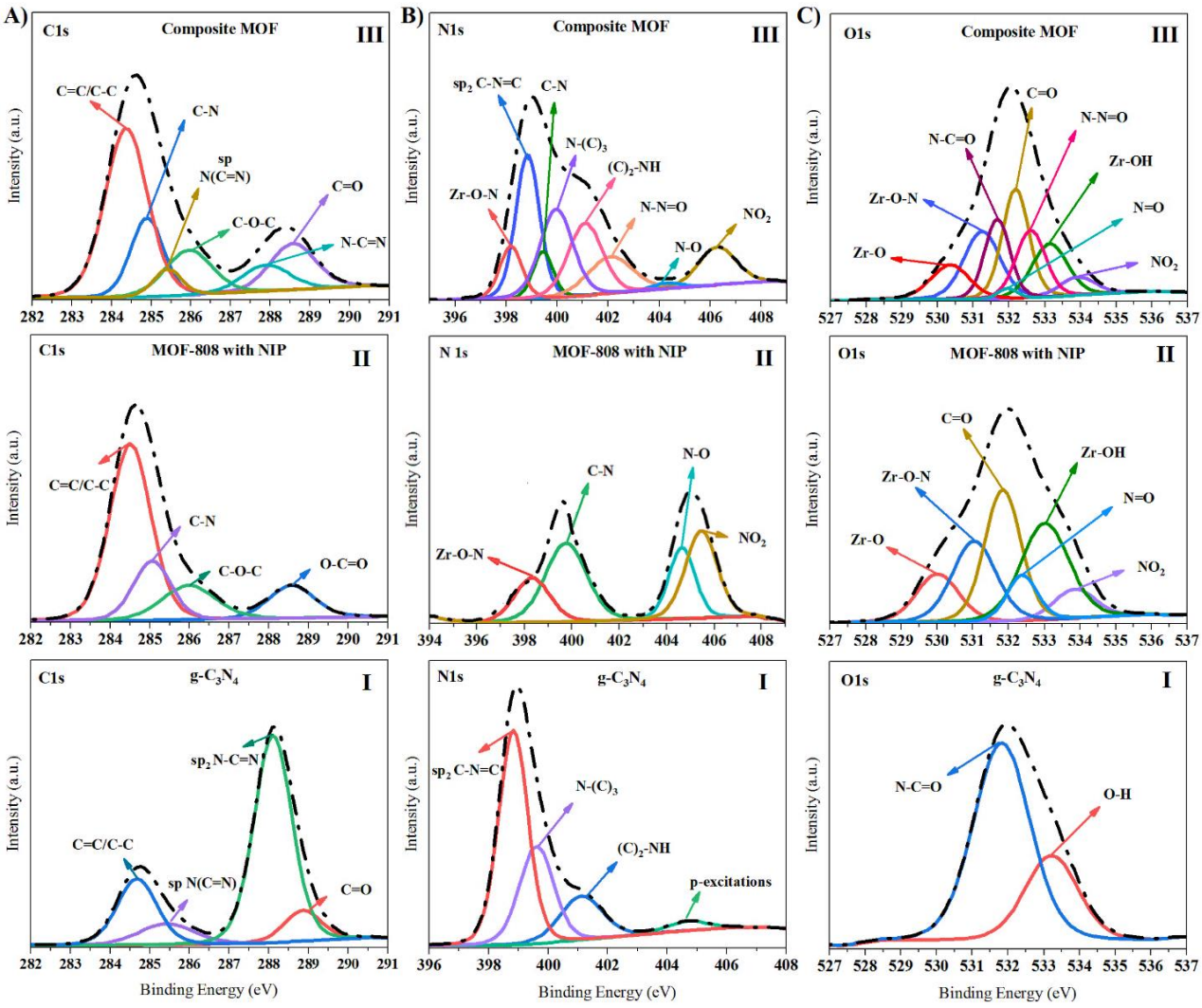

Figure 4.13. Core-level XPS scan of **A**) C 1s, **B**) N 1s and **C**) O 1s of the synthesized materials.

For all the samples, the Zr 3d spectra showed one double peak at approximately 182 and 184 eV corresponding to Zr $3d_{5/2}$ and Zr $3d_{3/2}$, respectively.[56] Based on the collected spectra, incorporating the NIP linker into the MOF-808 structure causes an electronic perturbation in the Zr 3d orbitals. The Zr 3d spectrum of MOF-808/NIP is displaced toward lower binding energies and can be divided into two main peaks with a shoulder (**Table 4.5**). Based on the spectrum analysis, it is apparent that the shoulder is more suitable for values related to a Zr-O-N bonding environment rather than Zr-O.[51,57] The Zr $3d_{5/2}$ orbital in the MOF-808/NIP structure has decreased binding energy from 182.63 to 182.35 eV (**Fig. 4.14-A**). This suggests that the

Zr node is binding with the less electronegative N-O group rather than the more electronegative aqua and hydroxide moiety. In MOF composite, in contrast to MOF structure (**Fig. 4.14-B**), these peaks shifted slightly to higher binding energies (from 182.35 to 182.73 eV and 184.69 to 185.05 eV). The positive shift observed appears to align with the interaction between g-C_3N_4 and MOF-808/NIP, which can enhance the electron density on Zr nodes.

Table 4.5. The fitting parameters of the high-resolution XPS spectrum of the Zr 3d of the synthesized materials.

Zr 3d		XPS parameters		
Sample	Assignments	Binding energy (eV)	FWHM	% Area
MOF-808	Zr $3d_{5/2}$-ZrO_2	182.63	1.41	58.87
	Zr $3d_{3/2}$-ZrO_2	185.00	1.47	41.13
MOF-808/NIP	Zr $3d_{5/2}$-Zr-O-N	181.72	1.17	10.10
	Zr $3d_{5/2}$-ZrO_2	182.35	1.52	47.77
	Zr $3d_{3/2}$-Zr-O-N	184.20	1.51	7.88
	Zr $3d_{5/2}$-ZrO_2	184.69	1.68	34.25
MOF-808/NIP@g-C_3N_4	Zr $3d_{5/2}$-Zr-O-N	182.24	1.09	10.58
	Zr $3d_{5/2}$-ZrO_2	182.73	1.37	48.23
	Zr $3d_{3/2}$-Zr-O-N	184.80	1.22	6.52
	Zr $3d_{5/2}$-ZrO_2	185.05	1.49	34.67

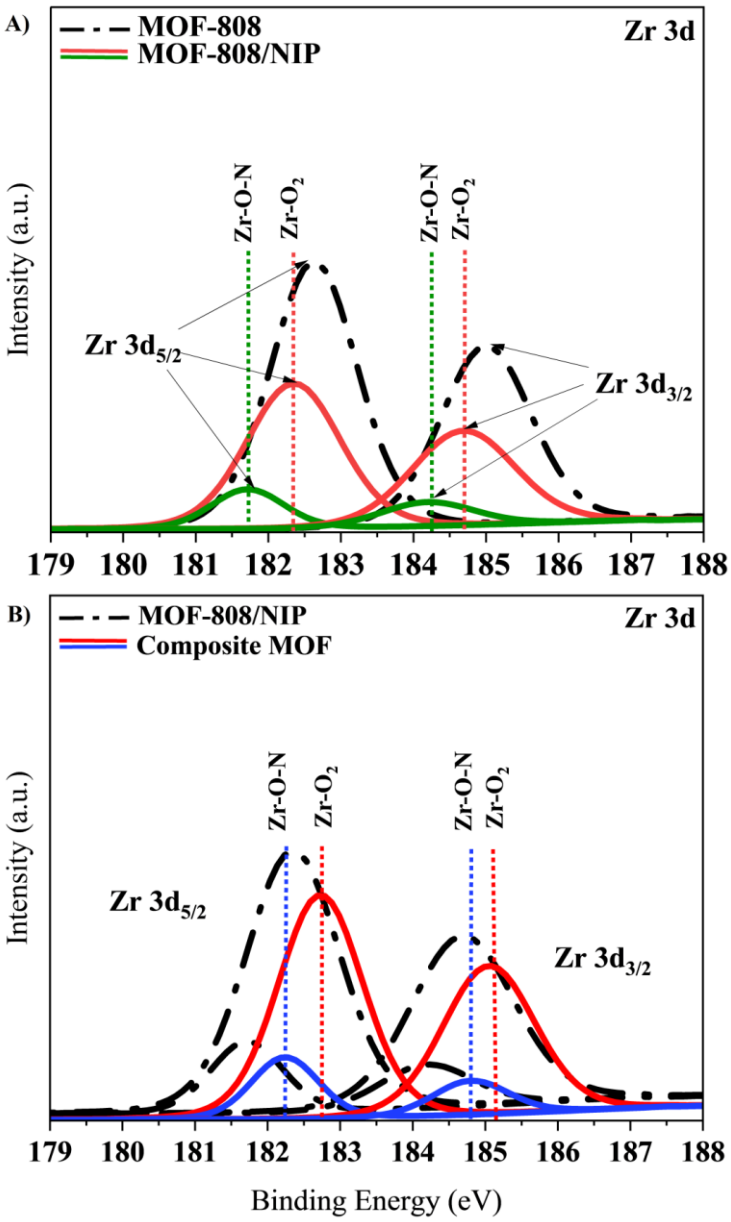

Figure 4.14. Zr 3d core level XPS spectra: (**A**) MOF- 808, mixed-linker structure MOF-808/NIP and (**B**) composite MOF-808/NIP@g-C_3N_4 compare with MOF-808/NIP.

4.3 Photocatalytic activity of the material

The Nessler's reagent method, a dependable and swift technique for detecting NH_3 under acidic conditions (**Fig. 4.15**)[58], was applied to measure the photocatalytic performance of the prepared samples. **Figure 4.16-a** illustrates the photocatalytic activity of g-C_3N_4, MOF-808/NIP, and MOF-808/NIP@g-C_3N_4 samples for reducing N_2 to NH_3 in water. Under visible light irradiation, the NH_3 evolution rate reached 178 and 327 μmol g^{-1} h^{-1} in the presence of MOF-

808/NIP and g-C_3N_4 photocatalysts, respectively. Interestingly, the g-C_3N_4 nanosheets coated with MOF-808-NIP nanoparticles exhibited a higher NH_3 generation rate of 490 μmol g^{-1} h^{-1}. Control experiments demonstrated that MOF composite was inactive for N_2 reduction in absence of irradiation and Ar-saturated solution under irradiation (**Figs. 4.17** and **4.16-a**).

To evaluate the reusability of the MOF-808/NIP@g-C_3N_4 photocatalyst, the N_2 reduction system was recycled four times (**Fig. 4.16-b**). In the initial three reaction cycles, there was little change in the efficiency of NH_3 production. In addition, the NH_3 production rate in the fourth cycle reached 91% of the initial value, indicating the good stability of the MOF composite photocatalyst. To ensure the stability of the structure after the reaction, FT-IR, PXRD, SEM, and XPS were performed on the recycled photocatalyst (**Fig. 4.18**). **Table 4.6** compares N_2 reduction rates of MOF composite (MOF-808/NIP@g-C_3N_4) with other MOF-based photocatalysts in this field. Based on the data presented in this table, it is evident that the MOF-808/NIP produced an adequate amount of ammonia. Notably, when compared to other MOF-based materials, MOF-808/NIP@g-C_3N_4 featured superior photocatalytic activity for N_2 reduction under comparable reaction conditions.

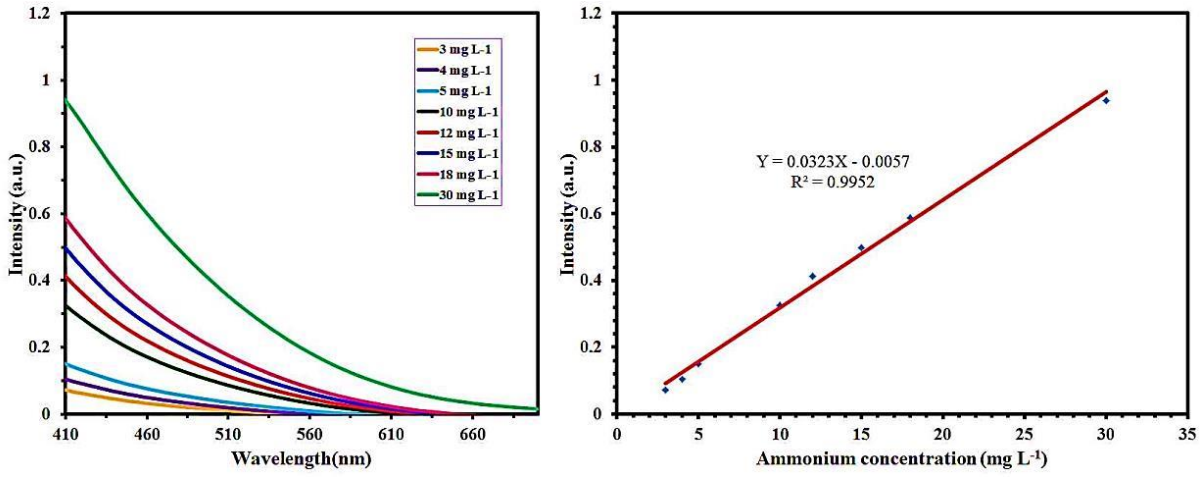

Figure 4.15. Standard plot using the Nessler's reagent method.

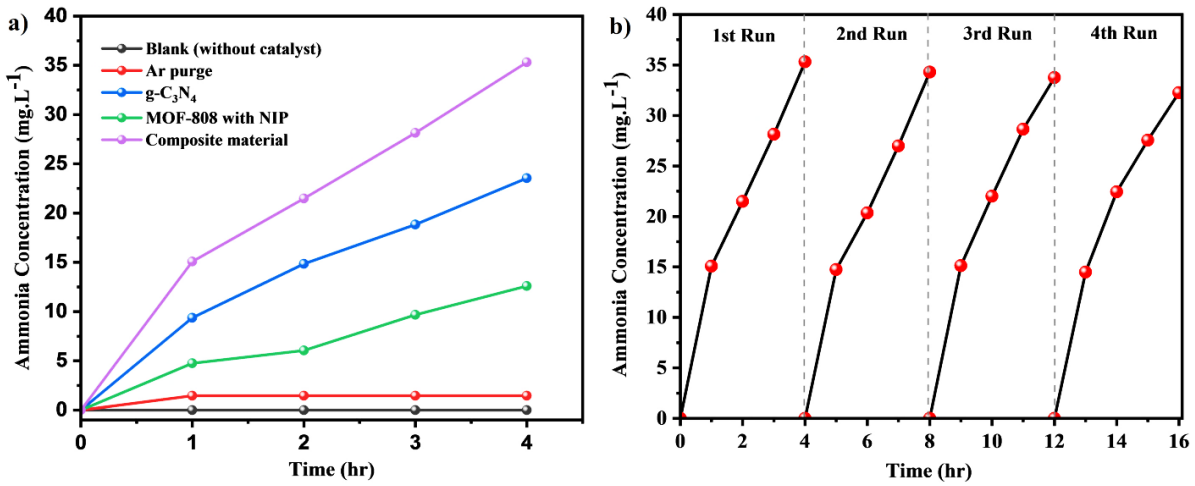

Figure 4.16. Photocatalytic performance of the different structures as determined by the Nessler's reagent method: (**a**) NH_3 evolution using MOF-808/NIP@g-C_3N_4 composite and its components, (**b**) Photocatalytic stability of MOF-808/NIP@g-C_3N_4 during 4-cycling tests, conditions: water, pH=2, visible light (420-700 nm), P = 0.2 W.

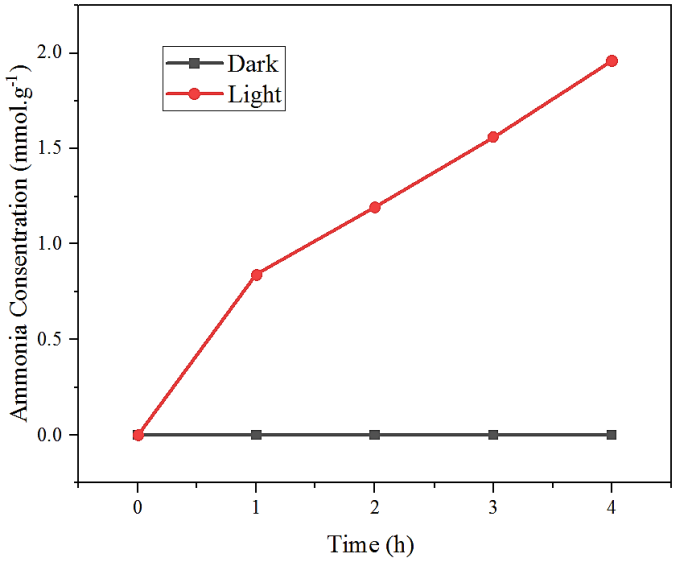

Figure 4.17. Photocatalytic nitrogen fixation activity of MOF-808/NIP@g-C_3N_4 under light irradiation and with no light irradiation.

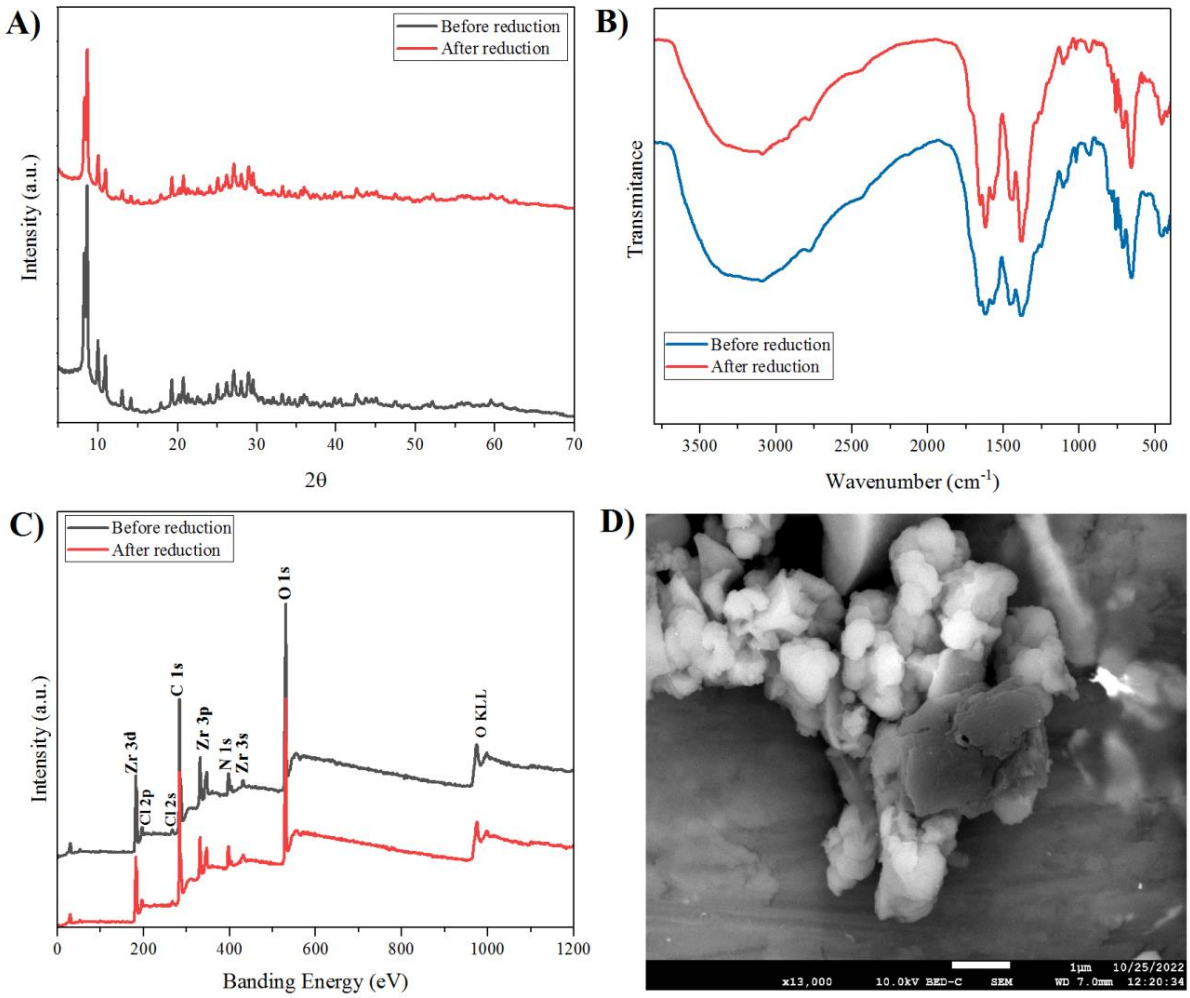

Figure 4.18. Characterization of the recovered MOF-808/NIP@g-C_3N_4: (A) PXRD patterns, (B) FT-IR spectra, (C) The full-scan XPS spectra, and (D) SEM image.

4.3.1 Optical and photoelectric properties

The UV-vis absorbance spectra of the synthesized materials in the 260–800 nm range are depicted in **Fig. 4.19-A**. According to the literature, the absorbance of the MOF-808 is below 400 nm, resulting in low photocatalytic activity in the visible region, due to its wide band gap (~3.8 eV).[59] The absorbance in the visible area was enhanced by incorporation of NIP linker into the MOF-808 structure. According to the Tauc plots (**Fig. 4.19-B**), the band gap energy of MOF-808/NIP and g-C_3N_4 samples were determined to be 2.63 and 2.78 eV, respectively. The close band gap values of these samples could be at the origin of the complete light absorption of their composite in the entire UV-visible region. The Mott-Schottky plots were measured to determine the flat-band position (**Fig. 4.20**). The flat-band potentials of g-C_3N_4 and MOf-

808/NIP were approximately -1.23 and -0.55 V, respectively. It is worth mentioning that the Mott-Schottky plot of the MOF composite validates the existence of the flat band potentials of both constituents of the photocatalyst (**Fig. 4.21**). In *n*-type semiconductors with a positive slope in the Mott-Schottky curves, the CB potential is usually around 0.1 V higher than the flat band potential.[60] As a result, the CB positions of g-C_3N_4 and MOF-808/NIP were determined to be -1.33 and -0.65 V, respectively. Finally, the valence band potentials were deduced from the band gap and CB for g-C_3N_4 and MOF-808/NIP as 1.55 and 2.08 V, respectively.

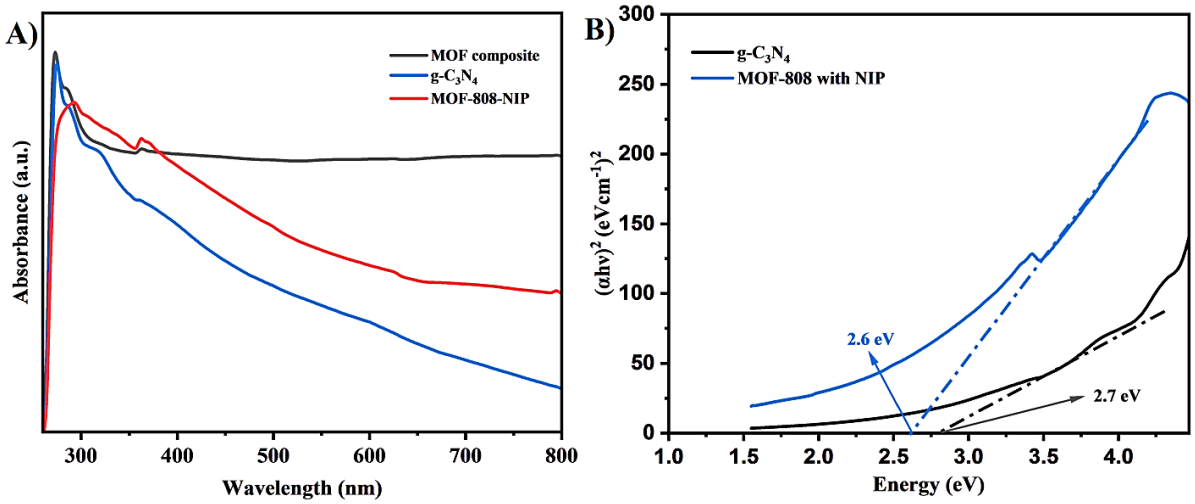

Figure 4.19. (A) UV-vis diffuse reflectance plots of the synthesized materials, (B) Tauc plots of MOF-808/NIP and g-C_3N_4.

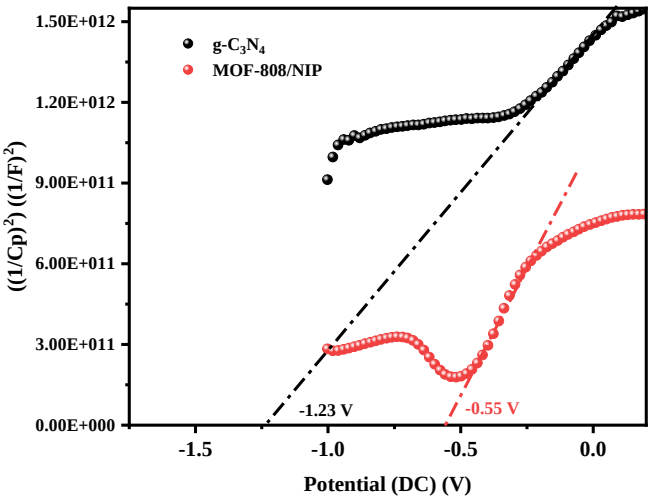

Figure 4.20. Mott−Schottky plots of MOF-808/NIP and g-C_3N_4.

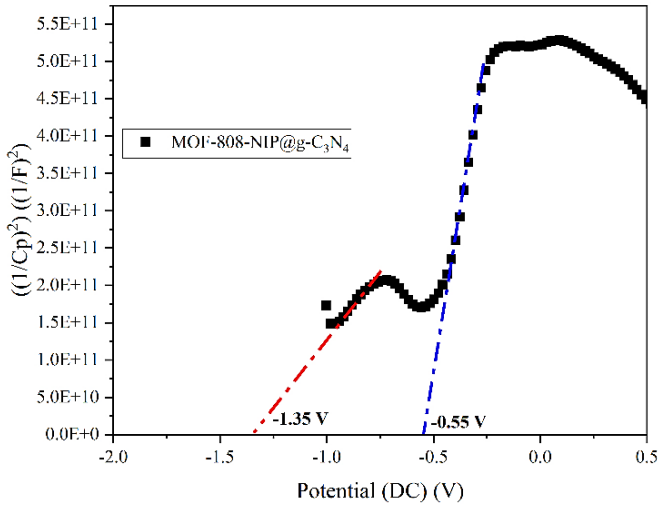

Figure 4.21. Mott−Schottky plot of MOF-808/NIP@g-C_3N_4 composite.

Fig. 4.22 illustrates the results of the electrochemical impedance spectroscopy and photocurrent measurements. In **Figure 4.22-a**, the MOF composite displayed a smaller radius than its components. This indicates that the interfacial resistance of the MOF composite was lower, leading to more efficient electron-hole pair separation and charge transfer. Additionally, as shown in **Figure 4.22-b**, a rapid photocurrent response was observed upon periodic light on−off cycles. The photocurrent intensity of MOF composite was higher than that of g-C_3N_4 and MOF-808/NIP, indicating better charge separation of the MOF composite. Based on the experimental findings, the MOF composite featured enhanced light absorption and photoelectrical characteristics than its individual components.

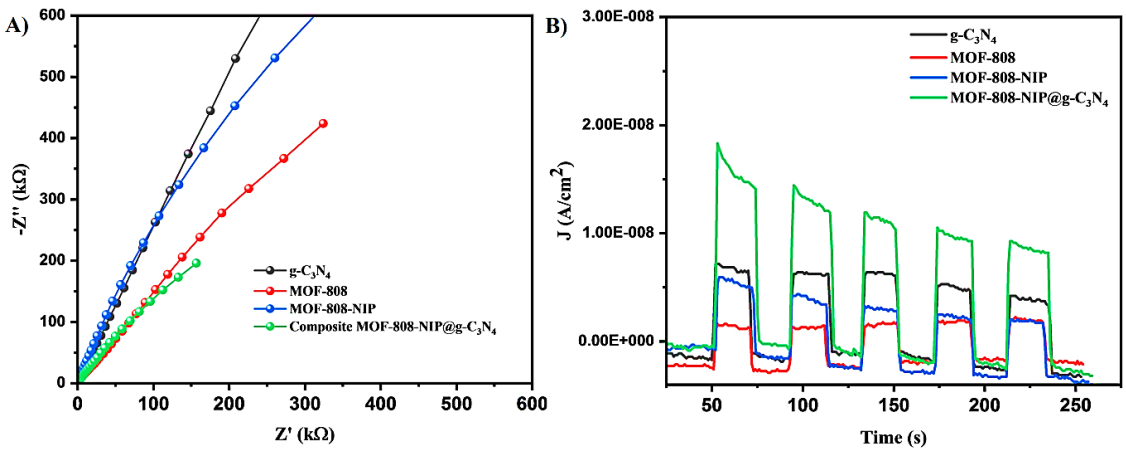

Figure 4.22. a) EIS spectra and b) photocurrent measurements of the prepared photocatalysts.

4.3.2 The Mechanism for Photocatalytic Nitrogen Fixation

To better understand the photochemical nitrogen fixation mechanism, it is crucial to identify the specific role of each component in the performance of the prepared MOF composite. There are several benefits in using MOF-808/NIP as a photocatalytic component. Firstly, the unsaturated metal sites act as Lewis acids and significantly improve the adsorption of N_2 molecules. Secondly, Zr_6 clusters can receive photoexcited electrons from ligands, generating a long-lived charge-separated state. Thirdly, the porous structure facilitates the movement of photoinduced carriers and reduces charge diffusion. Fourthly, the open framework structure allows for free access to substrates and products. Finally, the modified form with NIP linker has a lower band gap energy than MOF-808, making it an excellent source for harvesting visible light. While g-C_3N_4 nanosheets are effective semiconductors that provide a suitable surface for hosting MOF nanoparticles, they are also capable of capturing visible light and generating charge carriers to activate the particles. The combination of these two materials creates a heterojunction composite that can harness light energy to facilitate the reduction of N_2 into ammonia (NH_3). The mechanism of N_2 photoreduction using MOF-808/NIP@g-C_3N_4 as a photocatalyst involves several steps.

Light absorption: The g-C_3N_4 component of the MOF-808/NIP@g-C_3N_4 composite absorbs visible light, owing to its semiconducting properties. This absorption promotes electrons from the valence band to the conduction band, generating electron-hole pairs.

Electron transfer: The excited electrons from g-C_3N_4 are transferred to MOF-808. The latter acts as a co-catalyst, facilitating electron transfer and visible light absorption to provide active sites for subsequent reactions.

Protonation: Protons (H^+) from water as a sacrificial donor source and H_2SO_4 interact with the reduced MOF-808/NIP, forming metal hydrides (M-H). This step typically occurs at metal centres within the MOF structure.

N_2 adsorption: The N_2 molecules are adsorbed onto the MOF-808/NIP surface, specifically at metal sites. The presence of adsorbed N_2 is essential for the subsequent reduction reaction.

Electron and proton transfer to N_2: The excited electrons and protons, generated in the previous steps, are transferred to the adsorbed N_2 molecules. The electrons reduce N_2 to form adsorbed nitrogen intermediates, while the protons combine with these intermediates to form NH_3.

Desorption and release: The NH_3 product is desorbed from the surface of the MOF-808/NIP, completing the N_2 photoreduction process.

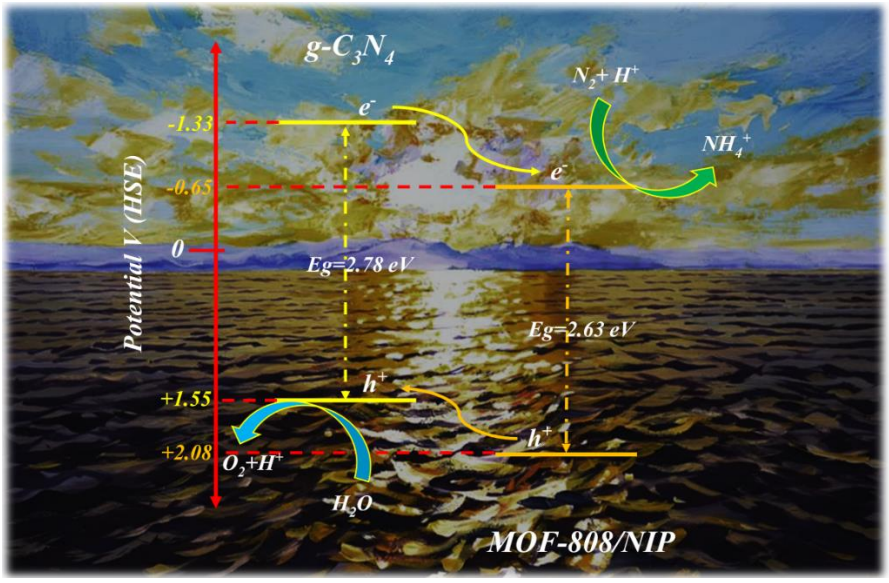

Scheme 4.2. Energy levels of g-C_3N_4 and MOF-808/NIP and mechanism of nitrogen reduction by MOF-808/NIP@g-C_3N_4.

Density functional theory (DFT) was performed to further explain the mechanism of photocatalytic nitrogen fixation.

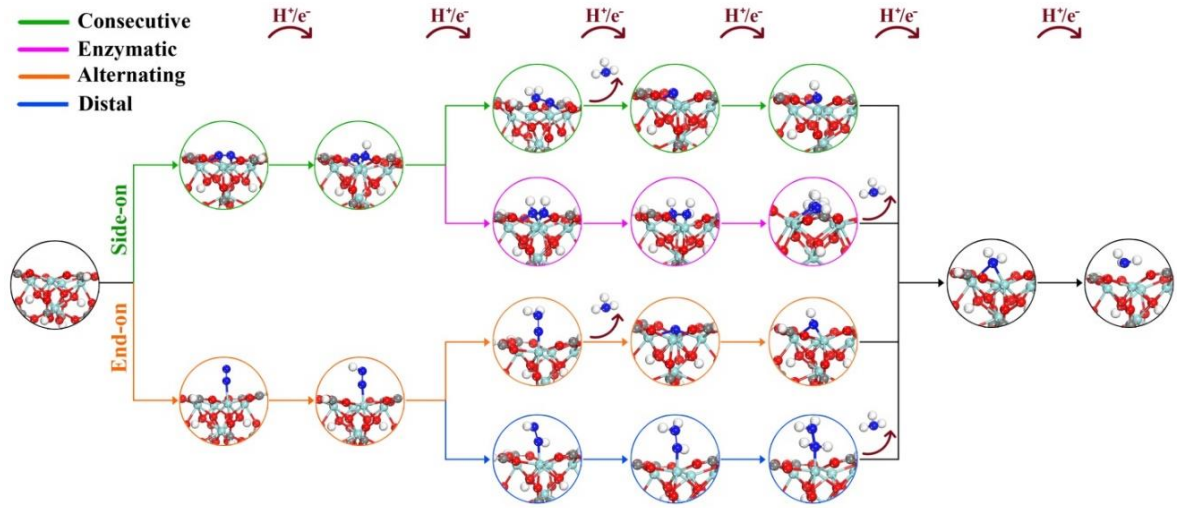

Figure 4.23. Optimized geometries of various mechanisms involved in the nitrogen reduction reaction (NRR).

The catalytic surface can accommodate the adsorbed N_2 in two initial configurations: the side-on and end-on configurations, as shown in **Figure 4.23**. The side-on configuration is composed of consecutive and enzymatic pathways, while the end-on configuration contains alternating and distal pathways, each involving six hydrogenation steps. In case of distal and consecutive mechanisms, the hydrogenation first targets one nitrogen pair, which is transformed into NH_3, followed by the interaction with the other N atom to produce the second NH_3 molecule. While, in alternating and enzymatic reduction pathways, the two nitrogen atoms undergo interaction with hydrogen alternatively. To assess the catalytic performance of MOF-808/g-C_3N_4 in reducing N_2 to NH_3, we examined all possible pathways, as shown in **Figure 4.24**. In case of side-on (end-on) configuration, the adsorbed N_2 reacts with hydrogenation to form *N-*NH (*N-NH) with a downhill free energy of -1.59 eV (-1.07 eV). This indicates that the parallel mode of N_2 adsorption is more energetically favourable than the perpendicular mode. However, the enzymatic pathway was found to have the highest limiting potential of 0.71 eV ($*NH_2$-$*NH_2 \rightarrow *NH_2$), while the consecutive pathway possesses 0.62 eV (*N-*NH $\rightarrow$ *N-$*NH_2$). In case of alternating and distal pathways, the limiting potential was determined to be 0.56 eV ($*NH_2 \rightarrow *NH_3$). Upon considering the side-on configuration, the second hydrogenation takes place on the reactive intermediate *N-*NH, resulting in either the formation of *NH-*NH

through an enzymatic mechanism or *N-*NH_2 via consecutive pathway. When the reactive intermediate is subjected to hydrogenation, it can either produce NH_3 or result in the formation of *NH-*NH_2. However, in case of end-on mechanism, the second and third hydrogenations lead to the formation of *NH-NH and *NH-NH_2 via the distal pathway, while the alternating mechanism results in the formation of *N-NH_2, followed by the release of NH_3. The highly exergonic adsorption of *NH_2-*NH_2 and the subsequent hydrogenation in the enzymatic pathway lead to the dissociation of N-N, thereby releasing the NH_3 molecule. However, the strong binding of the ammonia molecule to the catalyst in the enzymatic route could potentially hinder the effectiveness and practicality of the N_2 reduction. Both mechanisms share the same last two steps of hydrogenation, with the desorption of the *NH_3 molecule in the final step exhibiting a slight uphill trend. Overall, these findings suggest that MOF-808/g-C_3N_4 exhibits high efficiency in terms of exothermic N_2 adsorption, facilitating the reduction process and resulting in the release of NH_3.

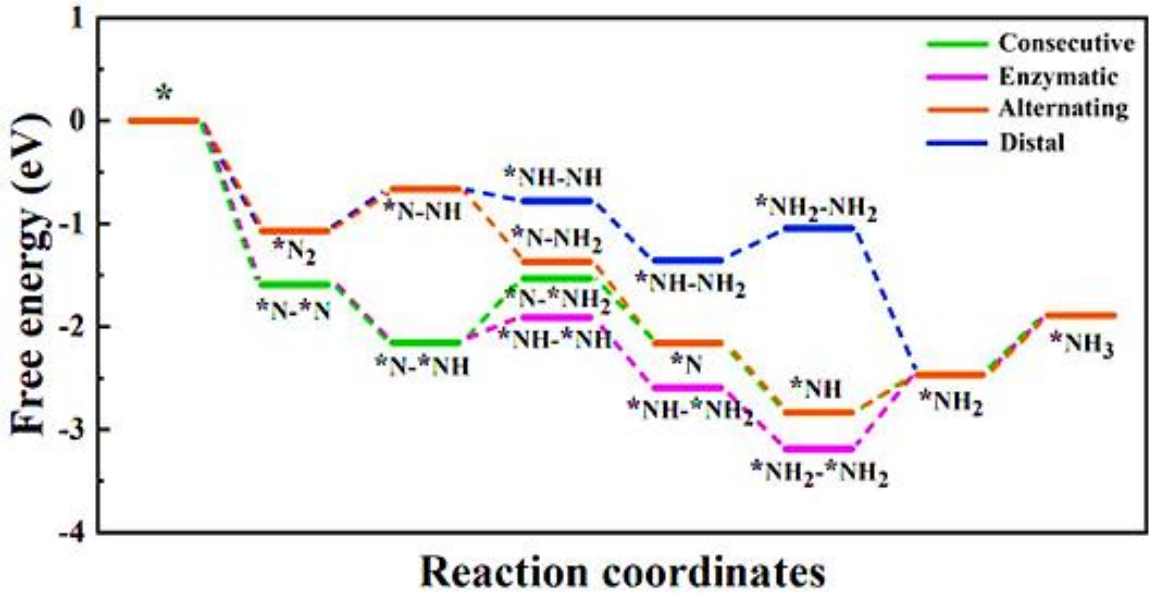

Figure 4.24. Free energy profile of the nitrogen reduction reaction (NRR) along consecutive, enzymatic, alternating and distal pathways.

Table 4.6. Performance comparison of various MOF-based photocatalysts for N_2 reduction.

Catalysts	Reaction medium	Scavenger	Light source	Detection Method	Ammonia generation rate (μmol $g_{cat.}^{-1}$ h^{-1})	Ref.
UiO-66-UV-vis	H_2O	None	Xenon Lamp (300 W) full spectrum	Colorimetry	198.4	[61]
ZIF-67@PMo_9V_3	H_2O/ Ethanol 80:20	None	Xenon Lamp (300w) Full spectrum	Nessler's reagent	149	[62]
Au@UiO-66/PTFE membrane	H_2O	None	Xenon lamp (300 W) λ≥400 nm	Nessler's reagent	330	[63]
MOF-74@C_3N_4	H_2O/ Methanol 48ml/2ml	None	Xenon lamp (300 W) λ≥400 nm	Nessler's reagent	2320	[64]
g-C_3N_4	H_2O pH=2	None	Xenon lamp (150 W) λ≥400 nm	Nessler's reagent	327	**This work**
MOF-808/NIP	H_2O pH=2	None	Xenon lamp (150 W) λ≥400 nm	Nessler's reagent	177.5	**This work**
MOF-808/NIP@ g-C_3N_4	H_2O pH=2	None	Xenon lamp (150 W) λ≥400 nm	Nessler's reagent	490	**This work**

4.4 Conclusion

In summary, 5-nitro isophthalic acid linker was incorporated into MOF-808 to create a photocatalyst that absorbs visible light. The modified structure was combined with g-C_3N_4 to synthesize the MOF-808/NIP@g-C_3N_4 heterojunction composite. This composite was used for photochemical N_2 fixation and NH_3 production in water under visible light irradiation and ambient conditions. The results of the N_2 photoreduction showed that the synthesized MOF composite had better optical properties and performance (490 μmol g^{-1} h^{-1}) than both of its components (g-C_3N_4 (327 μmol g^{-1} h^{-1}) and MOF-808/NIP (178 μmol g^{-1} h^{-1}) and can absorb

light in the entire UV-visible area. Based on the data analysis, the different parts of the composite worked together seamlessly. The acceptor groups in the MOF structure, consisting of nitro groups, effectively interacted with the N-$(C)_3$ free electron pairs in the g-C_3N_4 network nodes. Furthermore, the results of DFT calculations suggested that MOF-808/g-C_3N_4 features remarkable effectiveness in exothermic N_2 adsorption, which greatly aids in the reduction process and consequently leads to the release of NH_3. The findings from this study offer valuable insights into the engineering of band gap energy in MOF structures and the selection of appropriate semiconductors for hybridization. These insights can be applied in developing solar-driven photocatalytic reactions such as N_2 or CO_2 photoreduction processes.

4.5 References

(1) Tong, Y.; Guo, H.; Liu, D.; Yan, X.; Su, P.; Liang, J.; Zhou, S.; Liu, J.; Lu, G. Q. (Max); Dou, S. X. *Angew. Chemie Int. Ed.* **2020**, *59* (19), 7356–7361.

(2) Kobayashi, H.; Hayakawa, A.; Somarathne, K. D. K. A.; Okafor, E. C. *Proc. Combust. Inst.* **2019**, *37* (1), 109–133.

(3) Cong, S.; Yuan, Y.; Chen, Z.; Hou, J.; Yang, M.; Su, Y.; Zhang, Y.; Li, L.; Li, Q.; Geng, F.; Zhao, Z. *Nat. Commun.* **2015**, *6* (1), 7800.

(4) Wang, W.; Herreros, J. M.; Tsolakis, A.; York, A. P. E. *Int. J. Hydrogen Energy* **2013**, *38* (23), 9907–9917.

(5) Tanabe, Y.; Nishibayashi, Y. *Coord. Chem. Rev.* **2013**, *257* (17), 2551–2564.

(6) Medford, A. J.; Hatzell, M. C. *ACS Catal.* **2017**, *7* (4), 2624–2643.

(7) Zhang, H.; Liu, G.; Shi, L.; Liu, H.; Wang, T.; Ye, J. *Nano Energy* **2016**, *22*, 149–168.

(8) Kubacka, A.; Fernández-García, M.; Colón, G. *Chem. Rev.* **2012**, *112* (3), 1555–1614.

(9) Guo, X.; Liu, L.; Xiao, Y.; Qi, Y.; Duan, C.; Zhang, F. *Coord. Chem. Rev.* **2021**, *435*, 213785.

(10) Kou, J.; Lu, C.; Wang, J.; Chen, Y.; Xu, Z.; Varma, R. S. *Chem. Rev.* **2017**, *117* (3), 1445–1514.

(11) Weng, B.; Qi, M.-Y.; Han, C.; Tang, Z.-R.; Xu, Y.-J. *ACS Catal.* **2019**, *9* (5), 4642–4687.

(12) Li, J.; Li, H.; Zhan, G.; Zhang, L. *Acc. Chem. Res.* **2017**, *50* (1), 112–121.

(13) Shiraishi, Y.; Shiota, S.; Kofuji, Y.; Hashimoto, M.; Chishiro, K.; Hirakawa, H.; Tanaka, S.; Ichikawa, S.; Hirai, T. *ACS Appl. Energy Mater.* **2018**, *1* (8), 4169–4177.

(14) Li, M.; Huang, H.; Low, J.; Gao, C.; Long, R.; Xiong, Y. *Small Methods* **2019**, *3* (6), 1800388.

(15) Jia, H.-P.; Quadrelli, E. A. *Chem. Soc. Rev.* **2014**, *43* (2), 547–564.

(16) Guo, K.; Hussain, I.; Jie, G.; Fu, Y.; Zhang, F.; Zhu, W. *J. Environ. Sci.* **2023**, *125*, 290–308.

(17) Younis, S. A.; Kwon, E. E.; Qasim, M.; Kim, K.-H.; Kim, T.; Kukkar, D.; Dou, X.; Ali, I. *Prog. Energy Combust. Sci.* **2020**, *81*, 100870.

(18) Xiao, J.-D.; Jiang, H.-L. *Small* **2017**, *13* (28), 1700632.

(19) Bai, Y.; Dou, Y.; Xie, L.-H.; Rutledge, W.; Li, J.-R.; Zhou, H.-C. *Chem. Soc. Rev.* **2016**, *45* (8), 2327–2367.

(20) Shokouhfar, N.; Aboutorabi, L.; Morsali, A. *Dalt. Trans.* **2018**, *47* (41), 14549–14555.

(21) Zhang, X.; Tong, S.; Huang, D.; Liu, Z.; Shao, B.; Liang, Q.; Wu, T.; Pan, Y.; Huang, J.; Liu, Y.; Cheng, M.; Chen, M. *Coord. Chem. Rev.* **2021**, *448*, 214177.

(22) Aziz, A.; Ruiz-Salvador, A. R.; Hernández, N. C.; Calero, S.; Hamad, S.; Grau-Crespo, R. *J. Mater. Chem. A* **2017**, *5* (23), 11894–11904.

(23) Usman, M.; Mendiratta, S.; Lu, K.-L. *Adv. Mater.* **2017**, *29* (6), 1605071.

(24) Zhang, T.; Jin, Y.; Shi, Y.; Li, M.; Li, J.; Duan, C. *Coord. Chem. Rev.* **2019**, *380*, 201–229.

(25) Luo, H.; Zeng, Z.; Zeng, G.; Zhang, C.; Xiao, R.; Huang, D.; Lai, C.; Cheng, M.; Wang, W.; Xiong, W.; Yang, Y.; Qin, L.; Zhou, C.; Wang, H.; Zhou, Y.; Tian, S. *Chem. Eng. J.* **2020**, *383*, 123196.

(26) Wen, J.; Xie, J.; Chen, X.; Li, X. *Appl. Surf. Sci.* **2017**, *391*, 72–123.

(27) Dong, G.; Ho, W.; Wang, C. *J. Mater. Chem. A* **2015**, *3* (46), 23435–23441.

(28) Hu, S.; Chen, X.; Li, Q.; Li, F.; Fan, Z.; Wang, H.; Wang, Y.; Zheng, B.; Wu, G. *Appl. Catal. B Environ.* **2017**, *201*, 58–69.

(29) Zhang, S.; He, Z.; Xu, S.; Li, X.; Zhang, J.; Zhan, X.; Dai, M.; Wang, S. *Sol. RRL* **2021**, *5* (8), 2100233.

(30) Hasnan, N. S. N.; Mohamed, M. A.; Mohd Hir, Z. A. *Adv. Mater. Technol.* **2022**, *7* (5), 2100993.

(31) Ding, Z.; Wang, S.; Chang, X.; Wang, D.-H.; Zhang, T. *RSC Adv.* **2020**, *10* (44), 26246–26255.

(32) Wang, Z.; Wang, H.; Zeng, Z.; Zeng, G.; Xu, P.; Xiao, R.; Huang, D.; Chen, X.; He, L.; Zhou,

C.; Yang, Y.; Wang, Z.; Wang, W.; Xiong, W. *Appl. Catal. B Environ.* **2020**, *267*, 118700.

(33) Cedeno, R. M.; Cedeno, R.; Gapol, M. A.; Lerdwiriyanupap, T.; Impeng, S.; Flood, A.; Bureekaew, S. *Inorg. Chem.* **2021**, *60* (12), 8908–8916.

(34) Romero-Muñiz, I.; Romero-Muñiz, C.; del Castillo-Velilla, I.; Marini, C.; Calero, S.; Zamora, F.; Platero-Prats, A. E. *ACS Appl. Mater. Interfaces* **2022**, *14* (23), 27040–27047.

(35) Boronat, M.; Concepción, P.; Corma, A.; González, S.; Illas, F.; Serna, P. *J. Am. Chem. Soc.* **2007**, *129* (51), 16230–16237.

(36) Singh, N.; Patel, K.; Sahoo, S. K.; Pati, R. K.; Kumar, R. *J. Mater. Chem. A* **2017**, *5* (7), 3389–3403.

(37) Thirupathi, B.; Smirniotis, P. G. *Appl. Catal. B Environ.* **2011**, *110*, 195–206.

(38) Ye, L.; Liu, J.; Jiang, Z.; Peng, T.; Zan, L. *Appl. Catal. B Environ.* **2013**, *142–143*, 1–7.

(39) Mazumder, A.; Sebastian, E.; Hariharan, M. *Chem. Sci.* **2022**, *13* (30), 8860–8870.

(40) Gulaczyk, I.; Kręglewski, M.; Valentin, A. *J. Mol. Spectrosc.* **2003**, *220* (1), 132–136.

(41) Yang, D.; Gaggioli, C. A.; Ray, D.; Babucci, M.; Gagliardi, L.; Gates, B. C. *J. Am. Chem. Soc.* **2020**, *142* (17), 8044–8056.

(42) Thommes, M.; Kaneko, K.; Neimark, A. V; Olivier, J. P.; Rodriguez-Reinoso, F.; Rouquerol, J.; Sing, K. S. W. *Pure Appl. Chem*. **2015**, *87* (9–10), 1051–1069.

(43) Feng, X.; Hajek, J.; Jena, H. S.; Wang, G.; Veerapandian, S. K. P.; Morent, R.; De Geyter, N.; Leyssens, K.; Hoffman, A. E. J.; Meynen, V.; Marquez, C.; De Vos, D. E.; Van Speybroeck, V.; Leus, K.; Van Der Voort, P. *J. Am. Chem. Soc.* **2020**, *142* (6), 3174–3183.

(44) Dai, H.; Gao, X.; Liu, E.; Yang, Y.; Hou, W.; Kang, L.; Fan, J.; Hu, X. *Diamond Relat. Mater.* **2013**, *38*, 109–117.

(45) Hu, S.; Ma, L.; You, J.; Li, F.; Fan, Z.; Lu, G.; Liu, D.; Gui, J. *Appl. Surf. Sci.* **2014**, *311*, 164–171.

(46) Fu, X.; Hu, X.; Yan, Z.; Lei, K.; Li, F.; Cheng, F.; Chen, J. *Chem. Commun.* **2016**, *52* (8), 1725–1728.

(47) Zou, J.; Yu, Y.; Qiao, K.; Wu, S.; Yan, W.; Cheng, S.; Jiang, N.; Wang, J. *J. Mater. Sci.* **2020**, *55* (28), 13618–13633.

(48) Paz, R.; Viltres, H.; Gupta, N. K.; Romero-Galarza, A.; Leyva, C. *Environ. Sci. Adv.* **2022**, *1* (2), 182–191.

(49) Hendrickson, D. N.; Hollander, J. M.; Jolly, W. L. *Inorg. Chem.* **1969**, *8* (12), 2642–2647.

(50) Yao, S.-H.; Su, Y.-L.; Lai, Y.-C. *Materials. (Basel, Switzerland)* **2017**, *10* (10).

(51) Cubillos, G. I.; Romero, E. *Sci. Rep.* **2021**, *11* (1), 18926.

(52) Kabir, S.; Artyushkova, K.; Serov, A.; Kiefer, B. *Surf. Interface Anal.* **2016**, *48* (5), 293–300.

(53) Batich, C. D.; Donald, D. S. *J. Am. Chem. Soc.* **1984**, *106* (10), 2758–2761.

(54) Luo, C.; Ji, X.; Hou, S.; Eidson, N.; Fan, X.; Liang, Y.; Deng, T.; Jiang, J.; Wang, C. *Adv. Mater.* **2018**, *30* (23), 1706498.

(55) Brundle, C. R. *J. Vac. Sci. Technol.* **1976**, *13* (1), 301–309. https://doi.org/10.1116/1.568833.

(56) Fu, M.; Deng, X.; Wang, S.-Q.; Yang, F.; Lin, L.-C.; Zaworotko, M. J.; Dong, Y. *Sep. Purif. Technol.* **2022**, *288*, 120620.

(57) Baumann, A. E.; Han, X.; Butala, M. M.; Thoi, V. S. *J. Am. Chem. Soc.* **2019**, *141* (44), 17891–17899.

(58) Zhao, Y.; Shi, R.; Bian, X.; Zhou, C.; Zhao, Y.; Zhang, S.; Wu, F.; Waterhouse, G. I. N.; Wu, L.-Z.; Tung, C.-H.; Zhang, T. *Adv. Sci.* **2019**, *6* (8), 1802109.

(59) Taddei, M.; Schukraft, G. M.; Warwick, M. E. A.; Tiana, D.; McPherson, M. J.; Jones, D. R.; Petit, C. *J. Mater. Chem. A* **2019**, *7* (41), 23781–23786.

(60) Battula, V. R.; Kumar, S.; Chauhan, D. K.; Samanta, S.; Kailasam, K. *Appl. Catal. B Environ.* **2019**, *244*, 313–319.

(61) Gao, W.; Li, X.; Zhang, X.; Su, S.; Luo, S.; Huang, R.; Jing, Y.; Luo, M. *Nanoscale* **2021**, *13* (16), 7801–7809.

(62) Li, X.-H.; He, P.; Wang, T.; Zhang, X.-W.; Chen, W.-L.; Li, Y.-G. *ChemSusChem* **2020**, *13* (10), 2769–2778.

(63) Chen, L.-W.; Hao, Y.-C.; Guo, Y.; Zhang, Q.; Li, J.; Gao, W.-Y.; Ren, L.; Su, X.; Hu, L.; Zhang, N.; Li, S.; Feng, X.; Gu, L.; Zhang, Y.-W.; Yin, A.-X.; Wang, B. *J. Am. Chem. Soc.* **2021**, *143* (15), 5727–5736.

(64) Ding, Z.; Wang, S.; Chang, X.; Wang, D.-H.; Zhang, T. *RSC Adv.* **2020**, *10* (44), 26246–26255.

Chapter 5

Conclusion & Perspective

5.1 General Conclusion

Innovative approaches to sustainable water treatment and solar fuel conversion have been developed in response to worldwide concerns about water shortage and energy security. With their unique qualities and adaptable topologies, metal-organic frameworks (MOFs) have been recognized as potential materials in this field. In this thesis, we concentrated on the synthesis and characterization of Zr-based metal-organic frameworks (MOFs), particularly MOF-808/NIP@g-C_3N_4 for N_2 photoreduction and TMU-66 for water pollutant adsorption. Our study provided essential knowledge about these materials' properties and prospective uses.

In our study of adsorption using TMU-66, a hollow Zr-MOF sphere with isonicotinic acid N-oxide, we found that this material is an effective adsorbent for anionic dyes bearing multiple sulfonic or carboxylic acid groups and high negative charges. Among the investigated dyes, Congo Red (CR) exhibited the highest adsorption capacity on TMU-66 in the pH range of 5 to 10, where CR molecules carried the highest negative charge and displayed good solubility. TMU-66 achieved a high adsorption capacity of 475 mg g^{-1} for Congo red at pH 6.8 and 25 °C. The adsorption of CR onto TMU-66 was a two-step process, with a rapid initial adsorption followed by a slower process, indicating the involvement of micro-mesoporous shell structures and N-oxide functional groups in TMU-66 spheres. We confirmed the formation of a monolayer of CR molecules on the surface of TMU-66 by analyzing the adsorption isotherm and using various techniques, such as FT-IR, PXRD and XPS. Our findings revealed crucial interactions, such as electrostatic attraction, π-π stacking, and linker and Zr node interactions. These results provided valuable insights into the mechanism of CR adsorption on TMU-66 and highlighted its potential in effective removal of dyes from wastewater.

Next, we successfully synthesized a photocatalyst that can absorb visible light by incorporating a 5-nitro isophthalic acid linker into MOF-808. This modified structure was combined with g-C_3N_4 to produce a MOF-808/NIP@g-C_3N_4 heterojunction composite. Under ambient

conditions and visible light, this composite showed remarkable performance in photochemical N_2 fixation and NH_3 production. Our results demonstrated that the synthesized MOF composite had superior optical properties and performance (490 μmol g^{-1} h^{-1}) compared to its individual components, such as g-C_3N_4 (327 μmol g^{-1} h^{-1}) and MOF-808/NIP (178 μmol g^{-1} h^{-1}), as evidenced in the N_2 photoreduction tests. Our research revealed that the composite had a remarkable ability to absorb both UV and visible light. Through careful analysis of the data and DFT calculations, it was found that the acceptor groups, particularly the nitro groups, within the MOF structure interacted seamlessly with the N-$(C)_3$ free electron pairs in the g-C_3N_4 network nodes. Additionally, our results demonstrated that MOF-808/g-C_3N_4 was efficient in N_2 adsorption, which facilitated the reduction process and release of NH_3. These valuable findings provided crucial insights into band gap energy engineering in MOF structures and the selection of appropriate semiconductors for hybridization, with significant implications for advancing solar-driven photocatalytic reactions, such as N_2 or CO_2 photoreduction processes.

In summary, our research on Zr-MOFs revealed their immense potential for addressing critical global challenges related to water scarcity, energy security, and environmental degradation. The findings presented in this dissertation are significant in advancing sustainable water treatment and solar-to-fuel conversion solutions. Further investigation and improvement of these materials are promising for developing effective and eco-friendly technologies in environmental science and catalysis.

5.2 Perspectives

In this work, we have demonstrated the synthesis and characterization of Zr-MOFs and their composites for the adsorption of water pollutants and N_2 photoreduction. However, some limitations still need to be addressed, and some opportunities can be explored for further improvement and extension of this work. Some of the possible directions for future research are suggested below:

- ✓ Despite the inherent stability and catalytic activity of Zr-MOFs, it is crucial to note that these compounds possess a wide band gap, rendering them unsuitable for solar-fuel applications without modification or hybridization with other semiconductors. This thesis highlighted the importance of bandgap engineering and the exploration of mix-linker Zr-MOFs to enable their effective utilization in solar-fuel applications. As a step towards this goal, we also synthesized Bi-based MOFs for N_2 photoreduction.
- ✓ To mitigate the errors associated with colorimetry methods like Nessler's reagents, we suggest alternative direct methods such as ion chromatography or HNMR to accurately detect ammonia production during the N_2 photoreduction process.
- ✓ Overcoming the challenges involved in N_2 photoreduction, including the high stability of N_2, necessitates the exploration of methods such as photo-electrochemical or photo-piezo catalytic methods to enhance the ammonia production yield. In pursuit of this, we evaluated the N_2 fixation results using a Bi-Fe oxide compound under piezo and photocatalytic conditions.
- ✓ The synthesis methods employed in this research, namely solvothermal and vial methods, were relatively simple and convenient but had certain drawbacks, such as prolonged reaction time, high temperature, high pressure, or solvent consumption. Hence, it would be advantageous to develop alternative synthesis approaches like

microwave-assisted, ultrasound-assisted, or electrochemical methods that reduce synthesis time, energy consumption and environmental impact.

- ✓ The photocatalytic investigations conducted on MOF@g-C_3N_4 composites were primarily focused on N_2 photoreduction under visible light under ambient conditions. Further exploration of these composites in other photocatalytic reactions, such as CO_2 reduction, H_2O splitting, or organic degradation, would be worthwhile. Evaluating their efficiency and selectivity under different light sources and reaction conditions would provide valuable insights.